Earth Sciences and Mathematics

Volume II

Edited by
Antonio G. Camacho
Jesús I. Díaz
José Fernández

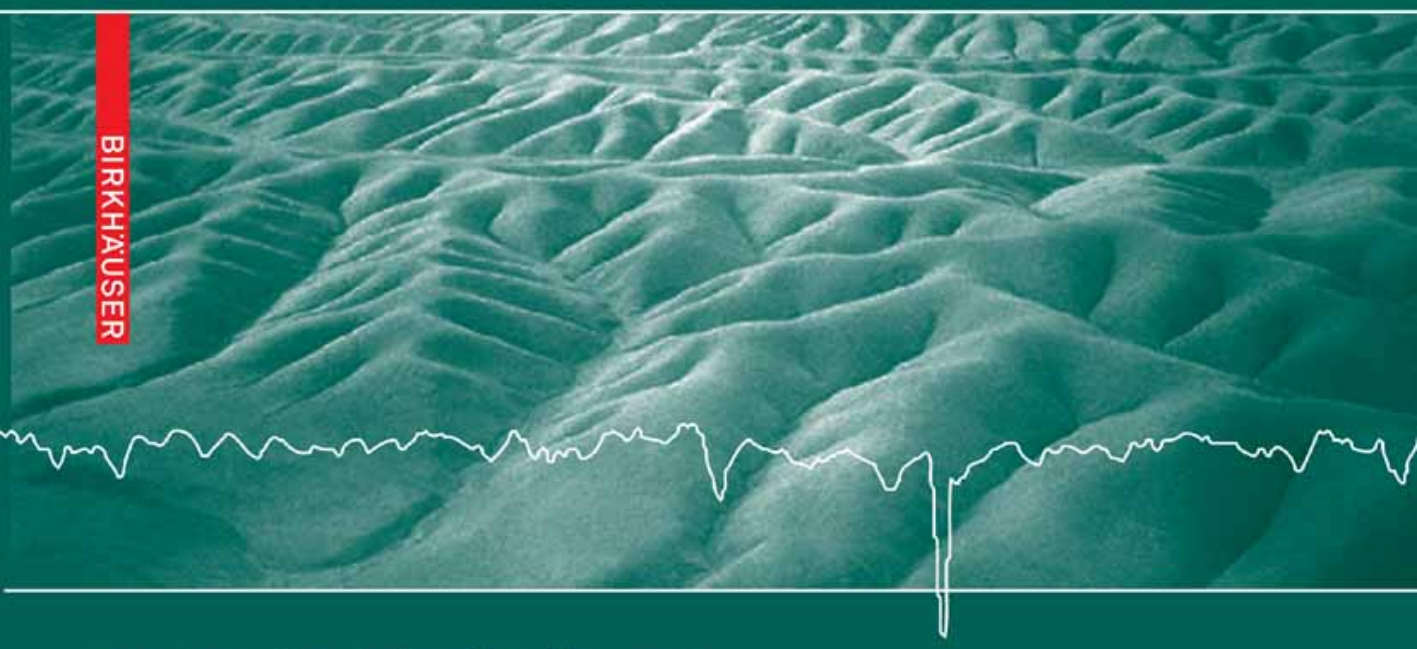

pageoph topical volumes

BIRKHÄUSER

Earth Sciences and **Mathematics**

Volume II

Edited by
Antonio G. Camacho
Jesús I. Díaz
José Fernández

Birkhäuser
Basel · Boston · Berlin

Reprint from Pure and Applied Geophysics
(PAGEOPH), Volume 165 (2008) No. 8

Editors:
Antonio G. Camacho
José Fernández
Instituto de Astronomía y Geodesia
(CSIC-UCM)
Facultad Ciencias Matemáticas
Universidad Complutense Madrid
Ciudad Universitaria
Plaza de Ciencias 3
28040 Madrid
Spain
Email: antonio_camacho@mat.ucm.es
jose_fernandez@mat.ucm.es

Jesús I. Díaz
Instituto de Matemática Interdisciplinar (IMI)
Departamento de Matemática Aplicada
Facultad Ciencias Matemáticas
Universidad Complutense Madrid
Ciudad Universitaria
Plaza de Ciencias 3
28040 Madrid
Spain
Email: diaz.racefyn@insde.es

Library of Congress Control Number: 2008932710

Bibliographic information published by Die Deutsche Bibliothek:
Die Deutsche Bibliothek lists this publication in the Deutsche Nationalbibliografie; detailed bibliographic data is available in the Internet at <http://dnb.ddb.de>

ISBN 978-3-7643-9963-4 Birkhäuser Verlag AG, Basel · Boston · Berlin

ISBN 978-3-7643-9963-4 e-ISBN 978-3-7643-9964-1

9 8 7 6 5 4 3 2 1 www.birkhauser.ch

Contents

Pure appl. geophys. 165 (2008) 1459–1463
0033–4553/08/081459–5
DOI 10.1007/s00024-008-0396-7

Pure and Applied Geophysics

Introduction to Earth Sciences and Mathematics, Volume II

A. G. Camacho,[1] J. I. Díaz,[2] and J. Fernández[1]

Knowledge of the Earth's structure and dynamics calls for a multi-disciplinary study that makes use of the most advanced methods of Physics, Chemistry, Geology, Mathematics and Information Technology, in the framework, or in close collaboration with, the different branches of Earth Sciences such as Geology, Geophysics and Geodesy. The research to be developed includes subjects ranging from data acquisition, both with traditional techniques and with the most advanced resources of our time; data treatment and processing; to the development of new modelling methodologies for the simulation and reproduction and prediction of the terrestrial processes on a local, regional and, by far the most ambitious, global scale.

The large amount of geological, geophysical and geodetic high precision observation data about the Earth available acquired both from the planet itself and from space, grows and grows. Currently one can obtain an abundance of high precision data that covers the widest areas desired. Often the time or space distribution of these data is almost continuous, and substantial data have been obtained by unconventional techniques. In view of the privileged state at present, we must reconsider the connection and utilization of the abundant data with the more theoretical studies that offer new and more refined mathematical models, capable of making the most of the technological breakthroughs in observation. In the words of Jacques-Louis Lions (1928–2001): "*If we accept that any mathematical models isolated of any experimental data have no predictive value, similarly, we must recognize that the most abundant data banks without good mathematical models produce nothing more than confusion*".

What is required is to develop new mathematical, analytical and numerical, models and methods for data processing and modelling, considering their ever-increasing quality, variety of origin (terrestrial and space), type (it is becoming increasingly possible to measure larger numbers of parameters simultaneously that can be related to one another), time (data acquired sporadically or continuously) and space extension (ranging from disperse spots to almost continuous observation in space).

[1] Instituto de Astronomía y Geodesia (CSIC-UCM), Fac. C. Matemáticas, Universidad Complutense de Madrid, Plaza de Ciencias, 3, 28040 Madrid, Spain. E-mail: antonio_camacho@mat.ucm.es

[2] Instituto de Matemática Interdisciplinar (IMI) and Departamento de Matemática Aplicada, Fac. C. Matemáticas, Universidad Complutense de Madrid, Ciudad Universitaria, Plaza de Ciencias, 3, 28040 Madrid, Spain. E-mail: ji_diaz@mat.ucm.es

The generalized use of the data obtained in observing the Earth from space (ESA, 2008; NASA, 2008), the ever-increasing number of problems in which they are applicable, and the need to combine them with the data acquired on Earth, poses new problems both in the field of the statistical processing of the data and in their use by society. All of this requires the involvement of specialists in such differing subjects as decision-making support, operational research and artificial intelligence.

Furthermore, the efficient use of these terrestrial and space data also requires the assistance of the most sophisticated mathematical models that permit the correct interpretation of these data together. At present, numerous problems remain to be solved in this field, and there is strong demand for inversion models and techniques, and for other mathematical tools, among the community of Earth Sciences specialists. One very illustrative example of that interaction with sophisticated mathematical techniques refers to the application of the latest mathematical developments on complex systems and chaos theory to the specific case of Earth Sciences. By the other side, Geosciences gives to mathematicians new, and difficult, problems which sometimes need new developments to be at least partially solved. Therefore a closer cooperation between researchers from both fields becomes everyday more necessary and is a basic aspect to carry out many works to understand and solve problems related to geodynamics, natural hazards, global change, etc.

From the need for a better application and integration of mathematics in the study of the Earth, the name of Geomathematics has been put forward to combine the research and works that seek to develop and incorporate new methods, approaches and solutions from different areas of mathematics, such as Statistics, Operational Research, Artificial Intelligence and, more general, from Applied Mathematics, with special emphasis on its Modelling, Analysis, Numerical and Computational Approximation methods and processes, and its Control Theory techniques.

Yet that mathematical study of the Earth could never be carried out successfully without the close collaboration with specialists of all branches (Geology, Geophysics and Geodesy) of Earth Sciences. The international (not to mention planetary) dimension at which these contacts must be maintained is evident (see e.g., IUGS, 2008; IUGG, 2008). This philosophy, many aspects of which are already in place, will make it possible to tackle the most current and ambitious scientific challenges that our society requires and will also trigger important advances in the frontier of knowledge and culture that will redound positively to the welfare of society.

Geomathematical research involves such diverse studies as flow models (porous materials, glaciers, etc.), sedimentation and diagenesis, global change models, wave propagation, classification of the Earth's surface, riskmap analysis, parameter sensitivity analysis in inverse problems, stochastic models for processing terrestrial and space data, direct deterministic models, chaos theory applied to Earth Sciences, geostatistical software, poor, incomplete or truncated information problems, time series analysis, information dimension reduction, information representation, interfaces for reports in specific fields, handling linguistic information, nonlinear processes in Earth Sciences,

study of geological structures and phenomena with invariance of scale by means of self-organized criticality methods and fractal-type space distributions, etc.

Considering this perspective of the evolution of Earth Sciences and with the idea of fostering the aforementioned collaboration, the Complutense International Seminar on "Earth Sciences and Mathematics" was organized and held in Madrid at the Facultad de Ciencias Matemáticas of the Universidad Complutense de Madrid from 13–15 September, 2006. Scientists from both fields, Mathematics and Earth Sciences, took part in this International Seminar, addressing scientific problems related with our planet from clearly complementary approaches, seeking to gain and learn from this dual approach and proposing closer collaboration in the near future.

This volume is the second one of a Topical Issue on "Earth Sciences and Mathematics" and contains 11 papers, most of which were presented at the International Seminar. They address different topics including analysis of InSAR time series, fuzzy classification for remote sensing, modelling gravitational instabilities, geodynamical evolution of the Alboran Sea, statistical warning systems for volcanic hazards, analysis of solutions for the hydrological cycle, study of the ice flow, magma intrusion in elastic layered media, river channel formation, Hartley transform filters for continuous GPS, etc.

The paper by Nunnari *et al*. describes a warning system of critical activity of the Stromboli Volcano (Sicily). After a statistical analysis of ground deformation time-series measured at Stromboli by the monitoring system THEODOROS, the paper describes the solution adopted for implementing the warning system. A robust statistical index given by fuzzy approach has been defined in order to evaluate the movements of the area and provide indication of the level of hazard of the volcano sliding.

Antonsev and Díaz deal with mathematical modelling of the hydrological cycle with emphasis on the coupling between the different types of water flows. The realistic models lead to systems of nonlinear partial differential equations and appropriate boundary conditions according to the interaction between the coupled physical processes. The paper presents more generally mathematical essential tools for studying the existence and uniqueness of nonlinear differential equations arising when modelling geophysical phenomena.

Zlotnik *et al.* describe the application of an extended finite-element method X-FEM combined with a level-set method to compute solutions to 2-D and 3-D problems in the physics of viscous fluids for modelling gravitational instabilities. A new code to solve multiphase viscous thermo–mechanical problems is presented. The examples put forward are of geodynamical interest to study slab detachment in subduction processes and Rayleigh–Tailor instabilities.

The paper by Gómez *et al*. assembles some techniques, previously developed by the authors, relative to fuzzy classification within a remote sensing setting. A segmentation of the image into homogeneous regions is introduced as information, previously to any classification procedure. The subject matter, in terms of training set delineation and accuracy assessment methodology, is important in the field of remote sensing. The approach is illustrated with a particular land surface problem.

Perlock *et al.* describe and apply two differential InSAR methods using the time series associated with the interferograms to perform a phase analysis on a data set for La Palma Island (Canary Islands). Both methods, the Coherent Pixel Time Series Technique and the Coherent Target Modelling Method, involve choosing a master image from the database and creating a series of interferograms with respect to this image. Authors detect significant deformation on La Palma Island (Teneguia Volcano).

The paper by Fontelos and Muñoz presents the analysis of a mathematical model describing the behavior of the isothermal ice flow in the neighborhood of the grounding line (the line where transition between ice attached to the solid ground and ice floating over the sea takes place) when the ice is assumed to follow a shear dependent viscosity relationship of power-law type. The paper is a valuable effort bringing recent mathematical work on ice flow closer to the geophysical audience.

Arjona *et al.* prove the existence and uniqueness of a weak solution of a linear elliptic system subject to boundary and transmission conditions. The system arises from a coupled elastic-gravitational model of magmatic intrusion in a layered configuration domain. The geological significance of the model is unquestionable and the iteration technique employed in establishing existence could be useful for other numerical simulations.

Díaz *et al.* present the deduction and mathematical analysis of a deterministic model describing river channel formation due to the overland flow of water over erodible sediment and the evolution of its depth. The model involves a degenerate nonlinear parabolic equation. Authors propose a global formulation of the problem which allows showing the existence of a solution and leads to a suitable numerical scheme for its approximation.

Tiampo *et al*. introduce the localized Hartley transform filter to the geodetic data analysis and geophysical modeling. This tool allows for the filtering of 1-D time series through the identification of the power at various spatial and temporal wavelengths. The authors choose the continuous GPS daily solutions to extract the post-seismic deformation signals of the 1994 Northridge (South California) earthquake to demonstrate the application of the localized Hartley transform filter.

The paper by Díaz and Wiltshire derives some similarity solutions of a nonlinear equation associated with a free boundary problem arising in the shallow-water approximation in glaciology. Authors offer a classical potential symmetry analysis of this second-order non-linear degenerate parabolic equation related to non-Newtonian ice-sheet dynamics in the isothermal case. The thorough Lie group analysis contains a systematic search for the symmetry groups associated with the ice-sheet equation.

The paper by Valera and Negredo utilizes a new thermo-mechanical algorithm to provide a quantitative evaluation of observations and a conceptual comparison of the geodynamical models proposed to explain the presence of extension in the development of the Alboran Sea. In contrast to the *in situ* convective removal process, the laterally propagating delamination mechanism is shown here to be consistent with first-order features of this controversial region.

We thank the splendid and generous work carried out by the many referees. They have worked in most cases, in the difficult intersection of two different fields such as Earth Sciences and Mathematics. The reviewers have been: D. Abrams, J. Almendros, M. Badii, M. Bebbington, A. Beliaev, P. Berardino, A. Bru, D. Chambers, D. F. Cook, A. Corral, A. Correig, D. Dong, B. Enescu, M. Fernández, D. García, G. Gagneux, F. Giraldo, J. Gottsmann, G. Hetzer, R. C. A. Hindmarsh, A. Hooper, G. Houseman, T. Jahr, G. Jentzsch, E. Kerre, L. Kuchment, M. Laba, R. Lanari, J. Langbein, A. Lodge, A. Lombard, I. Main, V. C. Manea, S. McNutt, T. Mikumo, P. Moczo, M. Pacella, Y. Pachepsky, J. W. Parker, A. Peresan, P. Prats, J. M. Rey Simó, T. Sagiya, U. Schlink, C. Schoof, D. Seber, R. Shcherbakov, E. Sturkell, D. Salstein, K. F. Tiampo, D. Tarling, C. Vázquez Cendón, G. Wadge, C. Wicks, G. Zoeller, and D. Zupanski.

We would like to take this opportunity to thank the Vicerrectorate for International Relations of the Universidad Complutense de Madrid, the Spanish Council for Scientific Research, the Interdisciplinary Mathematical Institute (IMI), and the Royal Spanish Academy of Sciences for their support in organizing the International Seminar. This International Complutense Seminar was also partially supported with funds from research projects CGL-2004-21019-E and CGL2005-05500-C02-01. The editors also thank Renata Dmowska for her assistance, suggestions and support received during the editorial process of the two volumes of this topical issue. In conclusion we wish to thank all the authors of this volume for their contributions.

References

ESA, European Space Agency, Observing the Earth (2008). http://www.esa.int/esaEO/index.html
IUGG, International Union of Geodesy and Geophysics (2008). http://www.iugg.org/
IUGS, International Union of Geological Sciences (2008). http://www.iugs.org/
NASA, National Aeronautics and Space Administration (2008). http://www.nasa.gov/

Pure appl. geophys. 165 (2008) 1465–1490
0033–4553/08/081465–26
DOI 10.1007/s00024-004-0385-x

Pure and Applied Geophysics

On the Mathematical Analysis of an Elastic-gravitational Layered Earth Model for Magmatic Intrusion: The Stationary Case

A. Arjona,[1] J. I. Díaz,[2] J. Fernández,[1] and J. B. Rundle[3]

Abstract—In the early eighties Rundle (1980, 1981a,b, 1982) developed the techniques needed for calculations of displacements and gravity changes due to internal sources of strain in layered linear elastic-gravitational media. The approximation of the solution for the half space was obtained by using the propagator matrix technique. The Earth model considered is elastic-gravitational, composed of several homogeneous layers overlying a bottom half space. Two dislocation sources can be considered, representing magma intrusions and faults. In recent decades theoretical and computational extensions of that model have been developed by Rundle and co-workers (e.g., Fernández and Rundle, 1994a,b; Fernández *et al*., 1997, 2005a; Tiampo *et al*., 2004; Charco *et al*., 2006, 2007a,b). The source can be located at any depth in the media. In this work we prove that the perturbed equations representing the elastic-gravitational deformation problem, with the natural boundary and transmission conditions, leads to a well-posed problem even for varied domains and general data. We present constructive proof of the existence and we show the uniqueness and the continuous dependence with respect to the data of weak solutions of the coupled elastic-gravitational field equations.

Key words: Gravity changes, elastic-gravitational Earth model, displacement, weak solution.

1. Introduction

Geological hazards have great destructive power (e.g., Sigurdsson *et al*., 2000; National Research Council of the National Academies, 2003), able to cause instantaneous and total destruction of life in the proximities of a volcano, fault or landslide. Geodetic techniques for the measurement of surface displacements, starting from classical terrestrial ones to the most modern space techniques like GPS campaigns, continuous GPS observation (Segall and Davis, 1997; Dixon *et al*., 1997; Sagiya *et al*., 2000; Larson *et al*., 2001; Fernández *et al*., 2004), satellite radar interferometry (Puglisi *et al*., 2001; Pritchard and Simons, 2002; Wright, 2002; Dzurisin, 2003; Fernández *et al*., 2005b; Manzo *et al*., 2006; Tamisiea *et al*., 2007), or their combination

[1] Instituto de Astronomía y Geodesia (CSIC-UCM), Facultad de Matemáticas, Plaza de Ciencias n.3, 28040 Madrid, Spain. E-mail: alicia_arjona@mat.ucm.es; jose_fernandez@mat.ucm.es.

[2] Departamento de Matemática Aplicada, Facultad de Matemáticas, Plaza de Ciencias n.3, 28040 Madrid, Spain. E-mail: ji_diaz@mat.ucm.es.

[3] Center for Computational Science and Engineering, University of California, Davis, CA 95616, USA. E-mail: rundle@ces.ucdavis.edu

(GUDMUNSSON and SIGMUNDSSON, 2002; LUNDGREN and STRAMONDO, 2002; BUSTIN *et al.*, 2004; LANARI *et al.*, 2004; SAMSONOV and TIAMPO, 2006). They have broadly demonstrated its capacity of detection of surface displacements which is useful to study seismic and volcanic events. These techniques allow determination of displacements with a precision of a centimeter or better.

Currently, there is a clear tendency to make a joint interpretation of displacement and variations of gravity, considering the clear improvements obtained in the results (see e.g., RUNDLE, 1982; FERNÁNDEZ *et al.*, 2001; YOSHIYUKI *et al.*, 2001; TIAMPO *et al.*, 2004; CHARCO *et al.*, 2006). The subject is of continuous interest (TAMISIEA *et al.*, 2007).

If we concentrate on geological hazards associated with volcanism, surface-ground deformation and gravity changes can be indicators of volcanic activity as well as precursors of an eruption. Usually they appear together with other volcanic activity indicators, such as seismicity, gas emission, fumarolic activity, etc. Considering this, ideal monitoring should consider all the possible parameters which allow detection of their changes in the active area and to obtain information about the magmatic source below surface (see e.g., SIGURDSSON *et al.*, 2000; DÍAZ and TALENTI, 2004; TIAMPO *et al.*, 2004); deformations, gravity or temperature changes, emitted gases, etc. within the dangerous zone.

Thus volcanic eruptions are the outcome of significant physical and geological processes. Among others there is magma formation in the mantle or crust, as well as its ascent to more superficial zones. These phenomena become apparent through changes in the volcanic building and the surroundings alike. One of the main challenges is to determine if an intrusion process will result in an eruption or not. On the other hand, to interpret geodetic anomalies (displacements, gravity changes, etc.) which may be tied to volcanic activity, mathematical models allowing the resolution of the inverse problem, which consists of obtaining a volcanic intrusion's properties from surface observation, are necessary. Therefore we need analytical models. Numerical models are more realistic in some aspects and allow a better approximation of the real problem in cases in which more time is available than in a criticical situation. Each model is characterized by a series of mathematical equations describing the problem's physics. Specifically, the model studied in this work is a deformation model in which surface deformation and gravity change, understood as possible symptoms of a future eruption, are coupled. This model responds to a system of partial differential equations.

As first elastic models we can consider LOVE's work (1911). He showed that a displacement field produced by a center of expansion within an elastic medium may be obtained from a suitable Green's function. With a base on these works, RUNDLE (1980) obtains and solves the equations that represent the elastic-gravitational problem for point sources in an elastic-gravitational half space, stratified in flat, isotropic and homogeneous layers. In order to introduce the layered medium in the problem, a matrix method is used to propagate the solutions from one layer to the next. That is to say, he obtains the solution on each layer and with the aforesaid matrices he joins these solutions together to obtain a global solution on the entire domain. RUNDLE (1981a) achieves the numerical evaluation of this problem. He also studies the problem of obtaining vertical displacements for a

rectangular fault (RUNDLE, 1981b). This model (RUNDLE, 1982) allows study of variations on the displacements, on the perturbed potential and gravity changes, as well as the sea-level variation caused by volcanic loading. RUNDLE (1982) proves the uniqueness of solutions for the elastic-gravitational case, but considering only a infinite medium, the basic solutions for the used methodology, although not for the case of a layered model.

The goal of this paper is to complete the work developed by RUNDLE (1982) and applying techniques of the weak solutions of partial differential equations theory, to prove the existence and uniqueness of solutions of the coupled elastic-gravitational model for the layered configuration on a general spatial section domain Ω. To consider a layered medium necessitates the consideration of a weak solution instead of the classical solutions in the whole of the spatial domain. Let us point out that it is a necessary study to be done considering the broad applications of this elastic-gravitational deformation model.

2. Problem

The deformation model we are going to work with consists of an Earth model composed of several elastic-gravitational layers overlying an elastic-gravitational half space. We consider that the contribution of the source term will be a magmatic intrusion, corresponding to body forces acting on the medium. This will be due to both volumetric change of the wall of the chamber and the sudden placement of a mass into the medium resulting from an injection of material into the chamber. This way, a force will be added to both equations due to an increase of pressure into the chamber which is called $\mathbf{f}_u$ and f_ϕ, giving way to a final coupled system (AKI and RICHARDS 2002):

$$\begin{cases} -\Delta \mathbf{u} - \dfrac{1}{1-2v}\nabla(\operatorname{div}\mathbf{u}) - \dfrac{\rho g}{\mu}\nabla(\mathbf{u}\cdot\mathbf{e}_z) + \dfrac{\rho g}{\mu}\mathbf{e}_z \operatorname{div}\mathbf{u} = \dfrac{\rho}{\mu}\nabla\phi + \mathbf{f}_u \\ -\Delta\phi = 4\pi\rho G \operatorname{div}\mathbf{u} + f_\phi \end{cases} \tag{1}$$

3. Weak Formulation

It is clear that under the boundary conditions any classical solution does not need to exist. Thus we have to introduce the notion of a weak solution which allows a greater generality. Firstly, let us define the spatial domain in the following way: We will assume p layers "overstrike" that we will denote as $\Omega_i\ \forall i = 1,...,p$, and which union determines global domain $\Omega, \Omega = \bigcup_{i=1}^{p} \Omega_i$.

Each layer is given through a common horizontal set: an open $\omega \subset \mathbb{R}^2$ and

$$\Omega_1 := \omega \times (d_1, d_1 + d_2), \quad \Omega_2 := \omega \times (d_1 + d_2, d_1 + d_2 + d_3), \quad \text{etc.}, \tag{2}$$

that is

$$\Omega_i := \omega \times \left(\sum_{j=1}^{i-1} d_j, \sum_{j=1}^{i} d_j \right) \subset \mathbb{R}^3, \quad \text{when} \quad i = 1, \ldots, p-1, \tag{3}$$

and

$$\Omega_p := \omega \times (H, H + d_r), \tag{4}$$

when $H := \sum_{j=1}^{i-1} d_j$ and d_r can be equal to $+\infty$.

Let $\mathbf{u}^i : \Omega_i \longrightarrow \mathbb{R}^3$ be the displacement vector in each layer, $\mathbf{u}^i = (u_x^i, u_y^i, u_z^i)$ and $\mathbf{f}_u^i : \Omega_i \longrightarrow \mathbb{R}^3$ be the force vector in each layer, $\mathbf{f}_u^i = (f_x^i, f_y^i, f_z^i)$. Both functions depend on $\mathbf{x} = (x, y, z)$.

Let us describe the boundary of our domain to establish the boundary conditions of the problem. We distinguish, for each layer comprised between the first and the $(p-1)$-th, side, upper and bottom boundary by means of the following notation (see Fig. 1):

$$\begin{cases} \partial_+ \Omega_i = \omega \times \left\{ \sum_{j=1}^{i-1} d_j \right\}, & \text{top boundary,} \\ \partial_- \Omega_i = \omega \times \left\{ \sum_{j=1}^{i} d_j \right\}, & \text{bottom boundary,} \\ \partial_l \Omega_i = \partial\omega \times \left[\sum_{j=1}^{i-1} d_j, \sum_{j=1}^{i} d_j \right], & \text{side lateral boundary.} \end{cases} \tag{5}$$

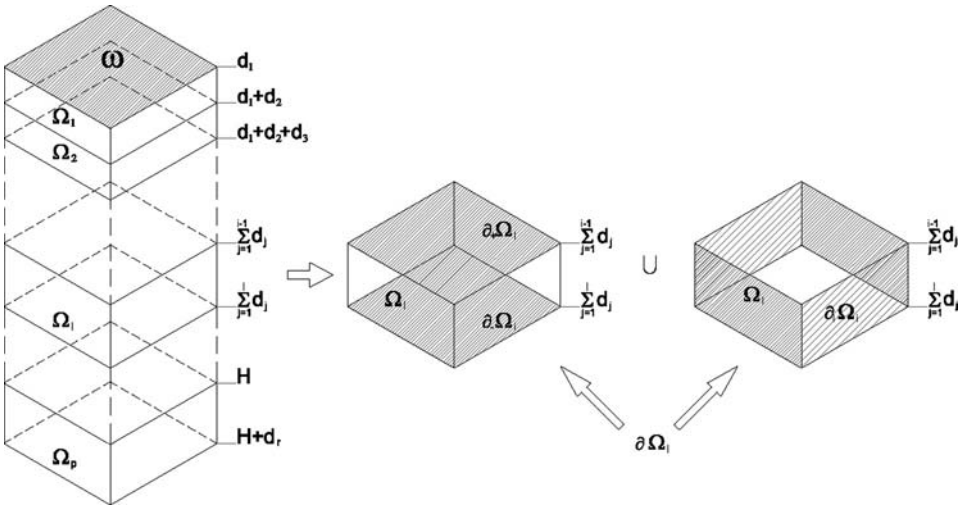

Figure 1
Domain of the problem.

Then

$$\partial\Omega_i = \partial_+\Omega_i \cup \partial_-\Omega_i \cup \partial_l\Omega_i \quad \forall i = 1,\ldots,p-1. \tag{6}$$

For the last layer, that is, the p-th one we have

$$\begin{cases} \partial_+\Omega_p = \omega \times \{H\}, \\ \partial_-\Omega_p = \omega \times \{H + d_p\}. \end{cases} \tag{7}$$

Let us denote the displacement vector and the gravitational perturbed potential in the following manner: $\mathbf{u}^i(\mathbf{x})$ represents the displacement vector field on each point of the layer i, for $i = 1,...,p$. Thus, actually the unknown we look for is $\mathbf{u} \equiv (\mathbf{u}^i)_{i=1,...,p}$. To simplify the notation, we will use $\mathbf{u}$ when it is not ambiguous. Again to simplify the equation the same way we denote $\phi^i(\mathbf{x})$ as gravitational perturbed potential on the point $\mathbf{x}$ of the layer i, that is the unknown we look for: $\phi \equiv (\phi^i)_{i=1,...,p}$. Again, to simplify the notation, we use ϕ when there is no ambiguity. Constitutive constants of the different layers take the following notation: $\rho \equiv (\rho^i)_{i=1,...,p}$, $\mu \equiv (\mu^i)_{i=1,...,p}$ and $\nu \equiv (\nu^i)_{i=1,...,p}$. In relation to the functions due to magmatic intrusion we use: $\mathbf{f}_u \equiv (\mathbf{f}_u^i)_{i=1,...,p}$ and $f_\phi \equiv (f_\phi^i)_{i=1,...,p}$.

On each layer Ω_i, $i = 1,...,p$, the following system of equations holds:

$$\begin{cases} -\Delta\mathbf{u}^i(\mathbf{x}) - \dfrac{1}{1-2\nu^i}\nabla\big(\operatorname{div}\mathbf{u}^i(\mathbf{x})\big) - \dfrac{\rho^i g}{\mu^i}\nabla\big(\mathbf{u}^i(\mathbf{x})\cdot\mathbf{e}_z\big) + \dfrac{\rho^i g}{\mu^i}\,\mathbf{e}_z \operatorname{div}\mathbf{u}^i(\mathbf{x}) = \dfrac{\rho^i}{\mu^i}\nabla\phi^i(\mathbf{x}) + \mathbf{f}_u^i(\mathbf{x}), \\ -\Delta\phi^i(\mathbf{x}) = 4\pi\rho^i G \operatorname{div}\mathbf{u}^i(\mathbf{x}) + f_\phi^i(\mathbf{x}), \quad \text{in } \Omega_i. \end{cases} \tag{8}$$

We will add the following boundary conditions to the set of partial differential equations. With regard to the displacement field we assume that on the side boundary, $\partial_l\,\Omega_i$, of $i = 1,...,p$, so let:

$$\mathbf{u}^i(\mathbf{x}) = \mathbf{0},\ \mathbf{x} \in \partial_l\Omega_i, \tag{9}$$

on the upper boundary of the first layer $\partial_+\Omega_1$

$$\frac{\partial\mathbf{u}^1(\mathbf{x})}{\partial z} = \mathbf{0},\ \mathbf{x} \in \partial_+\Omega_1, \tag{10}$$

and on the bottom boundary, $\partial_-\Omega_p$, gives

$$\mathbf{u}^p(\mathbf{x}) = \mathbf{0},\ \mathbf{x} \in \partial_-\Omega_p. \tag{11}$$

In general, we can assure only that the first derivatives of $\mathbf{u}$ are continuous on the boundaries of the layers, that is, on the boundary between layers. We will require "transmission conditions" between both upper and bottom boundaries of the layers excepting the first and the last layer. Thus, we must have, on $\partial_-\Omega_i = \partial_+\Omega_{i+1}$ with $i = 1,...,p-1$, the next conditions

$$\begin{cases} \mathbf{u}^i(\mathbf{x}) = \mathbf{u}^{i+1}(\mathbf{x}), & \mathbf{x} \in \partial_- \Omega_i, \\ \dfrac{\partial \mathbf{u}^i(\mathbf{x})}{\partial z} = \dfrac{\partial \mathbf{u}^{i+1}(\mathbf{x})}{\partial z}, & \mathbf{x} \in \partial_- \Omega_i. \end{cases} \tag{12}$$

In relation to gravitational perturbed potential we will assume that on the side boundary $\partial_l \Omega_i$ for $i = 1,...,p$

$$\phi(\mathbf{x}) = 0, \ \mathbf{x} \in \partial_l \Omega_i, \tag{13}$$

on the upper boundary of the first layer $\partial_+ \Omega_1$

$$\phi^1(\mathbf{x}) = \phi_0(\mathbf{x}), \ \mathbf{x} \in \partial_+ \Omega_1, \tag{14}$$

and on the bottom boundary, $\partial_- \Omega_p$

$$\phi^p(\mathbf{x}) = 0, \ \mathbf{x} \in \partial_- \Omega_p. \tag{15}$$

As mentioned, we will require a transmission condition between upper and bottom boundaries of the next layers, excepting on the first layer and the last layers. Thus, we must have, on $\partial_- \Omega_i = \partial_+ \Omega_{i+1}$ with $i = 1,..., p-1$, the following conditions:

$$\begin{cases} \phi^i(\mathbf{x}) = \phi^{i+1}(\mathbf{x}), & \mathbf{x} \in \partial_- \Omega_i, \\ \dfrac{\partial \phi^i(\mathbf{x})}{\partial z} = \dfrac{\partial \phi^{i+1}(\mathbf{x})}{\partial z}, & \mathbf{x} \in \partial_- \Omega_i. \end{cases} \tag{16}$$

Remark 1. *In what follows, we shall work with the boundary data ϕ_0 by extending it to the interior of the domain Ω_1: i.e., we assume that there exists a function $\widehat{\phi}_0(\mathbf{x})$ defined on the upper layer Ω_1 such that*

$$\widehat{\phi}_0 \in H^1(\Omega_1), \widehat{\phi}_0(\mathbf{x}) = \phi_0(\mathbf{x}) \text{ on } \partial_+ \Omega_1 \text{ and } \widehat{\phi}_0(\mathbf{x}) = 0 \text{ on } \partial_- \Omega_1 \cup \partial_l \Omega_1. \tag{17}$$

Here, and in what follows, $H^1(\Omega)$ denotes the Sobolev space given by

$$H^1(\Omega) = \left\{ \phi \in L^2(\Omega_1), \quad \frac{\partial \phi}{\partial x_i} \in L^2(\Omega_1) \forall i = 1, 2, 3 \right\}. \tag{18}$$

(see, e.g. BRÉZIS, 1984, for more details).

Firstly, we define the space formed by the test functions (which we shall denote as *space of energy*), for both displacement vector and gravitational perturbed potential, denoted by V_u and V_ϕ. In order to simplify the presentation of the results we shall assume that the horizontal projection ω is bounded, connected and "regular". Then,

$$V_u := \left\{ \left((\mathbf{u}^1, \phi^1), \ldots, (\mathbf{u}^p, \phi^p)\right) \in \prod_{i=1}^{p} H^1(\Omega_i)^3 \times H^1(\Omega_i) \text{ such that } \mathbf{u}^i \text{ verifies (9) to (12)} \right\},$$

$$V_\phi := \left\{ \left((\mathbf{u}^1, \phi^1), \ldots, (\mathbf{u}^p, \phi^p)\right) \in \prod_{i=1}^{p} H^1(\Omega_i)^3 \times H^1(\Omega_i) \text{ such that } \phi^i \right.$$
$$\left. \text{verifies (13), (15), (16) and } \phi^i \equiv 0 \text{ on } \partial_+\Omega_1 \right\}. \tag{19}$$

Remark 2. *V_u and V_ϕ are Hilbert's spaces with the natural inner product (for instance, for V_u with the inherited one of the $\prod_{i=1}^{p} H^1(\Omega_i)^3 \times H^1(\Omega_i)$ space), that is:*

$$(\mathbf{u}, \mathbf{w})_{V_u} = \sum_{i=1}^{p} \left\{ \int_{\Omega_i} \nabla \mathbf{u}^i : \nabla \mathbf{w}^i d\mathbf{x} + \int_{\Omega_i} \mathbf{u}^i \cdot \mathbf{w}^i d\mathbf{x} \right\},$$
$$(\phi, \theta)_{V_\phi} = \sum_{i=1}^{p} \left\{ \int_{\Omega_i} \nabla \phi^i \cdot \nabla \theta^i d\mathbf{x} + \int_{\Omega_i} \phi^i \theta^i d\mathbf{x} \right\}. \tag{20}$$

Moreover, if we introduce the dual space we will have the following embedding chain (BRÉZIS, 1984)

$$V_u \subset \prod_{i=1}^{p} H^1(\Omega_i)^3 \subset L^2(\Omega)^3 = (L^2(\Omega)^3)' \subset \prod_{i=1}^{p} H^{-1}(\Omega_i)^3 \subset V_u'$$
$$V_\phi \subset \prod_{i=1}^{p} H^1(\Omega_i) \subset L^2(\Omega) = (L^2(\Omega))' \subset \prod_{i=1}^{p} H^{-1}(\Omega_i) \subset V_\phi', \tag{21}$$

where we have used the fact that $\prod_{i=1}^{p} L^2(\Omega_i)$ can be identified with $L^2(\Omega)$ since

$$\int_\Omega \phi^2(\mathbf{x}) d\mathbf{x} = \sum_{i=1}^{p} \int_{\Omega_i} \phi_i^2(\mathbf{x}) d\mathbf{x} \tag{22}$$

Here $H^{-1}(\Omega_i)$ denotes the dual space of $H_0^{-1}(\Omega_i)$.

We also remark that the $H^{-1}(\Omega_i)$ spaces are Hilbert spaces and their norm is alternatively given in the following way: If $f^i \in H^{-1}(\Omega_i)$ then

$$f^i(\mathbf{x}) = f_0^i(\mathbf{x}) + \sum_{k=1}^{3} \frac{\partial f_k^i(\mathbf{x})}{\partial x_k} \quad \text{with} \quad f_j^i \in L^2(\Omega_i),\ j = 0, 1, 2, 3 \tag{23}$$

and

$$\|f^i\|_{H^{-1}(\Omega_i)} = \|f_0^i\|_{L^2(\Omega_i)} + \sum_{k=1}^{3} \|f_k^i\|_{L^2(\Omega_i)}. \tag{24}$$

We will assume the following regularity of the data

$$\mathbf{f}_u \in \prod_{i=1}^{p} H^{-1}(\Omega_i)^3, \tag{25}$$

$$f_\phi \in \prod_{i=1}^{p} H^{-1}(\Omega_i), \tag{26}$$

$$\phi_0 \in \prod_{i=1}^{p} H^{1}(\Omega_i) \tag{27}$$

and satisfy (17).

In order to justify the definition of the following weak solution, we shall consider, for a while, that $(\mathbf{u},\phi)$ is a classical solution of the system. Then we take a test function $(\mathbf{w},\theta) \in V$. We multiply first equation of the system (8) by $\mathbf{w}^i$ and apply the Green's theorem:

$$\int_\Omega \nabla\mathbf{u} : \nabla\mathbf{w} = -\int_\Omega \Delta\mathbf{u}\cdot\mathbf{w} + \int_{\partial\Omega} \nabla\mathbf{u}\mathbf{w}\cdot\mathbf{n} = -\int_\Omega \Delta\mathbf{u}\cdot\mathbf{w} + \int_{\partial\Omega} \frac{\partial\mathbf{u}}{\partial n}\cdot\mathbf{w}. \tag{28}$$

If we assume transmission conditions (12) and (16), and lateral side boundary $\partial_l\Omega_i$, the sum of normal derivatives vanishes since the normal vector to upper layers are opposites.

If moreover we assume that the test function vanishes on ∂_Ω, we conclude that:

$$\begin{aligned}\int_{\Omega_i} \left(-\Delta\mathbf{u}^i(\mathbf{x}) - \frac{1}{1-2\nu^i}\nabla\big(\operatorname{div}\mathbf{u}^i(\mathbf{x})\big) - \frac{\rho^i g}{\mu^i}\nabla\big(\mathbf{u}^i(\mathbf{x})\cdot\mathbf{e}_z\big) + \frac{\rho^i g}{\mu^i}\mathbf{e}_z \operatorname{div}\mathbf{u}^i(\mathbf{x})\right)\cdot\mathbf{w}^i(\mathbf{x})d\mathbf{x}\\ = \int_{\Omega_i} (\nabla\mathbf{u}^i(\mathbf{x}) : \nabla\mathbf{w}^i(\mathbf{x}) + \frac{1}{1-2\nu^i}\operatorname{div}\mathbf{u}^i(\mathbf{x})\operatorname{div}\mathbf{w}^i(\mathbf{x}) - \frac{\rho^i g}{\mu^i}\nabla\big(\mathbf{u}^i(\mathbf{x})\cdot\mathbf{e}_z\big)\cdot\mathbf{w}^i(\mathbf{x}) +\\ + \frac{\rho^i g}{\mu^i}\mathbf{e}_z \operatorname{div}\mathbf{u}^i(\mathbf{x})\mathbf{w}^i(\mathbf{x})d\mathbf{x}).\end{aligned} \tag{29}$$

We operate analogously with the second equation of (8) however, now multiplying by a test function θ^i:

$$-\int_{\Omega_i} \Delta\phi^i(\mathbf{x})\theta^i(\mathbf{x})d\mathbf{x} = \int_{\Omega_i} \nabla\phi^i(\mathbf{x})\cdot\nabla\theta^i(\mathbf{x})d\mathbf{x}. \tag{30}$$

In the same way, we multiply by $\mathbf{w}^i$ and by θ^i to the right-hand side of the equations of the system (8). By adding them we originate the terms

$$\begin{aligned}&\sum_{i=1}^{p}\left(-\frac{\rho^i}{\mu^i}\right)\int_{\Omega_i} \nabla\phi^i(\mathbf{x})\cdot\mathbf{w}^i(\mathbf{x})d\mathbf{x} + \langle\mathbf{f}_u,\mathbf{w}\rangle_{V_u'\times V_u},\\ &\sum_{i=1}^{p}(-4\pi\rho^i G)\int_{\Omega_i} \operatorname{div}\mathbf{u}^i(\mathbf{x})\theta^i(\mathbf{x})d\mathbf{x} + \langle f_\phi,\theta\rangle_{V_\phi'\times V_\phi}.\end{aligned} \tag{31}$$

We reach some integral equalities which any classical solution must verify. Thus, we are

going to use it in order to define the notion of a weak solution (without requiring the existence of any classical second derivative).

Definition 1. *We assume the regularity* (25), (26) *and* (27), *on the functions* $\mathbf{f}_u$, f_ϕ *and* ϕ_0. *We say that* $(\mathbf{u}, \phi)$ *is a weak solution of the problem* (8) *with the boundary conditions* (9)–(16) *if* $(\mathbf{u}, \phi - \phi_0) \in V$ *and for any test function* $(\mathbf{w}, \theta) \in V$ *the following identities hold:*

$$\sum_{i=1}^{p}\left[\int_{\Omega_i}\left(\nabla\mathbf{u}^i(\mathbf{x}) : \nabla\mathbf{w}^i(\mathbf{x}) + \frac{1}{1-2\nu^i}\operatorname{div}\mathbf{u}^i(\mathbf{x})\operatorname{div}\mathbf{w}^i(\mathbf{x}) - \frac{\rho^i g}{\mu^i}\nabla\big(\mathbf{u}^i(\mathbf{x})\cdot\mathbf{e}_z\big)\cdot\mathbf{w}^i(\mathbf{x})\right.\right.$$
$$\left.\left. + \frac{\rho^i g}{\mu^i}\mathbf{e}_z\operatorname{div}\mathbf{u}^i(\mathbf{x})\mathbf{w}^i(\mathbf{x})d\mathbf{x}\right) = \sum_{i=1}^{p}\left(-\frac{\rho^i}{\mu^i}\right)\int_{\Omega_i}\nabla\phi^i(\mathbf{x})\cdot\mathbf{w}^i(\mathbf{x})d\mathbf{x} + \langle\mathbf{f}_u, \mathbf{w}\rangle_{V_u'\times V_u}, \tag{32}$$

and

$$\sum_{i=1}^{p}\int_{\Omega_i}\nabla\phi^i(\mathbf{x})\cdot\nabla\theta^i(\mathbf{x})d\mathbf{x} = -\sum_{i=1}^{p}4\pi\rho^i G\int_{\Omega_i}\operatorname{div}\mathbf{u}^i(\mathbf{x})\theta^i(\mathbf{x})d\mathbf{x} + \big\langle f_\phi, \theta\big\rangle_{V_\phi'\times V_\phi}. \tag{33}$$

The mathematical treatment of the problem will require application of some technical results which may not be valid in some special cases. Due to that, it will be useful to introduce a change of scale $\mathbf{y} = \lambda\mathbf{x}$ allowing definition of a re-scaling function $\mathbf{v}(\mathbf{y}) = \mathbf{u}(\lambda\mathbf{x})$ which produces of emergence of some coefficients λ associated with the first derivatives of $\mathbf{u}$ and λ^2 associated with the second derivatives of $\mathbf{u}$. The new system of equations satisfied by $\mathbf{v}(\mathbf{y})$ are:

$$\begin{cases} -\Delta\mathbf{v}^i(\mathbf{y}) - \dfrac{1}{1-2\nu^i}\nabla\big(\operatorname{div}\mathbf{v}^i(\mathbf{y})\big) - \dfrac{\rho^i g\lambda}{\mu^i}\nabla\big(\mathbf{v}^i(\mathbf{y})\cdot\mathbf{e}_z\big) \\ + \dfrac{\rho^i g\lambda}{\mu^i}\mathbf{e}_z\operatorname{div}\mathbf{v}^i(\mathbf{y}) = -\dfrac{\rho_i\lambda}{\mu_i}\nabla\phi^i\big(\lambda^{-1}\mathbf{y}\big) + \lambda^2\mathbf{f}_u^i\big(\lambda^{-1}\mathbf{y}\big) \end{cases} \text{in } \Omega_i, \quad \text{(Dilatated equation)}$$

The main goal of this paper is to prove that under the above assumptions the system (8) is well posed (in the sense of Hadamard) on the space V.

Theorem 1. *Assume the regularity* (25), (26) *and* (27) *on the data* $\mathbf{f}_u$, f_ϕ, *and* ϕ_0. *Then there exists a unique weak solution* $\{\mathbf{u}, \phi\}$ *of the problem* (8). *Moreover, we have the following estimate of the continuous dependence with respect to the data*

$$\sum_{i=1}^{p}2\pi\rho^i G\big\|\nabla\mathbf{u}^i\big\|^2_{L^2(\Omega_i)} + \sum_{i=1}^{p}\frac{\rho^i}{2\mu^i}\big\|\nabla\phi^i\big\|^2_{L^2(\Omega_i)}$$
$$\le K\left(2\|\mathbf{f}_u\|^2_{V_u'} + \frac{1}{2}\big\|f_\phi\big\|^2_{V_\phi'} + 4C\rho^1\|\phi_0\|_{H^{1/2}(\partial_+\Omega_1)}\right), \tag{34}$$

where K *is a constant which depends on the scale* λ *and where* C *is the constant of the trace embedding* $H^1(\Omega_1) \to H^{1/2}(\partial_+\Omega_1)$.

First, we shall prove the uniqueness of the solution of weak solutions. Then we shall obtain the estimate of the continuous dependence with respect to the data. Finally we shall prove the existence of weak solutions by means of an iterative method which can be useful for numerical purposes.

4. Uniqueness of Solutions

Let us first prove the uniqueness of solutions of the coupled system. We assume two weak solutions for system (8), $\mathbf{u}_1^i$, $\mathbf{u}_2^i$, ϕ_1^i and ϕ_2^i with $i = 1,...,p$, and let

$$\begin{cases} \mathbf{u}^i(\mathbf{x}) = \mathbf{u}_1^i(\mathbf{x}) - \mathbf{u}_2^i(\mathbf{x}), \\ \phi^i(\mathbf{x}) = \phi_1^i(\mathbf{x}) - \phi_2^i(\mathbf{x}). \end{cases} \tag{35}$$

Since $\mathbf{u}_1^i$, $\mathbf{u}_2^i$, ϕ_1^i y ϕ_2^i are weak solutions, we verify (14), and by subtracting we obtain

$$\begin{aligned} &\sum_{i=1}^{p}\left(-(\Delta\mathbf{u}_1^i(\mathbf{x}) - \Delta\mathbf{u}_2^i(\mathbf{x})) - \left(\frac{1}{1-2\nu^i}\nabla(\operatorname{div}\mathbf{u}_1^i(\mathbf{x})) - \nabla(\operatorname{div}\mathbf{u}_2^i(\mathbf{x}))\right)\right. \\ &\quad \left. -\frac{\rho^i g}{\mu^i}\big(\nabla\big(\mathbf{u}_1^i(\mathbf{x})\cdot\mathbf{e}_z\big) - \nabla\big(\mathbf{u}_2^i(\mathbf{x})\cdot\mathbf{e}_z\big)\big) + \frac{\rho^i g}{\mu^i}\big(\mathbf{e}_z \operatorname{div}\mathbf{u}_1^i(\mathbf{x}) - \mathbf{e}_z \operatorname{div}\mathbf{u}_2^i(\mathbf{x})\big)\right) \\ &\quad = \sum_{i=1}^{p}\left(\frac{\rho^i}{\mu^i}\big(\nabla\phi_1^i(\mathbf{x}) - \nabla\phi_2^i(\mathbf{x})\big)\right). \end{aligned} \tag{36}$$

Then, by the linearity of the differential operators we have:

$$\begin{aligned} &\sum_{i=1}^{p}\left(-\Delta\mathbf{u}^i(\mathbf{x}) - \frac{1}{1-2\nu^i}\nabla\big(\operatorname{div}\mathbf{u}^i(\mathbf{x})\big) - \frac{\rho^i g}{\mu^i}\nabla\big(\mathbf{u}^i(\mathbf{x})\cdot\mathbf{e}_z\big) + \frac{\rho^i g}{\mu^i}\mathbf{e}_z \operatorname{div}\mathbf{u}^i(\mathbf{x})\right) \\ &= \sum_{i=1}^{p}\frac{\rho^i}{\mu^i}\nabla\phi^i(\mathbf{x}). \end{aligned} \tag{37}$$

Analogously:

$$\sum_{i=1}^{p}\big(-\Delta\phi^i(\mathbf{x})\big) = \sum_{i=1}^{p} 4\pi\rho^i G \operatorname{div}\mathbf{u}^i(\mathbf{x}). \tag{38}$$

Concerning the boundary conditions, since $\mathbf{u}_1^i$, $\mathbf{u}_2^i$, ϕ_1^i and ϕ_2^i verify the same boundary conditions of the system, on the lateral side boundary $\partial_l\Omega_i$, for $i = 1,...,p$, we have

$$\begin{aligned} &\mathbf{u}_1^i(\mathbf{x}) = \mathbf{0}, \mathbf{x} \in \partial_l\Omega_i, \\ &\phi^i(\mathbf{x}) = 0, \mathbf{x} \in \partial_l\Omega_i. \end{aligned} \tag{39}$$

The transmission conditions on the top and bottom boundaries, except the first and last layers, i.e., on $\partial_-\Omega_1 \cup (\partial_+\Omega_2 \cup \partial_-\Omega_2) \cup ... \cup \partial_+\Omega_p$ for $i = 1,...,p-1$ lead to

$$\begin{cases} \mathbf{u}^i(\mathbf{x}) = \mathbf{u}^{i+1}(\mathbf{x}), \\ \dfrac{\partial \mathbf{u}^i(\mathbf{x})}{\partial z} = \dfrac{\partial \mathbf{u}^{i+1}(\mathbf{x})}{\partial z}, \\ \phi^i(\mathbf{x}) = \phi^{i+1}(\mathbf{x}), \\ \dfrac{\partial \phi^i(\mathbf{x})}{\partial z} = \dfrac{\partial \phi^{i+1}(\mathbf{x})}{\partial z}, \end{cases} \tag{40}$$

on the top boundary, $\partial_+\Omega_1$:

$$\begin{cases} \frac{\partial \mathbf{u}^i(\mathbf{x})}{\partial z} = \mathbf{0}, & \mathbf{x} \in \partial_+\Omega_1, \\ \phi^i(\mathbf{x}) = 0, & \mathbf{x} \in \partial_+\Omega_1 \end{cases} \tag{41}$$

and on the bottom boundary, $\partial_-\Omega_p$:

$$\begin{cases} \mathbf{u}^p(\mathbf{x}) = \mathbf{0}, & \mathbf{x} \in \partial_-\Omega_p, \\ \phi^p(\mathbf{x}) = 0, & \mathbf{x} \in \partial_-\Omega_p. \end{cases} \tag{42}$$

Multiplying the equation (37) by the term $4\pi\rho^i G\mathbf{u}^i$ and the equation (38) by $(\rho^i/\mu^i)\phi^i$, we conclude that

$$\begin{aligned} &\sum_{i=1}^{p}\left(-\Delta\mathbf{u}^i(\mathbf{x}) - \frac{1}{1-2\nu^i}\nabla\big(\operatorname{div}\mathbf{u}^i(\mathbf{x})\big) - \frac{\rho^i g}{\mu^i}\nabla\big(\mathbf{u}^i(\mathbf{x})\cdot\mathbf{e}_z\big) + \frac{\rho^i g}{\mu^i}\,\mathbf{e}_z \operatorname{div}\mathbf{u}^i(\mathbf{x})\right)\cdot 4\pi\rho G\mathbf{u}^i(\mathbf{x}) \\ &\quad = \sum_{i=1}^{p}\frac{\rho^i}{\mu^i}\nabla\phi^i(\mathbf{x})\cdot 4\pi\rho G\mathbf{u}^i(\mathbf{x}). \end{aligned} \tag{43}$$

Let us omit for a while the symbol $\sum_{i=1}^{p}$. Multiplying term by term and integrating on the domain we obtain

$$\begin{aligned} &-\int_{\Omega_i} 4\pi\rho^i G\Delta\mathbf{u}^i(\mathbf{x})\cdot\mathbf{u}^i(\mathbf{x})d\mathbf{x} - \int_{\Omega_i}\frac{4\pi\rho^i G}{1-2\nu^i}\nabla\big(\operatorname{div}\mathbf{u}^i(\mathbf{x})\big)\cdot\mathbf{u}^i(\mathbf{x})d\mathbf{x} \\ &\quad -\int_{\Omega_i}\frac{4\pi(\rho^i)^2 Gg}{\mu^i}\nabla\big(\mathbf{u}^i(\mathbf{x})\cdot\mathbf{e}_z\big)\cdot\mathbf{u}^i(\mathbf{x})d\mathbf{x} + \int_{\Omega_i}\frac{4\pi(\rho^i)^2 Gg}{\mu^i}\mathbf{e}_z\operatorname{div}\mathbf{u}^i(\mathbf{x})\mathbf{u}^i(\mathbf{x})d\mathbf{x} \\ &\qquad = \int_{\Omega_i}\frac{\rho^i}{\mu^i}\nabla\phi^i(\mathbf{x})\cdot\big(4\pi\rho^i G\big)\mathbf{u}^i(\mathbf{x})d\mathbf{x}, \\ &4\pi\rho^i G\Big(-\int_{\Omega_i}\Delta\mathbf{u}^i(\mathbf{x})\cdot\mathbf{u}^i(\mathbf{x})d\mathbf{x} + \int_{\Omega_i}\frac{1}{1-2\nu^i}\operatorname{div}\mathbf{u}^i(\mathbf{x})\operatorname{div}\mathbf{u}^i(\mathbf{x})d\mathbf{x} \\ &\qquad -\int_{\Omega_i}\frac{\rho^i g}{\mu^i}\nabla\big(\mathbf{u}^i(\mathbf{x})\cdot\mathbf{e}_z\big)\cdot\mathbf{u}^i(\mathbf{x})d\mathbf{x} + \int_{\Omega_i}\frac{\rho^i g}{\mu^i}\mathbf{e}_z\operatorname{div}\mathbf{u}^i(\mathbf{x})\mathbf{u}^i(\mathbf{x})d\mathbf{x}\Big) \\ &\qquad = \int_{\Omega_i}\frac{4\pi(\rho^i)^2 G}{\mu^i}\nabla\phi^i(\mathbf{x})\cdot\mathbf{u}^i(\mathbf{x})d\mathbf{x}. \end{aligned} \tag{44}$$

Then:

$$4\pi\rho^i G a_u^i\left(\mathbf{u}^i,\mathbf{u}^i\right)=\frac{4\pi(\rho^i)^2 G}{\mu^i}\int_{\Omega_i}\nabla\phi^i(\mathbf{x})\cdot\mathbf{u}^i(\mathbf{x})d\mathbf{x}, \tag{45}$$

where we used $a_u^i(\mathbf{u}^i,\mathbf{u}^i)$ to denote to the corresponding bilinear form on $\mathbf{u}^i$. Integrating by parts we can see that the terms of the second member of the equation can be simplified. Bearing in mind the boundary conditions we obtain

$$\sum_{i=1}^{p}4\pi\rho^i G a_u^i\left(\mathbf{u}^i,\mathbf{u}^i\right)=\sum_{i=1}^{p}\left(\frac{4\pi(\rho^i)^2 G}{\mu^i}\left[\left(\int_{\partial\Omega_i}\phi^i(\mathbf{s})\mathbf{u}^i(\mathbf{s})\cdot\mathbf{n}\ ds\right)-\int_{\Omega_i}\phi^i(\mathbf{x})\mathrm{div}\ \mathbf{u}^i(\mathbf{x})d\mathbf{x}\right]\right), \tag{46}$$

and then:

$$\sum_{i=1}^{p}4\pi\rho^i G a_u^i\left(\mathbf{u}^i,\mathbf{u}^i\right)=-\sum_{i=1}^{p}\frac{4\pi(\rho^i)^2 G}{\mu^i}\int_{\Omega_i}\phi^i(\mathbf{x})\ \mathrm{div}\ \mathbf{u}^i(\mathbf{x})d\mathbf{x}. \tag{47}$$

We proceed with the second equation

$$\sum_{i=1}^{p}\left(-\Delta\phi^i(\mathbf{x})\frac{\rho^i}{\mu^i}\phi^i(\mathbf{x})\right)=\sum_{i=1}^{p}4\pi\rho^i G\ \ \mathrm{div}\ \mathbf{u}^i(\mathbf{x})\frac{\rho^i}{\mu^i}\phi^i(\mathbf{x}), \tag{48}$$

integrating on the domain Ω_i

$$\sum_{i=1}^{p}\left(-\frac{\rho^i}{\mu^i}\int_{\Omega_i}\Delta\phi^i(\mathbf{x})\phi^i d\mathbf{x}\right)=\sum_{i=1}^{p}\frac{4\pi(\rho^i)^2 G}{\mu^i}\int_{\Omega_i}\phi^i(\mathbf{x})\mathrm{div}\ \mathbf{u}^i(\mathbf{x})d\mathbf{x}. \tag{49}$$

Using Green's theorem and the boundary conditions we obtain

$$\begin{aligned}&\sum_{i=1}^{p}\frac{\rho^i}{\mu^i}\int_{\Omega_i}\nabla\phi^i(\mathbf{x})\cdot\nabla\phi^i(\mathbf{x})d\mathbf{x}\\&\quad=\sum_{i=1}^{p}\frac{\rho^i}{\mu^i}\int_{\Omega_i}\left|\nabla\phi^i(\mathbf{x})\right|^2 d\mathbf{x}\\&\quad=\sum_{i=1}^{p}\frac{4\pi(\rho^i)^2 G}{\mu^i}\int_{\Omega_i}\phi^i(\mathbf{x})\mathrm{div}\ \mathbf{u}^i(\mathbf{x})d\mathbf{x}.\end{aligned} \tag{50}$$

Summarizing, we have following equations:

$$\begin{aligned}&\sum_{i=1}^{p}4\pi\rho^i G a_u^i\left(\mathbf{u}^i,\mathbf{u}^i\right)=-\sum_{i=1}^{p}\frac{4\pi(\rho^i)^2 G}{\mu^i}\int_{\Omega_i}\phi^i(\mathbf{x})\mathrm{div}\ \mathbf{u}^i(\mathbf{x})d\mathbf{x},\\&\sum_{i=1}^{p}\frac{\rho^i}{\mu^i}\int_{\Omega}\left|\nabla\phi^i(\mathbf{x})\right|^2=\sum_{i=1}^{p}\frac{4\pi(\rho^i)^2 G}{\mu^i}\int_{\Omega_i}\phi^i\ \mathrm{div}\ \mathbf{u}^i(\mathbf{x})d\mathbf{x}.\end{aligned} \tag{51}$$

Adding both relations we inevitably conclude that

$$\sum_{i=1}^{p} 4\pi\rho^i G a_u^i(\mathbf{u}^i,\mathbf{u}^i) + \sum_{i=1}^{p} \frac{\rho^i}{\mu^i}\int_{\Omega_i} \left|\nabla\phi^i(\mathbf{x})\right|^2 d\mathbf{x} = 0, \tag{52}$$

and using the coercive inequality satisfied by $a_u^i(\mathbf{u}^i,\mathbf{u}^i)$ (which we shall show later) we obtain

$$\sum_{i=1}^{p} 4\pi\rho^i GK\left\|\nabla\mathbf{u}^i\right\|^2_{L^2(\Omega_i)} + \sum_{i=1}^{p} \frac{\rho^i}{\mu^i}\int_{\Omega_i} \left|\nabla\phi^i(\mathbf{x})\right|^2 d\mathbf{x} = 0, \tag{53}$$

for some constant K which can depend on the spatial scale. Therefore we deduce that

$$\mathbf{u}^i(\mathbf{x}) = \mathbf{0}, \quad \text{and} \quad \phi^i(\mathbf{x}) = 0. \tag{54}$$

since $\nabla\mathbf{u}^i = 0$ and from the boundary conditions we conclude that $\mathbf{u}^i(\mathbf{x}) = \mathbf{0}$, Similarly $|\nabla\phi^i(\mathbf{x})|^2 = 0$ implies that $\phi^i(\mathbf{x}) = cte$. However, as $\phi^i(\mathbf{x}) \equiv 0$ on the upper surface, necessarily $\phi^i(\mathbf{x}) = 0$ holds in all Ω_i. We conclude that $\mathbf{u}_1^i = \mathbf{u}_2^i$ and $\phi_1^i = \phi_2^i$ $\forall$ $i = 1,..., p$, this proves the uniqueness of a weak solution.

5. Continuous Dependence Estimate

The argument of cancellation to prove the uniqueness of solutions can be applied in the same way to every possible weak solutions $\mathbf{u}^i$, ϕ^i. Now, it appears f_ϕ^i and $\mathbf{f}_u^i$, the contributions of the body force terms and the term of the integration by parts $\partial_+\Omega_1$. In particular, on top of the first layer the next inequality appears

$$\begin{aligned}\sum_{i=1}^{p} 4\pi\rho^i GA(\lambda)\left\|\nabla\mathbf{u}^i\right\|^2_{L^2(\Omega_i)} + \sum_{i=1}^{p} \frac{\rho^i}{\mu^i}\int_{\Omega_i} \left|\nabla\phi^i(\mathbf{x})\right|^2 d\mathbf{x} \\ \leq \sum_{i=1}^{p} 4\pi\rho^i G\left\langle \mathbf{f}_u^i, \mathbf{u}^i\right\rangle + \sum_{i=1}^{p} \frac{\rho^i}{\mu^i}\left\langle f_\phi^i, \phi^i\right\rangle - \frac{4\pi(\rho^1)^2 G}{\mu^1}\int_{\partial_+\Omega_1} \phi_0(\mathbf{s})\mathbf{u}^1(\mathbf{s})\cdot\mathbf{n}\, ds,\end{aligned} \tag{55}$$

where $A(\lambda)$ is a positive constant depending on the scale. Applying Young's inequality (with $\varepsilon = 1/4$ in the first and third term and $\varepsilon = 1$ in the second one) and using the theorem of traces $H^1(\Omega_1) \to H^{1/2}(\partial_+\Omega_1)$, the estimate follows without difficulty.

6. Existence of Weak Solution

To prove the existence of a weak solution we are going to divide the proof into two different uncoupled problems: The first one when gravitational perturbed is known and the second one in which the displacements are known. In both cases we shall use the Lax-Milgram's theorem (see, e.g. BRÉZIS, 1984) which for the sake of the reader we recall here:

Let H be a Hilbert space and $a(u,v): H \times H \longrightarrow \mathbb{R}$ *being a continuous and coercive bilinear form on H. Let* $L: H \longrightarrow \mathbb{R}$ *be a linear and continuous form on H. Then there exists a solution* $u \in H$ *such that* $a(u,v) = L(v)\ \forall v \in H$. We shall also use an extension of this result stated in terms of the Fredholm alternative as presented in GILBARG and TRUDINGER (1977).

6.1. *Uncoupled Problem for the Potential* (***u*** *Assumed to be Known*)

First, we are going to consider the following problem namely $(P1)[\phi_0^1, \mathbf{u}_0^i, f_\phi^i]$, on the space of energy V_ϕ, where we assume that $\mathbf{u}$ is *a priori* known.

$$(P1)[\phi_0^1,\mathbf{u}_0^i,f_\phi^i]\begin{cases} -\Delta\phi^i(\mathbf{x}) = 4\pi\rho^i G \operatorname{div}\mathbf{u}^i(\mathbf{x}) + f_\phi^i(\mathbf{x}) \text{ in } \Omega_i, \\ \phi^i(\mathbf{x}) = 0 & \text{on } \partial_l\Omega_i \forall i = 1,\ldots,p, \\ \phi^i(\mathbf{x}) = \phi^{i+1}(\mathbf{x}) & \\ \dfrac{\partial\phi^i(\mathbf{x})}{\partial z} = \dfrac{\partial\phi^{i+1}(\mathbf{x})}{\partial z} & \text{on } \partial_-\Omega_i = \partial_+\Omega_{i+1} \forall i = 1,\ldots,p-1, \\ \phi^1(\mathbf{x}) = \phi_0^1(\mathbf{x}) & \text{on } \partial_+\Omega_1, \\ \phi^p(\mathbf{x}) = 0 & \text{on } \partial_-\Omega_p. \end{cases} \quad (56)$$

Definition 2. *We assume the above regularity* (26) *and* (27) *on the data* f_ϕ *and* ϕ_0. *We say that function* ϕ *is a weak solution of the problem* (56) *if* $\phi^* := \phi - \phi_0 \in V_\phi$ and for every test function $\theta \in V_\phi$ *the following integral identity holds*

$$\sum_{i=1}^{p}\int_{\Omega_i}\nabla\phi^{*i}(\mathbf{x})\cdot\nabla\theta^i(\mathbf{x})d\mathbf{x} = \sum_{i=1}^{p}\left(-4\pi\rho^i G\right)\int_{\Omega_i}\operatorname{div}\mathbf{u}^i(\mathbf{x})\theta^i(\mathbf{x})d\mathbf{x} + \left\langle f_\phi,\theta\right\rangle_{V'_\phi\times V_\phi}. \quad (57)$$

Theorem 2. *Assumed the* (26) *and* (27) *on the data* f_ϕ *and* ϕ_0, *there exists a unique weak solution*, ϕ, *of problem* $(P1)[\phi_0^1, \mathbf{u}_0^i, f_\phi^i]$.

Proof. In order to apply the Lax-Milgram theorem we define the bilinear form $a_\phi: V_\phi \times V_\phi \longrightarrow \mathbb{R}$ and the linear form $L_\phi: V_\phi \longrightarrow \mathbb{R}$ as follows:

$$\begin{aligned} a_\phi(\phi^*,\theta) &:= \sum_{i=1}^{p} a_\phi^i\left(\phi^{*i},\theta^i\right) = \sum_{i=1}^{p}\int_{\Omega_i}\nabla\phi^{*i}(\mathbf{x})\cdot\nabla\theta^i(\mathbf{x})d\mathbf{x} \\ &= \int_\Omega \nabla\phi^*(\mathbf{x})\cdot\nabla\theta(\mathbf{x})d\mathbf{x} \\ L_\phi(\theta) &:= -\sum_{i=1}^{p} 4\pi\rho^i G\int_{\Omega_i}\operatorname{div}\mathbf{u}^i(\mathbf{x})\theta^i(\mathbf{x})d\mathbf{x} + \left\langle f_\phi,\theta\right\rangle_{V'_\phi\times V_\phi} \end{aligned} \quad (58)$$

To apply this theorem we have to prove that the bilinear form $a_\phi(\cdot,\cdot)$ is continuous and coercive, and that the linear form $L_\phi(\cdot)$ is continuous. Let us see it:

i) $a_\phi(\cdot,\cdot)$ is a bilinear form. It is easy to see that

$$\begin{cases} a_\phi(\lambda\phi_1+\mu\phi_2,\theta)=\lambda a_\phi(\phi_1,\theta)+\mu a_\phi(\phi_2,\theta), \\ a_\phi(\phi,\lambda\theta_1+\mu\theta_2)=\lambda a_\phi(\phi,\theta_1)+\mu a_\phi(\phi,\theta_2). \end{cases} \tag{59}$$

ii) To prove that $a_\phi(\cdot,\cdot)$ is continuous we should prove that there exists a constant C such that

$$\left|a_\phi(\phi^*,\theta)\right| \le C\|\phi^*\|_{V_\phi}\|\theta\|_{V_\phi} \quad \forall\phi,\theta\in V_\phi. \tag{60}$$

But

$$\left|a_\phi(\phi^*,\theta)\right| \le \int_\Omega |\nabla\phi^*(\mathbf{x})\cdot\nabla\theta(\mathbf{x})|d\mathbf{x} \le \|\nabla\phi^*\|_{L^2}\|\nabla\theta\|_{L^2} \tag{61}$$

and by some well-known results (see, e.g., Lions, 1981) we know that the norm on $H^1(\Omega)$ is equivalent to the space V_ϕ.

iii) To prove that $a_\phi(\cdot,\cdot)$ is coercive we must to prove that there exists a constant $\alpha>0$ such that

$$a_\phi(\phi^*,\phi^*)\ge\alpha\|\phi^*\|^2 \quad \forall\phi^*\in V_\phi. \tag{62}$$

However by Poincare's inequality we have that

$$a_\phi(\phi^*,\phi^*)=\int_\Omega|\nabla\phi^*(\mathbf{x})|^2d\mathbf{x}=\|\phi^*\|^2_{V_\phi} \tag{63}$$

and by taking alpha equal to $\alpha=1$, we obtain it.

iv) It is easy to see that $L_\phi(\cdot)$ is linear.

v) To prove that $L_\phi(\theta)$ is continuous we have to prove that there exists a constant $D>0$ such that

$$L_\phi(\theta)\le D\|\theta\|_{V_\phi} \quad \forall\theta\in V_\phi. \tag{64}$$

But

$$\begin{aligned} L_\phi(\theta(\mathbf{x})) &\le \int_\Omega \left|\left(4\pi\rho G\mathrm{div}\mathbf{u}(\mathbf{x})\theta(\mathbf{x})+f_\phi(\mathbf{x})\theta(\mathbf{x})\right)\right|d\mathbf{x} \\ &\le 4\pi(\max_{i=1,\dots,p}\rho^i)G\|\mathbf{u}\|_{L^2(\Omega)^3}\|\theta\|_{V_\phi}+\left\|f_\phi\right\|_{V'_\phi}\|\theta\|_{V_\phi}, \end{aligned} \tag{65}$$

by taking D as

$$D=4\pi(\max_{i=1,\dots,p}\rho^i)G\|\mathbf{u}\|_{L^2(\Omega)^3}+\left\|f_\phi\right\|_{V'_\phi} \tag{66}$$

we obtain (64) ■

6.2. Uncoupled Problem for the Potential (ϕ Assumed to be Known)

Now, we consider the next problem on V_u:

$$(P2)[\phi_0^i, \mathbf{f}_u^i]\begin{cases} -\Delta\mathbf{u}^i(\mathbf{x}) - \dfrac{1}{1-2\nu^i}\nabla\big(\mathrm{div}\mathbf{u}^i(\mathbf{x})\big) - \dfrac{\rho^i g}{\mu^i}\nabla\big(\mathbf{u}^i(\mathbf{x})\cdot\mathbf{e}_z\big) \\ \quad + \dfrac{\rho^i g}{\mu^i}\mathbf{e}_z\mathrm{div}\mathbf{u}^i(\mathbf{x}) = -\dfrac{\rho_i}{\mu_i}\nabla\phi^i(\mathbf{x}) + \mathbf{f}_u^i(\mathbf{x}) & \text{in } \Omega_i, \\ \mathbf{u}^i(\mathbf{x}) = \mathbf{0} & \text{on } \partial_l\Omega_i \forall i = 1,\ldots,p, \\ \mathbf{u}^i(\mathbf{x}) = \mathbf{u}^{i+1}(\mathbf{x}) & \text{on } \partial_-\Omega_i = \partial_+\Omega_{i+1} \\ \dfrac{\partial\mathbf{u}^i(\mathbf{x})}{\partial z} = \dfrac{\partial\mathbf{u}^{i+1}(\mathbf{x})}{\partial z} & \forall i = 1,\ldots,p-1, \\ \mathbf{u}^1(\mathbf{x}) = \mathbf{0} & \text{on } \partial_+\Omega_1, \\ \mathbf{u}^p(\mathbf{x}) = \mathbf{0} & \text{on } \partial_-\Omega_p. \end{cases} \tag{67}$$

Definition 3. *We assume the regularity* (25) *and* (27) *on the data f_ϕ and ϕ_0. Given ϕ, with $\phi - \phi_0 \in V_\phi$, we say that function* $\mathbf{u}$ *is a weak solution of the problem* (67) *if* $\mathbf{u} \in V_u$ *and for every test function* $\mathbf{w} \in V_u$ *the following integral identity holds*:

$$\sum_{i=1}^{p}\Bigg[\int_{\Omega_i}\Bigg(\nabla\mathbf{u}^i(\mathbf{x}) : \nabla\mathbf{w}^i(\mathbf{x}) + \frac{1}{1-2\nu^i}\mathrm{div}\,\mathbf{u}^i(\mathbf{x})\mathrm{div}\,\mathbf{w}^i(\mathbf{x}) - \frac{\rho^i g}{\mu^i}\nabla\big(\mathbf{u}^i(\mathbf{x})\cdot\mathbf{e}_z\big)\cdot\mathbf{w}^i(\mathbf{x}) + \frac{\rho^i g}{\mu^i}\mathbf{e}_z\,\mathrm{div}\,\mathbf{u}^i(\mathbf{x})\mathbf{w}^i(\mathbf{x})d\mathbf{x}\Bigg)\Bigg] = -\sum_{i=1}^{p}\frac{\rho^i}{\mu^i}\int_{\Omega_i}\nabla\phi^i(\mathbf{x})\cdot\mathbf{w}^i(\mathbf{x})d\mathbf{x} + \langle\mathbf{f}_u, \mathbf{w}\rangle_{V_u'\times V_u}. \tag{68}$$

Theorem 3. *Assume* (25) *and* (27) *on the data f_ϕ and ϕ_0. Assume also that*

$$H(\rho,\mu,\nu)\frac{\Big(\max_{i=1,\ldots,p}\frac{\rho^i}{\mu^i}\Big)g}{2\Big(\min_{i=1,\ldots,p}\frac{1}{1-2\nu^i}\Big)}\text{is enough small.} \tag{69}$$

Then there exists a unique weak solution, $\mathbf{u}$, *of problem* (*P*2) [ϕ_0^i, $\mathbf{f}_u^i$].

Proof. We define the bilinear form a_u: $V_u \times V_u \longrightarrow \mathbb{R}$ and the linear form L_u: $V_u \longrightarrow \mathbb{R}$ as follows:

$$a_u(\mathbf{u},\mathbf{w}) := \sum_{i=1}^{p}\Bigg[\int_{\Omega_i}\Bigg(\nabla\mathbf{u}^i(\mathbf{x}) : \nabla\mathbf{w}^i(\mathbf{x}) + \frac{1}{1-2\nu^i}\mathrm{div}\,\mathbf{u}^i(\mathbf{x})\mathrm{div}\,\mathbf{w}^i(\mathbf{x}) - \frac{\rho^i g}{\mu^i}\nabla\big(\mathbf{u}^i(\mathbf{x})\cdot\mathbf{e}_z\big)\cdot\mathbf{w}^i(\mathbf{x}) + \frac{\rho^i g}{\mu^i}\mathbf{e}_z\,\mathrm{div}\,\mathbf{u}^i(\mathbf{x})\mathbf{w}^i(\mathbf{x})d\mathbf{x}\Bigg)\Bigg],$$

$$L_u(\mathbf{w}) := -\sum_{i=1}^{p} \frac{\rho^i}{\mu^i} \int_{\Omega_i} \nabla \phi^i(\mathbf{x}) \cdot \mathbf{w}^i(\mathbf{x}) d\mathbf{x} + \langle \mathbf{f}_u, \mathbf{w} \rangle_{V_u' \times V_u}. \tag{70}$$

We shall apply the version of the Lax-Milgram theorem given in GILBARG and TRUDINGER (1977). We must prove that the bilinear form $a_u(\cdot,\cdot)$ is continuous and coercive, and the lineal form $L_u(\cdot)$ is continuous. Indeed:

i) It is easy to see that $a_u(\cdot,\cdot)$ is a bilinear form.
ii) To prove that $a_u(\cdot,\cdot)$ is continuous we have to prove the existence of a constant C such that

$$|a_u(\mathbf{u}, \mathbf{w})| \leq C \|\mathbf{u}\|_{V_u} \|\mathbf{w}\|_{V_u} \quad \forall \mathbf{u}, \mathbf{w} \in V_u. \tag{71}$$

We have

$$\begin{aligned} |a_u(\mathbf{u}, \mathbf{w})| \leq{}& \|\nabla \mathbf{u}\|_{L^2} \|\nabla \mathbf{w}\|_{L^2} + \left(\max_{i=1,\ldots,p} \frac{1}{1-2\nu^i} \right) \|\text{div } \mathbf{u}\|_{L^2} \|\text{div } \mathbf{w}\|_{L^2} \\ &+ \left(\max_{i=1,\ldots,p} \frac{\rho^i}{\mu^i} \right) g [\|\nabla \mathbf{u}\|_{L^2} \|\mathbf{w}\|_{L^2} + \|\text{div } \mathbf{u}\|_{L^2} \|\mathbf{w}\|_{L^2}]. \end{aligned} \tag{72}$$

So by taking the constant C as

$$C = 1 + \left(\max_{i=1,\ldots,p} \frac{1}{1-2\nu^i} \right) + 2 \left(\max_{i=1,\ldots,p} \frac{\rho^i}{\mu^i} \right) g, \tag{73}$$

the inequality (71) holds.
iii) To prove that $a_u(\cdot,\cdot)$ is coercive we must prove the existence of a constant $\alpha > 0$ such that

$$a_u(\mathbf{u}, \mathbf{u}) \geq \alpha \|\mathbf{u}\|_{V_u}^2 \quad \forall \mathbf{u} \in V_u. \tag{74}$$

But due to:

$$\begin{aligned} &\sum_{i=1}^{p} \frac{\rho^i g}{\mu^i} \int_{\Omega_i} [-\nabla (\mathbf{u}^i(\mathbf{x}) \cdot \mathbf{e}_z) \cdot \mathbf{u}^i(\mathbf{x}) + \mathbf{e}_z \text{ div } \mathbf{u}^i(\mathbf{x}) \mathbf{u}^i(\mathbf{x}) d\mathbf{x})] \\ &\quad = 2 \sum_{i=1}^{p} \frac{\rho^i g}{\mu^i} \int_{\Omega_i} \mathbf{e}_z \text{ div } \mathbf{u}^i(\mathbf{x}) \mathbf{u}^i(\mathbf{x}) d\mathbf{x} \end{aligned} \tag{75}$$

we have,

$$\begin{aligned} &\left| \sum_{i=1}^{p} \int_{\Omega_i} \frac{\rho^i g}{\mu^i} [-\nabla (\mathbf{u}^i(\mathbf{x}) \cdot \mathbf{e}_z) \cdot \mathbf{u}^i(\mathbf{x}) + \mathbf{e}_z \text{ div } \mathbf{u}^i(\mathbf{x}) \mathbf{u}^i(\mathbf{x}) d\mathbf{x})] \right| \\ &\quad \leq 2 \left(\max_{i=1,\ldots,p} \frac{\rho^i}{\mu^i} \right) g \|\text{div } \mathbf{u}\|_{L^2} \|\mathbf{u}\|_{L^2}. \end{aligned} \tag{76}$$

By applying the Young's inequality $ab \leq \varepsilon a^2 + (1/4\varepsilon)\, b^2$ with

$$\varepsilon = \frac{\left(\min_{i=1,\ldots,p} \frac{1}{1-2\nu^i}\right)}{2\left(\max_{i=1,\ldots,p} \frac{\rho^i}{\mu^i}\right) g} \tag{77}$$

we deduce that

$$a_u(\mathbf{u},\mathbf{u}) \geq \|\nabla \mathbf{u}\|^2_{L^2} - C\|\mathbf{u}\|^2_{L^2} \qquad \text{(coercive)}$$

with

$$C = \frac{\left(\max_{i=1,\ldots,p} \frac{\rho^i}{\mu^i}\right) g}{2\left(\min_{i=1,\ldots,p} \frac{1}{1-2\nu^i}\right)}. \tag{78}$$

If we use the equivalence of norms in V_u

$$\|\nabla \mathbf{u}\|^2_{L^2} \geq \Theta(\|\nabla \mathbf{u}\|^2_{L^2} + \|\mathbf{u}\|^2_{L^2}) \tag{79}$$

we deduce that if

$$\Theta > \frac{\left(\max_{i=1,\ldots,p} \frac{\rho^i}{\mu^i}\right) g}{2\left(\min_{i=1,\ldots,p} \frac{1}{1-2\nu^i}\right)} \qquad \text{(ratio)}$$

then

$$a_u(\mathbf{u},\mathbf{w}) \geq \left(\Theta - \frac{\left(\max_{i=1,\ldots,p} \frac{\rho^i}{\mu^i}\right) g}{2\left(\min_{i=1,\ldots,p} \frac{1}{1-2\nu^i}\right)}\right) \|\nabla \mathbf{u}\|^2_{L^2} \tag{80}$$

and taking

$$\alpha = \Theta - \frac{\left(\max_{i=1,\ldots,p} \frac{\rho^i}{\mu^i}\right) g}{2\left(\min_{i=1,\ldots,p} \frac{1}{1-2\nu^i}\right)}. \tag{81}$$

iv) It is easy to see that $L_u(\cdot)$ is a linear form.

v) To prove that $L_u(\cdot)$ is continuous we have to prove the existence of a constant $D > 0$ such that

$$L_u(\mathbf{w}) \leq D\|\mathbf{w}\|_{V_u} \quad \forall \mathbf{w} \in V_u. \tag{82}$$

But we have

$$\begin{aligned} L_u(\mathbf{w}) &\leq \left(\max_{i=1,\ldots,p} \frac{\rho^i}{\mu^i}\right) \|\nabla \phi(\mathbf{x})\|_{L^2} \|\mathbf{w}(\mathbf{x})\|_{L^2} + \|\mathbf{f}_u(\mathbf{x})\|_{L^2} \|\mathbf{w}(\mathbf{x})\|_{L^2} \\ &\leq \left(\max_{i=1,\ldots,p} \frac{\rho^i}{\mu^i}\right) \|\nabla \phi\|_{L^2} \|\mathbf{w}\|_{L^2} + \|\mathbf{f}_u\|_{V'_u} \|\mathbf{w}\|_{V_u} \end{aligned} \tag{83}$$

and is enough to take

$$D = \left(\max_{i=1,\dots p}\frac{\rho^i}{\mu^i}\right)\|\nabla\phi\|_{L^2} + \|\mathbf{f}_u\|_{V_u'}. \tag{84}$$

To treat the general case we can take the Θ constant as

$$\Theta = \frac{1}{2}\min\left\{\frac{1}{C(\Omega)}, 1\right\} \tag{85}$$

where $C(\Omega)$ is the Poincaré constant on the domain Ω. We introduce the change of scale $\mathbf{y} = \lambda\ \mathbf{x}$ which allows definition of a rescaling function $\mathbf{v}(\mathbf{y}) = \mathbf{u}(\lambda\mathbf{x})$ which emerges from terms in λ associated with the first derivative of $\mathbf{u}$ and terms in λ^2 associated with the second derivatives of $\mathbf{u}$. In this way, equations satisfied by $\mathbf{v}(\mathbf{y})$ are:

$$\begin{cases} -\Delta\mathbf{v}^i(\mathbf{y}) - \dfrac{1}{1-2v^i}\nabla\big(\operatorname{div}\mathbf{v}^i(\mathbf{y})\big) - \dfrac{\rho^i g\lambda}{\mu^i}\nabla\big(\mathbf{v}^i(\mathbf{y})\cdot\mathbf{e}_z\big) \\ + \dfrac{\rho^i g\lambda}{\mu^i}\mathbf{e}_z \operatorname{div}\mathbf{v}^i(\mathbf{y}) = -\dfrac{\rho_i\lambda}{\mu_i}\nabla\phi^i\big(\lambda^{-1}\mathbf{y}\big) + \lambda^2\mathbf{f}_u^i\big(\lambda^{-1}\mathbf{y}\big) \end{cases} \text{ in } \Omega_i, \quad \text{(Dilatation equation)}$$

Next, we remark that new constant $C(\lambda\ \Omega)$ can be taken as $\lambda\ C(\Omega)$ since it depends only on the diameter of Ω. Therefore, in the new system of equations we must require that the following inequality is verified:

$$\frac{1}{2}\min\left\{\frac{1}{\lambda C(\Omega)}, 1\right\} > \frac{\lambda\left(\max_{i=1,\dots,p}\frac{\rho^i}{\mu^i}\right)g}{2\left(\min_{i=1,\dots,p}\frac{1}{1-2v^i}\right).} \tag{86}$$

But this is obtained by taking λ small enough. This takes into account avoiding the hypothesis on $H(\rho, \mu, v)$. ■

Remark 3. *If we do not have hypothesis $H(\rho, \mu, v)$ Fredholm's alternative (as stated e.g. in* Gilbarg *et al., 1977) also can be applied. The uniqueness of solutions of the problem with zero data would lead to the existence of a solution of the problem for arbitrary data.*

Remark 4. *In fact, by remarking that the last inequality and the change of variable do not modify the contour of level of* **u**, *without loss of generality, we can assume that the coercive constant is* $\alpha \geq 1$.

The above theorems on the uncoupled problems once proved, we proceed with the proof of the main theorem of this paper, that is, the existence of weak solutions for the coupled system (8).

6.3. General Idea of the Proof of Existence of Solutions of the Coupled System

The existence of weak solutions for both cases (ϕ known, problem ($P1$) $[\phi_0^1, \mathbf{u}_0^i, f_\phi^i]$, and $\mathbf{u}$ known, problem ($P2$) $[\phi_0^i, \mathbf{f}_u^i]$) has been proved. To prove the existence of weak

solutions of the coupled system we will use an iterative scheme which, as a matter of fact, is also interesting for the numerical analysis of the system. Firstly, we shall construct two sequences $\{\mathbf{u}^n(\mathbf{x})\}$ and $\{\phi^n(\mathbf{x})\}$ in the following way. We start with the vector $\phi^0(\mathbf{x})$ which has the boundary date $\phi_0(\mathbf{x})$ as a first component and the rest of the components 0. With this vector and problem $(P2)$ $[\phi_0^i, \mathbf{f}_u^i]$ we obtain a unique vector $\mathbf{u}^1(\mathbf{x})$. Then, putting it in problem $(P1)$ $[\phi_0^1, \mathbf{u}_0^i, f_\phi^i]$ we obtain a unique vector ϕ^1. We build the sequences:

$$\phi^0(\mathbf{x}) = \begin{pmatrix} \phi_0(\mathbf{x}) \\ 0 \\ \cdot \\ \cdot \\ \cdot \\ 0 \end{pmatrix} \xrightarrow{(P2)[\phi_0^i,\, \mathbf{f}_u^i]} \mathbf{u}^1(\mathbf{x}) = \begin{pmatrix} \mathbf{u}_1^1(\mathbf{x}) \\ \mathbf{u}_2^1(\mathbf{x}) \\ \cdot \\ \cdot \\ \cdot \\ \mathbf{u}_p^1(\mathbf{x}) \end{pmatrix} \xrightarrow{(P1)[\phi_0^1,\, \mathbf{u}_0^i, f_\phi^i]} \phi^1(\mathbf{x}) = \begin{pmatrix} \phi_1^1(\mathbf{x}) \\ \phi_2^1(\mathbf{x}) \\ \cdot \\ \cdot \\ \cdot \\ \phi_p^1(\mathbf{x}) \end{pmatrix} \xrightarrow{(P2)[\phi_0^i,\, \mathbf{f}_u^i]}$$

$$\mathbf{u}^2(\mathbf{x}) = \begin{pmatrix} \mathbf{u}_1^2(\mathbf{x}) \\ \mathbf{u}_2^2(\mathbf{x}) \\ \cdot \\ \cdot \\ \cdot \\ \mathbf{u}_p^2(\mathbf{x}) \end{pmatrix} \ldots \phi^{n-1}(\mathbf{x}) = \begin{pmatrix} \phi_1^{n-1}(\mathbf{x}) \\ \phi_2^{n-1}(\mathbf{x}) \\ \cdot \\ \cdot \\ \cdot \\ \phi_p^{n-1}(\mathbf{x}) \end{pmatrix} \xrightarrow{(P2)[\phi_0^i,\, \mathbf{f}_u^i]} \mathbf{u}^n(\mathbf{x}) = \begin{pmatrix} \mathbf{u}_1^n(\mathbf{x}) \\ \mathbf{u}_2^1(\mathbf{x}) \\ \cdot \\ \cdot \\ \cdot \\ \mathbf{u}_p^n(\mathbf{x}) \end{pmatrix} \xrightarrow{(P1)[\phi_0^1,\, \mathbf{u}_0^i, f_\phi^i]}$$

$$\phi^n(\mathbf{x}) = \begin{pmatrix} \phi_1^n(\mathbf{x}) \\ \phi_2^n(\mathbf{x}) \\ \cdot \\ \cdot \\ \cdot \\ \phi_p^n(\mathbf{x}) \end{pmatrix}.$$

Then we prove a weak convergence on V_u and V_ϕ

$$\{\mathbf{u}^n\} \xrightarrow{V_u} \mathbf{u}, \;\; \{\phi^n\} \xrightarrow{V_\phi} \phi \tag{87}$$

to some functions $(\mathbf{u}, \phi)$ and later we will see $\{\mathbf{u}, \phi\}$ is a weak solution of the coupled system.

A Priori Estimates on $\{\boldsymbol{u}^n, \phi^n\}$. Now we shall construct an iterative scheme by defining a linear operator L on the vector $\mathbf{u}$ as follows:

$$L\mathbf{u}(\mathbf{x}) := -\Delta\mathbf{u}(\mathbf{x}) - \frac{1}{1-2v}\nabla(\operatorname{div}\mathbf{u}(\mathbf{x})) - \frac{\rho g}{\mu}\nabla(\mathbf{u}(\mathbf{x})\cdot\mathbf{e}_z) + \frac{\rho g}{\mu}\mathbf{e}_z \operatorname{div}\mathbf{u}(\mathbf{x}). \tag{88}$$

We also define

$$\mathbf{F}^{n-1}(\mathbf{x}) := \frac{\rho}{\mu}\nabla\phi^{n-1}(\mathbf{x}) + \mathbf{f}_u(\mathbf{x}). \tag{89}$$

Assuming $\phi^{n-1}(\mathbf{x})$ is given, then (by the above theorem) we can define $\mathbf{u}^n(\mathbf{x})$ as the unique weak solution of

$$\begin{cases} L\mathbf{u}^n(\mathbf{x}) = \mathbf{F}^{n-1}(\mathbf{x}), \\ + \text{Boundary conditions}(9) - (12). \end{cases} \tag{90}$$

On the other hand, by defining $J^n(\mathbf{x}) : = 4\pi\, \rho G \text{ div } \mathbf{u}^n(\mathbf{x}) \ + f_\phi(\mathbf{x})$, we can define $\phi^n(\mathbf{x})$ as a unique weak solution of

$$\begin{cases} -\Delta\phi^n(\mathbf{x}) = J^n(\mathbf{x}), \\ + (13) - (16). \end{cases} \tag{91}$$

The iterative scheme we consider is the following

$$\begin{array}{ccccccccc} \phi^0 & & \phi^1 & & \phi^2 & \dots & \phi^{n-1} & & \phi^n \\ & \searrow & \uparrow & \searrow & \uparrow & & \uparrow & \searrow & \uparrow \\ & & \mathbf{u}^1 & & \mathbf{u}^2 & \dots & \mathbf{u}^{n-1} & & \mathbf{u}^n \end{array} \tag{92}$$

where the step $2n$ is determined by the iterative scheme (90) and the step $2n + 1$ is determined by (91). We obtain some *a priori* estimates (independent on n) in order to pass to the limit.

Lemma 1. *We assume that*

$$\varepsilon := \frac{4\pi^2 G}{\alpha_u}\left(\max_{i=1,\dots,p}\frac{(\rho^i)^2}{\mu^i}\right) < 1. \tag{93}$$

Then, for any natural n

$$\|(\phi^*)^n\|_{V_\phi} \le \varepsilon\left\|(\phi^*)^{n-1}\right\|_{V_\phi} + \delta_u, \tag{94}$$

$$\|\mathbf{u}^n\|_{V_u} \le \varepsilon\left\|\mathbf{u}^{n-1}\right\|_{V_u} + \delta_\phi, \tag{95}$$

$$\delta_u = \frac{\left(\max_{\mathrm{i}=1,\dots,p}\frac{\rho^i}{\mu^i}\right)}{\alpha_u}\left\|f_\phi\right\|_{V'_\phi} + \frac{1}{\alpha_u}\left\|\mathbf{f}_u^i\right\|_{V'_u} + \frac{\left(\max_{\mathrm{i}=1,\dots,p}\frac{\rho^i}{\mu^i}\right)}{\alpha_u}\|\phi_0\|_{L^2(\Omega)}$$

$$\textit{and } \delta_\phi = \frac{4\pi G\left(\max_{\mathrm{i}=1,\dots,\mathrm{p}}\rho^{\mathrm{i}}\right)}{\alpha_u}\left\|\mathbf{f}_u^i\right\|_{V'_u} + \frac{8\pi G\left(\max_{\mathrm{i}=1,\dots,p}\frac{(\rho^i)^2}{\mu^i}\right)}{\alpha_u}\|\phi_0\|_{L^2(\Omega)} + \left\|f_\phi\right\|_{V'_\phi}. \tag{96}$$

In particular,

$$\|(\phi^*)^n\|_{V_\phi} \le \frac{\delta}{1-\varepsilon}, \tag{97}$$

$$\|\mathbf{u}^n\|_{V_u} \leq \frac{\delta}{1-\varepsilon}. \tag{98}$$

The proof of Lemma 1 is given in the Appendix.

Remark 5. *If the hypothesis of the last lemma is not verified we can carry out a change of scale in the spatial variable* $\mathbf{y} = \lambda\mathbf{x}$ *so that the final coupled system for rescaled functions* $\varphi(\mathbf{y}) = \phi(\lambda\mathbf{x})$ *and* $\mathbf{v}(\mathbf{y}) = \mathbf{u}(\lambda\mathbf{x})$ *leads to some new constants (now dependent on* λ*), which implies that the new* ε *verifies this hypothesis. Then, we can always reconsider the system in an appropriate scale and, in this way, we can conclude that the subsequences* $\{\mathbf{u}^n, \phi^n\}$ *are uniformly bounded on the space V.*

6.4. Passing to the Limit

As V is a Hilbert space, from the *a priori* estimates we can state there exists a subsequence which converge weakly

$$\begin{cases} \mathbf{u}^m \rightharpoonup \mathbf{u} & \text{in} V_u, \\ \phi^m \rightharpoonup \phi & \text{in} V_\phi. \end{cases} \tag{99}$$

From the compact Sobolev embedding $H^1 \subset L^2$ we can say that this subsequence $\{\mathbf{u}^m, \phi^m\}$ converges strongly in L^2. Now, if we multiply by any test functions we can pass to the limit in all expressions and so the vectorial function $(\mathbf{u}, \phi)$ is a weak solution of the problem. Moreover, from the uniqueness of solutions (already proved), we can affirm that any subsequence of $\{\mathbf{u}^n, \phi^n\}$ has to converge to the same vectorial function $(\mathbf{u}, \phi)$. In this way the proof of the Theorem 1 is now completed.

7. Conclusions

We have proved the existence and uniqueness of solutions of an elastic-gravitational model representing an ideal plane layered Earth. We have now completed a part of the work started by Rundle in the eighties. We have applied certain techniques of the weak solutions of partial differential equations theory to provide a rigorous proof of the well-posedness of the model. Moreover, we have presented constructive proof of the existence this iterative scheme will serve us as a premise to construct a numerical method to compute the coupled effects of gravity and elastic deformations produced by possible sources embedded in the Earth (e.g., magma intrusions, faults,...). We also discover that there are suitable spatial scales in which the model is better determined than in others due to the delicate balance between the second and first differential terms in the displacement equation. In future works results obtained using these iterative schemes will be compared

with numerical results obtained by Rundle and coworkers from the eighties. Another future development will be to extend this formulation to viscoelastic and poroelastic formulation of the problem as well as to the associated dynamic systems.

Acknowledgements

Research by AA and JF has been supported by CICYT, Spain, research project CGL 2005-05500-C02-01/BTE. The research of JID was partially supported by the projects MTM2005-03463 of the DGISGPI (Spain) and CCG06-UCM/ESP-1110 of the DGUIC of the CAM and the UCM. Work by JBR has been supported through a US department of Energy of UC Davis DE-FG03-95ER14499.

Appendix Proof of Lemma 1

Let ϕ^{*n} be such that

$$a_\phi(\phi^{*n},\theta)=\langle J^n,\theta\rangle_{V'_\phi\times V_\phi}\quad\forall\theta\in V_\phi. \tag{100}$$

By taking $\theta=\phi^{*n}$ then

$$a_\phi((\phi^*)^n,(\phi^*)^n)=\langle J^n,(\phi^*)^n\rangle_{V'_\phi\times V_\phi}\le\|J^n\|_{V'_\phi}\|(\phi^*)^n\|_{V_\phi}. \tag{101}$$

But, on the other hand, as the bilinear form is coercive (with $\alpha_\phi=1$) we have

$$\|(\phi^*)^n\|^2_{V_\phi}\le a_\phi((\phi^*)^n,(\phi^*)^n)\le\|J^n\|_{V'_\phi}\|(\phi^*)^n\|_{V_\phi}, \tag{102}$$

and so

$$\|(\phi^*)^n\|_{V_\phi}\le\|J^n\|_{V'_\phi}. \tag{103}$$

Then, by the definition of the norm of the dual space, we obtain the *a priori* estimate:

$$\|\phi^n\|_{H^1(\Omega)}\le 4\pi\rho G\|\mathbf{u}^n\|_{L^2(\Omega)^3}+\|f_\phi\|_{V'_\phi}. \tag{104}$$

On the other hand, we remind that if $\mathbf{F}^{n-1}(\mathbf{x}):=-(\rho/\mu)\nabla\phi^{n-1}(\mathbf{x})+\mathbf{f}_u(\mathbf{x})$ then we have

$$a_u(\mathbf{u}^n,\mathbf{w})=\left\langle\mathbf{F}^{n-1},\mathbf{w}\right\rangle_{V'_u\times V_u}\ \forall\mathbf{w}\in V_u. \tag{105}$$

Taking as a test function $\mathbf{w}=\mathbf{u}^n$ we get

$$a_u(\mathbf{u}^n,\mathbf{u}^n)=\left\langle\mathbf{F}^{n-1},\mathbf{u}^n\right\rangle\le\left\|\mathbf{F}^{n-1}\right\|_{V'_u}\|\mathbf{u}^n\|_{V_u} \tag{106}$$

and from the coerciveness of the bilinear form a_u we conclude that

$$\alpha_u \|\mathbf{u}^n\|_{V_u} \leq \left\|\mathbf{F}^{n-1}\right\|_{V_u'}, \tag{107}$$

Substituting $|\phi^{*n-1}|_{L^2(\Omega)}$ into the estimate obtained in the last step we conclude

$$\|\mathbf{u}^n\|_{V_u} \leq \frac{4\pi\rho^2 G}{\mu\alpha_u}\left\|\mathbf{u}^{n-1}\right\|_{V_u} + \frac{\rho}{\mu\alpha_u}\left\|f_\phi\right\|_{V_\phi'} + \frac{1}{\alpha_u}\left\|\mathbf{f}_u^i\right\|_{V_u'} + \frac{\rho}{\mu\alpha_u}\|\phi_0\|_{L^2(\Omega)}. \tag{108}$$

Similarly, substituting $|\mathbf{u}^n|_{L^2(\Omega)^3}$ (in (104)) into the estimate obtained in the last step we arrive at

$$\|\phi^n\|_{H^1(\Omega)} \leq \frac{4\pi\rho^2 G}{\mu\alpha_u}\left\|\phi^{n-1}\right\|_{H^1(\Omega)} + \frac{4\pi\rho G}{\alpha_u}\left\|\mathbf{f}_u^i\right\|_{V_u'} + \frac{8\pi\rho^2 G}{\mu\alpha_u}\|\phi_0\|_{L^2(\Omega)} + \left\|f_\phi\right\|_{V_\phi'}, \tag{109}$$

which completes the first part of the lemma. The uniform estimates of the statement are obtained by a recurrence argument using the sum of a geometrical progression.

References

Aki, k., and Richards, P.G., *Quantitative Seismology*, (University Science Books, Sausalito, California., 2002).

Brézis, H., *Analyses fonctionelle: théorie et applications*, (Alianza, Madrid., 1984).

Bustin, A., Hyndman, R.D., Lambert, A., Ristau, J., He, J., Dragert, H., and Van der Kooij, M. (2004), *Fault parameters of the Nisqually earthquake determined from moment tensor solutions and the surface deformation from GPS and InSAR*, Bull. Seismol. Soc. Am. *94*, 2, 363–376.

Charco, M., Fernández, J., Luzón, F., and Rundle, J. B. (2006), *On the relative importance of self-gravitation and elasticity in modelling volcanic ground deformation and gravity changes*, J. Geophys. Res. *111*, B03404, doi:10.1029/2005JB003754.

Charco, M., Luzón, F., Fernández, J., and Tiampo, K.F. (2007), *Topography and selfgravitation interaction in elastic-gravitational modelling*, Geochem. Geophy. Geosystems (G3), 8, Q01001, doi:10.1029/2006GC001412.

Charco, M., Fernández, J., Luzón, F., Tiampo, K.F., and Rundle, J.B. (2007b), *Some insights about topographic, elastic and self-gravitation interaction in modelling ground deformation and gravity changes in active volcanic areas*, Pure appl. geophys. *164*/4, 865–878.

Díaz, J.I., and Talenti, G. (2004), *A free boundary problem related to the location of volcanic gas sources*, Pure Appl. Geophys. *161*, 1509–1517.

Dixon, T.H., Mao, A., Bursik, M., Heflin, M., Langbein, J., Stein, R., and Webb, F. (1997), *Continuous monitoring of surface deformation at Long Valley Caldera, California, with GPS*, J. Geophys. Res. *102*, 12017–12034.

Dzurisin, D. (2003), *A comprehensive approach to monitoring volcano deformation as a window on the eruptive cycle*, Rev. Geophys. *41*(1), 1001, doi:10.1029/2001RG000107 (Correction: 2003,41(2), 1009, doi:10.1029/2003RG000134).

Fernández, J., and Rundle, J.B. (1994a), *Gravity changes and deformation due to a magmatic intrusion in a two-layered crustal model*, J. Geophys. Res. *99*, 2737–2746.

Fernández, J., and Rundle, J.B. (1994b), *FORTRAN program to compute displacement, potential and gravity changes resulting from a magma intrusion in a multilayered Earth model*, Comp. Geosci. *20*, 461–510.

Fernández, J., Rundle, J.B., Granell, R.D.R, and Yu, T.-T. (1997), *Programs to compute deformation due to a magma intrusion in elastic-gravitational layered Earth models*, Comp. Geosci. *23*, 231–249.

Fernández, J., Charco, M., Tiampo, K.F., Jentzsch, G., and Rundle, J. B. (2001), *Joint interpreta- tion of displacement and gravity data in volcanic areas. A test example: Long Valley- Caldera, California*, J. Volcanol. Geotherm. Res. *28*, 1063-1066.

FERNÁNDEZ, J., TIAMPO, K.F., RUNDLE, J.B., and JENTZSCH, G. (2005a), *On the interpretation of vertical gravity gradients produced by magmatic intrusions*, J. Geodyn. *39*/5, 475–492. doi: 10.1016/j.jog.2005.04.005.

FERNÁNDEZ, J., ROMERO, R., CARRASCO, D., TIAMPO, K.F., RODRÍGUEZ-VELASCO, G., APARICIO, A., ARAÑA, V., and GONZÁLEZ-MATESANZ, F.J. (2005b), *Detection of displacements in Tenerife Island Canaries, using radar interferometry*, Geophys. J. Int. *160*, 33–45. doi:10.111/j.1365−246x.200502487x.

GILBARG, D., and TRUDINGER, N.S., *Elliptic Partial Differential Equations of Second Order*, (Springer-Verlag, Berlin., 1977)

GUDMUNSSON, S., and SIGMUNDSSON, F. (2002), *Three-dimensional surface motion maps estimated from combined interferometric systhetic aperture radar and GPS data*, J. Geo-phys. Res. *107*, B10, 2250. doi:10.1029/2001JB000283.

LANARI, R., BERARDINO, P., BORGSTRÖM, S., DEL GAUDIO, C., DE MARTINO, P., FORNARO, G., GUARINO, S., RICCIARDI, G.P., SANSOSTI, E., and LUNDGREN, P. (2004), *The use of IFSAR and classical geodetic techniques for caldera unrest episodes: Application to the Campi Flegrei uplift event of 2000*, J. Volcanol. Geotherm. Res. *133*, 247–260.

LARSON, K.M., CERVELLI, P., LISOWSKI, M., MIKLIUS, A., SEGALL, P., and OWEN, S. (2001), *Volcano monitoring using the Global Positioning System: Filtering strategies*, J. Geo-phys. Res. *106*, B9, 19453–19464.

LIONS, J.L. (1981), *Some methods in the mathematical analysis of systems and their control*, Science, Beijing.

LOVE, A.E.H., *Some problems in Geodynamics*, (Cambridge University Press, New York., 1911).

LUNDGREN, P., and STRAMONDO, S., (2002), *Slip distribution of the 1997 Umbria-Marche earthquake sequence: Joint inversion of GPS and sysnthetic aperture radar interferometry data*, J. Geophys. Res. *107*, B11, 2316. doi:10.1029/2000JB000103.

MANZO, M., RICCIARDI, G.P., CASU, F., VENTURA, G., ZENI, G., BORGSTRÖM, S., BERARDINO, P., DEL GAUDIO, C., and LANARI, R. (2006), *Surface deformation analysis in the Ischia Island (Italy) based on spaceborne radar interferometry*, J. volcanol. Geother. Res. *151*, 399–416.

NATIONAL RESEARCH COUNCIL OF THE NATIONALACADEMIES, *Living on an active Earth. Per- spectives on Earthquake Science*, (The National Academic Press, Washington, D.C., 2003, 33pp.)

PRITCHARD, M.E., and SIMONS, M. (2002), *A satellite geodetic survey of large-scale deformation of volcanic centres in the central Andes*, Nature *418*, 167–171.

PUGLISI, G., and COLTELLI, M. (2001), *SAR Interferometry applications on active volcanoes: state of the art and perspective for volcano monitoring*, Il Nuovo Cimento *24C*, 133–145.

RUNDLE, J.B. (1980), *Static elastic-gravitational deformation of a layared half space by point couple*, J. Geophys. Res., *85*, 5355–5363.

RUNDLE, J.B. (1981a), *Numerical Evaluation of static elastic-gravitational deformation of a layared half space by point couple sources*, Rep., Sand 80–2048.

RUNDLE, J.B. (1981b), *Vertical displacements from a rectangular fault in layered elasticgravitational media*, J. Phys. Earth *29*, 173–186.

RUNDLE, J.B. (1982), *Viscoeslastic-gravitational deformation by a rectangular thrust fault in a layered Earth*, J. Geophys. Res. *87*, 9 ,7787–7796. (Correction: J. Geophys. Res. *88*, 10.647–10.653).

RUNDLE, J.B. (1983), *Correction to "Deformation, gravity and potential changes due to volcanic loading of the crust"*, J. Geophys. Res, *88*, 10, 647–10, 653.

SAGIYA, T., MIYAZAKI, S., and TADA, T. (2000), *Continuous GPS array and present-day crustal deformation of Japan*, Pure appl. Geophys. *157*, 2303–2322.

SAMSONOV, S., and TIAMPO, K., (2006), *Analytical optimization of InSAR and GPS dataset for derivation of three-dimensional surface motion*, (Journal, etc. missing)

SEGALL, P., and DAVIS, J. (1997), *GPS applications for geodynamics and earthquakes studies*, Annual Rev. Earth Planet. Sci. *25*, 301-336.

SIGURDSSON, H., HOUGHTON, B., MCNUTT, S. R., RYMER, H., and STIX, J. (2000), *Encyclopedia of Volcanoes*, (Academic Press, 1417, 34pp.)

TAMISIEA, M.E., MITROVICA, J.X., and DAVIS, J. L. (2007), *GRACE Gravity Data Constrain Ancient Ice Geometries and Continental Dynamics over Laurentia*, Science *316*, 5826,

TIAMPO, K.F., FERNÁNDEZ, J., JENTZSCH, G., CHARCO, M., and RUNDLE, J.B. (2004), *Inverting for the parameters of a volcanic source using a genetic algorithm and a model for magmatic intrusion in elastic-gravitational layered Earth models*, Comp. Geosci. *30*/9- 10 985–1001.

WRIGHT, T.J. (2002), *Remote monitoring of the earthquake cycle using satellite radar interfer- ometry*, Phil. Trans. R. Soc. Lond. A *360*, 2873–2888.

YOSHIYUKI, T., SHUHEI, O., MORITO, M., ISAO, K., and TOSHIHIRO, K., (2001), *First detection of absolute gravity change caused by earthquake*, Geophys. Res. Lett. *28*, 2979–2981.

(Received July 17, 2007, revised May 7, 2008, accepted May 8, 2008)
Published Online First: October 18, 2008

Pure appl. geophys. 165 (2008) 1491–1510
0033–4553/08/081491–20
DOI 10.1007/s00024-004-0386-9

Pure and Applied Geophysics

Modelling Gravitational Instabilities: Slab Break–off and Rayleigh–Taylor Diapirism

Sergio Zlotnik,[1] Manel Fernández,[1] Pedro Díez,[2] and Jaume Vergés[1]

Abstract—A non-standard new code to solve multiphase viscous thermo–mechanical problems applied to geophysics is presented. Two numerical methodologies employed in the code are described: A level set technique to track the position of the materials and an enrichment of the solution to allow the strain rate to be discontinuous across the interface. These techniques have low computational cost and can be used in standard desktop PCs. Examples of phase tracking with level set are presented in two and three dimensions to study slab detachment in subduction processes and Rayleigh–Taylor instabilities, respectively. The modelling of slab detachment processes includes realistic rheology with viscosity depending on temperature, pressure and strain rate; shear and adiabatic heating mechanisms; density including mineral phase changes and varying thermal conductivity. Detachment models show a first prolonged period of thermal diffusion until a fast necking of the subducting slab results in the break–off. The influence of several numerical and physical parameters on the detachment process is analyzed: The shear heating exerts a major influence accelerating the detachment process, reducing the onset time to one half and lubricating the sinking of the detached slab. The adiabatic heating term acts as a thermal stabilizer. If the mantle temperature follows an adiabatic gradient, neglecting this heating term must be included, otherwise all temperature contrasts are overestimated. As expected, the phase change at 410 km depth (olivine–spinel transition) facilitates the detachment process due to the increase in negative buoyancy. Finally, simple plume simulations are used to show how the presented numerical methodologies can be extended to three dimensions.

Key words: Tectonic plates, subduction, numerical modelling, eXtended Finite Element Method (X–FEM).

1. Introduction

Currently available computer codes for geodynamic simulation involve the resolution of a mechanical problem, usually a nonlinear flow equation (conservation of mass and momentum), coupled with a thermal problem (conservation of energy). Additional equations are incorporated to describe material parameters. For example, the density is

[1] Group of Dynamics of the Lithosphere (GDL), Institute of Earth Sciences "Jaume Almera", CSIC CSIC Lluís Solé i Sabarís s/n, 08028 Barcelona, Spain. e-mail: szlotnik,mfernandez@ija.csic.es

[2] Laboratori de Càlcul Numèric, Departament de Matemàtica Aplicada III, Universitat Politècnica de Catalunya Campus Nord UPC, 08034 Barcelona, Spain. e-mail: pedro.diez@upc.edu

computed as a function of pressure and temperature. Strong nonlinearities are produced by the constitutive equation. Usually the viscosity depends on a power of the strain rate.

A main characteristic of this kind of models is the presence of several material phases corresponding to different types of rocks. From the numerical point of view each of these materials is described by a set of parameters defining its mechanical and thermal behavior. Tracking the location of the material along time is necessary to describe the evolution of the system, including the location of each material phase, though this is not a trivial task since flow problems are naturally described in a Eulerian framework. Several numerical techniques are used in present codes to solve the basic mechanical and thermal equations: Finite elements (e.g., SCOTT *et al.*, 1990; MORESI and GURNIS, 1996), finite differences (e.g., BABEYKO *et al.*, 2002; GERYA and YUEN, 2003) and variations of these are the more popular. Nevertheless, to the knowledge of the authors, all present codes in the context of geophysical modelling, use Lagrangian markers to track the location of the materials.

The markers technique consists in using a number, usually large, of Lagrangian points carrying the material parameters. The properties of a point of the Eulerian framework are computed as an average of the markers close to this point. This technique was originally designed to work in a finite difference framework, where the discretization is regular and structured and thus it is trivial to identify the markers close to each node. When the mesh becomes nonstructured, as with finite elements, the detection of the markers in the proximity of a node is a computationally time-consuming task. To reduce the computational time most current multiphase codes run on parallel multiprocessor computers. Despite the parallelization, the number of operations required is still high and therefore, a technique requiring less computational effort is desirable.

VAN KEKEN *et al.* (1997) study the material tracking problem and compare different tracking techniques to solve a Eulerian multiphase problem. They test three methods: the Lagrangian markers method (named as "tracers" in their work), a marker chain method where the interface between two materials is discretized using a series of markers and, finally, a field method where the material properties are described by a continuous field similar to temperature. They conclude that the Lagrangian marker approach is the most accurate method, alerting about the large number of markers needed. This huge number poses severe restrictions to the application of the technique to three-dimensional problems. According to VAN KEKEN *et al.* (1997) two-dimensional isoviscous materials require, at least 10 to 100 markers per element. For more realistic rheologies this ratio even increases.

Present applications of the marker technique use many more than 10 markers per element. The simulations of lithospheric structures related to subduction zones done by GERYA and GORCZYK (GORCZYK *et al.*, 2006) use, in average, 1.25×10^5 markers per element. That is, an amazing grand total of 10 billion markers. With these extremely high resolutions they can track meter–size structures. Leaving aside the super–populated simulations, in most 2D models the estimation of 100 markers per element is fair.

When models move from 2D to 3D, the relationships between markers and elements become a serious restriction. To maintain the resolution used by GERYA and GORCZYK (GORCZYK *et al.*, 2006) in a three-dimensional model, 1×10^{15} markers are needed. This possesses severe computational restrictions: If each marker employs only twelve bytes of memory—a minimum lower bound to store only its position—the amount of required memory is 366 times greater than the memory of the present world biggest computer, which has 32768 gigabytes of memory.

In this work a different approach to track the material phases is proposed. The idea is to reduce computational effort obtaining similar results to those obtained using markers. This reduction is achieved mainly by the description of the location of materials with a number of nodes similar to those used in the mechanical problem. In other words, the same interpolation (the same mesh) is used for the materials location and for the velocity field. Therefore, when moving from 2D to 3D, the tracking of materials does not add extra points to those describing the 3D velocity field. The similar number of nodes used to interpolate velocity and material locations results in a similar accuracy for both fields.

Moreover, the level set technique does not require averaging the material properties from markers to nodes, nor the temperature and pressure from nodes to markers. The level set approach may describe changes in the shape (topology) of the phases, thus allowing for the representation of detaching drops, merging bubbles, etc. This feature of the level set method is of great interest when used, for instance, to model slab break–off phenomena. The topological change in the interface due to the separation of the slab can be naturally handled by the level set function.

In addition to the level set method, the solution is improved in the vicinity of the interface using an *enrichment* technique. A standard linear finite-element (or finite-difference) solution allows for changes in its derivative only over the edges of the elements; whereas within the elements the solution is linear. The enriched solution allows for describing discontinuities in the gradient of the solution across the interface described by the level set, whether or not this interface conforms with the element edges.

The enrichment technique is particularly suitable for multiphase problems in which the strain rate is discontinuous across the interface due to the continuity of stress and the jump in the viscosity across the interface. None of the methods tested in (VAN KEKEN *et al.*, 1997) is well suited to resolve this discontinuity. Instead, it is approximated by a continuous function and effectively smeared out over a few grid elements (VAN KEKEN *et al.*, 1997). The enrichment technique adds dynamically some degrees of freedom to the mechanical solution to catch the discontinuity exactly where it is expected to happen, i.e., over the interface described by the level set.

These two techniques, *level sets* and *enrichment* are designed to work together and to fit naturally in a finite-element framework. This combination is usually called eXtended Finite-Element Method (X–FEM) and is commonly used in engineering problems to track materials (e.g., CHESSA and BELYTSCHKO, 2003; MOËS *et al.*, 2003), to model crack growth (e.g., BELYTSCHKO and BLACK, 1999; STOLARSKA *et al.*, 2001), to model holes and inclusions (SUKUMAR *et al.*, 2001), etc.

The aim of this paper is to introduce the X–FEM methodology to study geodynamic processes and to show its numerical capabilities. To this goal we use two complex geophysical examples: i) a 2D simulation of the break–off and sinking of a subducting lithospheric slab considering thermo–mechanical coupling and nonlinear rheology; and ii) a 3D simulation of a Rayleigh–Taylor instability using a simple phase-wise constant viscosity in a cubic space domain. We compare the obtained results with those from previous studies using the marker technique and we show some desirable properties of X–FEM: Its reduced computational cost, its straightforwardness in moving from 2D to 3D and the ability of the level sets to reproduce changes in topology, as it is the case of drops.

2. Extended Finite Elements

2.1. Level Sets and Phase Tracking

The location of the interface between two materials is described by a level set function ϕ on the computational domain. The interface is defined by the curve (the surface in 3D) where the level set vanishes. Thus, the sign of ϕ describes the material domains using the following convention

$$\phi(\mathbf{x},t) = \begin{cases} >0 & \text{for } \mathbf{x} \text{ in material domain 1} \\ =0 & \text{for } \mathbf{x} \text{ on the interface} \\ <0 & \text{for } \mathbf{x} \text{ in material domain 2} \end{cases} \tag{1}$$

where $\mathbf{x}$ stands for a point in the simulation domain and t is the time. Initially, ϕ is taken as a signed distance to the interface. Far enough from this interface, ϕ is truncated by maximum and minimum cutoff values.

Since this approach does not require that the interface conforms to the edges of the elements, the same mesh can be used throughout the entire simulation and remeshing procedures are not required. In practice, the function ϕ is discretized with the finite-element mesh (same as velocities or temperatures) and therefore the location of the interface is described with the same accuracy of the mechanical and thermal problem. While the model evolves and the materials move, the level set is updated with the velocity field $\mathbf{u}$ obtained from the mechanical problem by solving a pure–advective equation

$$\dot{\phi} + \mathbf{u} \cdot \nabla\phi + \phi \cdot \nabla\mathbf{u} = 0. \tag{2}$$

The last term of the right-hand side of equation (2), $\phi{\cdot}\nabla\mathbf{u}$, is neglected due to the incompressibility hypothesis (see section 3.1, equation (7)).

The numerical integration of this equation can be performed using several algorithms, for example, Runge–Kutta methods or Taylor–Galerkin methods. Details on the implementation of the space and time discretization of the level set can be found in (Zlotnik *et al.*, 2007).

The level set function, ϕ, is usually chosen to be a distance function, although it is well known that the solution to the evolution equation (2) (with a distance function as initial condition) does not necessarily remain a distance function and, sometimes, a procedure is required to reinitialize it without changing its zero level set. Different techniques have been proposed in many papers to preserve the level set to the signed distance function (e.g., CHOPP, 1993; SUSSMAN *et al*., 1994; GÓMEZ *et al*., 2005). However, as demonstrated in the examples given in sections 4 and 5 and in the tests performed in ZLOTNIK *et al*. (2007), for the current application this method is sufficiently accurate and it does not require any post-process to reconstruct the distance shape.

2.2. The Mechanical Problem and the Enriched Solution

The enrichment technique is introduced in this section and applied to the mechanical flow problem governed by the Stokes equation (see formulation in the next section). This equation is discretized in space using a mixed formulation, where the velocity and pressure fields are interpolated differently. Here the well-known mini-element is used (DONEA and HUERTA, 2002). This triangular element is composed of three pressure nodes at the vertices (linearly interpolated) and four velocity nodes (three linear nodes at the vertices and one central quadratic node). Denoting by $\mathcal{N}$ the set of indices associated with the velocity nodes, the approximation of the velocity $\mathbf{u}_h$ reads

$$\mathbf{u}(\mathbf{x},t) \simeq \mathbf{u}_h(\mathbf{x},t) = \sum_{j\in\mathcal{N}} N_j(\mathbf{x})\mathbf{u}_j(t) \tag{3}$$

where $\mathbf{u}_j$ is the velocity vector in the node j. This is the usual finite-element interpolation in terms of the shape functions N. In order to improve the ability of the interpolation to represent gradient discontinuities across the interface, the enrichment technique adds some extra degrees of freedom to the interpolation of the velocity (CHESSA and BELYTSCHKO, 2003; MOËS *et al*., 2003)

$$\mathbf{u}_h(\mathbf{x},t) = \sum_{j\in\mathcal{N}} \mathbf{u}_j(t)N_j(\mathbf{x}) + \sum_{j\in\mathcal{N}_{enr}} \mathbf{a}_j(t)M_j(\mathbf{x}) \tag{4}$$

where $\mathcal{N}_{enr}$ denotes the set of enriched nodes. The interpolation functions M_j associated with the enriched degrees of freedom $\mathbf{a}_j$ are built using the standard finite elements shape function N_j and a ridge function R defined as

$$R(\mathbf{x}) = \sum_{j\in\mathcal{N}_{enr}} |\phi_j| N_j(\mathbf{x}) - \left| \sum_{j\in\mathcal{N}_{enr}} \phi_j N_j(\mathbf{x}) \right|. \tag{5}$$

The ridge is defined such that it is only different from zero in the elements containing part of the interface. This technique improves the solution near the interface described by the level set. Figure 1 shows how the enrichment technique modifies the solution inside the elements crossed by the interface between materials. In these elements the enrichment

allows the solution to catch the kink produced by the jump of the material properties. Pressure is enriched in the same way as for velocity. Note that in the definition of the ridge the shape functions are not required to be linear. For a detailed description of the implementation of the enrichment technique we refer the reader to ZLOTNIK *et al.* (2007).

3. Physical Model

In order to show the abilities of the X–FEM, we apply it to a multiphase creep-flow problem. Moreover, a realistic geodynamical model including nonlinear rheology allows us to compare results with previous works.

The fundamental physical equations governing the dynamics of the model, namely, conservation equations of mass, momentum, and energy are presented. These equations are standard in geodynamic models (e.g., SCHOTT and SCHMELING, 1998; GERYA and YUEN, 2003; MANEA *et al.*, 2006; VAN HUNEN *et al.*, 2004) and can be employed to model any multiphase viscous fluid coupled with heat transport. Applications include salt tectonics and diapir formation models (e.g., POLIAKOV *et al.*, 1993; ZALESKI, 1992) or entrainment of a dense D" layer by mantle convection. The equations are presented in their compact or matrix form, in which the bold symbols denote vector variables.

3.1. Basic equations

The mechanical problem requiring conservation of momentum is governed by the Stokes equation in which, as usual for creeping flows, the inertia term is neglected. The equation, considered in its quasi–static version, can be written in terms of velocity $\mathbf{u}$ and pressure p as

$$\nabla \cdot (\eta \nabla^{\mathrm{s}} \mathbf{u}) + \nabla p = \rho \mathbf{g}, \tag{6}$$

where η is the viscosity, ρ the density, and $\mathbf{g}$ the gravitational acceleration vector. The operator ∇^{s} is defined as $1/2(\nabla^{\mathrm{T}} + \nabla)$. Solving the Stokes problem (6) provides velocities and pressures at every time. As the constitutive equation described in section 3.2 depends on the velocity gradient, a nonlinear behavior is introduced. The transient equation (6) is said to be pseudo–static as a consequence of neglecting inertia terms (infinite Prandtl number approximation), because it does not contain any explicit time dependence. The transient character of the solution is due to the motion of the phases and to the temperature field evolution.

As in the majority of existing codes (e.g., VAN KEKEN *et al.*, 1997; GERYA and YUEN, 2003; KING *et al.*, 1990), and despite its lack of consistency for the mass conservation equation, we have assumed incompressibility and the Boussinesq approximation, that is, the density is taken as constant in all terms except for the buoyancy force in the right-hand side of equation (6). Then, the mass conservation equation reads

$$\nabla \cdot \mathbf{u} = 0. \tag{7}$$

Although compressibility is not incorporated in the continuity equation, it is considered in terms of thermal expansion and phase changes which modify material densities and also in terms of adiabatic heating, which is incorporated in the energy conservation equation.

Usually, viscosity η and density ρ are temperature-dependent and consequently the mechanical and thermal problems are coupled.

The conservation of energy equation reads

$$\rho C_p\left(\dot{T} + \mathbf{u}\nabla T\right) = \nabla \cdot (k\nabla T) + \rho f, \tag{8}$$

where T is temperature, C_p the isobaric heat capacity, k the thermal conductivity, and f a heat source term. Solving the thermal problem provides nodal temperatures, which are used to calculate the density ρ, the thermal conductivity k and the viscosity η. For mantle simulations the heat source term f is composed of three sources: a constant term, f_r corresponding to the decay of radioactive elements; an adiabatic heating term f_{ah} accounting for the heat exchange due to compression and decompression of materials, being approximated as $f_{ah} \approx T\alpha\rho u_z g_z$ (GERYA *et al.*, 2004) where α denotes the thermal expansion and subscript z refers to the vertical component of the vectors; and finally a shear heating term, f_{sh}, associated with the mechanical heat dissipation. The shear heating is computed from the solution of the mechanical problem (6) as $f_{sh} = \sigma_{ij}\dot{\varepsilon}_{ij}$, where σ is the deviatoric stress tensor and $\dot{\varepsilon}$ the deviatoric strain rate tensor. This dependence of the heat source on the strain rate and stress enhance the coupling between the thermal and mechanical equations.

3.2. Constitutive Equation

Fluids are characterized by a constitutive equation in which stress is a function of strain rate. In Newtonian fluids this function is linear, whereas in non-Newtonian fluids the strain rate is proportional to the n-th power of the stress.

Rheological behavior of the mantle involves both Newtonian (diffusion) and non-Newtonian (dislocation) deformation mechanisms (KARATO and WU, 1993). Each one of these mechanisms can be stated using a power law, in which the viscosity depends on temperature, pressure and strain rate as follows (RANALLI, 1995)

$$\eta_{\text{creep}} = (\dot{\varepsilon}_{\text{II}})^{\frac{1-n}{n}}(A)^{\frac{-1}{n}}\exp\left(\frac{E + p\Delta V}{nRT}\right), \tag{9}$$

where $\dot{\varepsilon}_{\text{II}} = (1/2\dot{\varepsilon}_{ij}\dot{\varepsilon}_{ij})^{1/2}$ is the second invariant of the deviatoric strain rate tensor, n the exponent of the power law, and the material parameters are: the activation energy E, the activation volume ΔV and the material constant A. This expression is truncated if the resulting viscosity is either greater or lower than two imposed cutoff values (10^{18} to 10^{24} Pa s^{-1}). To include both deformation mechanisms, two equations of the form of (9)

are used. The effective viscosity is computed as the harmonic mean of the two viscosities obtained.

4. Slab Break–off

The slab break–off problem is especially well suited to demonstrate the ability of the level set to reproduce changes in the topology of the interface, for example the separation of part of the material. Moreover, the obtained results are compared with previous simulations (e.g., YOSHIOKA and WORTEL, 1995; DAVIES and VON BLANCKENBURG, 1995; GERYA *et al*., 2004), all using Lagrangian markers. This comparison allows us to check the correctness of our code and to show the capability of the X–FEM technique to obtain similar results as with the marker technique. In addition, we explore the role of shear heating, adiabatic heating, mineral phase changes and plate thickness as factors controlling the slab detachment. Rheological factors, like the maximum imposed viscosity, are also studied.

Several subduction zones exhibit a clear gap in the hypocentral distribution between 100 and 300 km depth. These gaps are believed to be an expression of a mechanically

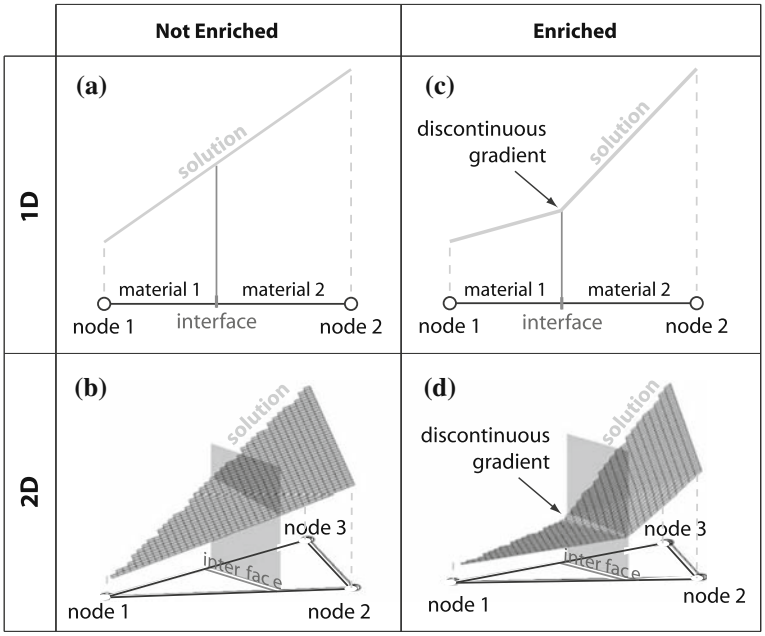

Figure 1
The ability of the enriched solution to have a discontinuous gradient is illustrated. The velocity gradient (and strain rate) will be discontinuous across the interface caused by the continuity of stress and the change of viscosity.

decoupling of the descending slab, or slab break–off, relative to the subducting lithospheric plate. This interpretation is supported by seismic tomography (XU *et al.*, 2000), theoretical considerations (VON BLANCKENBURG and DAVIES, 1995) and numerical modelling (GERYA *et al.*, 2004). Regions where the slab break–off has been proposed to operate are the New Hebrides (ISACKS and MOLNAR, 1969), the Carpathians (WORTEL and SPAKMAN, 2000), the Hellenic arc (SPAKMAN, 1988), the Alps (VON BLANCKENBURG and DAVIES, 1995) and Iran (MOLINARO *et al.*, 2005).

The main gravitational forces acting on the subducting lithosphere are the negative buoyancy of the slab (slab pull), the ridge push, and the negative and positive buoyancy of the mineral phase changes from olivine to wadleyite at 410-km depth and from spinel to perovskite and magnesiowüstite at 660-km depth. In order to include these forces in our model, the density is calculated as a function of the temperature and pressure as follows (SCHUBERT *et al.*, 2001)

$$\rho = \rho_0[1 - \alpha(T - T_0)][1 + \beta(p - p_0)], \tag{10}$$

where α and β are, respectively, the thermal expansion and compressibility coefficients, and T_0 and p_0 are reference values at surface.

The two mineral phase transitions incorporate sharp increments in the density field. The temperature and pressure region of stable mineralogy is delimited by the Claperyron curves of the mineral transition reactions (see Fig. 2). Therefore, the density ρ_0 in equation (10) is calculated as a reference olivine mantle density plus a $\Delta\rho$, depending on the temperature–pressure region, as $\rho_0 = \rho_{ol} + \Delta\rho$ where

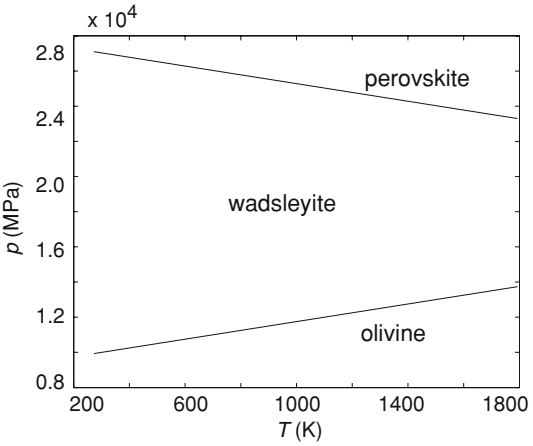

Figure 2
Phase diagram indicating stable mineral phases in the temperature–pressure plane. The phase diagram is divided into three regions corresponding to three distinct minerals: olivine, wadsleyite and perovskite.

$$\Delta\rho = \begin{cases} 0 & \text{if } T-\text{p is in the olivine region} \\ \Delta\rho_{sp} & \text{if } T-\text{p is in the wadsleyite region} \\ \Delta\rho_{per} & \text{if } T-\text{p is in the perovskite region.} \end{cases}$$

The parameters used to delimit regions are listed in Table 1.

It is worth noting that the ridge push-force is not included in the model because the detachment process is expected to happen after cessation of active subduction. In other words, in our simulation the convergence velocity is zero.

The thermal conductivity of rocks also depends on temperature and pressure. At high temperatures (T $\geq$ 1500 K) the electromagnetic radiation becomes important enough to be included as an extra heat transfer mechanism (HOFMEISTER, 1999). The following empirical expression, which includes both conductive and radiative effects, is used (CLAUSER and HUENGES, 1995)

Table 1

Notations

Symbol	Meaning	Value used	Dimension
$\mathbf{g}$	gravity acceleration vector	(0, −9.8)	m s^{-1}
R	gas constant	8.314510	J $K^{-1}mol^{-1}$
T_0	reference temperature	273	K
p_0	reference pressure	0.1	MPa
ρ_{ol}	reference density	3300	kg m^{-3}
α	thermal expansion coefficient	3×10^{-5}	K^{-1}
β	compressibility coefficient	5×10^{-5}	MPa^{-1}
C_p	thermal capacity	1200	J $kg^{-1}K^{-1}$
f_r	radiogenic heat production	0	W m^{-1}
S_{es}	Clapeyron slope for the 410 phase change	2.5	MPa K^{-1}
S_{per}	Clapeyron slope for the 660 phase change	−2.5	MPa K^{-1}
T_{es}	reference temperature of the 410 phase change	1700	K
T_{per}	reference temperature of the 660 phase change	1873	K
p_{es}	reference pressure of the 410 phase change	13500	MPa
p_{per}	reference pressure of the 660 phase change	23100	MPa
$\Delta\rho_{es}$	density increment at the 410 phase change	250	kg m^{-3}
$\Delta\rho_{per}$	density increment at the 660 phase change	250	kg m^{-3}
	Dislocation creep		
E	activation energy	540	kJ mol^{-1}
V^*	activation volume	14	J $MPa^{-1}mol^{-1}$
n	power-law exponent	3.5	-
A	pre–exponential factor	7.6×10^{-16}	$Pa^{-n}s^{-1}$
	Diffusion creep		
E	activation energy	300	kJ mol^{-1}
V^*	activation volume	4.5	J $MPa^{-1}mol^{-1}$
n	power-law exponent	1	-
A	pre–exponential factor	6.07×10^{-11}	$Pa^{-n}s^{-1}$

$$k = \mathrm{a} + \left(\frac{\mathrm{b}}{T + \mathrm{c}}\right)\exp(\mathrm{d}p), \tag{11}$$

where a $= 0.73$, b $= 1293$, c $= 77$, and d $= 0.00004$. Note that this expression is dimensional ($\mathrm{Wm}^{-1}\mathrm{K}^{-1}$) and therefore temperature and pressure must be expressed in K and MPa, respectively.

The initial configuration of our simulations corresponds to a subduction zone with the slab reaching a depth of 400 km, see Figure 3(b). The initial thermal structure has been generated by a previous simulation where a horizontal velocity of 2.5 cm yr^{-1} is imposed on the subducting plate while the overriding plate is fixed.

This model involves two material phases described by a level set: The lithosphere and the underlying mantle. In our approach we have used the thermal definition of lithosphere, and therefore the interface between the lithosphere and the sublithospheric mantle coincides with the initial 1300°C isotherm. Actually, the level set and the 1300°C isotherm roughly coincide during the whole evolution of the model due to the low thermal conductivity values of rocks which makes advection to be dominant over diffusion. In addition, the density ρ_0 assigned to the lithospheric material is an average bulk density for the lithosphere and incorporates the lower density of crustal materials.

Another configuration that might be used—and would give more accurate results—to model slab break-off, is to assign different materials for the crust and the mantle. We discarded this option because of the reduced thickness of the oceanic crust (usually <10 km) which requires to greatly increase the number of elements and consequently the

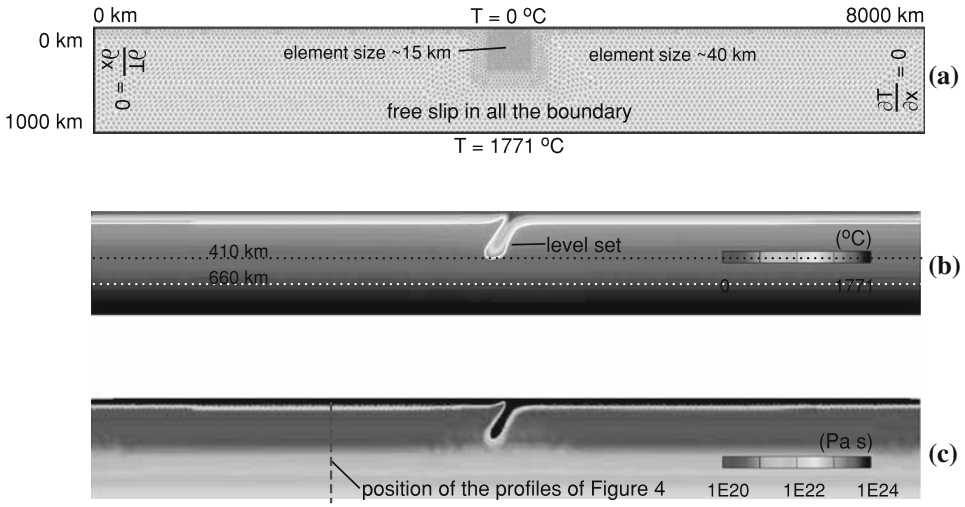

Figure 3
(a) Mesh and boundary conditions used to simulate slab detachment, (b) initial temperature distribution, the white line represents the level set location, dotted lines represent phase transitions. (c) viscosity field calculated with initial temperature, pressure and strain rate.

computation time. Since the main goal of this example is to show the X–FEM capabilities applied to geodynamical simulations, we consider that the chosen material configuration is a good trade-off between computation time and accuracy of the model.

The initial temperature structure of the subducting plate is horizontally homogeneous. Its thickness is 100 km and is defined by the 1300°C isotherm, which corresponds to a plate older than 80 Ma. During the evolution of the model the temperatures at the surface and at the bottom of the model (1000-km depth) are imposed to be zero and 1771°C, respectively. Across the side walls of the model domain a null heat flux is imposed.

Assuming that the detachment process will start after the cessation of plate convergence, the surface of the model is considered as a free surface and no velocity is imposed on it. Free slip conditions are used in the bottom and side walls of the domain.

4.1. Results

A reference model has been generated using the parameters listed in Table 1. The calculated initial viscosity is shown in Figure 3(c) and profiles of mechanical and thermal properties are shown in Figure 4. The evolution of the detachment process corresponding to the reference model can be followed in Figure 5. After a period of approximately 24 Myr of thermal diffusion, the slab undergoes a necking process lasting ~ 2 Myr and localized at a depth of 150–200 km. Necking concentrates extensive deformation in a narrow zone of the slab producing large stresses and shear heating (Fig. 5, 25 Myr row). The slab detachment is characterized by a high strain rate and a spread shear heating all around the slab (Fig. 5, 26 Myr row). The shear heating controls the dynamics of the system not only during the necking, but also during the sinking of the detached slab. Values of shear heating up to 3×10^{-5} W m^{-3} are obtained. This amount of heating is about three orders of magnitude larger than the radioactive heating of the mantle. Similar values were reported by GERYA *et al.* (2004). When shear heating is not considered the detachment occurs about 20 Myr later and the sinking velocity of the slab is about one third of the velocity obtained with the reference model.

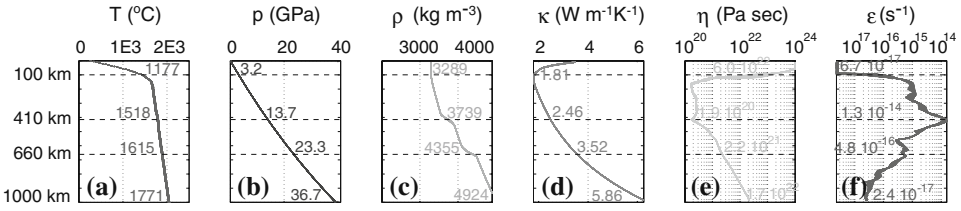

Figure 4
Profiles of mantle properties at the beginning of the simulation. Values at 100, 410, 660 and 1000 km depth are shown. (a) Temperature, (b) pressure, (c) density, (d) thermal conductivity, (e) viscosity, (f) strain rate. The position of the profiles is shown in Figure 3(c).

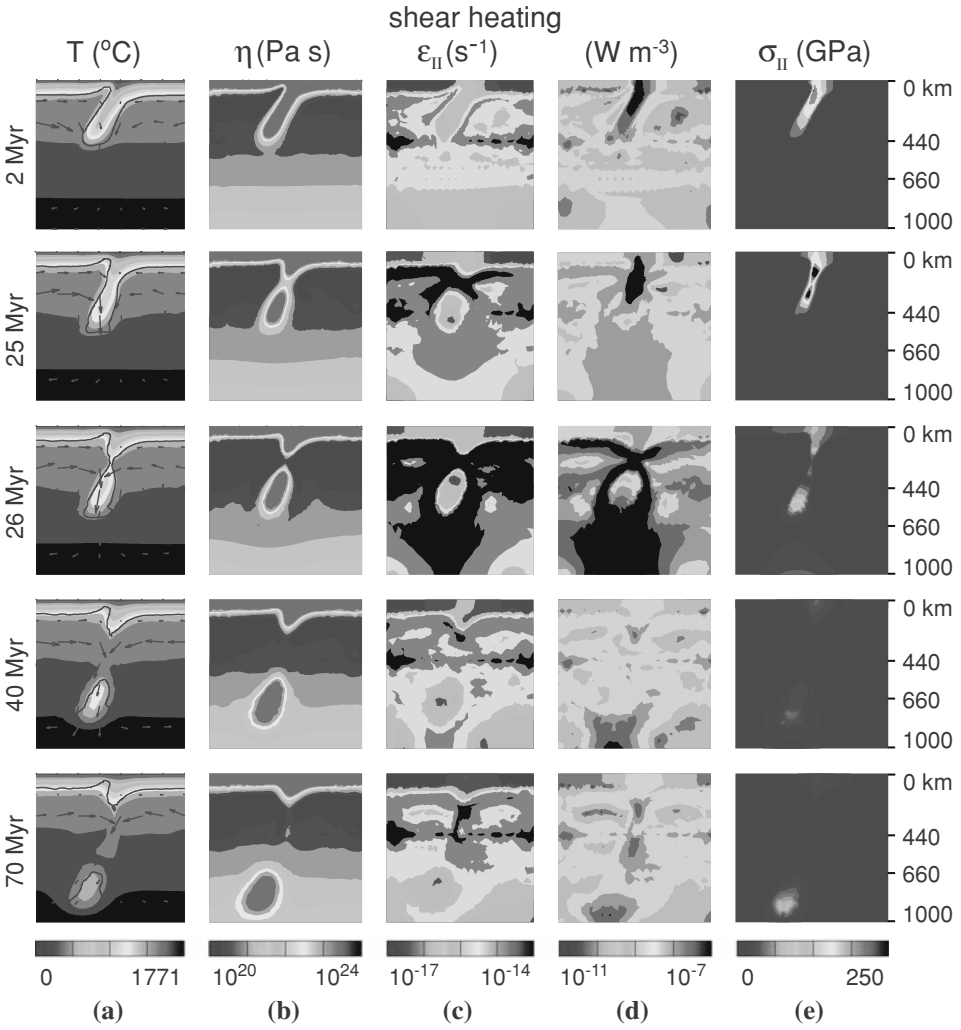

Figure 5
Evolution of the detachment calculated with the reference model. (a) Temperature, velocity and level set position, (b) viscosity, (c) strain rate second invariant, (d) shear heating, (e) stress second invariant.

The adiabatic heating term is important to reproduce the behavior of the mantle at great depths. Numerically it acts reducing the coupling between the mechanical and the thermal equations. As shown in Figure 6, the obtained mantle structure for a model with the same initial temperature distribution but lacking the adiabatic heating term in the energy conservation equation greatly differs from the reference solution, even before the detachment occurs. Therefore, excluding the adiabatic heating produces that hot material from the deeper part of the model is upwelled, forming large convective cells that involve

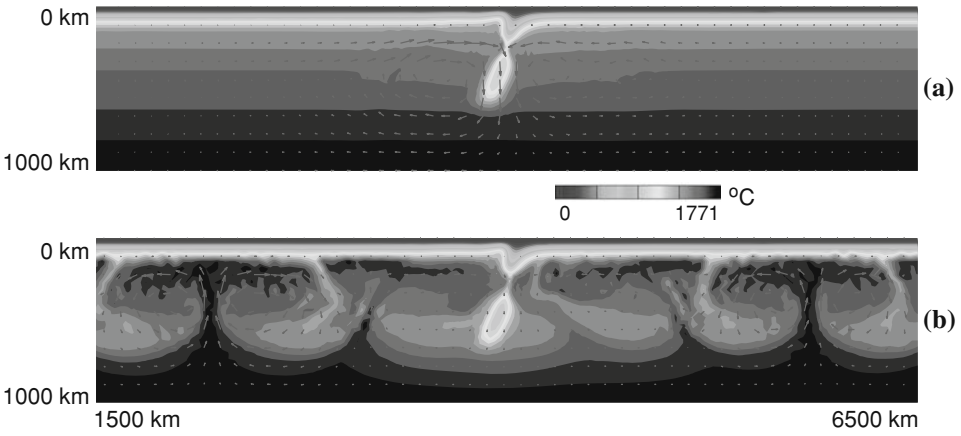

Figure 6
Comparison of the thermal state of the model with (a) and without (b) accounting for the adiabatic heating term in the energy balance equation.

the whole mantle. The mantle surrounding the slab at 200–300-km depth is hotter than in the reference model, enhancing the thermal diffusion and accelerating the detachment process, which happens about 1 Myr before. It must be noted however that the initial temperature distribution within the sublihospheric mantle incorporates an adiabatic gradient which is somehow inconsistent with neglecting the adiabatic heating term in the energy equation. Therefore Figure 6(a) reflects an extremely unstable mantle as a consequence of an initial geotherm which is too hot for a fully incompressible mantle.

The role of mineral phase changes at 410-and 660-km depth is crucial in determining the depth distribution of the mantle density. It is well known that the endothermic character of the olivine-wadleyite reaction developing at 410-km depth increases the slab pull force, and therefore helps the detachment to occur. According to this, the slab detachment may be delayed by about 20 Myr with respect to the reference model when the olivine–wadsleyite phase transition is not considered. Moreover, the maximum reached stress is about one half of that obtained with the reference model. The role of the spinel–to–perovskite/magnesiowüstite exothermic transition occurring at 660-km depth is less noticeable. Due to its exothermic character this transition prevents the penetration of the cold slab through the discontinuity. In the absence of this phase change, the detachment occurs at the same time and the maximum stresses and strain rates are similar to those obtained with the reference model and happen at similar times and depths. The main obvious difference is that the sinking velocity of the detached slab is not reduced when it reaches 660-km depth since, in this case, any discontinuity is imposed at this depth.

The effects of varying the mantle rheology also have been examined. Increasing the upper bound of the allowed viscosity to values of 10^{26} delays the break–off by about 15 Myr although it is not enough to inhibit the detachment of the slab. The time at which the maximum strain rate is reached suffers also a similar delay but the maximum stress

occurs 2 Myr later when compared with the reference model. In fact, the time at which the strain rate reaches its maximum value is a good proxy of the detachment time, while the time interval during which the stress is maximum is a proxy of the necking process.

Finally, reducing the lithospheric thickness to 70 km (the reference lithosphere is 100-km thick) causes the slab to detach 2 Myr earlier. The break–off occurs at a depth about 60 km shallower and the magnitudes of the generated stresses are almost a half with respect to the reference model. Relevant results like the maximum values of strain rate second invariant, shear heating, stress second invariant and velocity are listed in Table 2 together with the corresponding time and average depth at which they have been calculated.

5. *Rayleigh–Taylor Instabilities*

Compositional differences within the crust and mantle can produce local density perturbations in which relatively light material is embedded in a denser ground. In these situations, the lighter body exerts a positive buoyancy that can result in the development of diapirism. Examples of that are salt domes, granitic batholiths, or the entrainment of a chemically distinct D" layer in the lower mantle. Although most of these processes are also temperature-dependent, in this section we will only consider, for the sake of simplicity, the compositional aspect (multiphase mechanical behavior) in order to show the capabilities of the level set in 3D simulations.

Then, our simulation is based on an isothermal Rayleigh–Taylor instability that develops in a cubic domain, which has been discretized with a mesh of 23461 tetrahedra (element size is approximately 1/15 of the cubic domain side). The equations of

Table 2

Maximum values for second invariant of the strain rate, shear heating, second invariant of the stress and velocity for each model. Second and third columns of each box are the time and depth where the max values are obtained. Model labels: ref for the reference model, noSH for the model without shear heating, noAH for the model without adiabatic heating, no410 for the model without the 410-km depth mineral phase transition, no660 for the model without 660-km depth mineral phase transition, max η for the model with increased maximum allowed viscosity and lith70 for the model with 70-km thick lithosphere

Model	$\dot{\varepsilon}_{II}$			Shear heating			σ_{II}			Velocity		
	max s^{-1}	time Myr	depth km	max Wm^{-3}	time Myr	depth km	max MPa	time Myr	depth km	max cm yr^{-1}	time Myr	depth km
ref	7.6×10^{-14}	26	243	1.1×10^{-5}	26	252	423	23	158	10.1	26	400
noSH	2.4×10^{-14}	40	278	0	-	-	450	35	158	3.5	40	423
noAH	5.2×10^{-14}	25	468	1.1×10^{-5}	22	208	565	19	166	29.3	23	397
no410	3.2×10^{-14}	48	253	5.0×10^{-6}	47	224	230	38	147	4.7	48	239
no660	6.8×10^{-14}	26	219	2.4×10^{-5}	26	235	428	23	166	9.2	26	223
max η	8.2×10^{-14}	41	220	1.6×10^{-5}	41	241	456	25	130	10.86	41	400
lith70	1.3×10^{-13}	23	184	3.1×10^{-5}	23	184	273	21	107	16.8	23	383

conservation of momentum (6) and mass (7) are solved imposing: i) free slip conditions along the walls of the cube; ii) an initial sinusoidal perturbation on the phase boundary—level set—of amplitude $A = 0.05$ (dimensionless) and wavelength = 1; iii) a density ratio between the upper and lower material of $\rho_1/\rho_2 = 1.003$.

Figure 7 shows the evolution of a Rayleigh-Taylor instability with a viscosity ratio $\eta_1/\eta_2 = 1$ and a dimensionless lower layer thickness of 1/3. The plotted surface corresponds to the interface between the two materials described by the level set. The evolution of the diapir follows the three stages described by Whitehead and Luther (Whitehead Jr. and Luther, 1975) for a thin layer of a low Reynolds number fluid: the first stage of evolution, Figure 7(a), is described by a linear Rayleigh–Taylor instability. In the second stage, Figure 7(b), the fluid moves upward as a circular column surrounded by relatively broad regions of descending material. In the third stage, Figures 7(c) and (d), fully mature structures are formed, in this case the level set looses its radial symmetry and significant folds are developed at the base and the tail of the level set. These asymmetry and folds are related to the cubic shape and proximity of the walls of the model domain. When the level set reaches the upper boundary of the model domain the buoyant lower material is in contact with the top of the domain. This contact is not an interface between different materials and thus is not drawn. In fact, the level set function does not vanish at these points. Therefore, the moving interface between materials adopts a wineglass shape as shown in Figures 7(c) and (d).

Figure 8 shows some snapshots of models with different viscosity ratios and different initial thicknesses of the buoyant underlying material that is used as a simulation benchmark. Snapshots correspond to similar times after the modelling initiation for the four cases. In general terms, the viscosity ratio controls the size of the diapir head and the velocity at which the initial stratification overturns (Figs 8(a) and (b)). On the other hand, the initial thickness of the underlying layer mainly controls the velocity at which the head of the diapir rises and hence, the length of the tail.

All these examples show the capability of level sets to reproduce the geometry of the interface evolution between two (or more) deforming materials in three dimensions.

6. Discussion and Conclusions

The analysis presented in this study allows us to draw the following conclusions:

— Level sets, as used here, allow a description of the interface between two deforming materials with the same resolution as for the mechanical problem. Therefore, the minimum size of a body delimited by the level set is given by the element size. This is a very different characteristic from the marker technique, which can increment the number of markers independently of the element size. However, markers also require a dense grid to increase the resolution of the problem penalizing the computer time. Moreover, the X–FEM approach described here is especially well suited to use

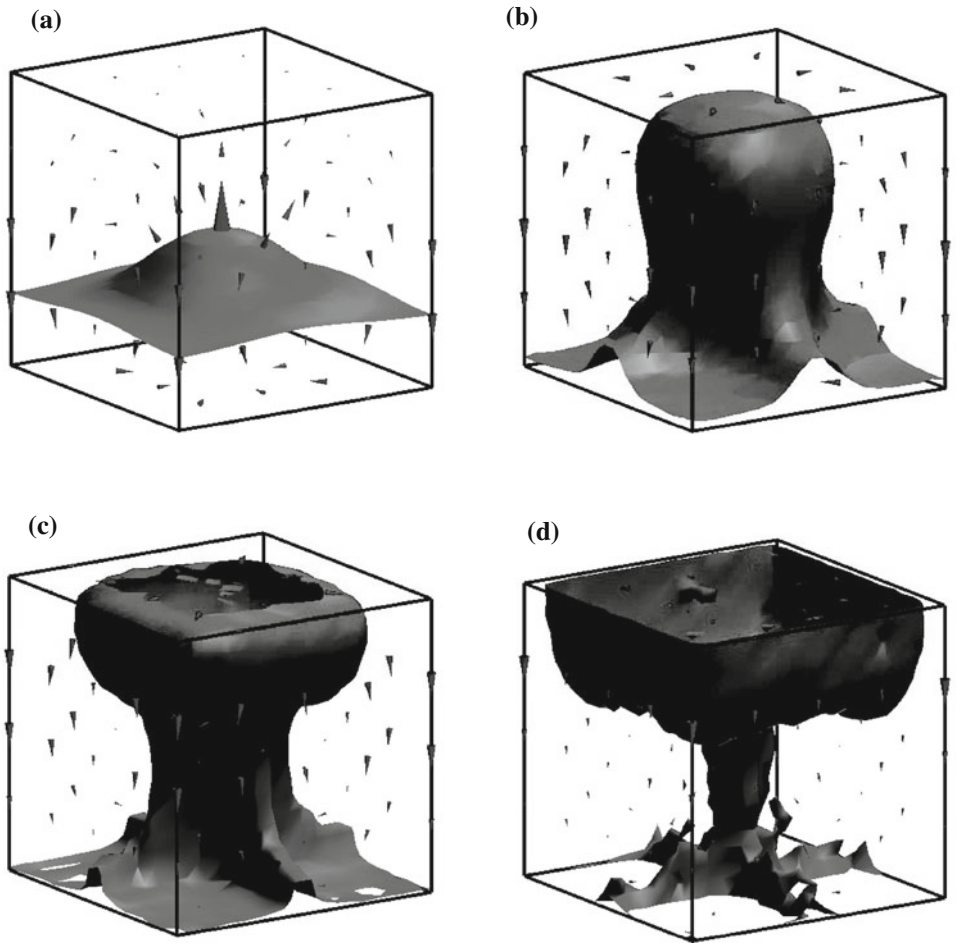

Figure 7
Evolution of a Rayleigh–Taylor instability. The red surface is the interface between two materials described by the level set. The blue triangles indicate the velocity directions and magnitude. The viscosity ratio is $\eta_1/\eta_2 = 1$ and the initial lower layer thickness $h = 1/3$.

adaptive mesh refinement. This allows for increasing locally accuracy of the numerical method and obtaining an accurate answer with the minimum computational cost.

— The transport of the interface described by the level set may introduce some numerical oscillations. Several *ad hoc* techniques have been proposed to avoid this undesirable behaviour. Nevertheless, our experience shows that for simple geometries, like the presented 2D and 3D numerical experiments, fair results are obtained even if the distance shape of the level set is not preserved.

— Using level set and enriched solution techniques (X–FEM) implies a very inexpensive computational cost. Running the thermo–mechanical 2D code for the presented

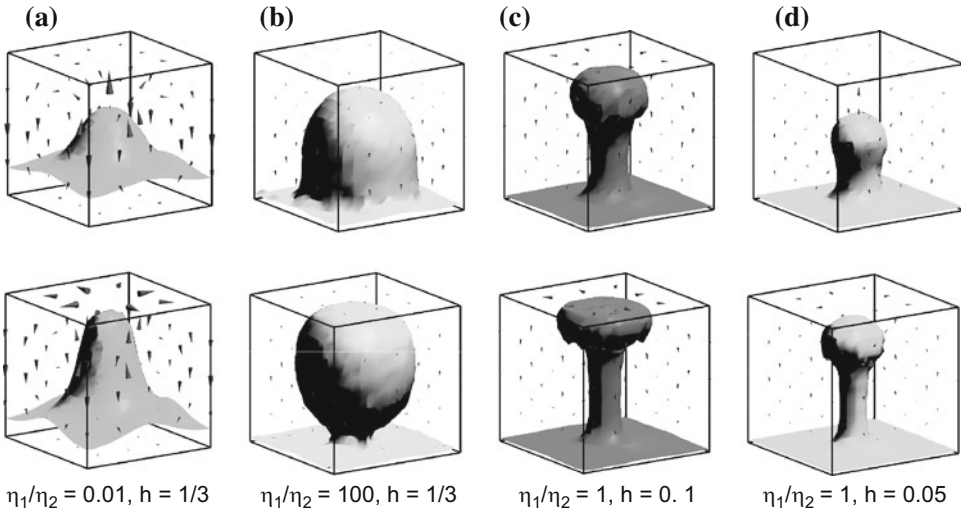

Figure 8
Two snapshots of the evolution of four different Rayleigh–Taylor instabilities. The viscosity ratios and thickness h of the lower layer determines the shape of the plume.

subduction simulations (including non linear rheology, phase changes, adiabatic heating, shear heating, etc.) lasts less than 12 hours in a desktop PC with a single 3 GHz processor and 2 GB of memory.

— A very attractive advantage of level sets is its straightforwardness in moving to 3D simulations: The simplicity of the coding is similar to the 2D case. Moreover, the increase in the computational cost for the 3D case is considerably lower than for the markers approach. The presented 3D simulations of Rayleigh–Taylor instabilities lasted 50 hours each with the same computer as used for 2D modelling.

— The results obtained from the subducting slab detachment experiments are quantitatively similar to those found in previous studies demonstrating the correct behavior of the code. The enrichment technique allows for accurate reproduction of the strain rate discontinuities produced across the interface due to sharp viscosity contrasts between the two modelled fluids.

— The numerical experiments shown in the present study use only one level set to describe a two-phase fluid problem. Nevertheless, we have done some tests for a multiphase fluid problem using a larger number of level sets and obtaining successful results.

Acknowledgments

This research has been supported by Ministerio de Educación y Ciencia, Grants DPI2007-62395, SAGAS CTM2005-08071-C03-03/MAR and the Spanish Team

Consolider-Ingenio 2010 nrCSD2006-00041. We thank Vlad Manea and an anonymous reviewer for discussion and comments.

References

Babeyko, A. Y., Sobolev, S. V., Trumbull, R. B., Oncken, O., and Lavier, L. L., (2002), *Numerical models of crustal scale convection and partial melting beneath the Altiplano–Puna plateau*, Earth Planet. Sci. Lett. *199*, 373–388.

Belytschko, T., and Black, T., (1999), *Elastic crack growth in finite elements with minimal remeshing*, Internat. J. Numer. Methods in Eng. *45*(5), 601–620.

von Blanckenburg, F., and Davies, J. H., (1995), *Slab breakoff: A model for syncollisional magmatism and tectonics in the Alps*, Tectonics *14*, 120–131.

Chessa, J., and Belytschko, T., (2003), *An extended finite element method for two–phase fluids*, Transact. ASME, 10–17.

Chopp, D. L., (1993), *Computing minimal surfaces via level set curvature flow*, J. Comput. Phys. *106*, 77–91.

Clauser, C., and Huenges, E., *Thermal conductivity of rocks and minerals*. In T. Ahren, editor, *Rock Physics and Phase Relations*, AGU Reference Shelf, part 3, pages 105–126. (AGU, Washington DC 1995), third edition.

Davies, J. H., and von Blanckenburg, F., (1995), *Slab breakoff: A model of lithosphere detachment and its test in the magmatism and deformation of collisional orogens*, Earth Planet. Sci. Lett. *129*, 85–102.

Donea, J., and Huerta, A., *Finite Element Methods for Flow Problems*, (Wiley, Chichester, West Sussex PO19 8SQ, England, 2002).

Gerya T. V., and Yuen, D. A., (2003), *Characteristics–based marker–in–cell method with conservative finite–differences schemes for modeling geological flows with strongly variable transport properties*, Phys. Earth Planet. Inter. *140*(4), 293–318.

Gerya, T. V., Yuen, D. A., and Maresch, W. V., (2004), *Thermomechanical modelling of slab detachment*, Earth Planet. Sci. Lett. *226*, 101–116.

Gómez, P., Hernández, J., and López, J., (2005), *On the reinitialization procedure in a narrow-band locally refined level set method for interfacial flows*, Int. J. Numer. Meth. Eng. *63*, 1478–1512.

Gorczyk, W., Gerya, T. V., Connolly, J. A. D., Yuen, D. A., and Rudolph, M., (2006), *Large–scale rigid–body rotation in the mantle wedge and its implications for seismic tomography*, Geochem. Geophys. Geosyst. *7*(5). doi:10.1029/2005GC001075.

Hofmeister, A. M., (1999), *Mantle values of thermal conductivity and the geotherm from phonon lifetimes*, Science *283*, 1969–1706.

Isacks, B., and Molnar, P., (1969), *Mantle earthquake mechanisms and the sinking of the lithosphere*, Nature *223*, 1121–1124.

Karato, S.-I., and Wu, P., (1993), *Rheology of the upper mantle: a synthesis*, Rev. Science *260*, 771–778.

King, S. D., Raefsky, A., and Hager, B. H., (1990), *ConMan: vectorizing a finite element code for incompressible two–dimensional convection in the Earth's mantle*, Phys. Earth Planet. Inter. *59*, 195–207.

Manea, V. C., Manea, M., Kostoglodov, V., and Sewell, G., (2006), *Intraslab seismicity and thermal stress in the subducted Cocos plate beneath central Mexico*, Tectonophysics *420*(3–4), 389–408.

Moës, N., Cloirec, M., Cartaud, P., and Remacle, J. F., (2003), *A computational approach to handle complex microstructure geometries*, Computer Methods in Appl. Mech. and Engin. *192*, 3163–3177.

Molinaro, M., Zeyen, H., and Laurencin, X., (2005), *Lithospheric structure beneath the south–eastern Zagros mountains, Iran: Recent slab break–off*? Terra Nova *17*, 1–6.

Moresi, L. N., and Gurnis, M., (1996), *Constraints on lateral strength of slabs from 3–D dynamic flow models*, Earth Planet. Sci. Lett. *138*, 15–28.

Poliakov, A. N. B., van Balen, R., Podladchikov, Yu., Daudre, B., Cloetingh, S., and Talbot, C., (1993), *Numerical analysis of how sedimentation and redistribution of surficial sediments affects salt diapirism*, Tectonophysics *226*, 199–216.

Ranalli, G., *Rheology of the Earth* (Chapman and Hall, 2–6 Boundary Row, London, second edition, 1995).

SCHOTT, B., and SCHMELING, H., (1998), *Delamination and detachment of a lithospheric root*, Tectonophys. *296*, 225–247.

SCHUBERT, G., TURCOTTE, D. L., and OLSON, P., *Mantle Convection in Earth and Planets* (Cambridge University Press, UK, 2001).

SCOTT, D. K., RAEFSKY, A., and HAGER, B. H., (1990), *ConMan: A vectorizing a finite element code for incompressible two–dimensional convection in the Earth's mantle*, Phys. Earth Planet. Inter. *59*, 195–2007.

SPAKMAN, W., *Upper mantle delay time tomography with an application to the collision zone of Eurasian, African and Arabian plates*. PhD thesis (Univ. of Utrech, Utrech, The Netherlands, 1988).

STOLARSKA, M., CHOPP, D. L., MOËS, N., and BELYTSCHKO, T., (2001), *Modelling crack growth by level set in the extended finite element method*, Internat. J. for Numer. Methods in Engin. *51*, 943–960.

SUKUMAR, N., CHOPP, D. L., MOËS, N., and BELYTSCHKO, T., (2001), *Modeling Holes and Inclusions by Level Sets in the Extended Finite–Element Method*, Computer Methods in Appl. Mech. and Engin. *190*, 6183–6200.

SUSSMAN, M., SMEREKA, P., and OSHER, S., (1994), *A level set approach for computing solutions to incompressible two-phase flow*, J. Comput. Phys. *114*, 146–159.

VAN HUNEN, J., VAN DEN BERG, A. P., and VLARR, N. J., (2004), *Various mechanisms to induce present–day shallow flat subduction and implications for the younger Earth: a numerical parameter study*, Phys. Earth Planet. Inter. *146*, 179–194.

VAN KEKEN, P. E., KING, S. D., SCHMELING, H., CHRISTENSEN, U. R., NUMEISTER, D., and DOIN, M.-P., (1997), *A comparison of methods for the modeling of thermochemical convection*, J. Geophys. Res. *102*(B10), 22477–22495.

WHITEHEAD, J. A., Jr. and LUTHER, D. S., (1975), *Dynamics of laboratory diapir and plume models*, J. Geophys. Res. *80*, 705–717.

WORTEL, M. J. R., and SPAKMAN, W., (2000), *Subduction and slab detachment in the Mediterranean–Carpathian region*, Science *290*, 1910–1917.

XU, P. F., SUN, R. M., LIU, F. T., WANG, Q., and CONG, B., (2000), *Seismic tomography showing, subduction and slab breakoff of the Yangtze block beneath the Dabie—Sulu orogenic belt*, Chin. Sci. Bull *45*, 70–74.

YOSHIOKA, S., and WORTEL, M. J. R., (1995), *Three–dimensional numerical modeling of detachment of subducted lithosphere*, J. Geophys. Res. *100* (B10), 20223–20244.

ZALESKI, S., and JULIEN P. (1992), *Numerical simulation of Rayleigh–Taylor instability for single and multiple salt diapirs*, Tectonophys. *260*, 55–69.

ZLOTNIK, S., DÍEZ, P., FERNÁNDEZ, M., and VERGÉS, J., (2007), *Numerical modelling of tectonic plates subduction using X–FEM*, Computer Methods in Appl. Mech. and Engin. *196*, 4283–4293.

(Received January 6, 2007, revised May 5, 2008, accepted June 5, 2008)
Published Online First: October 18, 2008

Pure appl. geophys. 165 (2008) 1511–1530
0033–4553/08/081511–20
DOI 10.1007/s00024-004-0387-8

Pure and Applied Geophysics

On the Coupling Between Channel Level and Surface Ground-Water Flows

S. N. Antontsev[1] and J. I. Díaz[2]

Abstract—This paper is devoted to a mathematical analysis of some general models of mass transport and other coupled physical processes developed in simultaneous flows of surface, soil and ground waters. Such models are widely used for forecasting (numerical simulation) of a hydrological cycle for concrete territories. The mathematical models that proved a more realistic approach are obtained by combining several mathematical models for local processes. The water-exchange models take into account the following factors: Water flows in confined and unconfined aquifers, vertical moisture migration allowing earth surface evaporation, open-channel flow simulated by one-dimensional hydraulic equations, transport of contamination, etc. These models may have different levels of sophistication. We illustrate the type of mathematical singularities which may appear by considering a simple model on the coupling of a surface flow of surface and ground waters with the flow of a line channel or river.

Key words: Mathematical models, coupled processes, channel and ground waters.

1. Introduction

It is well known that one of the central issues of the Mathematical Environment is the study of general mathematical models for the hydrological cycle (MMHC) obtained through the consideration of mass transport balances with other connected physical processes arising in the coupling of the different types of water flows: surface, soil and ground waters. The water exchange models (MMHC) take into account many different factors as, for instance: Water flows in confined and unconfined aquifers, vertical moisture migration with allowing earth surface evaporation, open-channel flow simulated by one-dimensional hydraulic equations, transport of contamination, etc. These models may have different levels of sophistication leading, in any case, to different systems of nonlinear partial differential equations. Some illustrations of the vertical and horizontal sections of the spatial modelling area are presented in Figures 1 and 2.

[1] CMAF. Universidade de Lisboa, Av. Prof. Gama Pinto 2, 1649-003 Lisboa, Portugal. E-mail: anton@ptmat.fc.ul.pt, antontsevsn@mail.ru

[2] Dpto. de Matemática Aplicada, Universidad Complutense de Madrid. Cuidad Universitaria, 28040 Madrid, Spain. E-mail: diaz.racefyn@insde

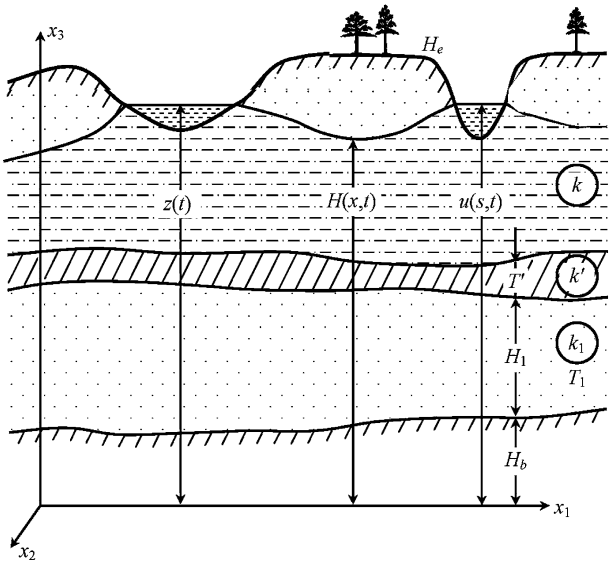

Figure 1
Vertical cross section of the flow domain. $z(t)$ and $u(s, t)$ are the levels of the water in reservoirs and in the channel. $H(x, t)$ and $H_1(x, t)$ are, respectively, the groundwater free surface in the upper layer and the piezometric head in the lower layer. k, k_1 and k' are the hydraulic conductivity (percolation) coefficients for the corresponding layers

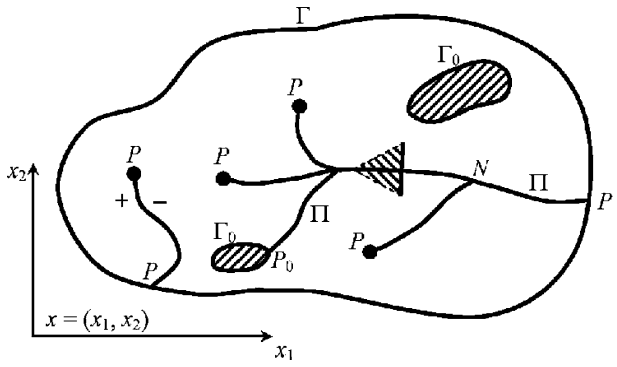

Figure 2
Planar view of the flow domain. Γ is the exterior boundary. Π describes channels or rivers. Γ_0 are boundaries of reservoirs

The mathematical treatment of such type of models (of a great diversity) started in the second half of the past century (see, for instance, Abbott *et al*., 1986; Antontsev *et al*., 1986; 1977a, 1977b, 1977c; Antontsev and Meirmanov, 1978, 1979; Bear and Verruijt, 1987; Crandall, and Tartar, 1980; Cunningham and Sinclair, 1979; Fowler, in press; Kashevarov, 1998; Kuchment *et al*., 1983; Luckher, 1978; Miles, 1985; Philip, 1969;

POLUBARINOVA-KOCHINA, 1977; USENKO and ZLOTNIK, 1978; VASILIEV, 1987 and their references). The study of these mathematical models and their numerical approximation has lead to important theoretical advances in the study of nonlinear partial differential equations (very often of mixed and degenerate type). The mathematical results can be of a very different nature: Questions concerning the mathematical well-posedness of the models (such as the existence and uniqueness of some suitable notion of solution), the study of the qualitative properties of such solutions (as, for instance, the asymptotic behavior with respect to time and spatial variables), the stability and continuous dependence with respect to initial data and physical parameters, etc.

In this paper we shall illustrate the type of mathematical singularities which may appear by considering a simple model on the coupling of a surface flow of the surface and ground waters with the flow of a line channel or river. After comments on the modelling, we present results on the mathematical treatment of this simple model. This type of consideration seems of relevance in the study of propagation of desert.

2. A Collection of Mathematical Models for the Hydrological Cycle

2.1. Basic Equations

To fix ideas, we start by making some comments on the spatial domain in study. We consider a bounded multiply connected region $\Omega \subset \mathbf{R}^2$ of exterior boundary $\Gamma = \partial\Omega = \sum_{i=1}^{n} \Gamma_i$ (see Fig. 2). We assume that at the interior of Ω there is a system of channels or rivers described by a set of curves $\Pi = \sum_{i=1}^{l} \Pi_i$. The interior of Ω may also contain some basins or lakes of boundaries given by some closed curves $\Gamma_0 = \sum_{j=1}^{m} \Gamma_{0j}$. We can assume also that some curves Π_i may have some points of intersection with the rest of Π (which we denote as $N = \sum_{i,j=1} N_{ij}$), with the boundary Γ (which we denote as $P = \sum_{i=1} P_i$), or with the lakes boundaries Γ_0 (which we denote as $P_0 = \sum_{i=1} P_{0i}$).

The different mathematical models on the hydrological cycle are based on the consideration of some of the following local subsystems:

1. Vertical filtration in a porous ground. By applying the Darcy law, it is well known that (see ABBOTT *et al*., 1986; PHILIP, 1969; VASILIEV, 1987) if we denote by ϑ to the volumetric moisture content and by ψ to the pressure of the soil moisture then we arrive at the so-called Richards equation

$$\frac{\partial \vartheta(\psi)}{\partial t} = \frac{\partial}{\partial x_3}\left[K(\psi)\left(\frac{\partial \psi}{\partial x_3} + 1\right)\right] + f(H, \vartheta, x_3, x, t), \tag{1}$$

where K is the hydraulic conductivity, $f(H, \vartheta, x_3, x, t)$ is an evaporation or transpiration term and x_3 is the vertical coordinate direct upward. The nonlinear parabolic equation takes place on the set

$$H(x,t) < x_3 < H_e(x), \quad x = (x_1, x_2) \in \Omega \in \mathbf{R}^2,$$

where $H(x, t)$ is the level of the ground water (elevation of the ground free surface) and $H_e(x_1, x_2)$ is the given surface of the earth. A typical constitutive law used to transform the equation in a self-contained equation for ψ is the one given in the following terms

$$\vartheta = \vartheta_s / \left[1 + \left(-\frac{\psi}{a}\right)^m\right], \psi < 0, K = K_s[(\vartheta - \vartheta_r)/(\vartheta_s - \vartheta_r)]^n,$$

2. Horizontal plane filtration equations for the levels of ground waters. By using the so-called Boussinesq and Shchelkachev equations, it is well known (KUCHMENT *et al.*, 1983; MILES, 1985; PHILIP, 1969; POLUBARINOVA-KOCHINA, 1977; VASILIEV, 1987) that if we denote by $H(x, t)$ and $H_1(x, t)$, respectively, to the elevation of the ground-water free surface in the upper layer and the piezometric head in the lower layer, then we arrive at the coupled system of

$$\mu \frac{\partial H}{\partial t} = \operatorname{div}(M \nabla H) - \frac{k'}{T'}(H - H_1) + f_\Omega, \quad x = (x_1, x_2) \in \Omega, \quad t \in (0, T), \tag{2}$$

$$\mu_1 \frac{\partial H_1}{\partial t} = \operatorname{div}(k_1 T_1 \nabla H_1) + \frac{k'}{T'}(H - H_1), \quad x \in \Omega, \quad t \in (0, T), \tag{3}$$

where

$$M = k(x)(H - H_1), \quad f_\Omega = f_\Omega(H, \vartheta, x, t),$$

μ is the yield coefficient (the deficiency of saturation), μ_1 the storage coefficient, k, k_1 and k' are the hydraulic conductivity (percolation) coefficients for the corresponding layers (see Fig. 1), f_Ω is a source function (see ANTONTSEV *et al.*; 1986; VASILIEV, 1987). Here the div operator must be understood only in the spatial variable. The last term in (3) characterizes the rate of vertical flow from the upper layer to the one through the semipermeable intermediate layer.

3. Water level flow in open channels. By applying a diffusion wave approximation to the Saint-Venant equations, it is well known (ANTONTSEV *et al.*, 1986; ANTONTSEV, and MEIRMANOV, 1977b; DALUZ VIEIRA, 1983; EPIKHOV, 1985; KUCHMENT *et al.*, 1983; VASILIEV, 1987 and their references) that if we denote by $u(s, t)$ to the water level in the channel stream, by ω to the cross-sectional area ($\omega_u = \partial\omega/\partial u = B$ is the width) and to s to the channel curvilinear length variably measured along its axial cross section, then we arrive at the nonlinear parabolic equation

$$\frac{\partial \omega}{\partial t} = \frac{\partial}{\partial s}\left(\psi \phi\left(\frac{\partial u}{\partial s}\right)\right) - Q + f_\Pi, \quad s \in \Pi, t \in (0, T), \tag{4}$$

under the constitutive laws

$$\omega = \omega(s,u), \phi\left(\frac{\partial u}{\partial s}\right) = \left|\frac{\partial u}{\partial s}\right|^{\frac{1}{2}} \operatorname{sign}\left(\frac{\partial u}{\partial s}\right),$$

and

$$Q = \alpha u|_{\Pi} - \alpha_0 \left[M\frac{\partial H}{\partial n}\Big|_{\Pi_+} + M\frac{\partial H}{\partial n}\Big|_{\Pi_-} \right],$$

where $\psi(s,u) = C\omega R^{2/3}$ is the discharge modulus, C is the coefficient Chezy, R is the hydraulic radius, f_Π is a source function,

$$[MH_n] = \left(MH_n|_{\Pi_+} + MH_n|_{\Pi_-} \right)$$

is the total filtration inflow of ground water from the right Π_+ and left Π_- banks of the channel, and $H_n = \partial H/\partial n$ is the outer normal derivative to the boundary of Π. We point out that in many other references the Saint Venant equations are applied to other constitutive laws leading to first-order hyperbolic equations (see, e.g., FOWLER, in press).

Water level balance in reservoirs. It is well known (ANTONTSEV *et al.*, 1986) that denoting by $z(t)$ to the level on the boundaries of reservoirs we arrive at the equation

$$\lambda\frac{dz}{dt} = -\oint_{\Gamma_0} M\frac{\partial H}{\partial n} ds - (\psi\phi)_{\Gamma_0}, \; t \in (0,T). \tag{5}$$

To obtain other models describing the quality of ground and surface water flows we need to couple the above equation with other equations expressing the mass transfer between the different chemical components (see, e.g., ANTONTSEV, and KASHEVAROV, 1999b; ANTONTSEV, 1990; KASHEVAROV, 1998):

a. Solute transport equation. For instance, in the case of a confined aquifer we must add the diffusion equation

$$\frac{\partial(mC)}{\partial t} = \operatorname{div}(D\nabla C - vC) - \Phi(C,N) + f, \tag{6}$$

where

$$v = -M\nabla H, \; D = D_0 + \lambda|v| \quad \text{and} \quad m = m_0 + \mu(H - H_p).$$

b. Dynamics of a reactive solid medium. In some cases, there is a chemical reaction modifying the skeleton of the porous medium and then we must add a kinetic equation of the form

$$\frac{\partial N}{\partial t} = -\Phi(C,N). \tag{7}$$

c. Solute transport phenomena in open-channels. In many cases, as for instance in rivers we must add a transport equation of the form

$$\frac{\partial(\varpi S)}{\partial t} = \frac{\partial}{\partial s}\left(D_1 \frac{\partial S}{\partial s} - v_1 S\right) - (q_1 C) + f, \tag{8}$$

under some constitutive law of the type

$$D_1 = D_0^1 + \lambda_1 |v_1|, v_1 = -\Psi(s,u)|u_s|^{1/2} sign(u_s), \left(u_s = \frac{\partial u}{\partial s}\right).$$

2.2. *Elaboration of a Coupled Model: The Case of Simultaneous Surface Ground Water and Open Channel Flows*

Usually the mathematical models for the hydrological cycle take into account several simultaneous processes and the modelling is carried out by coupling some of the above-mentioned equations involved in the phenomena under consideration completed with the corresponding initial and boundary conditions.

To illustrate this we consider now, for instance, the interplay process between surface (lake channel) and ground waters (on which, for the sake of simplicity in the formulation, we neglect the unsaturated zone and assume that there is only one nonpressure layer). A simplified representation can be found in Figs. 3 and 4. Then the mathematical model collects of the equations (2)–(5) which here we reduce to the following ones:

$$\mu \frac{\partial H}{\partial t} = \mathrm{div}(M \nabla H) + f_\Omega, x = (x_1, x_2) \in \Omega, \quad t \in (0,T), \tag{9}$$

$$\frac{\partial \omega}{\partial t} = \frac{\partial}{\partial s}\left(\psi \phi\left(\frac{\partial u}{\partial s}\right)\right) - Q + f, s \in \Pi, \quad t \in (0,T), \tag{10}$$

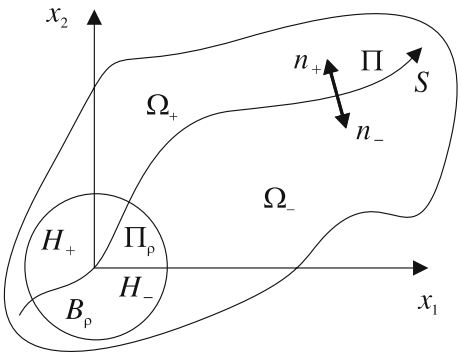

Figure 3
Horizontal cross section of the flow domain in a simplified model. $H_\pm$ are values of the level H on the opposite sides of H. $n_\pm$ are the normals to Π

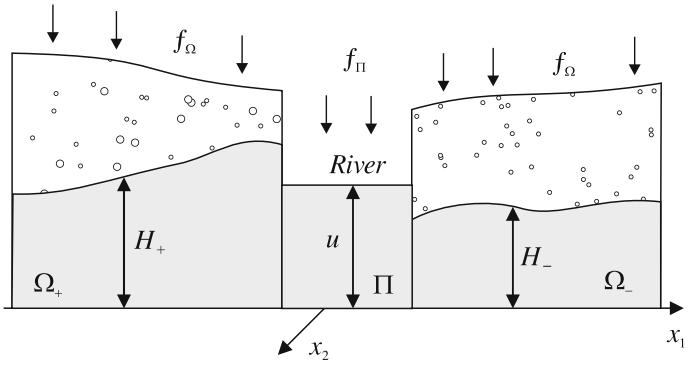

Figure 4
Vertical cross section in a simplified model. $H_\pm$ are levels of the underground waters on the opposite sides of the river. u is the water level in the river

$$\lambda\frac{\partial z}{\partial t} = -\oint_{\Gamma_0} M\frac{\partial H}{\partial n}ds - (\psi\phi)_{\Gamma_0}, \quad x \in \Gamma_0, \quad t \in (0,T), \tag{11}$$

for the unknown $\mathbf{W}(x,t) = (H(x,t), u(s,t), z(t))$.

Considered models are used when there is a strong hydraulic connection between aquifers and river beds. In this case filtration discharges of the water from channels into aquifers are comparable with the charge (volumes) of water in the channels (see Díaz, and Tello, 2005; Fowler, in press; Polubarinova-Kochina, 1977).

Obviously, the above system of parabolic partial differential equations must be completed by adding a set of initial and boundary conditions:

$$\mathbf{W}(x,0) = \mathbf{W}_0(x), \quad x \in \mathbf{\Omega}, \tag{12}$$

$$\sigma_1 M\frac{\partial H}{\partial n} + \sigma_2 H = g, \quad (x,t) \in \Gamma_T = \Gamma\times(0,T), \tag{13}$$

$$\kappa_1\psi(s,u)\phi\left(\frac{\partial u}{\partial s}\right) + \kappa_2 u = g, \quad (x,t) \in P_T = P \times (0,T), \tag{14}$$

$$-M\frac{\partial H}{\partial n}\bigg|_{\Pi^\pm} = \alpha(u - H_\pm) + \alpha_0(H_+ - H_-), \quad (x,t) \in \Pi_T = \Pi \times (0,T), \tag{15}$$

$$u_i = u_j, \sum_{i=1}\psi(s,u_i)\phi\left(\frac{\partial u_i}{\partial s}\right) = 0 (s,t) \in N_T = N \times [0,T], \tag{16}$$

$$H(x,t) = z(x,t), \quad x \in \Gamma_0, \quad t \in (0,T). \tag{17}$$

The complete mathematical model is then described by the equations (9)–(11), (12)–(17) and, as we shall develop in the following section, its mathematical treatment is far to be obvious. We shall require the analysis of a combined-type of nonlinear partial

differential Equations which are defined on different sets of space variables: Equation (9) is defined in the two-dimensional domain Ω, equation (10) on the curve Π and although equation (11) is a time ordinary differential equation, its right-hand side is given by a nonlocal operator depending on H and $\partial H/\partial n$. Moreover, the parabolic equations may degenerate changing type or order at certain values of the solution that is sought (case (9)) or/and its derivatives (case (10)). Finally, notice that all these equations contain numerous physical parameters which may lead to completely different behaviors of their solutions. We point out that the interaction between the different physical processes is given by the coupling source functions included within differential equations, as well as by the common boundary conditions.

Due to the presence of nonlinear terms, the solutions of such equations may exhibit many different behaviors that cannot occur in the (more or less well-known) case of linear models. The list of peculiar effects of this kind includes properties such as the finite time of localization (or extinction in finite time), finite speed of propagation of disturbances from the initial data, waiting time effect, etc.

A previous study of the questions of the mathematical well-posedness of the above system (existence, uniqueness and some qualitative properties of solutions) was carried out in Antontsev *et al*. (2002, 1986, 1999a), Antontsev and Meirmanov (1978, 1979, 1977b, 1977c). In the following section we shall recall a part of those results, adding some new ones and developing other qualitative properties which explain the mathematical peculiarities of such model.

3. *Mathematical Treatment of a Simplified Model Coupling the Channel Level and Surface Ground Water Flows*

In this section we shall convey an idea of the mathematical analysis of the model coupling the channel level and surface ground water flows mentioned. An illustration of the cross section and planar view of the modelling domain is presented in the Figures 3 and 4. As a matter of fact, for the sake of the exposition, we shall limit ourselves to the consideration of a simplified case in which the ground is assumed to be homogeneous and isotropic, the impermeable base is assumed to be horizontal

$$M = H, \tag{18}$$

the flow cross section of the channel is assumed to be uniform and with area given by

$$\omega(s, u) = u, \tag{19}$$

and we assume the constitutive relation $\psi(s,u) = |u|^{\alpha}$, where the parameter α is defined by the geometry of channel.

We shall assume also coefficients $\sigma_1 = \kappa_1 = 0$ and the coincidence among the levels of the ground waters on the left and right banks and the level of the channel water. The last condition corresponds, formally, to conclude that (15) holds for $\alpha = \infty$ and $\alpha_0/\alpha = 0$.

3.1. Statement of the Mathematical Problem

Under the above simplifications, the stated equations of the model reduce to the system (see Figs. 3, 4)

$$\frac{\partial H}{\partial t} = \nabla(H\,\nabla H) + f_\Omega, (x,t) \in \Omega_T^\Pi = \Omega^\Pi \times (0,T), \quad \Omega^\Pi = \Omega/\Pi, \tag{20}$$

$$\frac{\partial u}{\partial t} = \frac{\partial}{\partial s}\left(\mid u \mid^\alpha \left|\frac{\partial u}{\partial s}\right|^{-1/2} \frac{\partial u}{\partial s}\right) + \left[H\frac{\partial H}{\partial n}\right]_\Pi + f_\Pi, \quad (s,t) \in \Pi_T. \tag{21}$$

Under the above simplifications, the set of initial and boundary conditions takes the form

$$H(x,0) = H_0(x), \quad u(s,0) = u_0(s), \tag{22}$$

$$H_+ = H_- = u, \quad (s,t) \in \Pi_T = \Pi \times (0,T), \tag{23}$$

$$H = g, \quad (x,t) \in \Gamma_T, \quad u = g, \quad (x,t) \in P_T \cup N_T. \tag{24}$$

We shall assume (for simplicity) that there exist some functions $H_0(x, t)$, $u_0(x, t)$ defined on $\Omega \times (0, T)$ and such that

$$H_0|_{\Gamma_T} = g,\ u_0|_{\Pi_T} = g; H_0(x,0) = H_0(x), x \in \Omega \quad \text{and} \quad u_0(s,0) = u_0(s), s \in \Pi, \tag{25}$$

$$|H_0|, |u_0|, \| |\nabla H_0| + |H_{0t}| \|_{2,\Omega_T}, \|u_{0s}\|_{3/2,\Pi_T}, \|u_{0t}\|_{2,\Pi_T} \le C < \infty. \tag{26}$$

We assume also

$$\int_0^T \left(\max_x |f_\Omega(x,t)| + \max_s |f_\Pi(s,t)| \right) dt \le C < \infty. \tag{27}$$

The above conditions can be weakened in certain results which follow but we are not trying to enunciate the more general statements of our results.

Remark 3.1 *Note that due to the boundary coupling given by* (23)*, the partial differential for u can be understood as a boundary condition* (*on* Π_T) *for H. So that it is a dynamic boundary condition involving a diffusion term. This type of "boundary conditions" also arises in the study of some systems which appears when coupling the surface Earth temperature with those of a deep ocean* (see Díaz and Tello, 2005, 2008).

Remark 3.2 *As mentioned, the equation* (21) *becomes degenerate on the set of points where u = 0 and singular on the set of points where* $\partial u / \partial s = 0$. *This type of equations arises, mainly, in the study of suitable non-Newtonian flows (see, e. g.* Antontsev *et al.*, 2002). *Here, inversely, no assumption about the Newtonian type of the fluid is made (for other contexts leading to doubly nonlinear parabolic equations quite similar to equation* (21) *see the paper* Díaz *and* Thelin, 1994).

3.2. Existence and Uniqueness Theorems

A non negative pair of bounded functions $(H,u) = \mathbf{W}$ such that

$$0 \le H(x,t), u(s,t) \le C < \infty \tag{28}$$

and

$$\int_0^T \left(\int_{\Omega^\pm} H |\nabla H|^2 dx + \int_\Pi \left(u^\alpha |u_s|^{\frac{3}{2}} \right) ds \right) dt \le C < \infty \tag{29}$$

is called a weak solution of the model (20)–(24) if for every test function η such that

$$\eta \in W_2^{1,1}(\Omega_T) \cap W_2^{1,1}(\Pi_T), \eta = 0, (x,t) \in \Gamma_T = \Gamma \times (0,T)$$

and for every $t \in [0, T]$ the following identity holds

$$\begin{aligned} &\int_0^t \int_\Omega (-H\eta_t + H \nabla H \nabla \eta)\, dxdt + \int_\Omega H(x,\tau)\eta(x,\tau)\, dx|_{\tau=0}^{\tau=t} \\ &\quad + \int_0^t \int_\Pi (-u\eta_t + \psi\varphi(u_s)\eta_s)\, dsdt + \int_\Pi u(s,\tau)\eta(s,\tau)\, ds|_{\tau=0}^{\tau=t} \\ &\quad = \int_0^t \int_\Omega f_\Omega \eta dxdt + \int_0^t \int_\Pi f_\Pi \eta\, dsdt. \end{aligned} \tag{30}$$

The following result is proved in the Appendix.

Theorem 3.1 *Let us assume that* (26) *and* (27) *hold and*

$$0 \le f_\Omega, f_\Pi, H_0, u_0 \le C_0 < \infty, 0 < \alpha < \infty. \tag{31}$$

Then the above model has at least one weak solution $\mathbf{W}(x, t) = (H, u)$ *. If we consider that* $\mathbf{W}_t \in L^1$ *then the weak solution is unique. Moreover, if we assume additionally that*

$$0 < \delta \le u_0, H_0, g \le C_0 < \infty, \tag{32}$$

$$\int_0^T \left(\max_x |\partial f_\Omega / \partial t| + \max_s |\partial f_\Pi / \partial t| \right) dt \le C < \infty \tag{33}$$

$$H_{0xt}, H_{0tt} \in L^2(\Omega_T^\pm),\ u_{0s} \in L^\infty(0,T; L^{\frac{3}{2}}(\Pi)),\ u_{0st} \in L^2(\Pi_T), \tag{34}$$

then there exist a small $T_0 > 0$ *such that this weak solution is unique and the following estimates are valid*

$$\sup_{0 \le t \le T_0} \left(\int_{\Omega^\pm} |\nabla H|^2 dx + \int_\Pi |u_s|^{\frac{3}{2}} ds \right) \le C < \infty \tag{35}$$

$$\int_0^{T_0}\int_{\Omega^{\pm}}\left(H_t{}^2+\mid H_{xx}\mid^2\right)dxdt+\int_0^{T}\int_{\Pi}\left(u_t{}^2+\mid u_s\mid^{-1/2}\mid u_{ss}\mid^2\right)dsdt\le C<\infty. \quad (36)$$

Remark 3.3 *Note that presentation* (51) *may be used as an approximative solution if the functions* Φ_j,Ψ_j *may be constructed effectively.*

Remark 3.4 *The continuous dependence formula implies the comparison principle for* $\mathbf{W}_i$ *in the sense that if* $H(0, x)$, $u(0, s)$, $f_\Omega(t, x)$ *and* $f_\Pi(t, s)$ *are nonnegative in their respective domains, and if we assume* $g \ge 0$ *then the associated solutions satisfy that* H, $u \ge 0$ *(take one of the pair identically zero and apply the formula). In fact, the same arguments can be used to prove that the vectorial operator is T-accretive on the Banach space* $L^1(\Omega) \times L^1(\Pi)$. *Moreover by the arguments of* Díaz *and* Jimenez, (1985) *(see also* Crandall *and* Tartar, 1980;) *we can prove that the operators are m-accretive and thus the existence and uniqueness of the a mild solution follow automatically. This semigroup approach (with its implicit time discretization) has some independent interest (and also for numerical studies of the problem).We also point out that it seems possible to get the continuous dependence formula without the technical condition* $\mathbf{W}_t \in L^1$. *For instance, it could be useful to use the notion of renormalized solutions (see references in the monograph* Antontsev *et al*., 2002).

3.3. Splitting with Respect to Physical Process

For numerical proposes it can be useful to consider separately the two different processes appearing in the model (see Antontsev and Kashevarov, 1986; Antontsev *et al*., 1989).

We propose here an algorithm which uses the splitting of the initial problem into the two following independent problems:

I. *Plane filtration in the domain* $x \in \Omega/\Pi$, $t \in (0, T)$, $k = 1, 2,\ldots$

$$\frac{\partial H^k}{\partial t}=\nabla\left(H^k\nabla H^k\right)+f_\Omega,\quad x\in\Omega/\Pi, \quad (37)$$

$$H^k(x,0)=H_0(x),\quad x\in\Omega, \quad (38)$$

$$H^k\frac{\partial H^k}{\partial n}\Big|_{\pm}=\sigma\left(u^{k-1}-H^k{}_{\pm}\right),\quad x\in\Pi, \quad (39)$$

$$\left(\sigma_1 H^k\frac{H^k\partial H^k}{\partial n}+\sigma_2 H^k\right)=g,\quad x\in\Gamma=\partial\Omega. \quad (40)$$

II. *Level flow in the channel* Π

$$\frac{\partial u^k}{\partial t} = \frac{\partial}{\partial s}\left(\mid u^k \mid^{\alpha} \mid \frac{\partial u^k}{\partial s} \mid^{-1/2} \frac{\partial u^k}{\partial s} \right) + \left[H^k \frac{\partial H^k}{\partial n} \right]_{\Pi} + f_{\Pi}, \quad x \in \Pi, \tag{41}$$

$$\left(\kappa_1 \psi(s, u^k) \phi(\frac{\partial u^k}{\partial s}) + \kappa_2 u^k \right) = g, \quad x \in \Pi \cap \Gamma, \tag{42}$$

$$u^k(x, 0) = u_0(x), \quad x \in \Omega. \tag{43}$$

Let us introduce the notation $h^k = H^k - H^{k-1}$, $z^k = u^k - u^{k-1}$.

Theorem 3.2 *Let us assume the conditions* (31)–(33) *of the existence theorem. Then the "global error iterated energy"* $y_k(t) = ||h^k||^2_{2,\Omega} + ||\nabla h^k||^2_{2,\Omega_T} + ||u^k||^2_{2,\Pi} + ||u^k_s||^{3/2}_{3/2,\Pi_T}$ *satisfies the estimate*

$$y_k(t) \leq \frac{(Ct)^{k-1}}{(k-1)!} y_0(t) \to 0, \quad \text{as} \quad k \to \infty, \quad \text{for} \quad t \leq T.$$

Remark 3.5 *The numerical simulation of the independent problems I and II can now be obtained by well-known finite-differences or finite-elements schemes.*

4. Localization Properties of Solutions

Now we use the same philosophy as some of the localization properties of solutions presented in the papers Antontsev *et al*. (2002), Antontsev and Kashevarov (1982, 1996). Their proofs can be carried out with the techniques presented there. We start with the initial-boundary value problem for the uncoupled equation (equation (10) with $Q = 0$).

4.1. Pure Diffusion Channel Level Equation

Let us consider the following initial boundary value problem

$$\frac{\partial u}{\partial t} = \frac{\partial}{\partial s}\left(|u|^{\alpha} \left| \frac{\partial u}{\partial s} \right|^{-1/2} \frac{\partial u}{\partial s} \right) + f_{\Pi}, \quad s \in \Pi = [-1, 1], t \in [0, T], \tag{44}$$

$$u(i, t) = u^0(t), \; i = -1, 1, \left(\text{or} \frac{\partial u(1, t)}{\partial s} = 0 \right), \tag{45}$$

$$u(s, 0) = u_0(s), \quad t \in]0, T[, \tag{46}$$

$$0 < \delta \le (u^i(t), \quad u_0(s)) \le C_0. \tag{47}$$

4.1.1 Finite time stabilization to a non-zero state.

Theorem 4.1 *Let conditions* (47), (32) *be fulfilled and* $f_\Pi(s,t) \equiv 0$. *Then the solution of problem* (44)–(46) *becomes identically constant after a finite time* t^*, *i.e.*,

$$u(s,t) \equiv u^0 \quad \text{for} \quad s \in [0,1], \quad t \ge t^*.$$

Moreover if $f_\Pi \not\equiv 0$ *but*

$$\|f_\Pi(.,t)\|^{3/2}_{L^2(\Pi)} \le \varepsilon \left(1 - \frac{t}{t_f}\right)^4_+, \tag{48}$$

for some $t_f > t^*$, *and for some suitable small constant* ε, *then the following estimate holds:*

$$\left\|u(\cdot,t) - u^0\right\|^2_{L^2(\Pi)} \le C \left(1 - \frac{t}{t_f}\right)^4_+.$$

In particular,

$$u(s,t) \equiv u^0, \quad \text{for any } s \in [-1,1] \quad \text{and} \quad t \ge t_f.$$

In physical terms, the first assertion of the theorem means that the water level in the channel becomes constant in a finite time provided that the external source f_Π is absent (see Fig. 5). If $f \not\equiv 0$ and condition (48) is fulfilled, one can find a small source intensity $\varepsilon > 0$, such that the water level in the channel stabilizes at the same instant t_f when the source disappears.

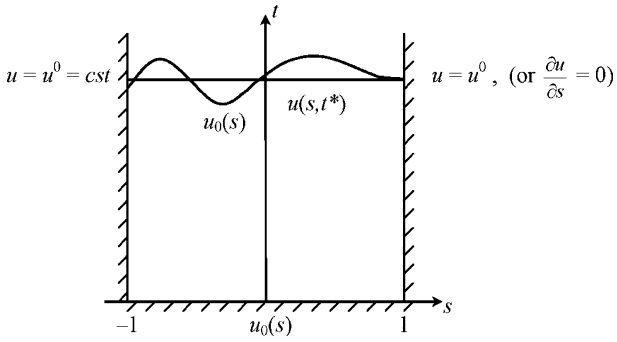

Figure 5
Model of diffusion waves (MDW). Stabilization of the initial level of the water $u_0(s)$ to a stationary horizontal state $u^0 = cst$

Remark 4.1 *We point out that we are considering here the so-called diffusion Saint-Vennant equation which results by neglecting the inertia terms in the original Saint-Venant system. Therefore, in the original system and on the range of small flux it would be just a linear function of* $\partial u/\partial s$. *Accounting for this fact, the effect of finite stabilization time for the diffusion version is due to the singularity in the expression for water flux, and the effect can be considered as an approximation for the original system.*

4.1.2 Wetting finite speed of propagation and formation of a wetting front. Waiting time phenomenon.

We consider now local properties of weak solution of (43) with zero initial data on some subinterval $[-\rho, \rho]$ (see Figs. 6 and 7).

Theorem 4.2 (Finite speed of wetting of a dry bottom) *Let* $u(s, t) \geq 0$ *be a weak solution of equation* (44) *with* $\alpha > 1/2$ *and let*

$$f_\Pi = 0, \quad u_0(s) = u(s, 0) = 0 \quad \text{for} \quad |s| \leq \rho_0, t \in (0, T). \tag{49}$$

Then

$$u(s, t) = 0 \quad \text{for} \quad |s| \leq \rho(t), \ \theta = \theta(\alpha) > 0. \tag{50}$$

where $\rho(t)$ *is defined by the formula*

$$\rho^{1+\sigma}(t) = \rho_0^{1+\sigma} - Ct^\theta$$

with constants $C = C(C_0, \alpha)$, $\theta = \theta(\alpha)$, $\sigma = \sigma(\alpha)$. *If, additionally to* (49) *we assume that*

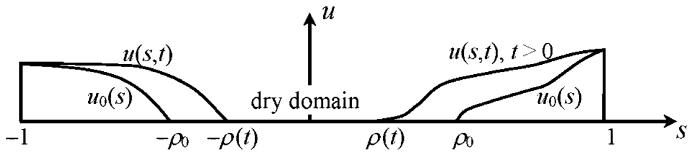

Figure 6
Finite speed of wetting (MDE). $u_0(s)$ is the initial level of the water ($u_0(s) = 0$, $s \in (-\rho_0, \rho_0) = 0$). $u(s, t)$ is the level of the water for $t > 0$

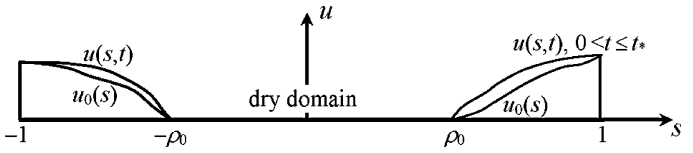

Figure 7
Waiting time of wetting (MDE). $u_0(s)$ is the initial level of the water ($u_0(s) = 0$, $s \in (-\rho_0, \rho_0) = 0$). $u(s, t)$ is the level of the water for $t > 0$

$$\int_{-\rho}^{\rho} |u_0(s)|^2\, ds + \int_0^T \int_{-\rho}^{\rho} |f_\Pi|^2 ds dt \le \varepsilon(\rho - \rho_0)_+^{1/(1-\nu)}, \quad \rho_0 \le \rho,$$

then there exists $t_* \in [0, T)$ *such that*

$$u(s, t) = 0, \quad \text{for } s \in [-\rho_0, \rho_0] \text{ and } t \in [0, t_*].$$

4.2. Coupled Channel Level and Surface Ground Water Flows

Let us return to the system of equations (15),(20),(21), with $\alpha_0 = 0$, describing the mentioned coupled flows. We consider the domain $B_\rho \times (0, T)$, $B_\rho = \{x \in \Omega |\ |x - x_0| < \rho\}$ (see ANTONTSEV *et al.*, 2002; ANTONTSEV and KASHEVAROV, 1982; 1996) Figures 3, 4, and 8).

4.2.1 Wetting finite speed of propagation. Waiting time phenomenon.

Theorem 4.3 *Let* $W = (H, u)$ *be a local weak solution of equations* (15), (20), (21) under the assumptions

$$H_0(x) = 0, \quad f_\Omega = 0 \quad (x, t) \in B_{\rho_0} \times [0, T),$$
$$u_0(s) = 0, \quad f_\Pi = 0 \quad (s, t) \in \Pi_{\rho_0} \times [0, T).$$

Then there exist $t_* \in (0, T)$ *and* $\rho(t)$ *such that*

$$H(x, t) = 0 \quad x \in B_{\rho(t)}, \quad u(s, t) = 0 \quad s \in \Pi_{\rho(t)}, \quad t \in [0, t_*]$$

with $\rho(t)$ *defined by the formula*

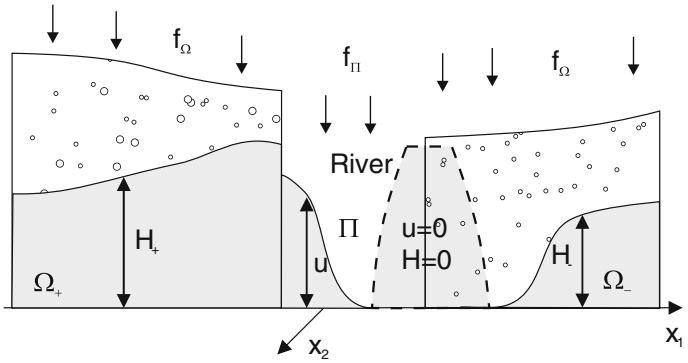

Figure 8
Finite speed of wetting (Coupled Model). $H_\pm$ are levels of the underground waters on the opposite sides of the river. u is the water level in the river

$$\rho^{1+\sigma}(t) = \rho_0^{1+\sigma} - Ct^{\theta},$$

with some constant C. If, moreover,

$$\|H_0\|^2_{L^2(B_\rho)} + \|u_0\|^2_{L^2(\Pi_\rho)} + \int_0^T \left(\|f_\Omega\|^2_{L^2(B_\rho)} + \|f_\Pi\|^2_{L^2(\Pi_\rho)} \right) d\tau$$

$$\leq \varepsilon(\rho - \rho_0)_+^{\vartheta}, \quad \rho > \rho_0, \quad \vartheta(\alpha) > 0,$$

then there exists $t_* \in [0, T)$ *such that*

$$H(x,t) = 0 \quad x \in B_{\rho_0}, \quad u(s,t) = 0 \quad s \in \Pi_{\rho_0}, \quad \text{for any } t \in [0, t_*]$$

In terms of the original physical problem we can understand the results as follows: If the domain B_{ρ_0} was dry at the initial time, i.e. the levels of the surface and ground water were zero therein, then the first assertion of the theorem gives some estimates on the location of the free boundaries (the curves and points where they are zero) generated by $H(x, t)$ and $u(s, t)$ (see Fig. 8). The second assertion states that whatever the flux is outside B_{ρ_0}, this domain can only be swamped not instantaneously but after a positive finite time.

Remark 4.2 *As mentioned in the introduction, equations* (20) *and* (21) *for water flow in the porous medium and in the channel include physical coefficients, and they are very contrasting. As a result, the typical time scale for the flow in channel is much smaller than for the ground-water dynamics. On the level of pure mathematics this fact is unimportant however, it is crucial in view of applications including numerical studies of realistic problems. In particular, the constant C in the energy error estimate from Theorem 3.2 can become too large or time* t_* *that describes localization properties of solutions can become negligibly small in practice. A careful study of this matter is beyond the subject of this paper.*

5. Appendix: Proof of Theorem 3.1

First we assume that (32) holds. Then it follows from the definition of the weak solution that $0 < \delta \leq H, u$. The weak solution can be constructed, for instance, as the limit of a sequence of Galerkin's approximations. From the assumptions of the domain Ω we know that there exists a complete system of the functions $\Phi_k \in W_2^1(\Omega)$, with $\Phi_k(\vec{x})_\Gamma = 0$, which are dense in $W_2^1(\Omega)$. Respectively. we can assume that the set of curves Π admits also a complete system of functions $\Psi_k \in W_{\frac{3}{2}}^1(\Pi)$, with $\Psi_k(s)_{\Gamma \cup \Pi} = 0$, which is dense in $W_{\frac{3}{2}}^1(\Pi)$. Moreover, without loss of generality we can assume that the functions Φ_k and Ψ_k are orthogonal in $L^2(\Omega)$ and $L^2(\Pi)$, respectively. Then we can construct a sequence of approximate solutions of the form

$$\mathbf{W}^N = (H^N, u^N) = \left(\sum_{k=1}^{N} H_k(t)\Phi_k(\vec{x}) + H_0, \sum_{k=1}^{N} u_k(t)\Psi_k(s) + u_0 \right), \tag{51}$$

where the functions H_0 and u_0 satisfy the corresponding boundary conditions.

We substitute the last expression into the corresponding partial differential equations, multiply by $\Phi_j^{\pm}(x)$ and $\Psi_j(s)$, respectively, and integrate over $\Omega_{\pm}$ and Π.

This leads us to a suitable Cauchy problem

$$\frac{d\mathbf{Y}^N}{dt} = \mathbf{F}(t, \mathbf{Y}^N), \quad \mathbf{Y}^N(0) = \mathbf{Y}_0^N, \quad (\mathbf{Y}^N = (H_1, \ldots, H_N, u_1, \ldots, u_N)), \tag{52}$$

for some given smooth (with respect to $\mathbf{Y}$) vectorial function $\mathbf{F}(t,\mathbf{Y})$. Multiplying equations (52) by the stop vector $\mathbf{Y}^N$ and summing, we arrive at the estimate (35). To prove the estimates (36) we differentiate (52) with respect to t and multiply by $d\mathbf{Y}^N/dt$. Obtained estimates permit us to pass to the limit when $N \to \infty$ and $\delta > 0$ and next to pass to the limit when $\delta \to 0$.

To prove the uniqueness of weak solutions under the additional information that $\mathbf{W}_t \in L^1$, we apply the following continuous dependence formula

$$\begin{aligned} \int_{\Omega^{\pm}} [H_1(t,x) - H_2(t,x)]_+ dx + \int_{\Pi} [u_1(t,s) - u_2(t,s)]_+ \, ds \\ \leq \int_{\Omega^{\pm}} [H_1(0,x) - H_2(0,x)]_+ dx + \int_{\Pi} [u_1(0,s) - u_2(0,s)] \\ + \int_0^t \int_{\Omega^{\pm}} [f_{1,\Omega}(\tau,x) - f_{2,\Omega}(\tau,x)]_+ dx + \int_{\Pi} [f_{1,\Pi}(\tau,s) - f_{2,\Pi}(\tau,s)]_+ \, ds, \end{aligned}$$

which holds when we work for two couples of solutions $\mathbf{W}_i(x, t) = (H_i, u_i)$ associated with two sets of data $H_i(0, x)$, $u_i(0, s)$, $f_{i,\Omega}(t, x)$ and $f_{i,\Pi}(t, s)$ (but satisfying the same Dirichlet boundary conditions $H_i = g, (x, t) \in \Gamma_T$, $u_i = g, (s, t) \in \partial\Pi_T$) for $i = 1, 2$. This formula is obtained by multiplying the difference of the associate equations (20) by a regularized approximation of the function $\text{sign}_+(H_1(t, x) - H_2(t, x))$[$= 1$ if $H_1(t, x) - H_2(t, x) > 0$ and $=0$ if $H_1(t, x) - H_2(t, x) \leq 0$]. Calling, for instance $p(H_1 - H_2)$ to this approximation, using the weak formulation (i.e., the integration by parts of the formula) and using that (thanks to the assumption (23) we obtain $p(H_1 - H_2) = p(u_1 - u_2)$ on Π_T, we end by using the equation (21) and passing to the limit as in the paper by Díaz and Thelin (1994).

6. Summary and Conclusions

The water-exchange models here considered take into account the following factors: Water flows in confined and unconfined aquifers, vertical moisture migration by allowing earth surface evaporation, open-channel flow simulated by one-dimensional hydraulic equations, transport of contamination, etc. These models may have different levels of

sophistication. We illustrate the type of mathematical singularities which may appear by considering a simple model on the coupling of a surface flow of the surface and ground waters with the flow of a line channel or river. An illustration of the cross-section and planar view of the modelling domain is presented in Figures 3 and 4. As a matter of fact, for the sake of the exposition, we limited ourselves to the consideration of a simplified case in which the ground is assumed to be homogeneous and isotropic, the impermeable base is assumed to be horizontal $M = H$, the flow cross section of the channel is assumed to be uniform and with area given by $\omega(s, u) = u$, and we assume the constitutive relation $\psi(s, u) = |u|^{\alpha}$, where the parameter α is defined by the geometry of channel. We assume also coefficients $\sigma_1 = \kappa_1 = 0$ and the coincidence among the levels of the ground waters on the left and right banks and the level of the channel water. The last condition corresponds, formally, to assume that (15) holds for $\alpha = \infty$ and $\alpha_0/\alpha = 0$. The resulting system is given by the two coupled nonlinear partial differential equations (20) and (21).

A previous study of the questions of the mathematical well-posedness of the above system (existence, uniqueness and some qualitative properties of solutions) was carried out in the papers Antontsev *et al.*, (2002, 1986), Antontsev and Kashevarov, (1999), Antontsev and Meirmanov (1979, 1977b; 1977c; 1978). In section 3 we recalled a part of those results, adding some new ones (as, for instance, the continuous dependence formula. In section 4 we presented some qualitative properties of solutions which explain the mathematical peculiarities of such model. Due to the presence of nonlinear terms, the solutions of such equations may exhibit many different behaviors that cannot occur in the (more or less well-known) case of linear models. The list of peculiar effects of this kind includes properties as the finite time of localization (or extinction in finite time), finite speed of propagation of disturbances from the initial data, waiting time effect, etc. Some comments on the physical meaning of theses properties are included.

Acknowledgements

The work of the first author was supported by the CMAF, University of Lisbon, Portugal and SAB-2005-0017 of the Secretaria de Estado de Universidades e Investigación (Spain). The research of the second author was supported by the projects MTM2005-03463 DGISGPI and 910480 UCM/CM. This paper was written when the first author was Sabbatical Professor at the UCM. The authors thank the anonymous referees for their constructive commentaries.

References

Abbott, M., Bathurst, J., and Cunge J. A. (1986), *An introduction to the European hydrological system (SHE)*, Part 2, J. Hydrol. *87*, 129–148.

Antontsev, S. N. and Díaz, J. I. (1991), *Space and time localization in the flow of two immiscible fluids through a porous medium: Energy methods applied to systems*, Nonlinear Anal. *16*, 299–313.

ANTONTSEV, S. N., DÍAZ, J. I., and SHMAREV, S., *Energy Methods for Free Boundary Problems: Applications to Non-linear PDEs and Fluid Mechanics*, (Bikhäuser, Boston, 2002) *Progress in Nonlinear Differential Equations and their Applications*, vol. 48.

ANTONTSEV, S. N., EPIKHOV, G. P., and KASHEVAROV A. A. (1986), *Mathematical system modelling of water exchange processes* (Nauka, Sibirsk. Otdel., Novosibirsk in Russian).

ANTONTSEV, S. N. and KASHEVAROV, A. A.,. *Finite Rate of Propagation of Perturbations in Simultaneous Flows of Surface and Ground Water*, (Dinamika Sploshnoi Sredy *57* Institute of Hydrodynamics, Novosibirsk. 1982) pp. 21–27.

ANTONTSEV, S. N. and KASHEVAROV, A. A. (1986), *Splitting according to physical processes in the problem of interaction between surface and underground water*, Dokl. Akad. Nauk SSSR, 288, pp. 86–90 (English translation: Soviet Phys. Dokl, v. 31, n. 5, pp.381–383).

ANTONTSEV, S. N. and KASHEVAROV, A. A. *Localization of solutions of nonlinear parabolic equations that are degenerate on a surface* (Dinamika Sploshnoi Sredy *111*, Institute of Hydrodynamics, Novosibirsk 1996) pp. 7–14.

ANTONTSEV, S. N. and KASHEVAROV, A. A., *Correctness of a hydraulic model of filtration for ground waters with an unsaturated zone*. In book *Mathematical Models in Filtration and its Applications*, (Institute of Hydrodynamics, Novosibirsk, 1999a) pp. 21–35.

ANTONTSEV, S. N. and KASHEVAROV, A. A. (1999b), *Mathematical models of mass transfer in interconnected processes of surface, soil and ground waters*. Abstracts of the International Conference *Modern Approaches to Flows in Porous Media*, September 6–8, Moscow, pp. 165–166.

ANTONTSEV, S. N., KASHEVAROV, A. A., and MEIRMANOV, A. M. (1981), *Numerical modelling of simultaneous motion of surface channel and ground waters*. Abstracts of the International Conference *Numerical Modelling of River, Channel over Land Flow for Water Resources and Environmental Applications*, May 4–8, Bratislava, Czechoslovakia, pp. 1–11.

ANTONTSEV, S. N., KASHEVAROV, A. A., and SEMENKO, A., *An Iterative Method for Solving a Stationary Problem on Saturated-Unsaturated Filtration in a Hydraulic Approximation*, (Dinamika Sploshnoi Sredy, Novosibirsk, Institute of Hydrodynamics, Novosibirsk 1989), Vyp. *90*, pp. 3–15.

ANTONTSEV, S. N., KAZHIKHOV, A. V., and MONAKHOV, V. N., *Boundary Value Problems in Mechanics of Nonhomogeneous Fluids* (North-Holland Publishing Co., Amsterdam, 1990 Translated from original Russian edition: Nauka, Novosibirsk, 1983).

ANTONTSEV, S. N. and MEIRMANOV, A. M., *Mathematical models of the coupled motion of surface and ground waters. Mechanics*. In Third Congress: Theoretical and Applied Mechanics (Varna, Sept. 13–16, 1977), vol. 1 (Acad. Sci. Bulgaria, Sofia 1977a) pp. 223–228.

ANTONTSEV, S. N. and MEIRMANOV, A. M., *Mathematical models of simultaneous motions of surface and ground waters* (Novosibirsk State University, Lecture Notes, 1979).

ANTONTSEV, S. N. and MEIRMANOV, A. M. *Mathematical questions of the correctness of initial-boundary value problems of a hydraulic model of diffusion waves* (Dinamika Sploshnoi Sredy, Institute of Hydrodynamics, Novosibirsk 1977b) 30, pp. 7–34.

ANTONTSEV, S. N. and MEIRMANOV, A. M., *Mathematical questions on the correctness of a model of the simultaneous motion of surface and underground water* (Dinamika Zhidkosti so Svobod. Granitsami, Institute of Hydrodynamics, Novosibirsk 1977c), Vyp. *31*, pp. 5–51.

ANTONTSEV, S. N. and MEIRMANOV, A. M. (1978), *Questions of correctness of a model of the simultaneous motion of surface and ground waters*, Dokl. Akad. Nauk SSSR, 242, pp. 505–508.

BEAR, J. and VERRUIJT, A., *Modelling Groundwater Flow and Pollution. Theory and Applications of Transport in Porous Media*, vol. 2. (Kluwer Academic Publisher, Dordrecht, Holland, 1987)

CRANDALL, M. G. and TARTAR, L. (1980), *Some relations between nonexpansive and order preserving mappings*, Proc. Amer. Math. Soc. *78*, 3, 385–390.

CUNNINGHAM, A. and SINCLAIR, P.J. (1979), *Application and analysis of coupled surface and groundwater model*, J. Hydrol. *43*, 129–148.

DALUZ VIEIRA, J.B. (1983), *Conditions governing the use of approximations for the Saint-Venant equations for shallow surface water flow*, J. Hydrol. *60*, 43–58.

DÍAZ, J. I. and JIMENEZ, R., *Aplicación de la teoría no lineal de semigrupos a un operador pseudodiferencial* (Actas del VI CEDYA, Univ. de Granada 1985) pp. 137–142.

Díaz, J. I. and Tello, L., *On a parabolic problem with diffusion on the boundary arising in Climatology*. International Conference *Differential Equations* (ed. World Scientific, New Jersey 2005) pp. 1056–1058.

Díaz, J. I. and Tello, L. (2008), *On a climate model with a dynamic nonlinear diffusive boundary condition*. Discrete and Continuous Dynamical Systems Series S, vol 1, No. 2, 253–262.

Díaz, J. I. and Thelin, F. (1994), *On a nonlinear parabolic problems arising in some models related to turbulence flows*. SIAM J. Math. Anal. *25*, 4, 1085–1111.

Epikhov, G. (1985), *Computation system modelling of water exchange in interactive regime*, Vodnue resursy *5*, 11–25.

Fowler, A., *Mathematics and the Environment*, (Springer-Verlag in press).

Kashevarov, A. A. (1998), *Mathematical modeling of salt transport by coupled subsurface and surface water flows*. J. Appl. Mech. Tech. Phys. *39*, 584–591.

Kuchment L., Demidov, V., and Motovilov, Y. G., *Formation of a River Basin* (Nauka, Moscow, Russia 1983).

Luckher, L. (1978), *Gekoppelte Grundwasser-Oberflächen-Wassermodell (a coupled model of ground and surface waters)*, Wasserwirt.-Wassertechn. (WWT) *29* (8), 276–278.

Miles, J., *Modelling the interaction between aquifers and rivers*. In *Advances in Water Engineering* (Elsevier. Publ., Ltd., London-New York 1985), pp. 94–100.

Philip, J. (1969), *The Theory of Infiltration*, Adv. Hydrosci. *5*, pp. 215–296.

Polubarinova-Kochina, P. Y., *Theory of the Motion of Ground Waters* (Nauka, Moscow, Russia 1977).

Usenko, V. and Zlotnik V. (1978), *Mathematical models and numerical methods in the problems of interconnection of unconfined grounwater and surface water*. Proc. of Third Int. Symp., Kiev, 1976, (Part 4, Naukova Dumka, Kiev, USSR, Providence, RI, pp. 108–117).

Vasiliev, O. F., 1987. *System modelling of the interaction between surface and ground waters in problems of hydrology*. Hydrolog. Sci., 32, pp. 297–311.

(Received May 2, 2007, revised April 21, 2008, accepted May 6, 2008)

Pure appl. geophys. 165 (2008) 1531–1554
0033–4553/08/081531–24
DOI 10.1007/s00024-004-0388-7

Pure and Applied Geophysics

Time Evolution of Deformation Using Time Series of Differential Interferograms: Application to La Palma Island (Canary Islands)

Patricia A. Perlock,[1] Pablo J. González,[2] Kristy F. Tiampo,[1]
Gema Rodríguez-Velasco,[2] Sergey Samsonov,[1] and José Fernández[2]

Abstract—Differential interferometry is a very powerful tool for detecting changes in the Earth's crust where coherence conditions are good, but is difficult to employ in some volcanic areas due to dense vegetation. We apply two differential InSAR methods using the time series associated with the interferograms to perform a phase analysis on a data set for La Palma island (Canary Islands) from the ERS-1 and ERS-2 European Space Agency (ESA) satellites for the time period 1992 to 2000. Both methods involve choosing a master image from the database and creating a series of interferograms with respect to this image. The "Coherent Pixel Time Series" (CPTS) technique chooses pixels with good average coherence, aligns the unwrapped interferograms with a stable area and then performs an inversion to calculate the linear velocity to quantify the deformation. The Coherent Target Modeling (CTM) method calculates the temporal coherence of each pixel to identify stable targets and then determines the best velocity for each pixel by using a linear fit that maximizes the temporal coherence. Using these two methods we have been able to detect deformation on La Palma Island that has been previously undetectable by conventional InSAR methods. There is a roughly circular region on the Southern part of the island that is actively deforming at ~ -4 to -8 mm/yr. This region is located near the Teneguia valcano, the host of the last known eruption on La Palma in 1971. A thorough investigation of the possible sources for this deformation revealed that it was most likely created by a subsurface thermal source.

Key words: Time series, La Palma, InSAR, ground deformation modeling, differential interferograms, permanent scatterers.

1. Introduction

Measuring changes on the Earth's surface by means of Interferometric Synthetic Aperture Radar (InSAR) has become a popular research subject among the geophysical community. Differential InSAR involves calculating the difference in the phase between two images taken at different times by a spaceborne Synthetic Aperture Radar (SAR) and then correcting for geometry and topography. Use of this technique can be applied to large spatial areas where it is difficult to deploy land-based geodetic monitoring networks. It is particularly useful in monitoring natural phenomena such as landslides,

[1] Department of Earth Sciences, University of Western Ontario, London, Ontario, Canada.
[2] Instituto de Astronomía y Geodesia, CSIC-UCM, Madrid, Spain.

volcanoes and earthquakes but can be limited due to the repeat time associated with acquiring images.

Ground deformation and gravity changes are well known geodetic observables that can reflect the state of activity at a volcano, and for this reason a geodetic monitoring program should be implemented at almost every volcano around the world, but this is a very difficult objective to meet. New space-based geodetic techniques could produce a limited, prior knowledge of the background level of the ground deformation on a volcano using past recorded SAR images from the ERS satellites (ERS-1/ERS-2) launched by the European Space Agency. In the last decade, radar interferometry has become more than just a promising geodetic tool. This technique has proven to be useful in volcanic areas, capable of detecting displacements caused by shallow intrusions. Using large datasets of SAR images and statistical methods, interferometry techniques could detect slow long-standing inflation-deflation processes on deep magmatic reservoirs.

Using InSAR methods on volcanically active areas can be difficult because of steep slopes and dense vegetation due to their fertile soil. SAR images taken in mountainous regions that have steep slopes may have low coherence or lost information due to the geometric effects of phenomena such as foreshortening, layover and shadowing. Vegetation poses a problem because it changes quite rapidly in time. This causes the scattering properties to also change rapidly with time causing temporal decorrelation. One way of dealing with this problem is to implement the"Permanent Scatterers Technique"^{TM} developed and patented by FERRETTI *et al.* (2000; 2001). This method involves finding a subset of pixels in the image that have their phase determined predominately by a stable point-like scatterer (PS). This reduces decorrelation because the degree of correlation in radar signals depends on the distribution of the scattering centers within a pixel. Therefore, analyzing only those pixels exhibiting correlation above a predefined threshold, should increase the chances of detecting deformation in a volcanic region.

The algorithm developed by FERRETTI *et al.* (2000; 2001) identifies PS pixels using the amplitude dispersions in a series of interferograms and uses temporal correlation in the phase analysis. This method tends to work best in areas where there is a high density of stable reflectors like man-made structures that will result in a large set of point scatterers. In natural terrains such as volcanic regions, this still poses a problem because there is a lack of natural point scatterers resulting in a small set of PS pixels and therefore, the results can be unreliable or misinterpreted. HOOPER *et al.* (2004) addressed this issue by modifying the algorithm to identify PS pixels based on phase analysis. The method chooses the initial set of PS pixels using a high amplitude dispersion threshold and then runs an iterative phase analysis on the pixels to determine a final set of PS pixels. Using temporal correlation in phase analysis is also not conducive to volcanic settings as volcanic deformation varies temporally. HOOPER *et al.* (2004) use spatial correlation in their phase analysis which allows the deformation to be calculated without making assumptions of its temporal history. By incorporating these two new aspects into the

algorithm HOOPER *et al*. (2004) were able to produce reliable deformation results in volcanic areas that were otherwise not detected.

The two methods presented here build upon the idea of using phase analysis to identify the deformation or linear velocity. Both approaches involve constructing a set of differential interferograms with respect to one master interferogram. The "Coherent Pixel Time Series" (CPTS) technique is based on the selection of pixels with good average coherence from the study period. Once these pixels are chosen, the unwrapped interferograms are "aligned" using a zero deformation zone, allowing for a complete reconstruction of the total deformation history for each pixel. The deformation history is then inverted to calculate the linear velocity and quantify the deformation. Finally, the linear model is adjusted by removing pixels with large RMS error or low average coherence. The Coherent Target Modeling (CTM) method uses the stability of the phase to identify coherent targets. It does this by evaluating the temporal coherence (a measure of how stable the scatterer is over time) of each pixel. The deformation is quantified by iteratively searching through a set of velocity and DEM errors to find the combination that produces a maximum temporal coherence. Using the two methods presented in this paper, we have been able to detect deformation on La Palma island, Canary Islands that has been previously undetectable by other InSAR methods.

2. *La Palma: Canary Islands Geological Settings*

The Canarian Archipelago, situated off the NW coast of the African continent, is formed by a group of seven major islands (Fig. 1A). Even after a century of study, its origins remain under discussion and several hypothesis are proposed, such as a hotspot or mantle plume (PÉREZ *et al*., 1994; CARRACEDO *et al*., 1998; DAÑOBEITIA and CANALES, 2000), a region of compressional block faulting (ARAÑA and ORTÍZ, 1991), a rupture propagating from the active Atlas Range (ANGUITA and HERNÁN, 1975) or a unifying model (ANGUITA and HERNÁN, 2000). The islands rest on a transitional crust that is overlain by a sedimentary cover with a maximum thickness of 10 km in the eastern zone and a minimum of 1 km in the western sector (BANDA *et al*., 1981). The island of La Palma is the emerged part of an oceanic edifice of predominantly basaltic composition with a submarine base lying over the North Atlantic abyssal plain ($\approx$ 4000-meter depth). La Palma is resting on oceanic lithosphere of Jurassic age ($\approx$155 Myr, the "M25-isochron"), has a subaerial exposure that extends approximately 708 km^2, and reaches an elevation of 2500 m above sea level. The island is geologically divided into two main units: the Basal Complex (BRAVO, 1964; FÚSTER *et al*., 1968) or Submarine Edifice (CARRACEDO *et al*., 2001) and the Subaerial Edifices. The subaerial edifices are composed of shield volcanoes in the north (Garafía, Taburiente, and Cumbre Nueva volcanoes) and Cumbre Vieja volcano located on the southern ridge (NAVARRO and COELLO, 1993; ANCOECHEA *et al*., 1994) (Fig. 1B).

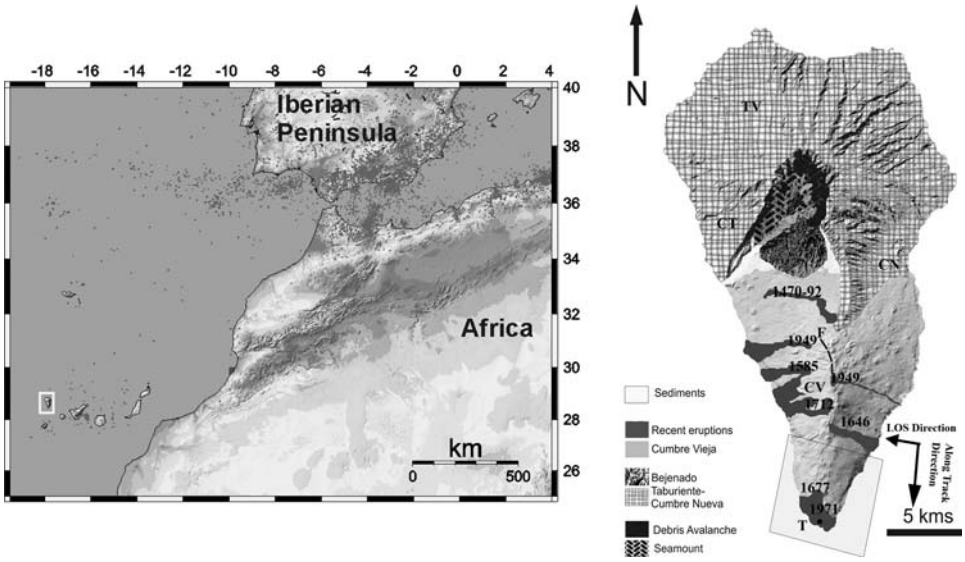

Figure 1

Figure 1A shows the geographical location of the Canary Islands and La Palma island (white rectangle) located off the NW coast of Africa. The grey dots represent seismicity at the region between 1973–2004 (Data source NEIC-USGS). Figure 1B is a geological map of La Palma redrawn after CARRACEDO *et al.* (2001) where TV = Taburiente Volcano; CT = Caldera de Taburiente; CN = Cumbre Nueva Volcano; F = Mapped Fracture at the summit of Cumbre Vieja (CV) volcano and T = Teneguia volcano. The area outlined in the south is the study area for our deformation, located near Teneguia volcano.

2.1. The Basal Complex: An Uplifted Seamount

The Basal Complex outcrops at the base of the Caldera de Taburiente (a large depression located in the northern sector of the island). It consists of a succession of 1800 m of pillow lavas, hyaloclastic rocks and breccias of basaltic composition, crossed by trachytic and phonolitic domes and a large, dense network of basaltic dikes and gabbroic intrusion bodies (DE LA NUEZ, 1984). This unit is approximately 3–4 Myr old. The material appears to be hydrothermally altered with a low grade metasomatism, that has caused the recrystallization of minerals indicative of temperature conditions around 450–500°C and a pressure of 1–1.5 kbar (under 3000 m of lithostatic pressure). Eruptive activity in the caldera ceased 3 Myr ago at which point continuous uplifting and southwest tilting occurred and a strong erosional stage began, resulting in the deposition of breccias and debris avalanche deposits.

2.2. Subaerial Volcanism

Northern Sector. Subaerial volcanism in the northern sector began approximately 1.7 Myr ago and ceased 0.4 Myr ago, creating several individual overlapping edifices

(CARRACEDO *et al.*, 2001; NAVARRO and COELLO, 1993). The first subaerial phase of the Northern Edifice (1.7–1.2 Myr) consisted of the Garafía volcano composed of basaltic lavas deposited unconformably over the submarine edifice. The Garafía volcano outcrops as erosive windows and its tabular formations are tilted 30°, concentrically centered on the submarine edifice (FERNÁNDEZ *et al.*, 2002). The volcano itself is approximately 400 m wide and rises approximately 2000 m above sea level. The second phase of development consists of the Taburiente volcano, which is separated from the Garafía volcano by an angular erosive unconformity suggesting that a large gravitational landslide must have destroyed the northern flank of the Garafía volcano (ANCOECHEA *et al.*, 1994; CARRACEDO *et al.*, 2001). The first phase was dominated by pyroclastic deposits which became progressively more lava-like. Subsequently, the emission centers were aligned in three rift zones (directed NW, NE and N-S) that extend concentrically out from the central part of the volcano which is approximately 3000 m in height.

The magmatic fertile zone migrated southwards along the N-S rift and a new high aspect ratio volcano known as the Cumbre Nueva Ridge formed, creating an instability in the northern sector. In the final building stage of this sector, Cumbre Nueva collapsed and generated a large landslide in the western flank around 0.56 Myr ago (NAVARRO and COELLO, 1993) leaving a depression that was quickly filled by lavas. The emission centers were limited to the interior of the depression creating the rapidly developed volcano, Bejenado (0.56–0.49 Myr) that is $\approx$600 m thick (CARRACEDO *et al.*, 2001).

Southern Sector: Present Activity. The southward migration of volcanic activity created a new and separate edifice in the south, the Cumbre Vieja volcano. The recent (upper Pleistocene-Holocene) volcanic activity in La Palma is concentrated in this volcano. Cumbre Vieja is formed by a succession of overlapping lavas and pyroclastic deposits from a large number of fissure eruptions that are oriented dominantly north-south. This volcano can be divided into two formations. The first is an older *cliff-forming* formation with basaltic and basanitic composition that is dated to be between 130–30 kyr. The second is a younger *scree-* and *platform-forming* formation created by strombolian activity with basaltic, basanitic and tephritic composition as well as sparse phonolitic domes that presently cover the Cumbre Vieja flanks (GUILLOU *et al.*, 1998; DAY *et al.*, 1999). Cumbre Vieja has been the most active volcano in the Canary Islands in historical and recent times, having had seven eruptions take place: Montaña Quemada (1470–1492), Tahuya (1585), Tigalate o San Martín (1646), San Antonio (1677), El Charco (1712), Nambroque or San Juan (1949) and Teneguía (1971) (ROMERO, 2000).

3. Data Processing and Time Series Analysis

3.1. Previous Geodetic Monitoring

La Palma island has not had a geodetic monitoring program in place to quantify the volcanic deformation until recently, and even now, only small steps have been

taken. Recently, Moss *et al.* (1999) have set up a geodetic network that has been used to produce three surveys using Electronic Distance Measuring (EDM) and Differential GPS (DGPS) techniques in the southern part of the island (between 1994–1997) and have detected displacements on the same order of magnitude as the associated errors. They argue that the western flank of the Cumbre Vieja volcano could potentially collapse in a megalandslide. At the same time, geological evidence of tectono-volcanic and purely volcanic ground movements on large time scales have recently been reported on the entire island (Hildenbrand *et al.*, 2003; Klügel *et al.*, 2005).

Campaign GPS missions that have been undertaken on La Palma have been unsuccessful in detecting the deformation found on Teneguia volcano because the area of deformation is very small and there are no GPS stations directly in this region. Classical interferometry that has been applied to detect deforming areas in the past (Massonnet and Sigmundsson, 2000; Fernández *et al.*, 2002) was not precise enough to detect the displacements thought to be present on Teneguia due to the dense vegetation in the area and the magnitude of the displacements. Here, two approaches are applied to obtain a complete history of the time-dependent evolution of the deformation from 1992 to 2000 on La Palma island.

3.2. Data

We have studied an eight-year period, between 1992 and 2000, using the existing archive dataset from ESA SAR missions (ERS-1/ERS-2), to generate continuous high-resolution maps of the surface ground deformation on La Palma island, in order to evaluate the deformation in this volcanic area. To generate the interferograms, we have used 16 descending ERS-1 and ERS-2 SAR images (Table 1). After analysis of the precise orbit information and the time of acquisition, we have excluded the image from June 29, 1993 due to its large spatial perpendicular baseline.

3.3. Selection of Master Images

One of the most important parts of the *Time Series Analysis of Interferograms* is the selection of the master image. It is necessary to have some independent parameters that can be used to determine that the master, chosen from the large dataset of SAR images, is reasonable. The Theoretical Cumulative Correlation (TCC) model is a simplified version of the model developed by Hooper (2006) that can be used to determine the best choice for a master image.

Suppose there are $N - 1$ single-look interferograms formed with respect to one master from N images. The master chosen to create these interferograms should be one that minimizes the decorrelation, and therefore maximizes the sum correlation of all the interferograms. The coherence can be modeled as the product of four terms: the temporal baseline (T), the spatial perpendicular baseline ($B_\perp$), the Doppler Centroid frequency

Table 1

Available SAR images over La Palma, Canary islands. Track: 395, Frame: 3033. Incidence angle in the scene center is 23.2°, $B_\perp$ is the spatial perpendicular baseline between satellite acquisition in meters and H_{amb}, is the height of the ambiguity in meters. LP_i stands for La Palma and the image number

Image	Date	Orbit	$B_\perp$ (m)	Time Span (days)	H_{amb} (m)	Satellite
LP1	29/05/1992	4548	− 130.4	− 1178	72.4	ERS-1
LP2	07/08/1992	5550	− 65.6	− 1108	143.7	ERS-1
LP3	29/06/1993	5550	− 451	− 933	20.9	ERS-1
LP4	23/07/1993	10560	− 37.7	− 758	− 250.4	ERS-1
LP5	01/10/1993	11562	12.7	− 688	− 745.8	ERS-1
LP6	11/06/1995	20423	− 110.8	− 70	85.2	ERS-1
LP7	20/08/1995	21425	*Master*	*Master*	*Master*	ERS-1
LP8	21/08/1995	1752	− 101.9	1	92.6	ERS-2
LP9	24/09/1995	21926	− 122.9	35	76.8	ERS-1
LP10	04/12/1995	3255	− 191.1	106	49.4	ERS-2
LP11	08/01/1996	3756	− 43.7	141	215.7	ERS-2
LP12	09/09/1996	7263	− 303.3	386	31.1	ERS-2
LP13	14/10/1996	7764	− 94.5	421	99.9	ERS-2
LP14	10/08/1998	17283	106.3	1086	− 88.7	ERS-2
LP15	21/06/1999	21792	− 110.7	1401	85.2	ERS-2
LP16	26/07/2000	26802	99.4	1751	− 94.9	ERS-2

(FDC) and the thermal noise (ZEBKER and VILLASENOR, 1992). A simple model for the total correlation is,

$$\rho_{\text{total}} = \rho_{\text{temporal}} \cdot \rho_{\text{spatial}} \cdot \rho_{\text{Doppler}} \cdot \rho_{\text{thermal}} \tag{1}$$

$$\rho_{\text{total}} = \left(1 - f\left(\frac{T}{T^c}\right)\right) \cdot \left(1 - f\left(\frac{B_\perp}{B_\perp^c}\right)\right) \cdot \left(1 - f\left(\frac{F_{DC}}{F_{DC}^c}\right)\right) \cdot \rho_{\text{thermal}} \tag{2}$$

where

$$f(x) = \begin{cases} x, & \text{for } x > 1 \\ 1 & \text{for } x < 1 \end{cases}$$

ρ represents the coherence and the superscript c denotes the critical parameter values. The critical parameter for a value is a threshold beyond which an interferogram will display almost complete decorrelation. These values are dependent on the dataset being used. Typical values for ERS data in arid regions are $T^c = 5$ years, $B_\perp^c = 1100$ m and $F_{DC}^c = 1380$ Hz (HOOPER, 2006). We have disregarded the Doppler Centroid frequency term for the following reason. The ERS-2 satellite was launched using three gyroscopes and functioned in this mode until the year 2000, at which time, a new one gyroscope mode was implemented. Since the year 2001, the satellite has been running in a zero-gyro mode. The Doppler Centroid frequency term included in Equation (2) is meant to account for the effect that the evolution of these gyroscope modes has had on the SAR Doppler Centroid frequency (MIRANDA *et al.*, 2004). Because we are dealing with images prior to the year 2001, we are able to neglect this term in our calculations. A master is chosen that

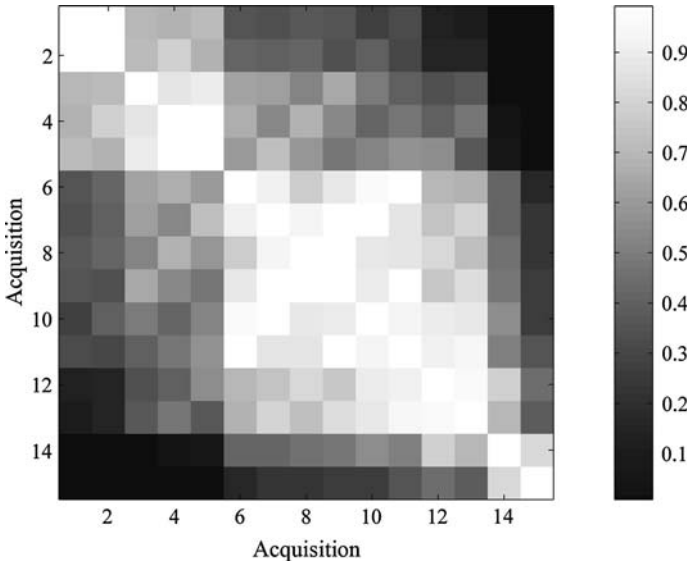

Figure 2
Theoretical coherence values for all combinations of individual interferograms using the Theoretical Cumulative Coherence model. The main diagonal containing high coherence values refers to the combination of interferograms with themselves and the highest values on this diagonal correspond with the master-master combination.

maximizes $\sum_{i=1}^{N-1} \rho_{\text{total}}$, assuming a constant value for ρ_{thermal}. Figure 2 shows the theoretical correlation values for each of the 15 interferograms using the TCC model. The main diagonal showing the highest theoretical correlation can be excluded as it is the master-master combination that cannot be used. Plotting the theoretical cumulative correlations for each master image (Fig. 3) shows that the images temporally centered in the database that have the highest theoretical correlations also have the highest theoretical cumulative correlations. These images are: image 6 = June 11, 1995; image 7 = August 20, 1995; image 9 = September 24, 1995; image 10 = December 4, 1995 and image 11 = January 8, 1996. From the TCC calculation, we have determined that the best images to use as master images are August 20, 1995 and December 4, 1995.

3.4. Preparation for Deformation Modeling

The analysis begins by coregistering all of the slave images with one master to find an optimal transformation model that will transform the slave images into alignment with the master. The second step is to resample all of the interferograms into the same size by processing them all with the same region of interest (ROI). In this case, the original images are of the full island and the ROI processed is the southern most part of the island. The phase that is present in these interferograms, ϕ, has eight components:

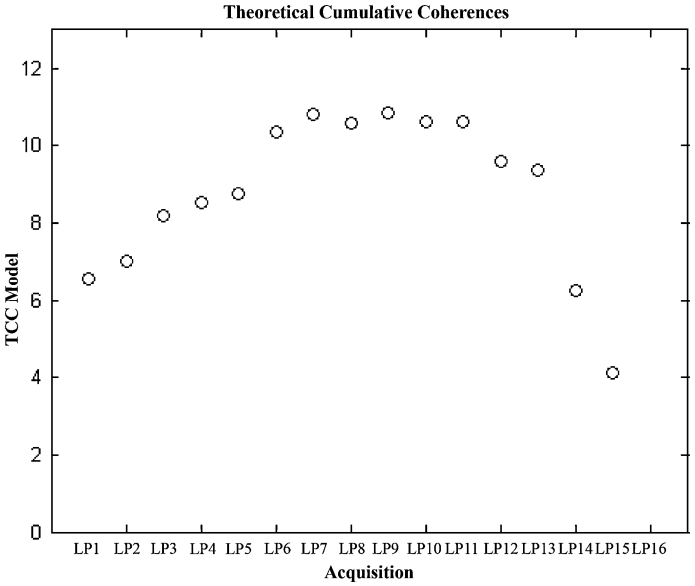

Figure 3
The theoretical cumulative coherences for each interferogram as a potential master image using the cumulative sum of the results from the TCC model.

$$\phi = \phi_{\text{geo}} + \phi_{\text{topo}} + \phi_{\text{atmos}} + \phi_{\text{offset}} + \phi_{\text{defo}} + \phi_{\text{dem\_error}} + \phi_{\text{noise}} + \phi_{\text{orbit\_error}} \quad (3)$$

The topographic phase, ϕ_{topo}, can be removed during the generation of differential interferograms by subtracting the phase of the external DEM. The flat earth phase, ϕ_{geo}, is removed using knowledge of the satellite positions. The slight difference in satellite position between two images ($\phi_{\text{orbit\_error}}$) produces a stereoscopic effect that can be removed by using using precise orbits calculated by TU Delft, Nederlands (SCHARROO and VISSER, 1998). Once these three components are removed, the typical components of a differential interferogram remain (ϕ_{diff}),

$$\phi_{\text{diff}} = \phi_{\text{defo}} + \phi_{\text{atmos}} + \phi_{\text{offset}} + \phi_{\text{dem\_error}} + \phi_{\text{noise}}. \quad (4)$$

For N images, there will be $N - 1$ differential interferograms. Therefore, there will be $N - 1$ phases, ϕ_i, where $i = 1, 2, \ldots N - 1$. ϕ_{defo} accounts for the path length difference due to surface motion that occurs at different satellite passes, ϕ_{atmos} represents phase changes due to variations in the atmosphere, ϕ_{offset} takes into account that there will be an offset introduced during interferometric processing, $\phi_{\text{dem\_error}}$ represents the residual phase that is introduced by the difference in position between the DEM elevation and the scatterer, and ϕ_{noise} is the residual phase error due to noise. To accurately depict the deformation that is occurring on the island, the deformation component, ϕ_{defo}, must be separated from the rest of the components.

4. Method 1: The Coherent Pixel Time Series Approach

High vegetation areas, characteristic of the North Atlantic subtropical islands with high topography, make differential radar interferometry more difficult because the vegetation causes the backscatter properties of the ground to change rapidly, causing the SAR pulses to reflect unequally over time resulting in a random component addition to the phase signal. Consequently, if an attempt is made to interpret decorrelated results produced by classical differential interferometry it could lead to a misinterpretation of the delayed differential phase. For this reason, we have applied a time series approach to the available SAR images that identifies the more reliable pixels based on a coherence threshold. The differential phase pattern of deformation is a relative measurement. Therefore, we can minimize the constant offset between interferograms to retrieve time continuous deformation information.

We have produced 15 independent interferograms using the *DORIS* software (KAMPES *et al*., 2003) implementing the two-pass differential interferometry method (MASSONNET and FEIGL, 1998). These interferograms have a 2:10 (range:azimuth) multi-look factor applied to them to gain coherence through spatial averaging. The topographic phase is removed from the raw interferograms using the SRTM3 Digital Elevation Model (DEM) and the stereoscopic effect is removed (derived from the perpendicular baseline) using precise orbits calculated by TU Delft, Nederlands (SCHARROO and VISSER, 1998). To remove the two-dimensional phase ambiguity (phase unwrapping), we used the average coherence ($\bar{\rho} = \frac{1}{N-1}\sum_{i=1}^{N-1} \rho_i$ with $i = 1, 2, \ldots, N-1$) on a pixel by pixel basis and substituted zeros for the complex values of the interferogram (phase/magnitude) associated with pixels that display low coherence (here, $\bar{\rho} < 0.35$) and then unwrapped the interferograms using the public software SNAPHU (CHEN, 2001). This selective rejection of pixels allows us to minimize the contribution of the low coherence areas (e.g. areas covering the sea and densely vegetated areas). Samples of unwrapped interferograms can be seen in Figure 4.

4.1. Removing Constant Offset

Differential interferograms produce a relative measurement, so we expect that the deformation data possess a constant offset for the whole interferogram that the unwrapping process cannot resolve. In order to estimate the time evolution of the deformation from the information contained in the differential interferograms, the constant offset must be removed from each one. It can be seen in Figure 5, that the coherence is low for most of the island. However, a large portion of the interferograms cover the sea which contains a large amount of random phase due to decorrelation. To deal with this decorrelation created by the water we want to refer all of the interferograms to an area known to be vertically stable.

To do this, a finite window taken about this stable region on the interferogram will be chosen. An average estimation of the phase value in a $n \times n$ finite window can be used to

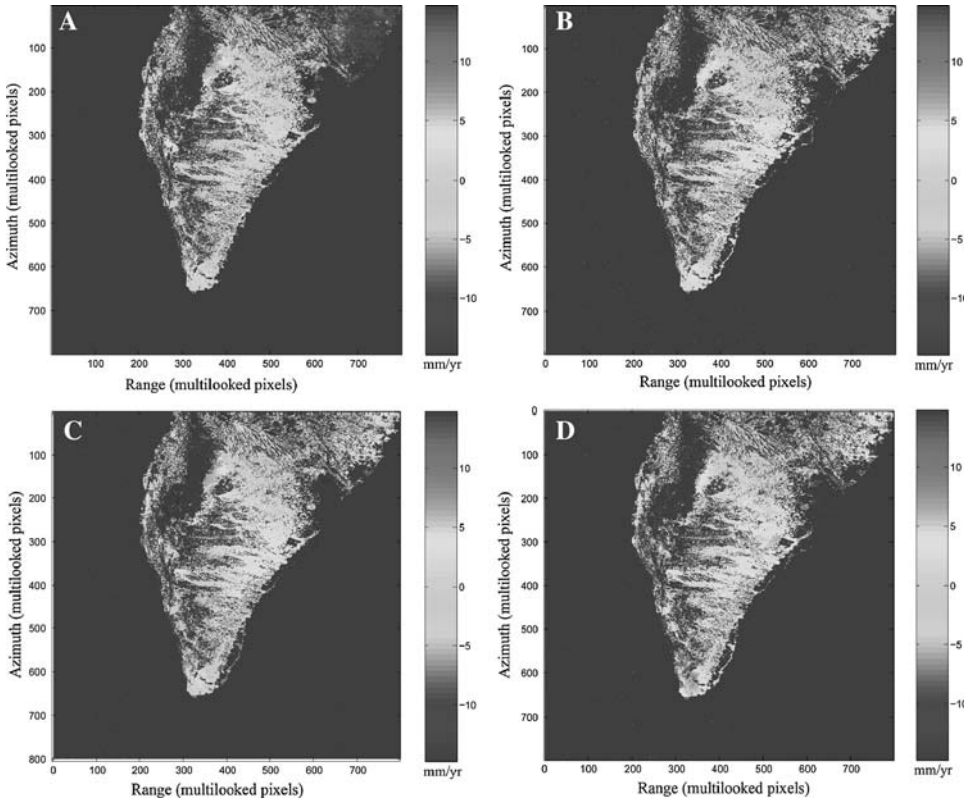

Figure 4

Unwrapped interferograms produced by the CPTS method with respect to the master image August 20, 1995. The dates for slave images used in each interferogram are as follows: A - May 29, 1992; B - September 9, 1996; C - October 14, 1996; D - June 21, 1999. For all images, the reference frame is in radar coordinates and deformation is presented in mm/yr.

approximate and remove the constant offset. Windows of different dimensions are considered to show the average offset values as a function of the window size, to determine how small a window can be and still be representative of the mean value that can be used to correct all of the interferograms. We test the mean value and standard deviations on the unwrapped phase inside 4 windows of variable size (10×10, 20×20, 30×30, and 40×40) and find that the 20×20 window has almost the same mean phase value as the 30×30 and 40×40 windows (Fig. 6). From this analysis, we determined that a 20×20 pixel window is a good representation of the real mean-offset value.

4.2. Estimation of the Linear Velocity

After removing the offset by addition or subtraction of the estimated phase value, we have an $N - 1$ time series. We transform these phase values to displacements in

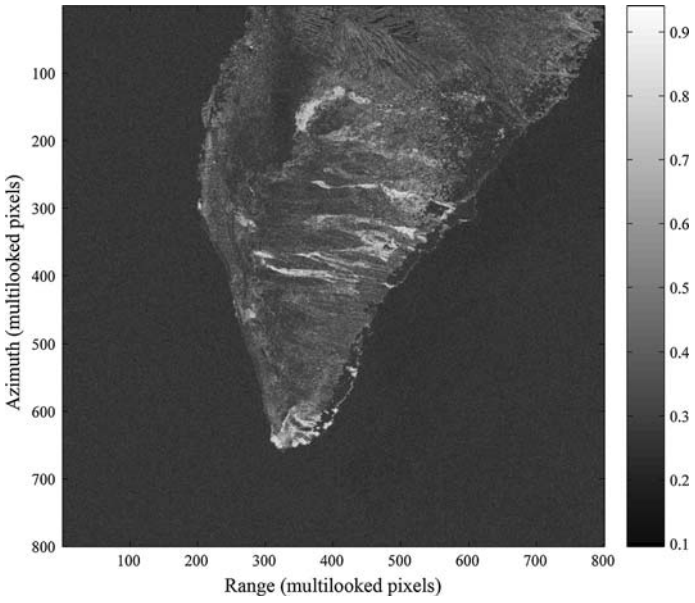

Figure 5
Average coherence for the 15 interferograms using August 20, 1995 as a master. The figure is represented in radar coordinates.

centimeters (using the knowledge of the carrier wavelength, for the ERS case $\lambda = 56.6$ mm). Using only 16 images, we are not able to distinguish the difference between nonlinear components due to atmospheric uncertainties and nonlinear components due to deformation. Consequently, we have only calculated an estimated map of the linear velocity of the displacement time series for the whole study area.

To estimate the linear velocity, we need to fit a line to our collection of displacement values. Let t be the independent variable and let $y(t)$ denote a linear function of t that we want to approximate. Assume there are $N - 1$ observations, i.e., values of $\hat{u}_{los}$ measured at specified values of t:

$$u_{losi} = y(t_i), \tag{5}$$

where $i = 1, 2, \ldots N - 1$. We want to model $y(t)$ using the equation,

$$y(t_i) = \beta_1 t + \beta_2. \tag{6}$$

To do this, we minimize the residuals using a least-squares method. We then estimate the linear velocity, by inverting to obtain the coefficients β_j (where $j = 1, 2$) of the simple linear model. After fitting the linear model we use the norm of the error to reject points with high values that can be determined as a poor fit to the model. We construct the estimated map of linear velocity by simply multiplying the slope (β_1) of the model by 365, to obtain an estimate in mm/yr. Two masks are then applied to the maps. The first

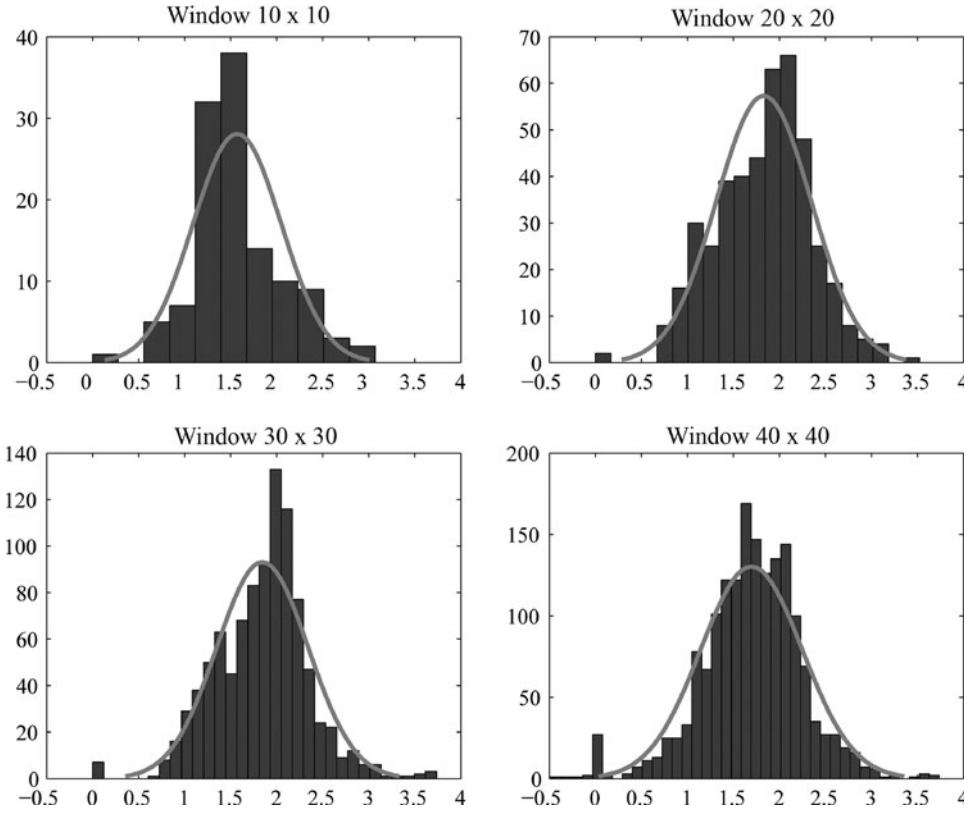

Figure 6
Histograms showing the constant offset estimation as a function of the window size. a) 10 × 10, b) 20 × 20, c) 30 × 30, and d) 40 × 40 (in pixels).

mask removes pixels below $\bar{\rho} = 0.35$ and the second mask removes the pixels that possess a high norm of errors (RMSError > 12 mm), under the assumption that these pixels do not contribute to the linear behavior with time. The results obtained here are presented in more detail in Section 6.

4.3. Error Estimation

As stated by KAMPES (2006), a model for the PS method is given by the equation,

$$\phi^k = \phi^k_{\text{topo}} + \phi^k_{\text{defo}} + \phi^k_{\text{atmo}} + \phi^k_{\text{noise}}. \tag{7}$$

Therefore, there are four separate terms that contribute independently to the reliability of the calculated differential phase (ϕ^k) for each interferogram k.

The residual topographic component (ϕ^k_{topo}) is present because the topographic phase that is removed from the interferogram is not exactly the same as the elevation read from the DEM, leaving a residual difference in elevation that will be added to the differential interferometric phase (RODRIGUEZ and MARTIN, 1992). To remove the topographic phase from the raw interferograms we have used the SRTM3 Digital Elevation Model (DEM), a global DEM released by NASA with a spatial resolution of 3 arcsec ($\approx$90 m) instead of estimating the errors as is done by FERRETTI *et al.* (2000; 2001) and HOOPER *et al.* (2004). This is done because the residual topographic phase is proportional to the perpendicular baseline and the SRTM3 DEM has relative errors of less than 7 m and absolute errors less than 16 m (FARR et al., 2007). Using the relation given by MASSONNET and FEIGL (1998), the cumulative sum of the perpendicular baseline for the La Palma images would be 1540 m (a cumulative error of 3.5 cm) over 27 years which translates to an error of approximately 1.8 mm/yr in linear velocity. This means we can have an error in the differential phase less than 1/2 of a half cycle in the *LOS* (MASSONNET and FEIGL, 1998). The contribution of this phase is also minimized by using multi-looked interferograms because in a multi-looked pixel, the phase value is the spatial average of many scatterers inside the pixel instead of a single point-like scatterer that could differ in altitude with respect to the reference DEM used to remove the topographic phase.

The deformation phase (ϕ^k_{defo}) is computed using a linear model and estimated least-squares method that produces a relatively small error in the estimated slope between 0.5–1 mm/yr. Validation of this model was also done by performing a robust regression on the data. The difference in the results between these two methods was less than 0.5 mm/yr.

The atmospheric phase (ϕ^k_{atmo}) is accounted for by applying an iterative robust regression to estimated the linear velocity from the interferometric phase time series. This acts as a time domain high pass filter, assigning lower weights to pixels that deviate significantly from the linear trend. Large residuals between the estimated model and the time series provide an additional parameter to assess the estimated linear velocity as they are used to mask pixels with high residual norms. Pixels with strong nonlinear behavior are most likely unwrapped poorly or contain significant atmospheric contributions.

The noise phase (ϕ^k_{noise}) is either due to changes in the dielectric constant due to moisture content or to the sensor noise and is assumed to be a second-order effect that is purely random and therefore is not explicitly treated here.

By assessing the cumulative contribution of all of these errors to the differential phase, it is evident that linear velocities larger than 3–4 mm/yr identified by the CPTS approach are reliable.

5. Method 2: Coherent Target Analysis

Coherent Target Modeling (CTM) was performed using commercial software developed by Atlantis Scientific Inc. version 3.1. CTM disregards the amplitude and uses

the phase stability of each pixel to determine its persistent scatterers. This is done by evaluating the temporal coherence (TC) of each pixel which is a measure of the stability of a scatterer over time. TC values tend to range between 0 and 1. More coherent pixels approach a TC value of 1 whereas incoherent pixels will tend towards a value of 0 (for further description see Equation (9)).

5.1. Deformation Model

The model begins by removing the atmospheric phase, ϕ_{atm}, and the offset, ϕ_{offset}. The phase is averaged over a 20 $\times$ 20 pixel window covering a stable region near the suspected deformation area and is used as an estimate of $\phi_{\text{atm}} + \phi_{\text{offset}}$. This estimate is then subtracted from the phase of the differential interferogram, ϕ_{diff}, resulting in $\phi_{\text{atm\_corr}}$,

$$\phi_{\text{atm\_corr}} = \phi_{\text{defo}} + \phi_{\text{dem\_error}} + \phi_{\text{noise}}. \tag{8}$$

To separate out the vertical surface deformation from the phase, an iterative procedure searches a range of velocities ($\pm\ \phi_{\text{defo}}$) and a range of DEM errors, ($\pm\phi_{\text{dem\_error}}$) for each pixel. The process begins by calculating ϕ_i to $\phi_{N\text{-}1}$ by subtracting ϕ_{defo} and $\phi_{\text{dem\_error}}$ from $\phi_{\text{atm\_corr}}$. The temporal coherence for each pixel is then calculated,

$$TC = \frac{\sqrt{\left(\sum_{i=1}^{N-1}\cos(\phi_i)\right)^2 + \left(\sum_{i=1}^{N-1}\sin(\phi_i)\right)^2}}{N-1}. \tag{9}$$

The pair of ($\phi_{\text{defo}}, \phi_{\text{dem\_error}}$) that produces the highest temporal coherence value for each iteration is used as an estimate for the deformation, ϕ_{defo}, and DEM error, $\phi_{\text{dem\_error}}$, respectively for each pixel.

To produce an enhanced image of the model, a second iteration of the procedure is performed using the temporal coherence threshold as a mask. At this point, the phase average used to remove the $\phi_{\text{atmos}} + \phi_{\text{offset}}$ is done over ϕ_{diff} using only those pixels that have a temporal coherence larger than the threshold. In each search window there must be a significant number of points with an appropriate value of temporal coherence for the average to be calculated, otherwise the average of the adjoining windows is used.

5.2. Specifics for La Palma

The processing for La Palma island was done using the Coherent Target Monitoring Panel software developed by Atlantis Scientific Inc. (Version 3.1). For coregistration, a minimum spatial overlap of 30% is defined and for both the range and azimuth, the minimum spectrum overlap is 50%. The search range for the deformation is $\pm$ 0.2 cycle/yr incremented in steps of 0.025 cycles/yr. The DEM error has a search range of $\pm$ 20.0 m with incremental steps of 1.0 m. The temporal coherence threshold used was 0.3.

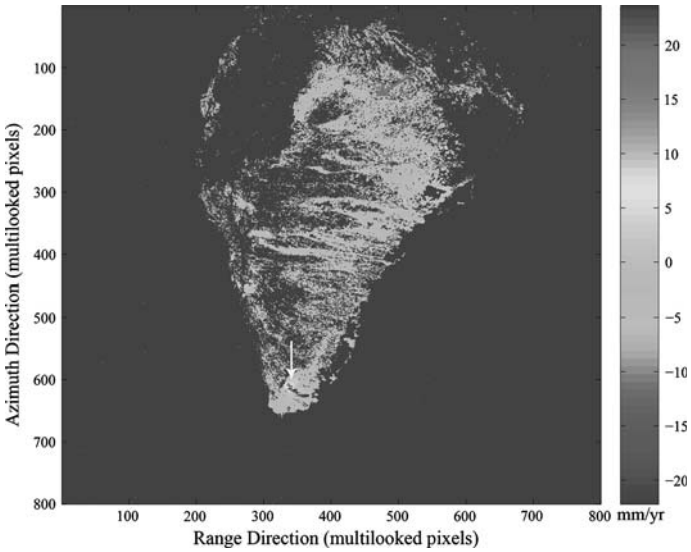

Figure 7

Map showing the estimation of the linear velocities for all of La Palma island determined by the CPTS approach. The deformation is presented in mm/yr using August 20, 1995 as a master image and is in radar coordinates. This image looks as if it has been flipped compared to Figure 10. This is due to the fact that this image is in radar coordinates and is therefore a mirror image of the geocoded image. Arrows represent the locations for the time series in Figures 12 and 13. The red arrow points to the stable location on the island used for constant offset removal and the white arrow points to the area of deformation around Teneguia volcano.

6. Results

An important feature to notice in the CPTS application to the entire island (Fig. 7) is the absence of deformation in the northern section affecting the Cumbre Vieja volcano in its entirety. There has recently been discussion of a potential detachment surface beneath this ridge that has the possibility to create a landslide (Moss *et al.*, 1999; Day *et al.*, 1999). Differential InSAR tends to be more sensitive to vertical motion, but will still detect a projection of the horizontal motion in the LOS. Generally, if the motion is directed E-W then approximately 35% of the magnitude of the horizontal motion will be detected and similarly if the motion is in the N-S direction then the signal will be approximately 5% of the horizontal motion's magnitude. Therefore, it is unlikely that our processing would not detect at least a fraction of the horizontal motion's magnitude if it were present. Having said this, we also recognize the fact that this area could potentially be inactive during this time period and suggest that future studies should be conducted to monitor this region for activity.

In the CPTS approach we have neglected to estimate the atmospheric terms using filtering as in Ferretti *et al.* (2000; 2001) or Hooper *et al.* (2004). This is done by filtering phase values in a certain time window to remove the presence of outliers from

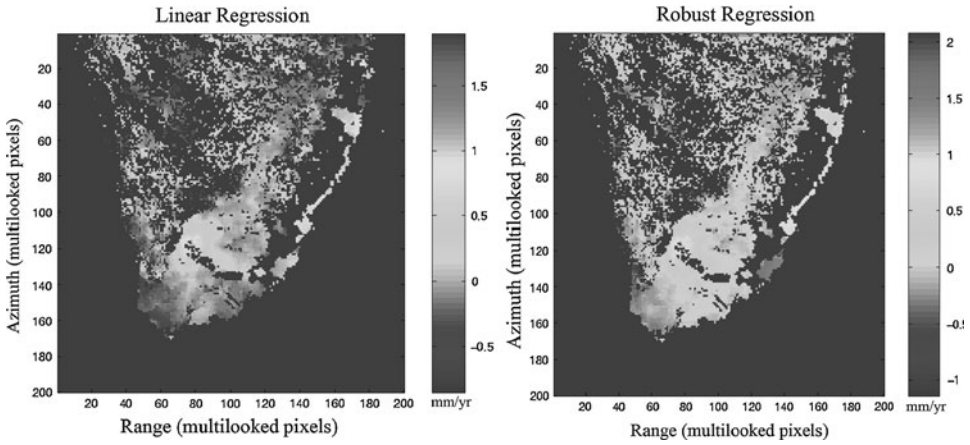

Figure 8

Left image is a map of the estimated linear velocity produced by the CPTS technique where deformation values have been fit using a linear regression. The image on the right represents estimated linear velocities produced by using a robust regression in the CPTS method. Both images are presented in radar coordinates and deformation is in mm/yr.

the actual deformation. To test if we were introducing a bias into the linear velocity by using a least-squares model (where all of the observations are weighted equally), we applied a robust regression to the same time series of phase values, and have found that the difference is negligible (Fig. 8). Therefore, we saw it as unnecessary to apply any time filtering using only 16 images.

In this method, it is the general trend of the time series being used to estimate the linear velocity that is important. When linear velocity is estimated in this way, the results show to be consistent with that of an independent method of stacking independent interferograms (Fig. 9).

Most importantly, the purpose of this paper is to present deformation that has previously not been identified by other InSAR techniques on La Palma island. There is a signal associated with this deformation in the southern part of the island (Figs. 10 and 11), where we observe a well-defined area of subsidence with a relatively high linear velocity. The time series associated with the deformation for the CPTS and CTM methods can be seen in Figure 12 and Figure 13, respectively. Comparing the results from the two techniques, there is a distinct, spatially consistent deforming area that defines a roughly circular shape with linear velocities of approximately -4 to -8 mm/year with a diameter on the order of 1 km centered on the Teneguia volcano (host of the last known eruption on La Palma in 1971). Classical interferometry methods have been unsuccessful at identifying any deformation on La Palma. Therefore, this is the first time that this deformation has been detected on La Palma using InSAR methods.

The signal is more easily identified using the results from the CPTS technique which could be due to the small number of SAR images used. It is suggested that a minimum of 30 images should be used for the best results with CTM (Atlantis Scientific Inc., 2004)

Figure 9

Stack of 5 independent interferograms with long time separation and small perpendicular baselines. Interferograms used are: 19920529-19950924 (1213 days; − 29.1 m); 19920807-19960108 (1249 days; 30.8 m); 19930723-20000726 (2509 days; 72.1 m); 19950611-19961014 (491 days; 21.8 m); and 19950821-19990621 (1400 days; − 14.7 m) where bracketed values are (time difference; perpendicular baseline). Linear velocity values are expressed in mm/yr.

Figure 10

Map showing the estimation of the linear velocities calculated using the CPTS approach for the southern part of La Palma island focusing on the region of deformation detected in Figure 7. The deformation is presented in mm/year using August 20, 1995 as a master image.

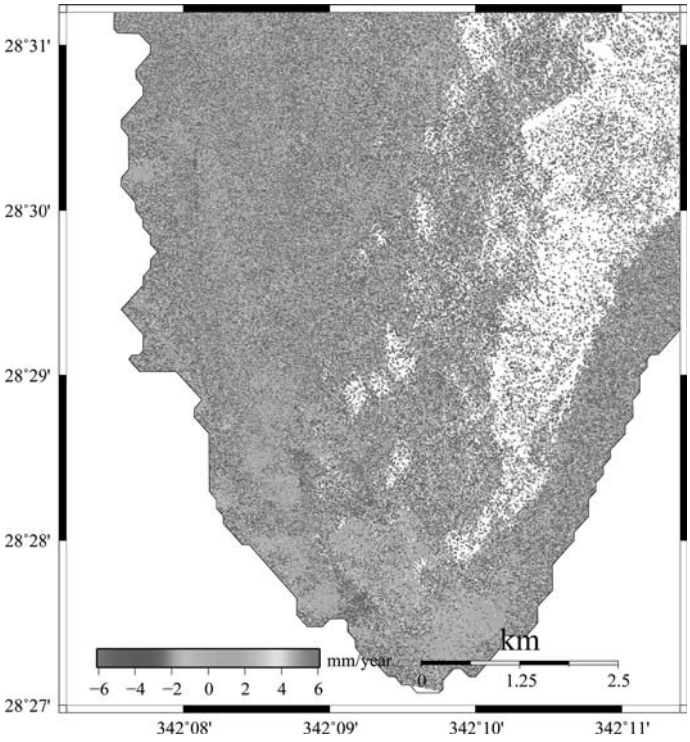

Figure 11
Map showing the estimation of the linear velocities calculated using the Coherent Target Modeling method for the southern part of La Palma island focusing on the region of deformation detected in Figure 7 using August 20, 1995 as a master image.

but due to a lack of images we were forced to process the data with only 15 images. Regardless of the noise due to this issue, a circular pattern comparable to that seen in the CPTS approach is still identifiable in the image.

7. *Discussion*

Water vapor is a major source of error when measuring ground deformation using differential interferometry (HANSSEN, 2001). In general, water molecules will absorb and reflect radar signals differently depending on their phase state (liquid, solid or gaseous) (SKOLNIK, 1990). Water vapor in the gaseous phase delays radar waves more than liquid drops or ice crystals, resulting in phase delays proportional to the number of clouds in the region. Due to the high topography in the Canary Islands we can distinguish three different layers in the lower troposphere: (1) A fresh and moist layer located below 700 m, (2) a thermal inversion layer between 700 m and 1500 m that prevents convection

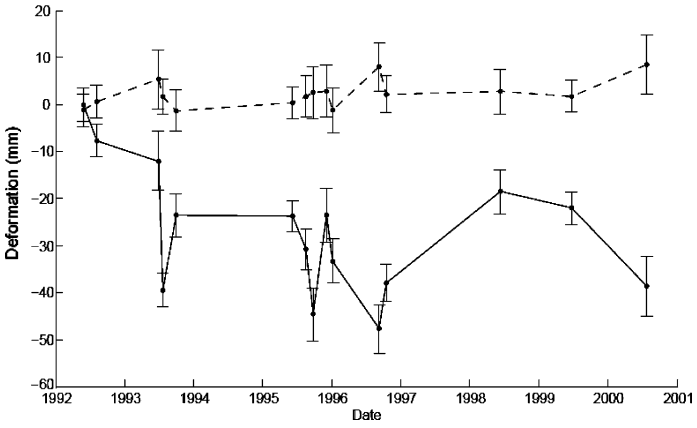

Figure 12

Time series produced for 2 separate pixels using the CPTS technique. Data connected by a solid line correspond to a pixel in the deforming Teneguia region represented by a white arrow in Figure 7 and data connected by a dotted line correspond to a pixel located in the stable area used to remove the constant offset represented by a red arrow in Figure 7. Errorbars are estimated as the standard deviation in the 20 × 20 pixel window and assigned for each date. Negative values indicate an increase in LOS.

of the water vapor, and (3) a higher dry layer above 1500 m (García Herrera *et al.*, 2001). Therefore, when interpreting differential interferograms for the whole island, vertical stratification and its presence over time should be taken into account. However, the Fuencaliente area where we have detected deformation is a smaller region located at a lower elevation and due to its size, we believe that it is too small to contain prevalent atmospheric signals, either from turbulent behavior of the water vapor or from a horizontal pattern that reflects the vertical stratification of the lower troposphere. Also, the effects of tropospheric water vapor on the velocity estimates are likely to be quite small as tropospheric water vapor is generally uncorrelated on the timescales of InSAR image acquisition repeat time. We can therefore, assume that the signal that is detected is due strictly to ground surface motion.

Possible sources for the deformation detected include gravitational loading from previously erupted material, withdrawal of magma from a shallow magma chamber, ground water removal, or a thermal anomaly. If the deformation were due to gravitational loading from erupted material, the signal should be similar to that of the size of Teneguia's cone. However, Teneguia's cone is approximately 500 m and the deformation detected here extends approximately 1 km horizontally. Likewise, the withdrawal of magma from a shallow magma chamber is usually simulated using deep point sources that generate vertical deformations that extend radially with a magnitude of approximately half the depth to the point source. Therefore, the withdrawal of magma from the chamber would be associated with a much larger signal than we are seeing here. Groundwater removal can be discredited as a source because there is no known aquifer in this

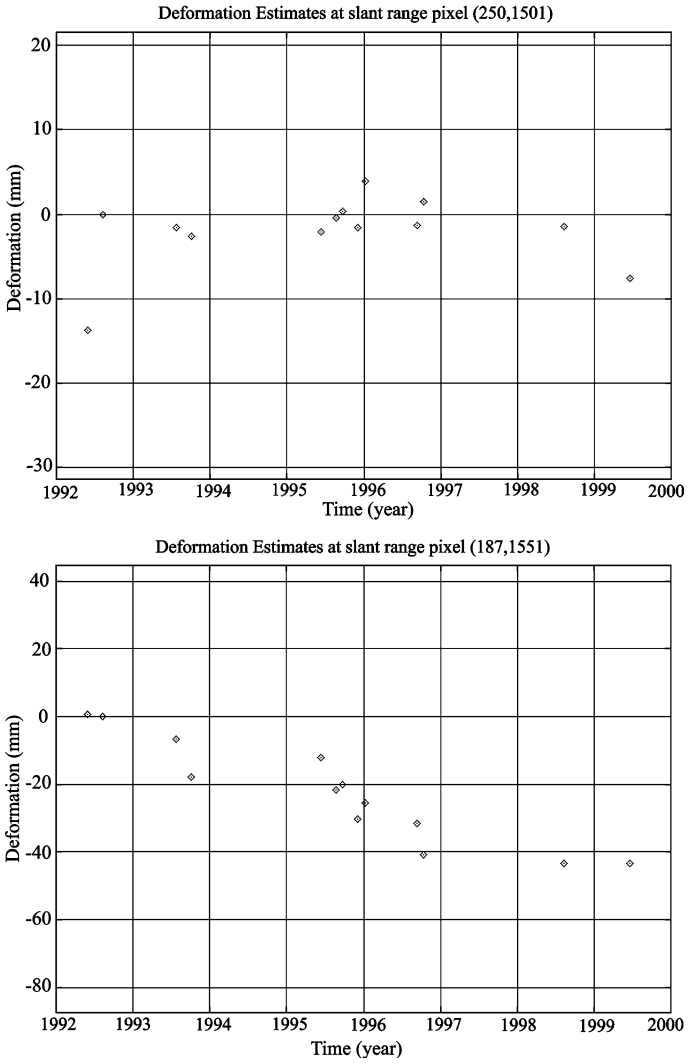

Figure 13

Figure 13A is the time series produced for a pixel in the stable region used for atmospheric corrections in the CTM approach taken from the area identified by the red arrow in Figure 7. Figure 13B is the time series produced for a pixel in the deforming area around Teneguia volcano determined by the CTM approach, represented by a white arrow in Figure 7.

region. However, La Palma island is known to have thermal anomalies with subsurface temperatures that exceed 300° Celsius (ABAD FERNÁNDEZ and SÁNCHEZ GUZMÁN 1985) and contains a recognized shallow depth Hot Dry Rock geothermal system (HDRS) in its southern part in the Fuencaliente region. In addition to this, to the southwest of the Teneguia volcano, the existence of a hot spring well at the base of the cliff has been

verified. This evidence leads us to conclude that a thermal source is the most likely possibility for this deformation.

8. Conclusions

Large advances have been made in the last decade in the study of radar interferometry as a geodetic tool. The technique has proven useful in volcanic areas to detect rapid displacements cause by shallow intrusions, as well as slow long-standing inflation-deflation processes in deep magmatic reservoirs. Despite these advances, the monitoring of natural terrains with dense vegetation can still be difficult and troublesome.

We studied an eight year period from 1992 to 2000 using data from the ERS-1 and ERS-2 satellites to create maps of the surface ground deformation on the densely vegetated island of La Palma. By applying two different InSAR phase analysis techniques (CPTS technique and CTM) we have detected a spatially consistent deforming area that defines a roughly circular shape with linear velocities of approximately -4 to -8 mm/year covering an area of ~ 1 km in diameter centered on the Teneguia volcano. We have also noticed that there is an absence of deformation (at the precision level of this study) in the northern region previously linked to a detachment surface beneath the Cumbre Vieja volcano. However, there is a possibility of inactivity in this area during the time period studied and suggest that future studies be done to continue monitoring this region for activity.

Classical interferometry methods have been unable to detect any deformation on La Palma because of difficulties due to the atmospheric interference, terrain and dense vegetation on the island. The methods presented here are limited by the small set of SAR images available and by the fact that the CPTS approach produces only estimates of the mean velocities. However, they have been successful over previous conventional differential InSAR methods because they have a higher sensitivity and a fine spatial resolution, allowing us to detect deformation at La Palma island for the first time using InSAR processing. Future research will involve acquiring more SAR images of the island and modeling the thermal anomalies causing deformation. These techniques can also be applied for the semi-continuous monitoring of large scale landslides and to obtain a better knowledge of the thermal ground deformation in the Fuencaliente area.

Acknowledgements

This research is part of the GEOMOD project funded by the Spanish Ministry of Education and Science (MEC) under contract (CGL2005-05500-C02). Data was kindly provided by ESA, in the frame of the Category-1 Project (ID:2679) and the DECIDE Volcano projects. Research by KFT was funded by an NSERC Discovery Grant. The work by PP was funded by a Province of Ontario Early Researcher Award. This research has also been partially supported by the Spanish Research Project PCI2006-A7-0660.

References

Abad Fernández, J. and Sánchez Guzmán, J. (1985), *Geothermal energy in the Spanish energy plan: Present status of the most advanced projects*, Geothermics *14*, 379–384.

Ancoechea, E., Hernán, F., Cendrero, A., Cantagrel, J. M., Fúster, J. M., Ibarrola, E., and Coello, J. (1994), *Constructive and destructive episodes in the building of a young Oceanic Island, La Palma, Canary Islands, and the genesis of the Caldera de Taburiente*, J. Volcanol. Geotherm. Res. *60*, 243–262.

Anguita, F. and Hernán, F. (1975), *A propagating fracture model versus a hotspot origin for the Canary Islands*, Earth Planet. Sci. Lett. *27*, 1119.

Anguita, F. and Hernán, F. (2000), *The Canary Islands origin: A unifying model*, J. Volcanol. Geotherm. Res. *103*, 1–26.

Araña, V. and Ortíz, R., *The Canary Islands: Tectonics, magmatism and geodynamic framework*. In *Magmatism in Extensional Structural Settings: The Phanerozoic African Plate* (eds. Kampunzu, A. B. and Lubala, R. T.) (Springer-Verlag, Berlin, 1991), pp 209–249.

Atlantis Scientific Inc., *EV-InSAR Version 3.1 User's Guide* (Atlantis Scientific Inc., Nepean, Ontario, 2004).

Banda, E., Dañobeitia, J. J., Suriñach, E., and Ansorge, J. (1981), *Features of crustal structure under the Canary Islands*, Earth Planet. Sci. Lett. *55*, 11–24.

Bravo, T. (1964), *Estudio Geológico y Petrográfico de la Isla de La Gomera*, Estudios Geológicos *20*, 93–108.

Carracedo, J. C., Day, S., Guillou, H., Rodríguez, E., Canas, J. A., and Pérez, F. J. (1998), *Hotspot volcanism close to a passive continental margin*, Geological Magazine *135*, 591–604.

Carracedo, J. C., Rodríguez-Badiola, E., Guillou, H., Nuez, J. D. L., and Pérez-Torrado, F. J. (2001), *Geology and volcanology of La Palma and El Hierro, Western Canaries*, Estudios Geológicos *57*, 175–273.

Chen, C. W. (2001), *Statistical-Cost Network-Flow Approaches to Two-Dimensional Phase Unwrapping for Radar Interferometry*, Ph.D. Thesis, Stanford University.

Dañobeitia, J. J. and Canales, J. P. (2000), *Magmatic underplating in the Canary Archipelago*, J. Volcanol. Geotherm. Res. *103*, 27–41.

Day, S., Carracedo, J. C., Guillou, H., and Gravestock, P. (1999), *Recent structural evolution of the Cumbre Vieja Volcano La Palma, Canary Islands: Volcanic rift zone reconfiguration as a precursor to volcano flank instability?*, J. Volcanol. Geotherm. Res. *94*, 135–167.

De La Nuez, J. (1984), *El Complejo Intrusivo Subvolcánico de la Caldera de Taburiente* (La Palma, Canarias), Ph.D. Thesis, Universidad Complutense de Madrid.

Farr, T. G., Rosen, P. A., Caro, E., Crippen, R., Duren, R., Hensley, S., Kobrick, M., Paller, M., Rodriguez, E., Roth, L., Seal, D., Shaffer, S., Shimada, J., Werner, J. U. M., Oskin, M., Burbank, D., and Alsdorf, D. (2007), *The Shuttle Radar Topography Mission*, Rev. Geophys. *45*, doi:10.1029/2005RG000183.

Fernández, C., De la Nuez, J., Casillas, R., and García-Navarro, E. (2002), *Stress fields associated with the growth of a large shield volcano (La Palma, Canary Islands)*, Tectonics *21*, 41–57.

Ferretti, A., Prati, C., and Rocca, F. (2000), *Nonlinear subsidence rate estimation using permanent scatterers in differential SAR interferometry*, IEEE Trans. Geosci. Remote Sens. *38*, 2202–2212.

Ferretti, A., Prati, C., and Rocca, F. (2001), *Permanent scatterers in SAR interferometry*, IEEE Trans. Geosci. Remote Sens. *39*, 8–20.

Fúster, J. M., Araña, V., Brändle, J. L., Navarro, J. M., Alonso, V., and Aparicio, A., *Geología y Volcanología de Las Islas Canarias: Tenerife* (Instituto Lucas Mallada, CSIC, 1968).

García Herrera, R., Gallego Puyol, D., Hernández Martín, E., Gimeno Presa, L., and Ribera Rodríguez, P. (2001), *Influence of the North Atlantic oscillation on the Canary Islands precipitation*, J. Climate *14*, 3889–3903.

Guillou, H., Carracedo, J. C., and Day, S. (1998), *Dating of the upper Pleistocene-Holocene volcanic activity of La Palma using the unspiked K-Ar technique*, J. Volcanol. Geotherm. Res. *86*, 137–149.

Hanssen, R. F., *Radar Interferometry: Data Interpretation and Error Analysis* (Kluwer Academic Publishers, Dordrecht, 2001).

Hildenbrand, A., Gillot, P.-Y., Soler, V., and Lahitte, P. (2003), *Evidence for a persistent uplifting of La Palma* (*Canary Islands*), inferred from morphological and radiometric data, Earth Planet. Sci. Lett. *210*, 277–289.

Hooper, A. (2006), *Persistent Scatterer Radar Interferometry for Crustal Deformation Studies and Modeling of Volcanic Deformation*, Ph.D. Thesis, Stanford University.

HOOPER, A., ZEBKER, H., SEGALL, P., and KAMPES, B. (2004), *A new method For measuring deformation on volcanoes and other non-urban areas using InSAR persistent scatterers*, Geophys. Res. Lett. *31*, L23611, doi:10.1029/2004GL021737.

KAMPES, B. M., *Radar Interferometry: Persistent Scatterer Technique*, Remote Sensing and Digital Image Processing Series (Springer Ed., Dortrecht, The Netherlands, 2006).

KAMPES, B. M., HANSSEN, R. F., and PERSKI, Z., *Radar Interferometry with Public Domain Tools*. In Proc. FRINGE 2003 Workshop, Frascati, Italy (2003).

KLÜGEL, A., HANSTEEN, T. H., and GALIPP, K. (2005), *Magma storage and underplating beneath Cumbre Vieja Volcano, La Palma (Canary Islands)*, Earth Planet. Sci. Lett. *236*, 211–226.

MASSONNET, D. and FEIGL, K. L. (1998), *Radar interferometry and its application to changes in the Earth's surface*, Rev. Geophys. *36*, 441–500.

MASSONNET, D. and SIGMUNDSSON, F., *Remote sensing of volcano deformation by radar interferometry from Various Satellites*. In *Remote Sensing of Active Volcanism* (eds Mouginis-Mark, P. J., Crisp, J. A., and Fink, J. H.), Geophysical Monographs *116* (Am. Geophys. Union, Washington, DC, 2000), pp 207–221.

MIRANDA, N., ROSICH, B., SANTELLA, C., and GRION, M., *Review of the impact of ERS-2 piloting modes on the SAR Doppler stability. In Proc. 2004 Envisat & ERS Symp., 6-10 September 2004*, Salzburg, Austria (ESA SP-572, April 2005) (2004).

MOSS, J., MCGUIRE, W., and PAGE, D. (1999), *Ground deformation monitoring of a potential landslide at La Palma, Canary Islands*, J. Volcanol. Geotherm. Res. *94*, 251–265.

NAVARRO, J. M. and COELLO, J. J., *Mapa Geológico del Parque Nacional de la Caldera de Taburiente* (ICONA. Ministerio de Agricultura, Pesca y Alimentación, 1993).

PÉREZ, N. M., WAKITA, H., NAKAI, S., SANO, Y., and WILLIAMS, S. N. (1994), ^{3}He/^{4}He *isotopic ratios in volcanic hydrothermal discharges from the Canary Islands, Spain: Implications on the origin of the volcanic activity*, Mineralogical Magazine *58A*, 709–710.

RODRIGUEZ, E. and MARTIN, J. M. (1992), *Theory and design of interferometric synthetic aperture radars*, IEE Proceedings-F *139*, 147–159.

ROMERO, C., *Actividad Volcánica Histórica en Las Islas Canarias*. In *Curso Internacional de Volcanología y Geofísica Volcánica* (Excmo. Cabildo Insular de Lanzarote, Lanzarote, Islas Canarias, 2000), pp 115–128.

SCHARROO, R. and VISSER, P. (1998), *Precise orbit determination and gravity field improvement for the ERS satellites*, J. Geophys. Res. *103*, 8113–8127.

SKOLNIK, M., *Radar Handbook* (McGraw-Hill Inc., 1990).

ZEBKER, H. A. and VILLASENOR, J. (1992), *Decorrelation in Interferometric Radar Echoes*, IEEE Transactions on Geoscience and Remote Sensing *30*, 950–959.

(Received May 14, 2007, revised May 4, 2008, accepted May 6, 2008)

Pure appl. geophys. 165 (2008) 1555–1575
0033–4553/08/081555–21
DOI 10.1007/s00024-004-0389-6

Pure and Applied Geophysics

Improvements to Remote Sensing Using Fuzzy Classification, Graphs and Accuracy Statistics

Daniel Gómez,[1] Javier Montero,[2] and Gregory Biging[3]

Abstract—This paper puts together some techniques that have been previously developed by the authors, but separately, relative to fuzzy classification within a remote sensing setting. Considering that each image can be represented as a graph that defines proximity between pixels, certain distances between the characteristic of contiguous pixels are defined on such a graph, so a segmentation of the image into homogeneous regions can be produced by means of a particular algorithm. Such a segmentation can be then introduced as information, previously to any classification procedure, with an expected significative improvement. In particular, we consider specific measures in order to quantify such an improvement. This approach is being illustrated with its application into a particular land surface problem.

Key words: Classification, fuzzy sets, fuzzy partition, multicriteria analysis, image segmentation.

1. Introduction

Remote sensing is a wide branch of science with tremendous development in the last several decades. Over two dozen optical satellites are currently in orbit doing earth imaging (see, e.g., Congalton and Green, 1999). Quite often, this systematic remotely sensed observation requires classification to improve interpretation.

Classification can be considered a useful representation in most of decision problems, simplifying information by means of an informative scheme of the main issues to be taken into account (see, e.g., Montero, 2004; Gómez *et al*., 2008a).

In this context, fuzzy sets play a very important role in many of those classification problems, since they allow one to model non-statistical imprecision that appears in the definition of classes (see, E.g., Kerre and Nachtegael, 2000; Matsakis *et al*., 2000; Pal *et al*., 2000; Petry *et al*., 2005).

But since the Earth's surface is amazingly complex, different and difficult preprocessing techniques should be applied before facing any classification problem.

[1] Escuela de Estadística, Complutense University, Madrid, Madrid (Spain). E-mail: dagomez@estad.ucm.es

[2] Faculty of Mathematics, Complutense University, Madrid (Spain). E-mail: monty@mat.ucm.es

[3] Department of Environmental Science, Policy and Management, University of California, Berkeley, CA, (U.S.A.). E-mail: biging@nature.berkeley.edu.

Some of them can be summarized in the following items (see, e.g., CONGALTON and BIGING, 1992; CONGALTON and GREEN, 1999 for details):

(1) **Sensor determination**: The choice of the sensor must be made taking into account the objects or classes of the study, in order to discriminate classes. Fuzzy sets theory appears in a natural way when the preferences and aims of the decision maker are modelled.
(2) **Management data and transformation**: Errors and fuzziness are often present in data acquisition processes. Furthermore, sometimes a reduction of the amount of information is needed when the image is extremely complex (for example more that 100 spectral bands).
(3) **Training site and pattern recognition**: In order to know the main features associated with each class, a previously unsupervised classification or expert classification is needed. Here the segmentation and non-supervised classification techniques (hard and soft) are the most common. In the following section a segmentation algorithm is presented as an alternative to solve this step.
(4) **Supervised classification algorithm**: This step ends with a classification (crisp or fuzzy) of the image. Each pixel or unit sample is classified into crisp or fuzzy classes, taking into account the information received from the training site.
(5) **Post classification**: In order to smooth the classification and improve the classification accuracy, some learning process will be needed. Some logical rules should be considered in order to improve and smooth results.
(6) **Analysis results**: Once classification and post-classification are finished, the accuracy of the process and classifiers must be determined. For example, by considering different agreement measures between the reference data set and the final classification. In recent research fuzzy sets have become an important tool in analysis of the accuracy of remote sensing classification.

This paper will focuss on the 1st and the 5th problems, leaving for future research the implementation of appropriate procedures for the remaining problems. In section 2 we establish the valued-fuzzy graph that will describe our image, and then we introduce a coloring algorithm in order to produce a segmentation of the image, which will be subsequently applied to the determination of training zones. In section 3 we introduce a class of accuracy measures based on a weighted Manhattan distance, so errors and performance of each classifier can be evaluated when the classification is not crisp and errors are not considered equal. Finally, in section 4 we apply all those techniques to a particular remote sensing image, showing how the segmentation produced by our coloring process improves the quality and accuracy of the evaluation with respect to a standard unsupervised algorithm.

2. *Segmentation of the Image*

As pointed out above, we are assuming that the image under study has been pre-processed, so we can proceed to the identification of homogeneous regions into the

image. These regions will allow the decision maker to identify training sites for further classification. The identification of homogeneous regions can be therefore associated with the *training site and pattern recognition step*. In fact, we realize that the first approach to an image is the identification of a few key relevant classes allowing a global explanation of the picture, not being too sensitive to discordant behavior of isolated pixels. Scene identification does not pursue an exact classification of each pixel, but the determination of those key concepts, usually associated with homogeneous regions.

As pointed out in GÓMEZ *et al*. 2007 and GÓMEZ *et al*. 2006 (see also MONTERO, 2004; GÓMEZ *et al*., 2008a), coloring algorithms should play a key role as a decision-making aid under fuzziness, in the same way they already play a key role within crisp approaches. Understanding a problem quite often requires a nice picture that reduces information but keeps the relevant structure of the problem. This approach implies a procedure for a sequence of classifications, each one subject to improvement depending on its accuracy and the decision makers is abilities to manage numerous levels of information.

The most common way to find homogeneous regions in remote sensing is to use an expert that analyzes and divides the image into regions. Although this approach is based on the experience of an expert, this methodology presents many inconveniences. One of them is that the remote sensing group may not have such an *expert* capable of segmenting the images. Thus, using an expert can be both economically and computationally expensive. For this reason, statistical methods are a common technique for determining homogeneous regions. Unfortunately, standard available statistical methods typically take into account only the spectral information of each isolated pixel, and do not consider the spatial information contained in the neighborhood of each pixel. In this way we can obtain clusters, but they may not represent the real classes in which the decision maker is interested. Consequently, there is an absolute need to include contextual information within those algorithms. With this aim, in this section we present a segmentation algorithm that takes into account spectral and contextual information of each pixel to find homogeneous regions in a remotely sensed image. In general, the goal of a segmentation algorithm is to simplify the image into a more meaningful and easier to analyze representation. In this paper, we propose the use of these techniques to determine the training sites, necessary in any supervised classification. The segmentation algorithm that we propose here was developed in GÓMEZ *et al*. 2007 and modified for the use of fuzzy information in GÓMEZ *et al*. 2006. This algorithm is based on the well-known coloring problem for graphs.

It is important to emphasize that there exists an absolute need to develop automatic processes to determine homogeneous regions in remote sensing images in order to improve the standard statistical methods. Quite often we do not have access to an expert, or the expert has incomplete knowledge of the study area or there are budget constraints limiting our ability to produce a meaningful segmentation. And in case such an expert is available, the information given by the segmentation algorithm here proposed could be taken into account to improve this knowledge.

2.1. The Model

As a first stage, we model the remote sensing image as a fuzzy graph where the nodes are crisp and the edges-links are fuzzy (see GÓMEZ *et al.*, 2006). Mathematically, a remote sensing image with k bands can be initially defined as a set

$$P = \{(i,j)/1 \leq i \leq r, 1 \leq j \leq s\}$$

of $r \times s$ information units -pixels-, where

$$p = (i,j) = \left(p^1, p^2, \ldots, p^k\right)$$

is the pixel associated with the coordinate (i, j).

In order to find homogeneous regions in the image, we consider this image as a planar graph (see again GÓMEZ *et al.*, 2006). The graph is planar in the sense that two pixels $p = (i, j)$ and $p' = (i', j')$ are not connected if $|i - i'| + |j - j'| > 1$ (see Fig. 1).

Fuzzy uncertainty appears when we consider a dissimilarity measure between these pixels. For example, in many instances the distance between two elements includes some lack of precision or ambiguity. In order to capture such a natural fuzzy uncertainty, and in order to give more flexibility to other already existing crisp classification procedures, we shall consider that a fuzzy distance (in the sense of KABVA and SEIKKALA, 1994) expresses the relation between the measured properties of pixels, $d : P \times P \longrightarrow [0, \widetilde{\infty})$, where $[0, \widetilde{\infty})$ is the set of fuzzy numbers with domain in R^+ (see DUBIOS and PRADE, 1980, for more details). We will denote by $\widetilde{d_{pp'}} = d(p, p')$ the fuzzy distance between the pixels p and p'. We will denote its membership function by $\mu_{pp'}$: $R^+ \rightarrow [0,1]$ and by $\widetilde{D} = \{\widetilde{d_{pp'}}/(p, p') \in P \times P\}$ we will denote its associated fuzzy distance matrix.

Hence, a basic distance has to be previously defined based on experience and objectives. A natural generic possibility is to consider an extension of the Euclidean distance into the fuzzy framework. For example, if we use symmetric triangle fuzzy numbers, then the *fuzzy Euclidean distance* could be defined as follows: $d(p, p') = (d - er, d, d + er)$, where

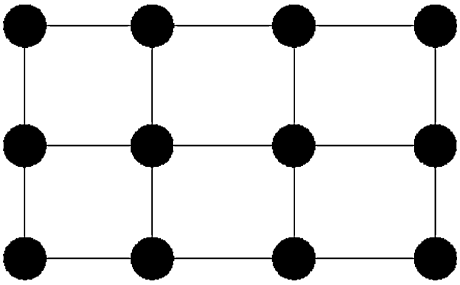

Figure 1
Planar graph with $r = 3$ and $s = 4$.

$$d = \sqrt{\sum_{k=1}^{b} (x_p^k - x_{p'}^k)^2} \quad \forall (p, p') \in P$$

is the deterministic Euclidean distance and *er* is the error measurement considered by the expert (see GÓMEZ *et al*., 2006 for more details). The membership function of the fuzzy number $(d - er, d, d + er)$ can be viewed in Figure 2.

Therefore, a fuzzy graph $\tilde{G} = (P, \tilde{A})$ is defined, $\tilde{A} = \{\widetilde{d_{pp'}}/(p, p') \text{ adjacents}\}$ where $\widetilde{d_{pp'}}$ are fuzzy numbers with domain in R^+. Some possible dissimilarity functions are given in GÓMEZ *et al*. 2006.

2.2. The Coloring Algorithm

The coloring algorithm for valued-fuzzy graphs we have proposed in GÓMEZ *et al*. 2006 is a sequence of binary coloring procedures. The first binary coloring analyzes the pixel's set P, coloring each pixel as 0 or 1. The second binary coloring is applied separately to the subgraph generated by those pixels colored as 0, to obtain the color classes 00 and 01, and to the subgraph generated by those pixels colored as 1, to obtain the color classes 10 and 11. This hierarchical process of binary coloring is repeated a number of iterations until the image segmentation is obtained. Hence, we consider as homogeneous any region or subset of pixels whenever these pixels are connected and have the same color. Once this algorithm is finished, the segmentation information can be included in any of the standard unsupervised classification algorithms, in order to improve the overall accuracy of classical algorithms that only take into account the spectral information of each pixel. The key to this segmentation algorithm is therefore the basic binary coloring process we apply to each step, and the result is a *grey* of gradation picture of the image.

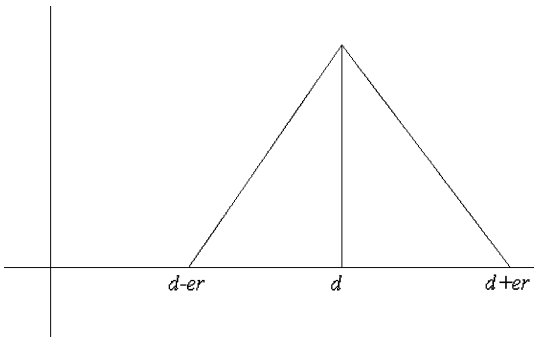

Figure 2
Membership function for a symmetric triangle fuzzy number.

2.3. The Basic Binary Coloring Algorithm

The basic binary coloring of a graph $G = (V, E)$ we shall sequentially apply to the image is a particular case of a 2-coloring, i.e., a mapping $col : V \to \{0,1\}$. According to such a basic procedure, two adjacent pixels are colored as 0 or 1 depending on the fuzzy dissimilitude between them, when compared with a prescribed threshold α (a procedure based on distribution percentiles is suggested in Gómez *et al.*, 2007). How to determine if a fuzzy number ($d_{(i,\ j),(i',\ j')}$ in our case) is lower or greater than a crisp or fuzzy number (α in our case) is a well-known problem in fuzzy sets theory that has been studied by many authors (see, e.g., Dubois and Prade, 1983; Facchinetti and Ricci, 2004). An interesting approach is to transform fuzzy numbers into real numbers by means of a ranking function (see Dubois and Prade, 1983).

Definition 2.1 *Let* $\aleph$ *be the set of fuzzy numbers and let* $a, b \in \aleph$. *Then* $a \mathrel{\widetilde{\geq}} b \longleftrightarrow F(a) \geq F(b)$.

Example 2.1 *Let a be a triangular fuzzy number in* $\aleph$. *We will identify a with the triplet* (a_1,a_2,a_3). $F_1(a) = \dfrac{a_1 + a_2 + a_3}{3}$, $F_2(a) = \sqrt{\int_0^1 g(t)}$ *where* $g(t) = (c_1 \quad + tc_2)^2 + c_3(1 - t)$, $c_1 = \dfrac{a_1 + a_3}{2}$, $c_2 = a_2 - \dfrac{a_1 + a_3}{2}$ *and* $c_3 = \dfrac{(a_3 - a_1)^2}{12}$, *are possible examples of ranking functions.*

Once we are able to compare two fuzzy numbers we can start with the coloring process. To define the first binary coloring round, a value α is fixed.

We can start, for example, with pixel (1,1) in the top-left corner of the image, so pixels can be colored from left to right and from top to bottom, in the following way:

$$col(i+1,j) = \begin{cases} col(i,j) \text{if } d((i,j),\ (i',j')) \mathrel{\tilde{\geq}} \alpha \\ 1 - col(i,j) \text{if } d((i,j)(i',j')) \mathrel{\tilde{\leq}} \alpha \end{cases} \quad \forall (i,j) \in \{1,\ldots r\} \times \{1,\ldots s-1\}$$

and

$$col(i,j+1) = \begin{cases} col(i,j) \text{ if } d((i,j)\ (i',j')) \mathrel{\tilde{\geq}} \alpha \\ 1 - col(i,j) \text{ if } d((i,j)\ (i',j')) \mathrel{\tilde{\leq}} \alpha \end{cases} \quad \forall (i,j) \in \{1,\ldots r-1\} \times \{1,\ldots s\}$$

Hence, given a colored pixel $p = (i, j)$, the adjacent pixels $(i + 1, j)$ and $(i, j + 1)$ can then be colored similarly if the distance $d((i, j), (i',j'))$ is lower than α. Otherwise, different colors are assigned to adjacent pixels.

However, since pixel $(i + 1, j + 1)$ can be colored either from pixel $(i + 1, j)$ or from pixel $(i, j + 1)$, both coloring processes may not produce the same color. When this occurs we refer to it as an *inconsistent* coloring (our binary coloring procedure is of course dependent on the particular order we have chosen for coloring).

For $i \in \{1,..., r-1\}$ and $j \in \{1,..., s-1\}$, $sq(i, j)$ will denote the square associate to the pixel (i, j), i.e $sq(i, j) = \{(i, j), (i+1, j), (i, j+1), (i+1, j+1)\}$. We will denote by PS the set of all squares defined in the fuzzy graph. The total number of squares of a given $r \times s$ image is $|PS| = (r-1)(s-1)$.

Definition 2.2 *Given a pixel's fuzzy graph* $\tilde{G} = (P, \tilde{A})$, *a square* $sq(i, j) = \{(i, j), (i+1, j), (i, j+1), (i+1, j+1)\}$, *for* $i \in \{1,..., r-1\}$ *and* $j \in \{1,..., s-1\}$, *is consistent at level* α *if given an arbitrary color* $col(i,j)$, *the above binary coloring procedure assigns the same color to pixel* $(i+1, j+1)$, *no matter if it is done from pixel* $(i, j+1)$ *or pixel* $(i+1, j)$. *Otherwise, the pixel square is inconsistent.*

Consequently, the above binary coloring of pixels depends on the chosen threshold value α, and we have two extreme cases:

$$\overline{\alpha} = \inf\left\{\alpha / \widetilde{d_{p,p'}} \mathrel{\widetilde{\leq}} \alpha \ \forall\ (p,p') \in P\right\},$$

and

$$\underline{\alpha} = \sup\left\{\alpha \ / \ \alpha \mathrel{\widetilde{<}} \widetilde{d_{p,p'}} \ \forall\ (p,p') \in P\right\}.$$

Hence, if we fix a threshold $\alpha > \overline{\alpha}$, then the whole picture is considered as a unique class, $col(i, j) = col(1, 1)\ \forall (i, j) \in P$. And in case $\alpha < \underline{\alpha}$, the picture looks like a chess board, because all adjacent pixels are alternatively classified as "0" and "1" (only the interval $[\underline{\alpha}, \overline{\alpha}]$ should be properly considered). Clearly determining an appropriate intermediate α level is not a trivial task.

Definition 2.3 *Given a value* α, *the pixel's fuzzy graph* $\tilde{G} = (P, \tilde{A})$ *is consistent at level* α *if all squares* $sq(i, j) \in PS$ *are consistent at level* α.

Definition 2.4 *Given a pixel's fuzzy graph* $\tilde{G} = (P, \tilde{A})$, *its consistency level, denoted as* α^*, *is the maximum value* $\alpha \in [\underline{\alpha}, \overline{\alpha}]$ *for which the fuzzy graph is consistent.*

Existence of such a consistency level α^* is always assured, at least while our image contains a finite number of pixels. If some inconsistency is detected for a certain value α, a decreasing procedure can be introduced in order to find a lower level α^* assuring consistency.

Since we anticipate the existence of quite a number of inconsistencies when dealing with medium or large size images, it may be the case that our decreasing search for α^* reaches the value $\underline{\alpha}$. In that event, the obtained segmentation is a trivial one, which looks like a chess board. Consequently, pixels cannot be properly colored. In order to avoid such a problem, it is necessary to allow some inconsistencies (in terms of some percentage, for example). However, since evaluating all inconsistencies is a computationally complex

problem, it is possible to approximate this percentage considering only the minimal cycles (in the sense of fewest number of edges), that is, cycles generated by four adjacent pixels. In this way we shall bound the percentage of *inconsistencies squares*.

At each iteration, let *ratio* be defined as the ratio of inconsistent squares of a binary coloring process, i.e., the number of inconsistent squares divided by the total number of squares subject to inconsistency. Large values of *ratio* are associated with a low number of color classes (the value α does not need to be decreased), although the greater this value *ratio*, the greater the number of pixels with a *wrong* color. Hence, we can look for some compromise between these two arguments. Such a compromise can be attained for small inconsistency ratios, lets say 0.01. Each inconsistent square should then be *isolated* so that its inconsistency does not induce inconsistency of adjacent squares.

The iterative binary coloring process is based on the pixel square set *PS*. These squares are arranged (left to right and up to down) and then analyzed.

The inconsistent squares must be appropriately managed in the sense that their pixels must be isolated in order to avoid contamination of adjacent squares; these pixels can be arbitrarily colored. Subsequent iterations will smooth the effects of such arbitrary coloring.

In order to avoid the exponential growth of computations, the number of binary partitions must be bounded again. Let us denote such a bound by m. Once the value of parameter m has been fixed, different values of α must be selected: Let $\{\alpha_{it}/it = 0,1, \ldots, it_M\}$ be the family of these selected values verifying $\overline{\alpha} > \alpha_0 > \alpha_1 > \cdots > \alpha_m > \underline{\alpha}$. The decreasing scheme of the coloring algorithm uses this sequence of values, with $\alpha = \alpha_0$ being the initial value. If for some value α the proportion of inconsistent squares is greater than a prescribed threshold *ratio*, the parameter α is updated to the next lower value.

It is clear that this process is strongly dependent on the α value selection (α_i) in each iteration. Of course, this selection is not a trivial task. If all selected values are close to $\overline{\alpha}$, we shall be able to identify only regions being very different. If we consider all values close to $\underline{\alpha}$, we will be sensitive to small variations and a noninformative segmentation will be given with too many regions. In order to discriminate in terms of similar size sets of pixels at each step, a possibility is to choose those α values taking into account quartiles of the distance distribution. In this way we can impose certain equilibrium in coloration, of course subject to the final goal of segmentation.

As in any representation technique, the tool presented in this section pursues a better understanding of the image (not a decision nor a proposal regarding the possible class). As pointed out in Gómez *et al.* 2008a, there is an absolute need for manageable descriptive tools in order to show fuzzy uncertainty. In fact, the information given by this algorithm can be included in different classical unsupervised classification methods in order to improve the training site description. Our particular claim here is that the hierarchical output we obtain offers a systematic sequence of colored images that can be carefully analyzed by decision makers for a more global understanding of the image (depending on their objectives and capabilities). In addition, different significative regions can give key information to improve unsupervised (or even supervised) procedures with low associated cost, as will be shown in the example below.

3. Accuracy Measures for Soft Classification

In order to show such an improvement, we had to solve the accuracy assessment issue, otherwise comparisons cannot be based on objective measurements. In fact, a key problem in remote sensing is that analysts often subjectively compare the quality of different techniques, algorithms or approaches. In this section we present a measure for the quality of a classification so an objective comparison between different solutions can be made.

As already pointed out, training sites have to be determined prior to classifying the image. Training sites are divided in two subsets. The first subset of pixels is used for the supervised/learning classification process, and the second subset of pixels is used to determine the accuracy measures of the classification (data reference set). The *true* or reference values for each pixel are determined by means of this training site. As anyone will expect, this step is very complex and there are several possible approaches, most of them requiring the final decision of an expert in charge of matching each sample to a well known class.

Moreover, it must be pointed out that although most approaches force experts to be crisp in their final classification, recent research considers fuzzy classes to be a more accurate solution (see, e.g., Driese *et al*., 2004; Laba *et al*., 2002; Woodcock and Gopal, 2000).

Regardless, even if the final classification is crisp or soft, it is necessary to compare the results obtained by the classifier with the reference data set. Most common measures compare the agreement between the classifier and the expert based on an error matrix (see, e.g., Congalton and Green, 1999).

In the crisp framework, the error matrix is built from the data reference set, which contains the classification given by the expert for some pixels, and the classification given by the classifier. The diagonal of such a matrix will represent the set of pixels in which the classifier and the data reference set coincide.

However, as pointed out by Congalton and Green (1999), standard accuracy assessment based on the error matrix cannot be directly applied when dealing with fuzzy classifiers or when the expert opinion is given in fuzzy terms.

In order to be able to assess the accuracy of fuzzy classifications, some approaches consider measures based on a linguistic scale of accuracy (see, e.g., Foody, 1999; Laba *et al*., 2002 for alternative solutions to the one developed in this paper). A standard approach, still useful within a fuzzy classification, is based on a fuzzy error matrix that generalizes the classical crisp error matrix. In particular, Binaghi *et al*. (1999) consider (for each pixel) the degree to which a pixel has been classified in class i by the classifier and in class j by the expert (by means of the *min* operator). A fuzzy error matrix is then obtained from this information. Then we can obtain the overall accuracy, the producer's accuracy and the user's accuracy for each pixel, to be normalized by the sum of membership degrees of the expert opinion (see Binaghi *et al*., 1999 for details).

With the same aim but with a different point of view, in this section we propose a new disagreement measure that takes into account a decision maker's preferences. Such a measure generalizes the classical measure for crisp experts and crisp classifiers in the case where the decision maker considers all errors equally important. Moreover, our proposal allows for the existence of fuzzy experts and fuzzy classifiers, without imposing a Ruspini's partition (Ruspini 1969) on the basic classification system (see Amo *et al.*, 2004).

3.1. Measuring Errors

From a mathematical point of view, a sampling unit (pixel) that has been classified by the expert (E) or by a classifier (C) into the class i, can be modelled as a k-dimensional vector $(0,...,1_i,...,0)$, where k represents the number of different classes under consideration. A classifier and a reference data set can be considered, respectively, as a function

$$E : P \longrightarrow H$$

and a function

$$C : P \longrightarrow H,$$

where

$$H = \left\{ x \in \{0,1\}^k \text{such that } \sum_i x_i = 1 \right\}.$$

Traditionally, for crisp classifications, if $E(p) \neq C(p)$ for a given pixel $p \in P$, we say that this pixel has been misclassified. From a mathematical point of view, this error can be expressed by means of a distance assigning a real value for each pair of vectors in H. Such an error takes value 0 if the pixel has been well classified, and value 1 if the pixel has been incorrectly classified (alternatively, Woodcock and Gopal, 2002 consider five possible linguistic values for the evaluation of such an error).

The error function also can be viewed as a disagreement function

$$D : T \subset P \longrightarrow R$$

that assigns a real value to each pixel in a subset of pixels T, randomly selected for the accuracy assessment. The problem is how an error function should be built allowing for decision maker's preferences and objectives.

Note that in the case of a fuzzy classifier we should assume the closed interval [0,1] instead of the binary value set {0,1}. More formally,

$$H = \left\{ x \in [0,1]^k \text{such that } \sum_i x_i = 1 \right\}$$

when we follow Ruspini's assumptions (Ruspini, 1969). Alternatively, we can take $H = \{ x \in [0,1]^k \}$ when we adopt the weaker approach developed in Amo *et al.* (2001) and Amo *et al.* (2004) (see also Montero *et al.*, 2007).

In order to assemble the main ideas above, let us introduce the following definition.

Definition 3.1 *Given a remote sensing image P, let us consider a family of classes* $A_1 \ldots A_k$. *Let E be the expert function and let C be the classifier function. Then the error D of pixel p given by the classifier C with reference data set E is defined as*:

$$D(E(p), C(p), p) = \mathrm{Min}\left\{1, \sum_{j=1}^{k} w_{ij} |E(p)_j - C(p)_j|\right\},$$

where $E(p)_j$ *is the j-*th *coordinate of* $E(p)$, $C(p)_j$ *is the j-*th *coordinate of the classifier function* $C(p)$, *i represents the class to which p is assigned the largest degree of membership*,

$$\mathrm{Max}\left\{(E(p))_{1 \le r \le k}\right\} = (E(p))_i$$

and each $w_{ij} \in \Re$ *represents the importance of the error when a sampling unit that belongs to class i is classified into class j*.

Notice that the above definition requires that the maximum in the $E(p)$ vector is unique. In case the maximum is reached in more than one component we will take the average of the different errors between these two pixels. Therefore, if we have, for example, $E(p) = (0.4, 0.4, 0.2)$ and $C(p) = (0.4, 0.4, 0.3)$, two different disagreement measures (depending on where the maximum is reached) can be defined: $0.1\ w_{13}$ if we take A_1 as the maximum and $0.1\ w_{23}$ if we take A_2 as the maximum. In this example, the definition for disagreement D that we propose is the average, that is $0.05\ w_{13} + 0.05\ w_{23}$. Taking this into account, the final disagreement will be Min $\{1, 0.05\ w_{13} + 0.05\ w_{23}\}$.

More generally, importance errors w_{ij} may depend on the whole vector $E(p)$, so its dispersion can be considered.

We note that if all errors are considered equally important ($w_{ij} = 1$ for all $i \neq j$ and $w_{ii} = 0$ for all i), and both classifier and expert are crisp, then the error function defined above coincides with the classical approach, i.e.,

$$D(E, C, p) = \begin{cases} 0 & \text{if } E(p) = C(p) \\ 1 & \text{if } E(p) \neq C(p) \end{cases}.$$

Note also that $1 - D(E, C, p)$ can be viewed as the agreement between the expert and the classifier for the classification of pixel p. Henceforth we will denote the agreement measure between expert and classifier by

$$A(E, C, p) = 1 - D(E, C, p)$$

Hence, the agreement measure defined here can be viewed as the dual of a (bounded) Weighted-Manhattan distance. We can therefore utilize standard distance properties such as symmetry ($A(E, C, p) = A(C, E, p)$ if $w_{ij} = w_{ji}$ and the max coordinate in E and C coincides).

Once the disagreement (agreement) function has been built, the standard accuracy measures (*overall accuracy*, *producer's accuracy* and *user's accuracy*) can be obtained by aggregating errors, as shown in the next section.

4. Accuracy Measures

In the previous section, an extension of the classical error was given. Once the error (agreement) function is obtained and the weights are determined, and following Gómez *et al*. 2008b, we can propose a new family of measures for the *overall accuracy*, the *producer's accuracy* and the *user's accuracy* by aggregating the error for each pixel.

Definition 4.1 *Given a remote sensing image P with classes* $A_1, \ldots A_k$, *the accuracy data set* $T \subset P$ *with cardinality t (the number of distinct elements of the finite set T), the reference data set E(p) for all* $p \in T$, *the classifier C, and the error D(E, C, p) for all* $p \in T$, *the producer's accuracy for a class* A_i *is defined as:*

$$P_{A_i} = \sum_{p \in T \text{ s.t. } \mathrm{Max}\left\{(E(p))_{1 \le r \le k}\right\} = (E(p))_i} \frac{A(E,C,p)}{n_{+i}}$$

where n_{+i} *is the number of sampling units which satisfy*

$$\mathrm{Max}\left\{(E(p))_{1 \le r \le k}\right\} = (E(p))_i$$

Definition 4.2 *Given a remote sensing image P with classes* $A_1, \ldots A_k$, *the accuracy data set* $T \subset P$ *with cardinality t, the reference data set E(p) for all* $p \in T$, *the classifier C, and the error D(E, C, p) for all* $p \in T$, *the user's accuracy for a class* A_i (P_{U_i}) *is defined as*:

$$P_{U_i} = \sum_{p \in P \text{ s.t. } \mathrm{Max}\left\{(C(p))_{1 \le r \le k}\right\} = (C(p))_i} \frac{(A(E,C,p))}{n_{i+}},$$

where n_{i+} *is the number of sampling units that satisfy*

$$\mathrm{Max}\left\{(C(p))_{1 \le r \le k}\right\} = (C(p))_i.$$

Definition 4.3 *Given a remote sensing image P with classes* $A_1, \ldots A_k$, *the accuracy data set* $T \subset P$ *with cardinality t (the number of distinct elements of the finite test set T), the reference data set E(p) for all* $p \in T$, *the classifier C, and the error D(E, C, p) for all* $p \in T$, *the overall accuracy* (O^C) *is defined as*:

$$O^C = \sum_{p \in T} \frac{1 - D(E,C,p)}{|T|} = \sum_{p \in T} \frac{A(E,C,p)}{|T|}.$$

Let us note that if the classifier produces a Ruspini's partition (i.e., $\sum_{i=1}^{k} C_i(p) = 1$, $\forall p \in T$*), and the expert is crisp, then the overall accuracy measure above defined coincides with the overall accuracy defined by* BINAGHI *et al.* (1999).

Proposition 4.1 *Given a digital image P with a large enough accuracy training site set* $T \subset P$*, E an expert classification that creates the data reference set for each pixel of T, and C a (fuzzy or crisp) classifier, if* p_0 *represents the expected value of the frequency of exact matches between the expert and the classifier for all classes, then the overall accuracy of the previous definition can be approximated by the Normal distribution*

$$N\left(\mu = p_0, \sigma^2 = \frac{p_0(1-p_0)}{t}\right).$$

Proof Fixed C and E, $D(C, E,.)$ or $A = 1 - D(C, E,.)$ can be viewed as a random variable for each $p \in P$. If the expected value of $D(C, E,.)$ is μ, then the expected value of $A(C, E,.)$ will be $1 - \mu$. Hence, $\hat{p_0} = \sum A(E, C, p)/t$ will be its random sample mean, and assuming independence between pixels, the result follows from the classical central limit theorem. ■

In case that, for example, $D(C, E,.) \in \{0,1\}$ (i.e., the crisp problem), $D(C, E,.)$ follows a Bernoulli distribution and μ represents the proportion of disagreement $1 - p_c$. For a more general case, μ (or $1 - p_c$) represents the mean error between the classifier C and the reference data E. For the random variable $A(C, E,.)$, $1 - \mu$ (or p_c) will represent the mean agreement between the classifier C and the reference data E.

4.1. Obtaining Weights

As it can be perceived from the disagreement measure given in definition 3.1, the weights that represent the importance of the different errors play an extremely important role. In the following two subsections we propose two alternative techniques in order to determine the importance of errors. The first one is based on a multi-criteria decision-making approach, and the second one is based on the distance between fuzzy sets.

4.1.1 A multi-criteria approach. It is a standard assumption in accuracy assessment that all errors are equally important. Introducing weights to account for the relative importance of errors will take into account the opinion of the expert, and therefore the main objectives of the study. As a consequence, a different weight matrix for each measure (producer, user and overall) is required.

There are different ways to obtain an appropriate weight matrix. If we are building the producer weight matrix, it can be imposed that all coefficients sum to $k(k - 1)$, as in the classical approach.

From a multi-criteria point of view there are several approaches available in order to determine weights (see, e.g., González-Pachon *et al.*, 2003a-b; Saaty, 1994). One of the most well-known methodologies is given by Saaty (1994). According to this approach, we obtain first the Saaty matrix (asking the decision maker to compare each pair of errors in order to define $w_{i,j}$ and $w_{i',j'}$, by means of linguistic values: 1– Same Importance, 3– Moderate Importance, 5– Strong Importance, 7– Very Strong Importance and 9– Extreme Importance, with 2,4,6,8 intermediate values). Once the Saaty matrix has been defined, the weights are computed as the eigenvector associated with the maximum eigenvalue (see Saaty, 1994).

4.1.2 Fuzzy distances. The classes of a remote sensing problem can be described in fuzzy terms by means of the spectral features of each class. Consequently, for each class A_i, and for each band B_r, we have the functions $\mu_{A_k}^{B_r}$. Considering that for each A_j we have $\left(\mu_{A_j}^{B1}, \ldots, \mu_{A_j}^{Bm}\right)$, a distance function between fuzzy sets could be applied for each pair of classes, $D(A_i, A_j) = d_{ij}$. On one hand, short distances d_{ij} represent a hight similitude between classes, thus errors will not be relevant. On the other hand, high values of d_{ij} represent different classes or major errors. Allowing for this information, the weights matrix could be calculated proportional to distance values.

5. Application to a Remote Sensing Image

This section will summarize and describe how previous processes can be aggregated in order to obtain a final fuzzy classification for further analysis. As pointed out, the classification process is complex and requires preprocessing. We want to emphasize how representation techniques can be useful for improving *training sites and the pattern recognition* step. Given a remote sensing image or digital image, we will briefly describe the interactive process proposed in this paper.

- The image is preprocessed in the sense described in the introduction. The ideal sensor is chosen and any necessary transformation of the date is made.
- After preprocessing with our methods, we model the remote sensing image as a fuzzy planar graph $\tilde{G} = (P, \tilde{A})$, where the nodes set P represent the pixels of the image. The link set $\tilde{A}$ is given by a matrix of fuzzy numbers, each one of them represents the dissimilarity degree between two adjacent pixels.
- Once the model is built, the coloring algorithm is applied to the fuzzy graph. This coloring process divides the set of nodes-pixels P into homogeneous regions R_k, in such a way that $P = \cup R_k$ and R_k are connected in the crisp graph $(P, \overline{P})$.
- The homogeneous regions determined in the above step, together with the information from the segmentation process, can be useful in improving standard non-classification algorithms. In particular, we apply here the non-supervised fuzzy classification algorithm suggested in Amo *et al.* (2004). This process begins with an initial fuzzy

classification given by the fuzzy *c*-means algorithm (see BEZDEK 1981; BEZDEK and HARRIS, 1978). This initial fuzzy classification can be improved using a learning algorithm that takes into account the concepts of relevance, redundancy and covering, previously defined in AMO *et al*. (2001). But this algorithm classifies each pixel without taking into account the spectral reflectance of neighborhood pixels. For this reason, we will combine the information contained in the above steps with the algorithm proposed in AMO *et al*. (2004). In particular, we modify the fuzzy *c*-means algorithm (considered in AMO *et al*., 2004 as the initial solution) keeping the two bigger homogeneous regions found in the segmentation process. After that, classification learning can follow the algorithm described in AMO *et al*. (2004). Other learning algorithms could be applied here as the given ones described in SEDANO *et al*. (2007).

5.1. A Particular Case

We apply our step process to a remote sensing image from Rio de Janeiro (coast of Brazil, see Fig. 3), producing a classification based upon a previous segmentation.

In order to compare the improvement introduced by our segmentation process, we begin with two different fuzzy classifications (Figs. 4 and 5). Figure 4 has been obtained by means of the classical *fuzzy c-means* algorithm (see BEZDEK 1981; BEZDEK and HARRIS 1978). We can observe that some pixels have been misclassified, most likely because this

Figure 3
Remotely sensed image of Rio de Janeiro.

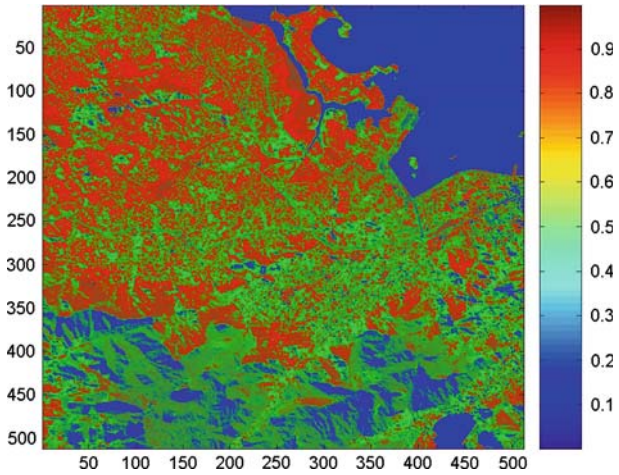

Figure 4
Classification by means of the fuzzy *c*-means.

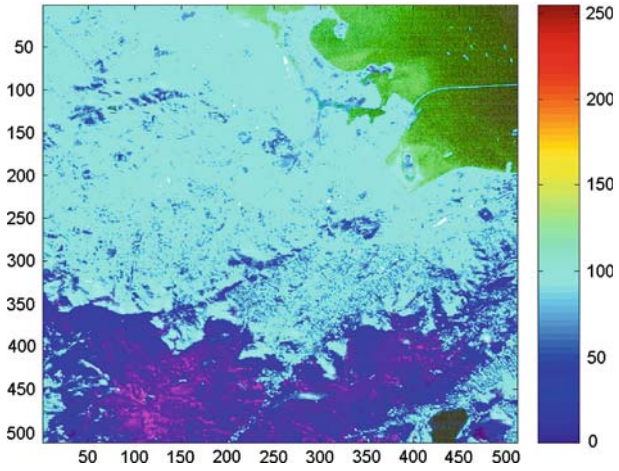

Figure 5
Fuzzy classification after segmentation.

classification does not take into account the information associated with the, surroundings of each pixel. The location of errors easily can be investigated by comparing Figure 4 with the fuzzy classification after segmentation (Fig. 5) or to the simplified crisp classification (see Fig. 6).

The second classification (see Fig. 5) results from applying our segmentation methodology previously to the fuzzy *c*-means classification. The segmentation process utilizes the coloring algorithm applied to the fuzzy graph. In this way, the information given by our segmentation process is taken into account, producing a fuzzy classified

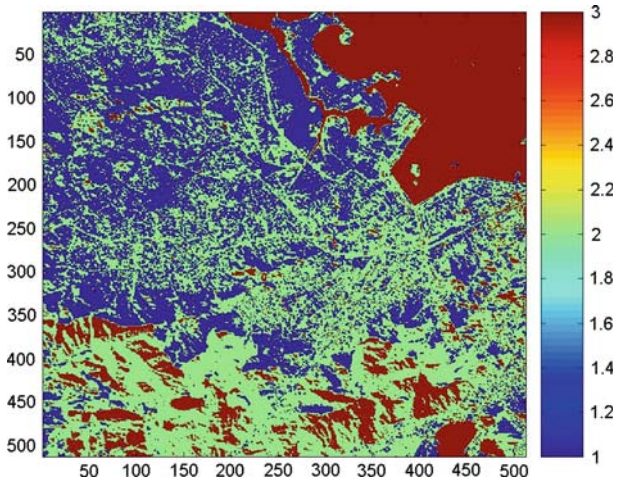

Figure 6
Crisp classification (fuzzy *c*-means).

picture in three classes, which is shown in Figure 5. From this fuzzy classification, a simplified crisp classification (Fig. 7) is analogously derived as before. Note the great analogy of Figure 7 to the first classification the human eye will most likely make when examing the image of Rio de Janeiro in Figure 3, distinguishing three main classes present in this picture: water, forest and urban area.

We also show below intermediate information that we can compare with both procedures. Degrees of membership in the three main classes obtained by fuzzy *c*-means is shown in Figure 8 that could be understood as a disaggregation of the Figure 4. High

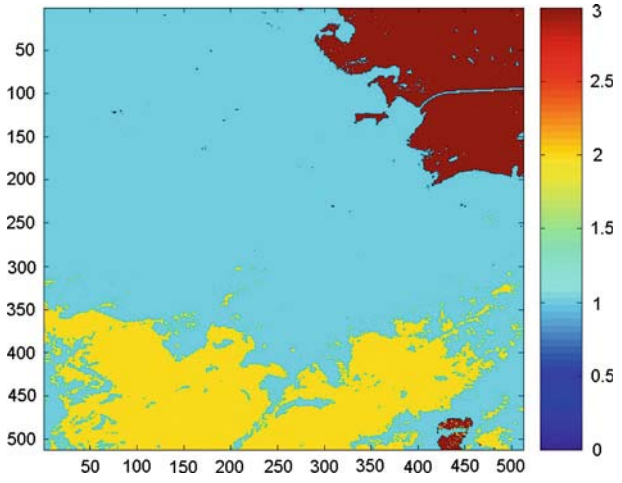

Figure 7
Crisp classification after segmentation.

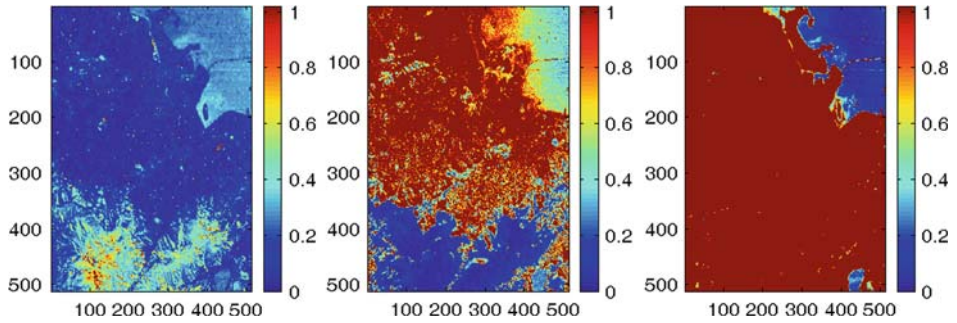

Figure 8
Degrees of membership of the three main classes given by the fuzzy *c*-means.

degrees of membership appear associated with dark tones (red in our original colored picture).

Although we present grey pictures here, it should be noted that their comprehension is not at all easy, even in their original colored version. Since both classifications are being made pixel by pixel, patterns are difficult to capture. The simplified crisp segmented image given in Figure 7 is indeed helping us to identify the existence of the three main classes explaining the image.

After producing our fuzzy classification and segmentation we are then ready to assess the accuracy of this image product. We can utilize previously introduced accuracy measures to quantify improvements between classification, and to get objective quality evaluations. For the crisp case, the two error matrix bellow represents the two classifiers.

Using the classical accuracy measures for the crisp framework, we find that for the crisp classification of Figure 7 obtained by our approach, the accuracy measure is 0.9813 (i.e., 9813% of the total data has been classified correctly). This result represents a clear improvement if compared with the crisp classification given in Figure 6, obtained by standard fuzzy *c*-means, where the total accuracy is 0.689.

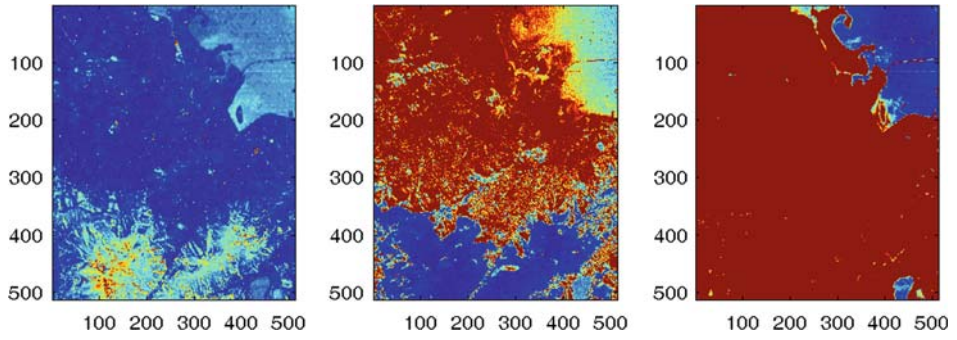

Figure 9
Degrees of membership of the three main classes given by our fuzzy classification.

Table 1

Confusion Matrix for classifier 1: Hard Classification

Confusion Matrix CE	E: Reference Class			
C: Classified	Forest	Wetland	Urban	Total
Forest	28003	6	9	28018
Wetland	4	19974	21	20000
Urban	1993	20	59970	61983
Total	30000	30000	40000	110000

Table 2

Confusion Matrix for classifier 2: Hard Classification

Confusion Matrix CE	E: Reference Class			
C: Classified	Forest	Wetland	Urban	Total
Forest	19917	0	24017	43934
Wetland	9000	19996	20	29016
Urban	1013	4	35963	36980
Total	30000	30000	40000	110000

Of course this comparison could be considered unfair, since both classifications we have considered (fuzzy *c*-means and fuzzy *c*-means with segmentation image information) are fuzzy, therefore classical accuracy assessment requires transforming the fuzzy classification into a crisp one. It is very important to observe that there are too many fuzzy or probabilistic classifiers that will have the same error matrix when they are transformed into crisp classifiers. So, we can conclude that the classical accuracy measures are not sufficient for determining if a fuzzy classifier is better than another fuzzy or crisp classifier.

The correct way to evaluate the fuzzy classifiers is with the accuracy statistics presented in Section 4. We find that, if all errors are considered equal for the three classes, then the fuzzy classification of Figure 5 obtained by our approach has an overall accuracy (Oc) of 0.8. This result represents a clear improvement too, if compared with the fuzzy classification given in Figure 4 and Table 2, obtained by the standard fuzzy *c*-means, where the overall accuracy (Oc)is 0.51.

Notice that we have assumed that all errors are of equal importance. Of course, other situations could be considered, depending on the main aim of the study. For example, if the objective is to discriminate between the *Forest* and the *Urban* classes, we could increase the weighting function for misclassification between these two classes. The new accuracy measures introduced in this work allow this alternative approach.

6. Final Comments

In this paper we have shown how an unsupervised classification procedure can be improved by means of a segmentation algorithm which utilizes fuzzy graphs and a

coloring algorithm. In this way we have produced a supervised classification procedure. Moreover, these improvements can be assessed by new accuracy statistics for judging soft classification which we have introduced.

Acknowledgements

This research has been partially supported by the Government of Spain, grant *TIN*2006 − 06190, together with a *Del Amo* grant from a joint programme between Complutense University and the University of California.

References

Amo, A., Gómez, D., Montero, J., and Biging, G. (2001), *Relevance and redundancy in fuzzy classification systems*, Mathware and Soft Computing *8*, 203–216.

Amo, A., Montero, J., Biging, G., and Cutello, V. (2004), *Fuzzy classification systems*, Europ. J. Operat. Res. *156*, 459–507.

Bezdek, J.C., *Pattern Recognition with Fuzzy Objective Function Algorithms* (Plenum Press, New York 1981).

Bezdek, J.C., and Harris, J.D. (1978), *Fuzzy partitions and relations: An axiomatic basis for clustering*, Fuzzy Sets and System *1*, 111–127.

Binaghi, E., Brivio, P.A., Ghezzi, P., and Rampini, A. (1999), *A fuzzy set based accuracy assessment of soft classification*, Pattern Recognition Lett. *20*, 935–939.

Congalton, R.G., and Biging, G. (1992), *A pilot study evaluating ground reference data collection efforts for use in forestry inventory*, Photogrammetric Engin. Remote Sensing *58*, 1669–1671.

Congalton, R.G., and Green, K. *Assessing the Accuracy of Remote Sensed Data, Principles and Practices* (Lewis Publishers, London 1999).

Driese, K.L., Reiners, W.A., Lovett, G.M., and Simkin, S.M. (2004), *A vegetation map for the Catskill Park, NY, derived from multi-temporal Landsat imagery and GIS data*, Northeastern Naturalist *11*, 421–442.

Dubois, D., and Prade, H., *Fuzzy sets and Systems, Theory and Applications* (Academic Press, New York 1980).

Dubois, D., and Prade, H. (1983), *Ranking fuzzy numbers in the setting of possibility theory*, Information Sci. *30*, 183–224.

Facchinetti, G., and Ricci, R.G. (2004), *A characterization of a general class of ranking functions on triangular fuzzy numbers*, Fuzzy Sets and Systems *146*, 297–312.

Foody, G.M. (1999), *The continuum of classification fuzziness in thematics mapping*, Photogrammetric Engin. Remote Sensing *65*, 443–451.

González-pachón, J., Gómez, D., Montero, J., and Yánez, J. (2003a), *Soft dimension theory*, Fuzzy Set and Systems *137*, 137–149.

González-pachón, J., Gómez, D., Montero, J., and Yánez, J. (2003b), *Searching for the dimension of binary valued preference relations*, Internat. J. Approx. Reasoning *33*, 133–157.

Gómez, D., Montero, J., Yánez, J., and Poidomani, C. (2007), *A graph coloring algorithm approach for image segmentation*, Omega *35*, 173–183.

Gómez, D., Montero, J., and Yánez, J. (2006), *A coloring algorithm for image classification*, Infor. Sci. *176*, 3645–3657.

Gómez, D., Montero, J., and López, V., *The role of fuzziness in decision making*, In *Fuzzy Logic: A Spectrum of Applied and Theoretical Issues* (eds. Ruan, D. *et al.*) (Springer 2008a) pp. 337–349.

Gómez, D., Biging, G., and Montero, J. (2008b), *Accuracy statistics for judging soft classification*, Internat. J. Remote Sensing, *29*, 693–709. DOI: 10.1080/01431160701311325.

Kabva, O., and Seikkala, S. (1994), *On fuzzy metric spaces*, Fuzzy Sets and Systems *12*, 215–229.

Kerre, E.E., and Nachtegael, M. *Fuzzy Techniques in Image Processing* (Physica-Verlag, Heidelberg 2000).

LABA, M., GREGORY, S.K., BRADEN, J., OGURCAK, D., HILL, E., FEGRAUS, E., FIORE, J., and DEGLORIA, S.D. (2002), *Conventional and fuzzy accuracy assessment of the New York Gap Analysis Project land cover map*, Remote sensing of Environ. *81*, 443–455.

MATSAKIS, P., ANDRÈFOUËT, S., and CAPOLSINI, P. (2000), *Evaluation of fuzzy partitions*, Remote Sensing of Environ. *74*, 516–533.

MONTERO, J., Classifiers and decision makers. In *Applied Computational Intelligence* (eds. Ruan D. *et al*.) (World Scientific, Singapore 2004) pp. 19–24.

MONTERO, J., GÖMEZ, D., and BUSTINCE, H. (2007), *On the relevance of some families of fuzzy sets*, Fuzzy Sets and Systems. *158*, 2429–2442.

PAL, S.K., GOSH, A., and KUNDU, M.K., *Soft Computing for Image Processing* (Physica-Verlag, Heidelberg 2000).

PETRY, F.E., ROBINSON, V.B., and COBB, M.A., *Fuzzy Modeling with Spatial Information for Geographic Problems* (Springer, Berlin. 2005).

RUSPINI, E.H. (1969), *A new approach to clustering*, Inform. and Control *15*, 22–32.

SAATY, T.L., *Fundamentals of Decision Making with the Analytic Hierarchy Process (RWS Publications, Pittsburgh (1994), revised in 2000)*.

SEDANO, F., GÓMEZ, D., GONG, P., and BIGING, G. (2008), *Tree density estimation in a tropical woodland ecosystem with multiangular MISR and MODIS data*, Remote Sensig Eviron., *112*, 2523–2537.

WOODCOCK, C.E., and GOPAL, S. (2000), *Fuzzy set theory and thematics maps, accuracy assessment and area estimation*, Internat. J. Geograph. Inform Sci. *14*, 153–172.

(Received May 4, 2007, revised April 2, 2008, accepted April 3, 2008)
Published Online First: October 29, 2008

Pure appl. geophys. 165 (2008) 1577–1602
0033–4553/08/081577–26
DOI 10.1007/s00024-008-0390-0

Pure and Applied Geophysics

Postseismic Deformation Following the 1994 Northridge Earthquake Identified Using the Localized Hartley Transform Filter

K. F. TIAMPO,[1] DAWIT ASSEFA,[2] J. FERNÁNDEZ,[3] L. MANSINHA,[1] and H. RASMUSSEN[4]

Abstract—Here we present a new mathematical tool, the localized Hartley (HL) transform (HARTLEY, 1942; BRACEWELL, 1990), that allows for the filtering of 1-D time series through the identification of the power at various spatial and temporal wavelengths. Its application to and the associated results are presented from its application to continuous Global Positioning System (GPS) data from southern California for the time period 1994 through 2006. The HL transform filter removes the high-frequency components of the data and effectively isolates the longer period signal. This long-period signal is modeled as time-dependent postseismic deformation using the viscoelastic-gravitational model of FERNÁNDEZ and RUNDLE (2004) for six stations selected for their proximity to the Northridge earthquake. The x-, y-, and z-components of the postseismic deformation are compared to the filtered data. Results suggest that this long-period deformation is a result of postseismic relaxation and that the HL transform filter provides an important new technique for the filtering of geophysical data consisting of the superposition of the effects of numerous complex sources at a variety of spatial and temporal scales.

Key words: Hartley transform, GPS time series analysis, spatio-temporal filtering, postseismic deformation, Northridge earthquake.

1. Introduction

Data assimilation is the process by which observations are incorporated into models to set their parameters, and to tune them in real time as new data become available. The initial steps in the process of data assimilation often involve performing complicated geophysical inversions for the underlying physical sources using geodetic or seismic data. The end result of the data assimilation process is a framework that is maximally consistent with the observed data, producing a model that is useful in ensemble

[1] Department of Earth Sciences, University of Western Ontario, N6A 5B7 London, Canada.
E-mail: ktiampo@uwo.ca
[2] Radiation Physics Department, Radiation Medicine Program, Princess Margaret Hospital, M5G 2M9 Toronto, Canada.
[3] Institutio de Astronomía y Geodesia (CSIC-UCM), Facultad de CC. Matemáticas, Ciudad Universitaria, Madrid, Spain.
[4] Department of Applied Mathematics, The University of Western Ontario, N6A 5B7 London, Canada.

forecasting. The idea is that the state of the model follows an evolutionary path through state space as time progresses, and that observations can be used to periodically adjust model parameters. One of the observations that potentially can be used to constrain large-scale models of the fault network in southern California is the horizontal and vertical deformation measurements produced by continuous GPS (CGPS) data.

The ability to incorporate CGPS data into models is limited by the difficulty in differentiating between the multitude of different geophysical signals in the aggregate geodetic measurement. For example, relatively large seasonal effects, including those with both annual and semiannual signals, can mask the small interseismic tectonic crustal deformation that concentrated CGPS networks are deployed to identify and quantify (The SCIGN Project Report to NSF, 1998; DONG *et al.*, 1998; 2002; WATSON *et al.*, 2002).

Here we show that the decomposition of CGPS data from southern California using a filtering technique based upon the application of an innovative mathematical transform can identify modes at particular spatial or temporal wavelengths whose sources then can be modeled appropriately. This technique, which is developed based on the the Hartley transform (HARTLEY, 1942), is similar to the Fourier based S transform (MANSINHA *et al.*, 1997a, 1997b; STOCKWELL, 2007), where a localizing window of varying widths is incorporated into the transform. The advantage of the localized Hartley (HL) transform is that it offers joint frequency-time information of signals with no complex arithmetic involved. Many operations such as convolution are simpler in the Hartley space than in Fourier space. The Hartley transform uses the same forward and inverse formulas and that is an added advantage in computing the HL transform conveniently using Hartley-based fast algorithms. Moreover, there is no redundancy in the Hartley transform, which the Fourier transform possesses, due to the hermitian symmetry. That makes the HL transform a very convenient tool in doing local signal analysis. In addition, while it is not of concern in this application, the Hartley phase (distinct from the Fourier phase) has no phase-wrapping problem, but the Fourier phase requires phase unwrapping algorithms to make the phase information useful (BELBACHIR *et al.*, 2003; CHILTON and HASSANAIN, 2006). Finally, while we do not use this particular property here, as a time-frequency representation that isolates local spectral phase properties, it combines a frequency-dependent resolution of the time-frequency space and absolutely referenced local phase information. This allows one to define the meaning of phase in a local spectrum setting. Here we illustrate the usefulness of the HL transform as a filtering technique by identifying and modeling time-dependent post seismic signal in CGPS data after the 1994 Northridge earthquake in southern California.

We begin by describing the Hartley transform and the implementation of the filtering methodology using a simplified localized Hartley transform with a scalable Gaussian window (section 2). We follow with a description of the CGPS network and associated data in section 3. The 1994 Northridge earthquake and the viscoelastic model that we employ to model the time-dependent postseismic relaxation signal from that event are

described in section 4. We provide examples of and results for the filtering technique on a particular subset of CGPS data in section 5. We also present a synthetic data analysis in which we apply the HL transform filter to time series formulated to replicate the historic GPS data, in order to evaluate the residual effects due to plate velocities and seasonal signals. Our conclusions are presented in section 6.

2. The Hartley Transform

The Hartley transform is an integral transform with a real kernel as opposed to the Fourier complex kernel (HARTLEY, 1942). It has been shown by many authors (BRACEWELL, 1990; BELBACHIR *et al.*, 2003; THEUSSL *et al.*, 2000; LEGRAND *et al.*, 1990; CHILTON *et al.*, 2006) that the real valued Hartley transform (HARTLEY, 1942) has several applications in different disciplines. With no complex arithmetic involved, the Hartley transform has both memory saving and speed advantages over the Fourier transform and its computational simplicity makes the Hartley transform more convenient in several signal and image analysis areas. The Hartley transform also has been successfully applied in local spectral analysis for time variant signals, with time-dependent frequency characteristics (LIU and LIN, 1993; PINNEGAR and MANSINHA, 2004). To that end, we present here a simplified localized Hartley (HL) transform with a frequency-dependent scalable Gaussian window in the analysis of CGPS data.

Many scientific data sets are contaminated with noise, either because of the data acquisition process or because of naturally occurring phenomena. Noise will contribute heavily to the high frequency components of the signal when it is considered in Hartley space. Thus if we reduce the high frequency components, we should reduce the amount of noise in the signal. The removal of noise from data to obtain the unknown signal is often referred to as denoising, and is usually done through time-domain filtering and frequency domain filtering, with tools such as the Fourier transform.

While these tools may be adequate for stationary data, where the signal component of the data is time-independent and the noise component is time-independent, for non-stationary data, where the frequency response of the signal varies in time or time-dependent noise components exist, joint time-frequency filtering may be more appropriate. The HL transform can be employed to accomplish this type of analysis.

The original Hartley transform (HARTLEY, 1942; BRACEWELL, 1986) of a function $h(t)$ is given by

$$H(f) = \int_{-\infty}^{\infty} h(t) cas(2\pi ft)\, dt, \tag{1}$$

where $cas(2\pi ft) = \cos(2\pi ft) + \sin(2\pi ft)$, t is time and f is frequency. The inverse of the Hartley transform is given by

$$h(t) = \int_{-\infty}^{\infty} H(f) cas(2\pi ft)\, df. \tag{2}$$

To formulate the HL transform, a given function of time $h(t)$ is multiplied by an appropriate window function and the Hartley transform of the product is taken. To derive the full expression, the original Hartley transform with a localizing window function is represented as (PINNEGAR and MANSINHA, 2004):

$$HL(f) = \int_{-\infty}^{\infty} h(t) w(t) cas(2\pi ft)\, dt, \tag{3}$$

where *w(t)* is a windowing function. Following STOCKWELL *et al* (1996), we chose a Gaussian window given by

$$w(t) = \frac{1}{\sigma\sqrt{2\pi}} e^{-t^2/(2\sigma^2)} \tag{4}$$

with the assumption that the window width $\psi\psi$ is inversely proportional to the frequency $f\psi$ for $f\psi 0$, and allow the Gaussian to be a function of translation ψ, then the localized Hartley transform (HL transform) is given by:

$$HL(\tau, f) = \frac{|f|}{|k|\sqrt{2\pi}} \int_{-\infty}^{\infty} h(t) e^{-(t-\tau)^2 f^2/(2k^2)} cas(2\pi ft)\, dt, \tag{5}$$

where k is a constant. The parameter k dictates the time-frequency resolution of the HL transform. A value of unity has been used in this study.

We can rewrite Equation (5) as the convolution of two functions,

$$HL(\tau, f) = A(\tau, f) * B(\tau, f), \tag{6}$$

where $A(\tau, f) = h(\tau) cas(2\pi\tau f)$ and $B(\tau, f) = \left(|f| / \left|k\sqrt{2\pi}\right|\right) e^{-\left(\tau^2 f^2/(2k^2)\right)}$, the Hartley transform of Equation (4) above with $\sigma = |k|/|f|$, for $f \neq 0$. For $f = 0$, $HL(\tau, 0)$ is defined to be independent of time and is equal to the average of the function $h(t)$

$$HL(\tau, 0) = \lim_{\alpha\to\infty} \frac{1}{\alpha} \int_{-\alpha/2}^{\alpha/2} h(t)\, dt. \tag{7}$$

If we take the Hartley transform (from τ to α) of both sides of Equation (6) and use the 1-D convolution theorem in Hartley space (BRACEWELL, 1986), we obtain

$$E(\alpha, f) = C(\alpha, f) e^{-2\pi^2\alpha^2 k^2/f^2}, \tag{8}$$

where E is the Hartley transform of $HL(\tau, f)$ and $C(\alpha, f)$ is the Hartley transform of $A(\tau, f)$, both from τ to α. The above simplification is possible because the Hartley transform of the Gaussian is an even function of τ. Hence the HL transform is the inverse Hartley transform (from α to τ) of E given by

$$HL(\tau, f) = \int_{-\infty}^{\infty} C(\alpha, f) e^{-2\pi^2\alpha^2 k^2/f^2} cas(2\pi\alpha\tau)\, d\alpha, \tag{9}$$

where $C(\alpha, f)$ is the Hartley transform of $h(t)cas(2\pi ft)$. Hence the HL transform can be computed using one forward and one inverse (which is the same as the forward) Hartley transform.

The global Hartley transform $H(f)$ of $h(t)$ can be recovered from $HL(\tau, f)$ through integration over τ

$$\int_{-\infty}^{\infty} HL(\tau, f) d\tau = H(f)$$

The original $h(t)$ can then be computed through the inverse transform of $H(f)$. Combining the two operations we get the following inversion formula.

$$h(t) = \int_{-\infty}^{\infty} \int_{-\infty}^{\infty} HL(\tau, f) cas(2\pi ft)\, d\tau df$$

If $h(t)$ can be written as a sum of the main signal component $d(t)$ and the noise component $\varepsilon(t)$ as

$$h(t) = d(t) + \varepsilon(t), \tag{10}$$

then due to linearity of the HL transform we can write

$$HL(\tau, f) = D(\tau, f) + E(\tau, f), \tag{11}$$

where D and E are the HL transform of the main signal and the noise, respectively.

Thus we want a filtering function $A(\tau,f)$ such that

$$\tilde{D}(\tau, f) = A(\tau, f) HL(\tau, f). \tag{12}$$

Remark: When the filtering function $A(f)$ is independent of τ, the above procedure reduces to the standard nonlocalized Hartley filtering. Hence, using the inversion formula, the denoised (primary) signal, $\tilde{h}(t)$, can be recovered using

$$\tilde{h}(t) = \int_{-\infty}^{\infty} \int_{-\infty}^{\infty} \tilde{D}(\tau, f) cas(2\pi ft)\, d\tau df = \int_{-\infty}^{\infty} \tilde{H}(f) cas(2\pi ft)\, df, \tag{13}$$

where

$$\tilde{H}(f) = \int_{-\infty}^{\infty} \tilde{D}(\tau, f)\, d\tau \tag{14}$$

Such time-frequency filtering is not possible with the standard nonlocalized Hartley (Fourier) transform as there is no temporal information available in the transform. Use of the Hartley-based localized filtering has two major advantages over Fourier-based transforms. Primarily, the forward and inverse Hartley transforms are identical, which makes the implementation handy. Moreover, no complex arithmetic is involved in that computation can be done efficiently, requiring more speed and less memory.

The discrete version of Equation (9) is given by

$$HL\left(jT, \frac{n}{NT}\right) = \sum_{m=0}^{N-1} C\left(\frac{m}{NT}, \frac{n}{NT}\right) e^{(-2\pi^2 k^2 m^2/n^2)} cas\left(\frac{2\pi jm}{N}\right), \tag{15}$$

where j, m, and n are discrete variables defining $\tau = jT$, $f = n/NT$, and $\alpha = (m/NT), n \neq 0$, and T is the sampling interval. The discrete Hartley kernel function *cas* has the following orthogonality property

$$\sum_{n=0}^{N-1} cas\left(2\pi n \frac{j}{N}\right) cas\left(2\pi n \frac{k}{N}\right) = \begin{cases} N, & j = k \\ 0, & j \neq k \end{cases}.$$

Hence, multiplying $HL(jT, n/NT)$ with the filtering function $A(jT, n/NT)$ will give the HL transform of the denoised signal. Using the inversion formula we arrive at a denoised signal:

$$\tilde{h}(jT) = \frac{1}{N^2} \sum_{j'=0}^{N-1} \sum_{n=0}^{N-1} A\left(j'T, \frac{n}{NT}\right) HL\left(j'T, \frac{n}{NT}\right) cas\left(\frac{2\pi nj}{N}\right), \tag{16}$$

where $\tilde{h}(jT)$ is the filtered signal.

The above formula corresponds to a column sum of $A(jT, n/(NT))$ $HL(jT, n/(NT))$ followed by application of the inverse Hartley transform.

For our purposes, the filtering function we employ for $A(\tau, f)$ is the low-pass Butterworth filter, as given by

$$A(\tau, f) = \frac{1}{1 + \left(\frac{f^2}{f_o^2(\tau)}\right)^p}, \tag{17}$$

where p is the order and f_o corresponds to the cutoff frequency. A number of different ranges of f were tested in an attempt to filter out uninteresting signals while isolating particular frequencies over certain time periods. In the following section, we apply this filtering technique to CGPS data in southern California for the years 1995 to 2006 in

order to study the longer wavelength postseismic deformation following the 1994 Northridge earthquake.

3. Data

The Southern California Integrated GPS Network (SCIGN) is a regional network of GPS stations that was originally installed in and around the Los Angeles basin for the purpose of measuring the response of the large, complex southern California fault system to regional strains, to identify localized, unknown fault features and sources such as blind thrust faults, to estimate earthquake potential, and to quantify the physical parameters of the fault system itself. Important work related to this continuous array includes the calculation of station velocities (The SCIGN Project Report to NSF, 1998), the estimation of coseismic and postseismic displacements relating to both the 1992 Landers earthquake and the 1994 Northridge earthquake and their aftershocks (Bock, *et al*., 1997; Donnellan, *et al.*, 2002; Hudnut *et al.*, 1996; Wald *et al.*, 1996), and the analysis of various error or noise sources (Zumberge *et al*., 1997; Dong *et al.*, 2002; 2006; Williams *et al*., 2004). However, much still remains to be accomplished toward the quantization of fault parameters and fault mechanics, and the identification and detailing of those local faults or events which are integral to the system but currently unidentified, such as blind thrusts. In addition, it has been difficult to study time-dependent motions such as viscoelastic response to local or regional strain. The large, complex nature of the fault network, the often obscure underlying dynamics, and their coupling with anthropogenic and natural signals also present in the data, precludes a simple analysis of its surficial expression (Watson *et al.*, 2002).

The first SCIGN stations were installed in 1991, and the network was expanded rapidly after the occurrence of the 1994 Northridge earthquake. While today the original network is managed by other organizations, including UNAVCO and USGS, there are over 250 stations throughout southern California, many of which are concentrated in the Los Angeles basin, and the data are available from the Scripps Orbit and Permanent Array Center (SOPAC) at www.sopac.org. Preprocessed data, where previously identified error sources have been removed upon acquisition, were obtained for this study, with repeatabilities of 1.2 mm latitude, 1.3 mm longitude, and 4.4 mm vertical (Zumberge *et al.*, 1997; Dong *et al.*, 2002; Williams *et al.*, 2004). This GPS data was filtered using the SOPAC refined model prior to download (Nikolaidis, 2002), in the ITRF 2000 reference frame and the offsets that are nongeophysical in origin were subsequently removed, based on offset files also available from SOPAC.

Stations within approximately fifteen kilometers of the 1994 Northridge event were identified and the data downloaded from the above website. HL transform filtering was applied to the data, as discussed above, for the purpose of filtering out the high frequency noise and to remove additional signals at moderate wavelengths, in order to better study the longer wavelength signal.

Table 1

Fault Parameters.

Layer thickness H (km)	Depth to Top of Fault h (km)	Fault Length L (km)	Dip θ (degrees)	Width w (km)	Strike φ (degrees)	Slip u (cm)	Center Latitude	Center Longitude
30	5	15	40	20	122	132	34.34N	118.50W

Values approximated from WALD and HEATON, (1997)
Poisson's ratio = 0.25

4. Postseismic Modeling of the 1994 Northridge Earthquake

The M $\sim$ 6.7 Northridge earthquake occurred on a previously unidentified blind thrust fault under the Ventura basin north of Los Angeles on January 17, 1994. The fault plane was well-constrained, southwest dipping, with a hypocentral depth of approximately 18 km (HUDNUT *et al.*, 1996; WALD *et al.*, 1996; DONNELLAN and LYZENGA, 1998). For this study we have used the fault parameters as determined by WALD *et al.* (1996) for the postseismic modeling, as shown in Table 1. Because of its sensitive location, several GPS stations were in operation in the vicinity. A simplified schematic of the fault plane and its relation to the CGPS stations used in this study is shown in Figure 1. Previous attempts to characterize the postseismic deformation have included modeling of aftershock related deformation, afterslip, and postseismic viscoelastic deformation, or some combination thereof (UNRUH *et al.*, 1997; DONNELLAN and LYZENGA, 1998; DONNELLAN *et al.*, 2002). Note that, in each of these cases, the regional deformation associated with plate motion both before and after the earthquake had to be modeled and removed from each station individually, providing the potential for incorporation of uncertainties associated with the individual stations, particularly in the case of shorter time series.

Here we apply the postseismic viscoelastic-gravitational model of RUNDLE (1982), updated in recent years by FERNÁNDEZ *et al.* (1996a, 1996b) and FERNÁNDEZ and RUNDLE (2004). This model solves the coupled elastic-gravitational problem of a point source thrust fault inserted into a layered earth model over a viscoelastic half space. Generally, the Green's functions for the elastic-gravitational field are computed, and then the Laplace-transformed viscoelastic solutions are calculated. The inverse transform is integrated over the finite source region to obtain the time-dependent viscoelastic deformations at various multiples of τ_a, the characteristic relaxation time $\tau_a = 2\eta/\mu$, where η is the viscosity and μ is the shear modulus of the half space. The most important feature of the model is the resulting time-dependent long-wavelength postseismic deformation field that is not seen in purely elastic earthquake fault models (FERNÁNDEZ *et al.*, 1996a, 1996b). Similar results were obtained by other authors for a layered spherical Earth (e.g., POLLITZ, 1997).

For the Northridge earthquake, the parameters shown in Table 1 were used in the viscoelastic fault model of FERNÁNDEZ and RUNDLE (2004). Here we use a single layer

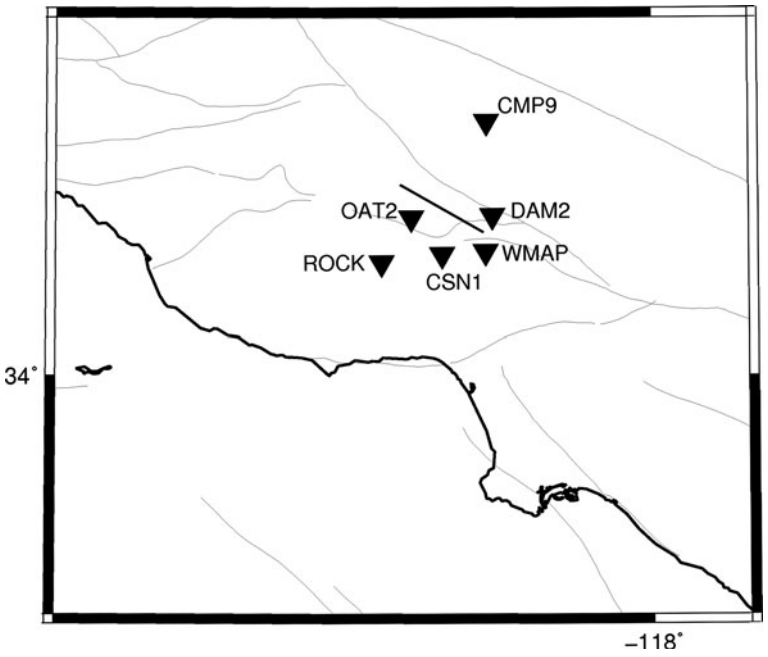

Figure 1
Approximate location of Northridge fault trace (red) and GPS stations used in this analysis.

over a viscoelastic half space, where the upper extension is as shown as in Figure 1. The model consists of a dipping thrust fault in a layered medium composed of a 30-km thick layer over an infinite half space, with a coordinate system as specified in RUNDLE (1981). Layer and half space densities are 3300 and 3800 kg/m^3. The elastic Lamé parameters of the half space are $\lambda = \mu = 3 \times 10^{10}$ Pa for both the layer and half space.

While the rupture plane and the crustal model are simplified here for the purposes of performing an initial analysis and comparison, the most important simplification is for the slip itself. This slip is modeled as entirely reverse, or up-dip, with no along-strike component to the motion. The resulting deformation is quantified in terms of multiples of τ_a, so that it was necessary to fit the results to the data filtered by the HL transform in order to determine the appropriate characteristic time for this event.

5. GPS Filtering with the HL Transform

The purpose of noise smoothing of this type is to reduce various spurious effects in the data, often of a high-frequency nature, perhaps caused by features such as noise in the data acquisition system, or noise arising as a result of transmission of the data. The data we acquire using the GPS techniques are no different. In most cases the data are

contaminated by high-frequency noise related to site effects such as monument motion or multipath, as well as longer wavelength regional anthropogenic or seasonal signals, and removing many of these effects remains a challenge (WATSON *et al.*, 2002).

There are two fundamental reasons for applying the HL transform to denoise the GPS signals. The first is to demonstrate the computational efficiency of using the HL transform in denoising, based on the efficiencies discussed above. While computational efficiency is not significant for six continuous GPS stations, as applied here, it can be a substantial effect for an entire network, or in the processing and analysis of remote sensing images such as InSAR. This particular algorithm is performed using convolution in Hartley space, which is more efficient when compared to other methods such as the wavelet or S transforms, and provides information on varying wavelengths in both space and time. The second is to filter the data in order to gain more insight into its various components at particular spatial and temporal wavelengths and thereby identify for analysis previously indeterminate geophysical signals such as postseismic relaxation.

Here we analyze GPS data sets recorded at CMP9, CSN1, DAM2, OAT2, ROCK, and WMAP, as shown in Figure 1. These time series include data that begins as early as 1995 and continues through the mid-2000s. The time series are then truncated to either 4096 daily data points or 2048 daily data points for analysis, depending upon the original length of the time series. In both cases the GPS data are given in the form of a time series along each spatial direction, x (north), y (east) and z (vertical). We apply the HL transform on each component separately.

Figure 2 shows the raw data for station CMP9. The linear trend that is the regional plate velocity is apparent in both the x-component (east-west) and y-component (north-south) signal. Prior to applying the HL transform this trend is removed by subtracting out a best-linear fit to the data. In addition, a seasonal signal exists in every component, and is most noticeable in the vertical component. The resulting HL amplitude spectrum for CMP9 is shown in Figure 3. Note the high frequency noise content present in all three components. However, signal exists at the mm to cm level in the lower frequencies as well. We applied a cutoff frequency, also shown in Figure 3, that corresponds to 512 days (4096 days/8 cycles), and only frequencies lower than that were inverted back to the time domain. Note that the annual tidal signal, visible on the vertical (z) component just above the cutoff frequency, is removed in this analysis.

It should be remarked that in the Hartley space the signal spectrum is computed by combining both the positive as well as the negative frequencies. This is an added advantage of Hartley based transforms over Fourier based transforms, in that there is no redundancy in the Hartley space which the Fourier transform possesses due to the hermitian symmetry.

For example, the amplitude of the *HL* transform is given by

$$|HL(\tau,f)| = \sqrt{HL(\tau,f)^2 + HL(\tau,-f)^2}, \text{ for f} \in (0, \infty).$$

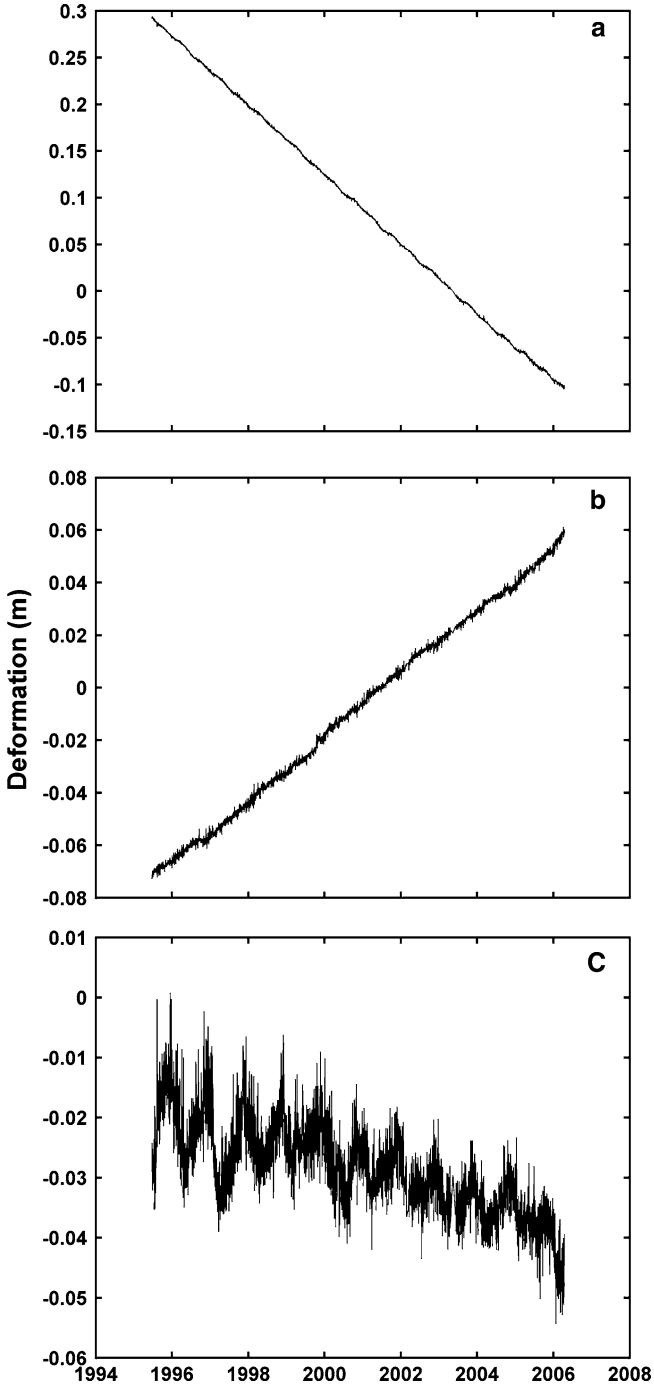

Figure 2
GPS time series for CMP9 (Fig. 1), obtained from SOPAC after regional filtering (http://sopac.ucsd.edu). In a) is shown the x-component, b) is the y-component, and c) is the z-component.

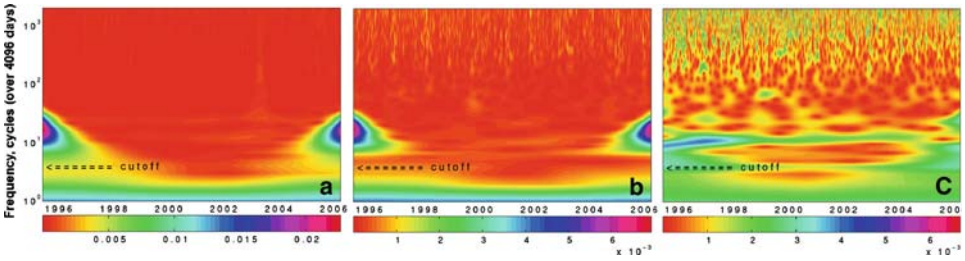

Figure 3
Logarithmic plot of the localized Hartley spectrum for the GPS time series of station CMP9 (Figs. 1 and 2), where a) is the x-component, b) is the y-component, and c) is the z-component. Color bars are amplitude spectrum at the given wavelength and time, in meters. The frequency cutoff used for filtering is noted in black.

The same formula applies in the discrete case where we only have to replace $(-f_n)$ by $(N - f_n)$, where $(-f_n)$ is the n^{th} discrete frequency.

In order to study the postseismic signal, the data were filtered such that all signal above a particular cutoff was removed from the data, using the technique described above, and after examination of the individual spectra. Again, the cutoff was at a temporal wavelength of 512 days for all stations. The HL transform filtered signal for CMP9 is shown in Figure 4. The first item to note is that, while the seasonal signal has been reduced in all three components, it is still recognizable, particularly in the z-component. However, there remains a longer wavelength time-dependent signal after the removal of the higher frequencies.

In discrete space the HL transform suffers from edge effects due to sampling, finite lengths, and the convolution operation. In order to reduce these, we utilized a two step mechanism. The first is to pad the discrete data with a slowly decaying function. After that we applied a 5% hanning window taper (STOCKWELL, 1999) to smooth out the edges. These operations cannot remove the total effect, however, and the residual temporal extent varies from six months to one year.

6. Results and Discussion

The viscoelastic model, detailed above, is superimposed on the HL filtered results in Figures 5 through 10. This simplified model, developed here in order to provide a baseline comparison in order to test whether the HL transform is capable of isolating long-wavelength time-dependent geophysical signals in continuous GPS data, provides a good fit to the temporal wavelength at a $\tau_a = 1.5$ years (Table 1). For each station, it was necessary to provide an offset in each of the x-, y-, and z-components of the deformation, in order to account for the local coordinate system associated with each station. The offsets that provide the best fit to these data are shown in Table 2. Also

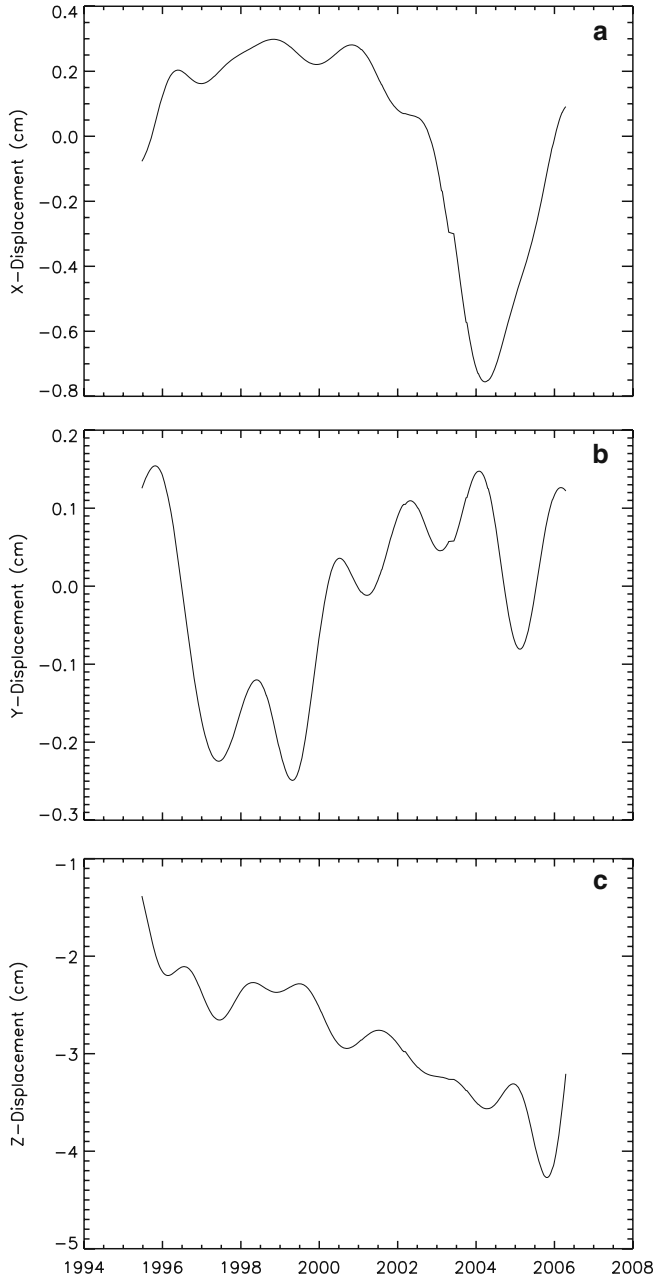

Figure 4
Denoised GPS time series for CMP9, where the additional filtering is performed using the Hartley transform of Figure 3. In a) is shown the x-component, b) the y-component, and c) the resulting z-component.

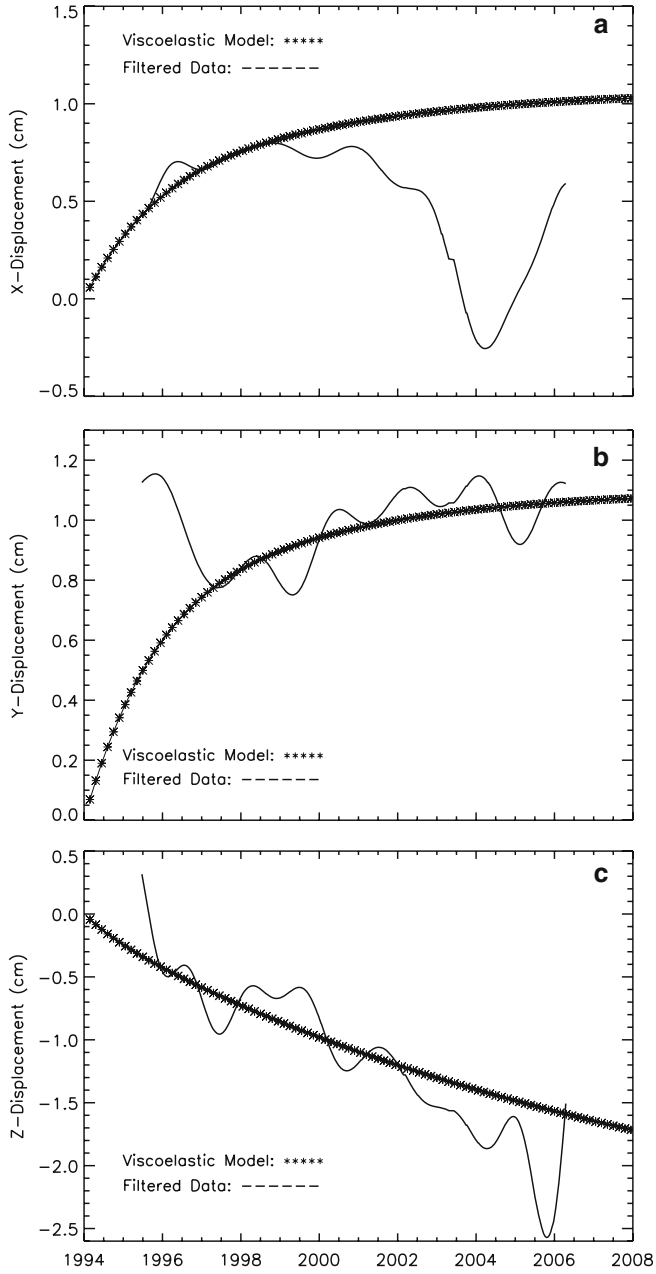

Figure 5

Comparison of filtered GPS time series for CMP9 and viscoelastic model (FERNÁNDEZ and RUNDLE, 2004), for $\tau_a = 1.5$ years. a), b), and c) show x-, y-, and z- displacement, respectively, in cm. Fault parameters are given in Table 1; modeled offsets are given in Table 2.

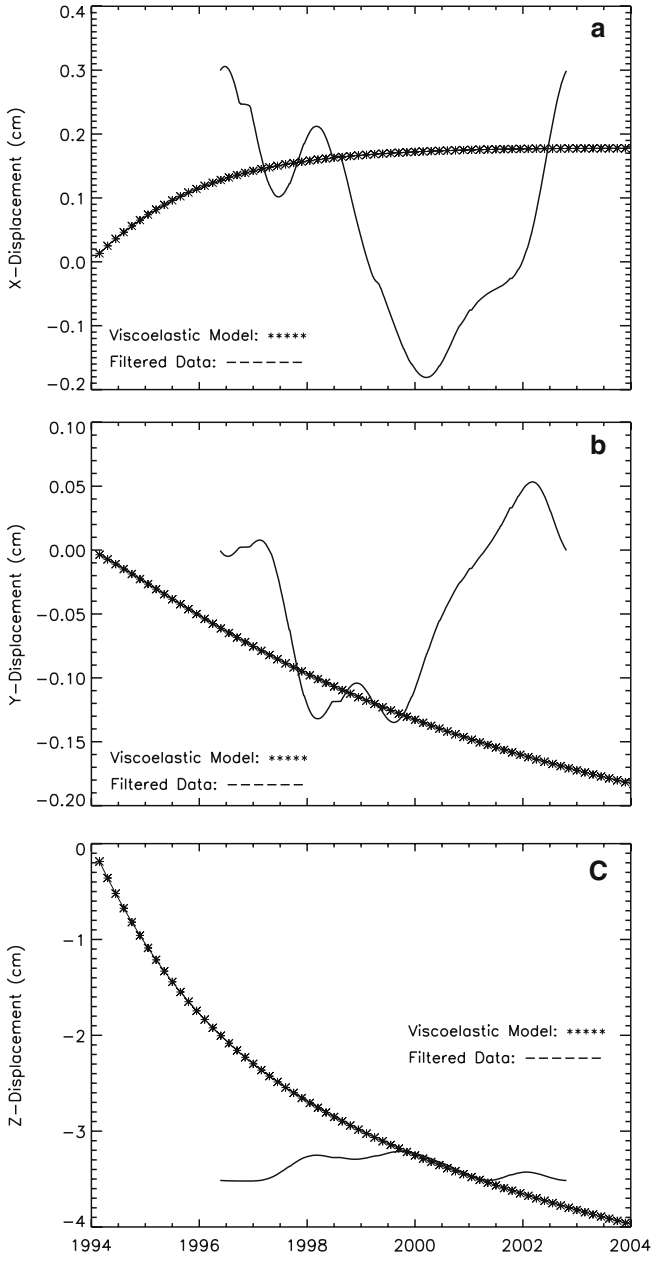

Figure 6

Comparison of filtered GPS time series for CSN1 and viscoelastic model (Fernández and Rundle, 2004), for $\tau_a = 1.5$ years. a), b), and c) show x-, y-, and z- displacement, respectively, in cm. Fault parameters are given in Table 1; modeled offsets are given in Table 2.

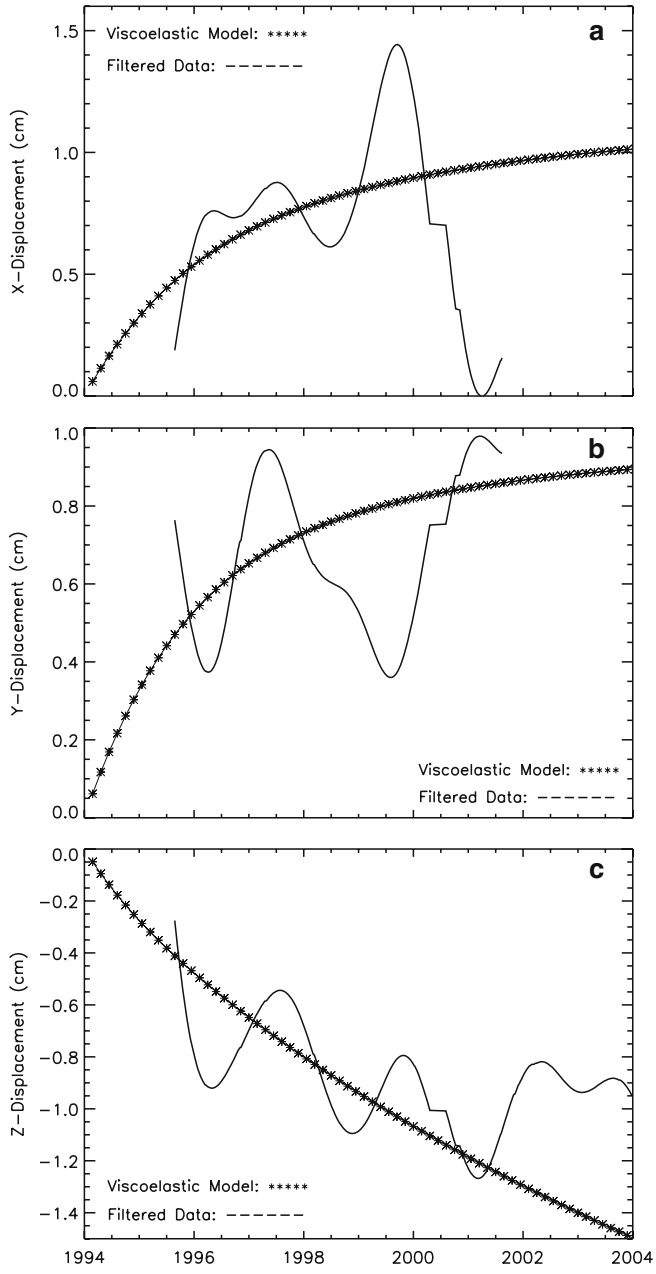

Figure 7

Comparison of filtered GPS time series for DAM2 and viscoelastic model (FERNÁNDEZ and RUNDLE, 2004), for $\tau_a = 1.5$ years. a), b), and c) show x-, y-, and z- displacement, respectively, in cm. Fault parameters are given in Table 1; modeled offsets are given in Table 2.

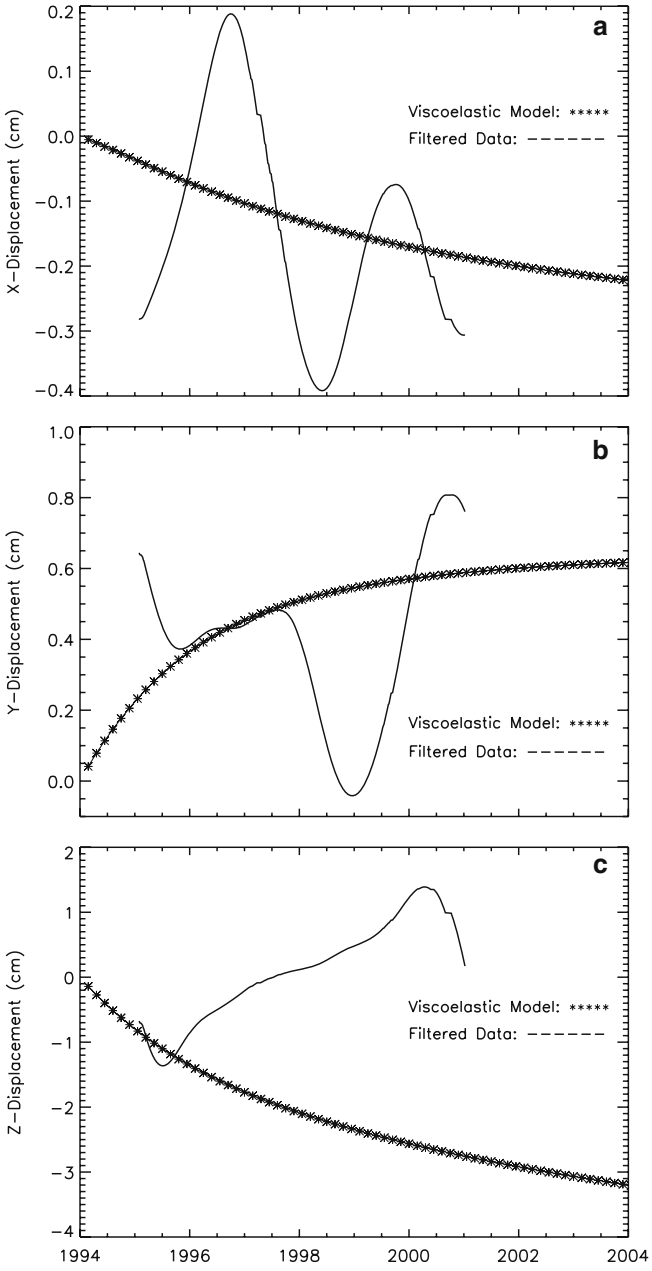

Figure 8

Comparison of filtered GPS time series for OAT2 and viscoelastic model (FERNÁNDEZ and RUNDLE, 2004), for $\tau_a = 1.5$ years. a), b), and c) show x-, y-, and z- displacement, respectively, in cm. Fault parameters are given in Table 1; modeled offsets are given in Table 2.

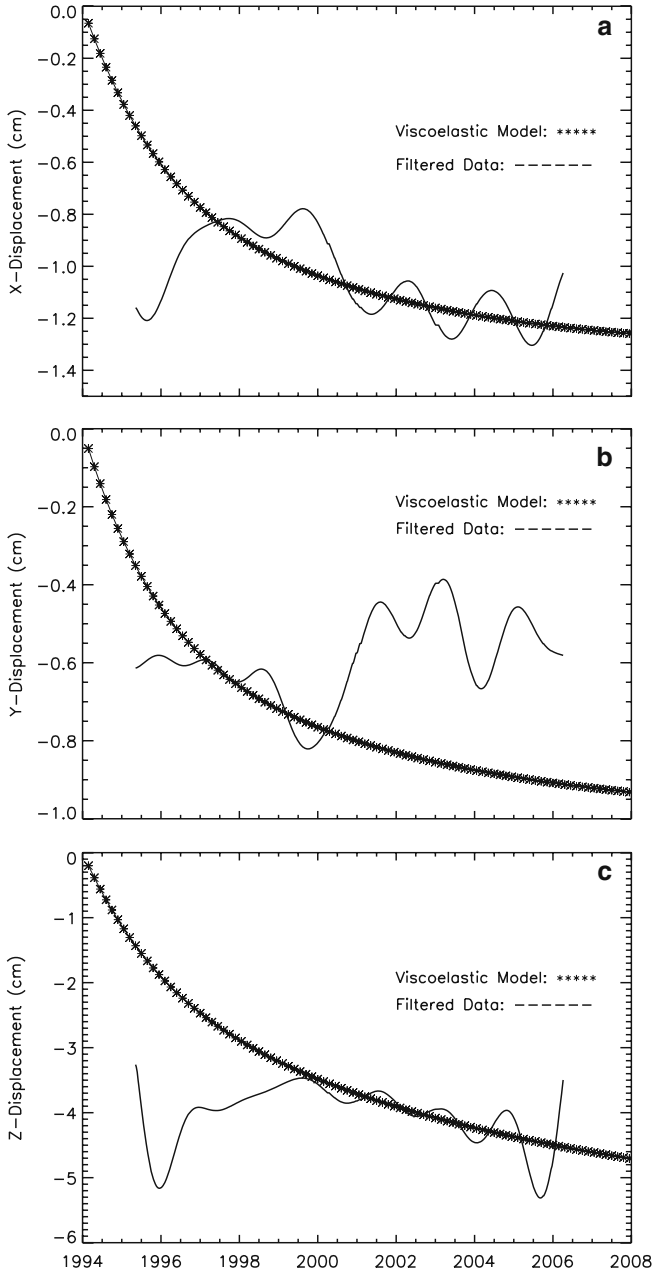

Figure 9

Comparison of filtered GPS time series for ROCK and viscoelastic model (FERNÁNDEZ and RUNDLE, 2004), for $\tau_a = 1.5$ years. a), b), and c) show x-, y-, and z- displacement, respectively, in cm. Fault parameters are given in Table 1; modeled offsets are given in Table 2.

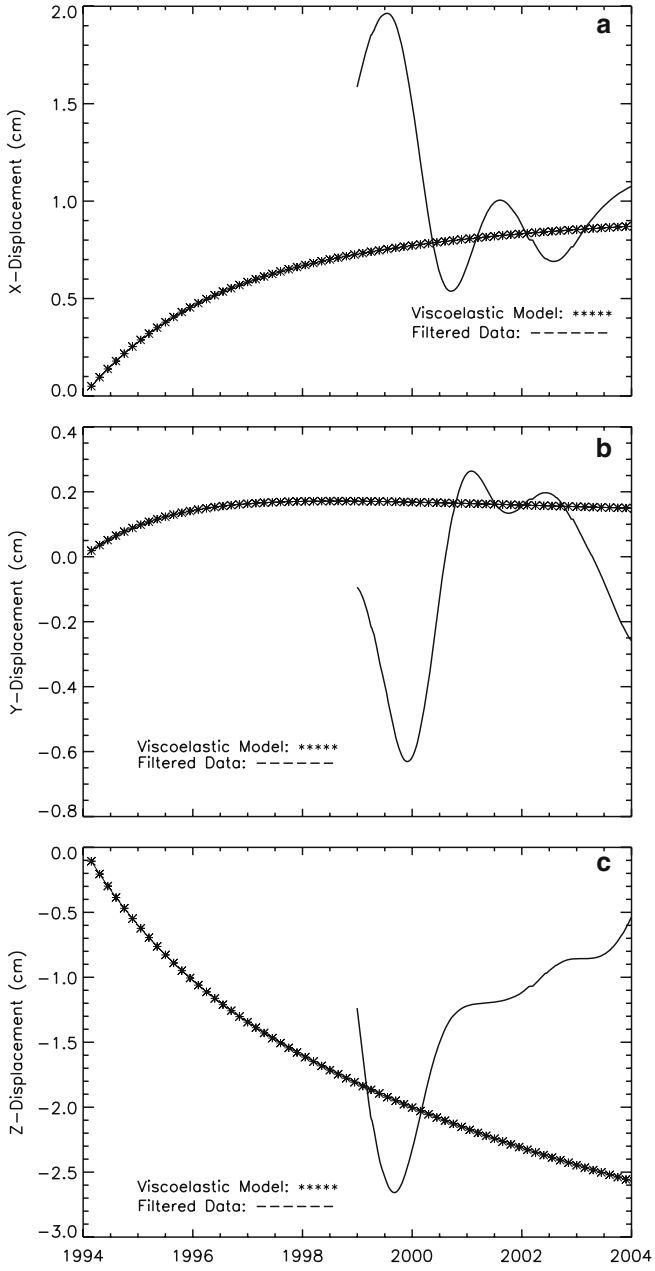

Figure 10

Comparison of filtered GPS time series for WMAP and viscoelastic model (Fernández and Rundle, 2004), for $\tau_a = 1.5$ years. a), b), and c) show x-, y-, and z- displacement, respectively, in cm. Fault parameters are given in Table 1; modeled offsets are given in Table 2.

shown in Table 2 is the least-squares residual associated with the model fit to each station and component. As comparisons with the standard deviations of the original data are of little use because significant portions of the data have been removed through the HL filtering, and standard error analysis on the model parameters are not available without a full inversion analysis, the corresponding standard deviation for each filtered component is also shown for comparison. With the exception of the vertical component at OAT2 and WMAP, the least-squares residual for the time series is on the order of the calculated standard deviation for this filtered component.

The viscoelastic model provides a good fit to the data for a number of stations and components for some subset of the time period through 2000, although it is certainly poor for certain stations and time periods. We have not windowed these time periods here, or removed obvious outliers, in order to improve the fit. Early, large offsets are likely a result of edge effects inherent in the transform itself and discussed earlier. Deviation of the model from the data in later years is likely due to ongoing tectonic processes in the complicated southern California fault system that are larger or more significant than the decreasing postseismic signal.

Note that a very simple model was constructed for this initial study. The preliminary model does not include a strike-slip component, and the resulting horizontal components would likely be improved by including an along-strike component to the fault motion, as the Northridge earthquake contained a small, but significant, strike-slip component. In addition, certain stations, such as WMAP, are only operational in later years, and the postseismic effect from the original 1994 earthquake is likely minimal at that time. Finally, a full inversion, using a more complicated model, would help determine the optimal parameters to maximize the fit to the data. For example, it is likely that the layer thickness lies somewhere between 20 and 30 km, but only the two end members were tested for this application.

The fit is visually better in the z-component for stations CMP9, CSN1, DAM2, and ROCK, than at OAT2 and WMAP. where the trend is incorrect. These last two stations are located quite close to the fault on the southwest side, while the others lie further away. This discrepancy in part may be due to the lack of a strike-slip component in the model and the layer thickness, but is also likely the result of variable slip distribution on the fault plane, which has a greater effect on stations that lie above the dipping section. Again, here we model only average slip over the entire fault area.

One additional feature of interest is the change in the filtered data before and after 1998, that can be seen in several components and at several stations. The best example, for all three components, is at DAM2, where the model fits the filtered data best before 1998 in both the x- and y-components, and there is an apparent offset of the z-component of the time series, suggesting that superposition of similar time-dependent signals might be occurring in the region, as a result of response to aftershocks or separate events. This can also be seen at CMP9, where the x-component fits the postseismic curve well before 1998, while the y-component has a good long-term fit after 1998. The z-component

Table 2

GPS Stations Parameters for Model Fit

Station	x-offset (cm)	y-offset (cm)	z-offset (cm)	x-component LSR (cm)	x-component SD (cm)	y-component LSR (cm)	y-component SD (cm)	z-component LSR (cm)	z-component SD (cm)
CMP9	0.500	1.000	1.700	0.356	0.315	0.112	0.122	0.236	0.595
CSN1	0.100	−0.045	0.100	0.160	0.146	0.085	0.062	0.393	0.109
DAM2	0.350	0.800	0.650	0.142	0.359	0.092	0.203	0.247	0.320
OAT2	−0.150	0.410	0.200	0.133	0.166	0.194	0.225	2.090	0.769
ROCK	−1.010	−0.580	1.100	0.132	0.163	0.204	0.103	0.698	0.450
WMAP	1.100	−0.080	−0.900	0.334	0.394	0.261	0.256	1.214	0.636

LSR: Least-Squares Residual
SD: Standard Deviation

Table 3

Synthetic Data Parameters

	Linear Trend (cm/yr)	Gaussian Noise Standard Deviation (cm)	Sinusoidal Amplitude (cm)
x-component	−4.02	0.13	0.080
y-component	1.20	0.13	0.080
z-component	N/A	0.20	0.800

matches the general trend quite well, but with the same shift in 1998. The inverse is seen in the horizontal components at ROCK, and both ROCK and CSN1 show a better fit to the time-dependent signal after 1998. One potential explanation is that larger aftershocks or even independent events could potentially perturb the time-dependent deformation field. For example, two earthquakes of $M \sim 5$ occurred to the northwest of the 1994 fault plane in March of 1997 (anss.org), and these might have been superimposed on the original viscoelastic deformation. Again, additional modeling could confirm or refute this hypothesis.

Finally, we have applied the HL transform filter to synthetic data. This work was prompted by concerns that the application of the HL filter to the GPS time series might propagate a spurious time-dependent signal into the results. Of particular concern was the possibility that some portion of the linear plate velocities or seasonal signal remains, but might be transformed, alone or in combination, into an apparent relaxation signal through the forward and inverse transform process. In addition, should residuals remain, this technique can be used to estimate their magnitude, for the purpose of error analysis or modeling.

The synthetic data consist of, horizontally, a linear trend equivalent to that of the estimated plate velocities. Superimposed on that signal is a sinusoidal function of amplitude and wavelength corresponding to that seen in the historic data, and Gaussian noise with a standard deviation commensurate, again, with the noise levels observed in the time series records. Synthetic data for the z-component are formulated in a similar

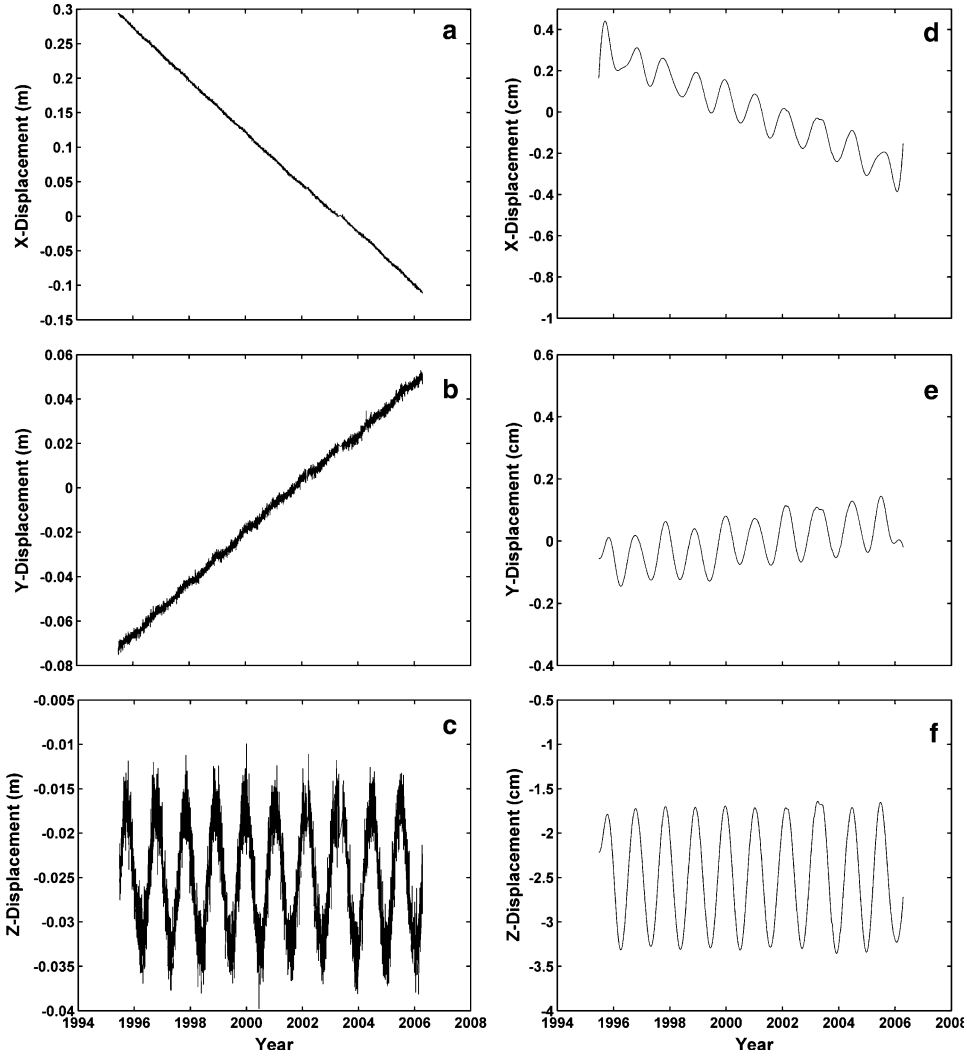

Figure 11
Synthetic time series corresponding to CMP9 for a) x-component, b), y-component and c) z-component, in m. The results after applying the HL transform filter for the d) x-component, e) y-component, and f) z-component, in cm.

fashion, without the linear trend. Table 3 details the values of the parameters used to formulate each of the various components of the synthetic time series.

Figure 11 shows the original synthetic time series and results after the HL transform filter is applied to each component. Note that the procedure for the x- and y-components is to remove the estimated linear trend of the noisy synthetic data prior to applying the transform, as is done for the historic CGPS data, by using a least-squares estimation. This

results in a small residual linear trend which remains in the filtered results, and can be seen in Figures 11e and 11f (note the change in units from Figures 11a, b, and c to Figures 11e, f, and g). This has been confirmed by examining the interim results directly prior to applying the HL transform filter. The x-component residual is less than 0.1 cm/yr, while the y-component residual is on the order of 0.04 cm/yr. Note that while the general direction of the linear residual for both horizontal synthetic components will remain the same for all stations, the observed sense of motion in the actual filtered station varies for each station and component, depending on its location relative to the fault. For example, at CMP9, the filtered x-component demonstrates no significant linear trend (Fig. 4a), while the filtered y-component has an increasing, nonlinear trend of as much as 0.2 cm/yr between 2000 and 2004. This lack of correlation between the residual seen in the synthetic analysis and the actual filtered results persists throughout the analysis. At ROCK, the trend in the filtered x-component data is far too high, while the sign of the filtered y-component data is incorrect. Therefore, while in the future this residual should be calculated for each station using a Monte Carlo simulation process, and taken into account prior to the analysis or inversion of CGPS signals (i.e., removed after the HL filter is applied), it is clear that we are not manufacturing spurious time-dependent signals through the application of the HL filter. It should be noted that the same synthetic Monte Carlo simulation analysis could be performed for any filtering technique to be used on CGPS data, and should be considered as a standard practice.

Also evident in Figure 11 is the residual sinusoidal signal that the filter has not removed entirely, as observed in the filtering of the actual data (Figs. 6, 7, 8, 9, 10). The high-frequency noise has been removed completely. Again, there is no evidence of temporal deformation with the magnitude and frequency of that seen in either the filtered or modeled data and observed in Figures 6 through 10, confirming that the observed relaxation signal is not an artifact of the filtering process. This supports the conclusion that the HL transform filter is isolating a long-period deformation signal that occurred subsequent to the Northridge earthquake.

7. Conclusions

In this work we have described a new mathematical tool, the HL transform filter, that allows for the filtering of 1-D time series through the identification of the power available at various spatial and temporal wavelengths. We have detailed its application and given results from an example using historic CGPS data from southern California for the time period 1994 through 2006.

Initial processing involved applying the HL transform to the available time series. Formulation of the HL transform spectra provided information suggesting that there was measurable signal at longer periods in the data, for the years following the 1994 Northridge earthquake. Subsequently, we applied the HL transform filter to the same data in order to remove high-frequency noise and isolate the longer period signal. A long

period signal is evident in the filtered time series (Figs. 5 through 10). We apply the same filtering technique to synthetic data containing simplified versions of the particular time-dependent signals that are evident in the historic data (Fig. 11), and conclude, from the lack of a long-period time-dependent signal in the filtered synthetic data, that the historic data do contain these features, and that while they are difficult to identify in the raw data, they can be isolated with the HL transform filter.

We show that the predominant features of the remaining signal can be modeled as time-dependent postseismic deformation using one potential model, the viscoelastic-gravitational model of FERNÁNDEZ and RUNDLE (2004). This model was calculated for the locations of six stations selected for their proximity to the Northridge epicenter, and the x-, y-, and z-components of the postseismic deformation were modeled and compared to the filtered data (Figs. 6 through 10). While the resulting fit to this simplified model clearly is not adequate for several stations, the fit is substantially better for several sites and time periods, and supports the hypothesis that this long-period deformation is a result of postseismic relaxation processes.

A more detailed study that will include an attempt to remove the remaining sinusoidal signal, better quantification of the residual linear effect, a more detailed fault model and slip distribution, and that also will consider other potential postseismic models such as afterslip or poroelastic effects, will be performed in the future. However, preliminary results presented here suggest that the HL transform filter provides an important new technique for the filtering of geophysical data consisting of the superposition of the effects of numerous complex sources at a variety of spatial and temporal scales.

Acknowledgments

The authors would like to thank Dr. D. Dong and an anonymous reviewer for their comments, which greatly improved the manuscript. The research by DA and HR was funded by an NSERC Discovery Grant. The research by KT was funded by an NSERC Discovery Grant and the NSERC and Benfield/ICLR Industrial Research Chair in Earthquake Hazard Assessment. JF has been funded under Spanish MEC project CGL2005-05500-C02. This research also has been partially supported by the Spanish Research Project PCI2006-A7-0660.

REFERENCES

BELBACHIR, N., CHILTON, T., DUNN, M., NUNKESER, M., SIDHOM, S., and SZAJNOWSKI, G. (2003), *Image Compression using the Hartley Transform*, Pattern Recognition and Image Processing Group, Inst. Comput. Aided Automation, Vienna, Austria, Tech. Rep. PRIP-TR-087.

BRACEWELL, R. N. (1983), *Discrete Hartley transform*, J Opt Soc Am *73*, 1832–1835.

BRACEWELL, R. N., *The Hartley transform* (Oxford University Press, New York. (1986)).

BRACEWELL, R. N. (1990), *Assessing the Hartley Transform: Correspondence*, IEEE Trans. on Acou. Speech and Sig. Proc. *38*, 2174–2176.

BOCK, Y., WDOWINSKI, S., FANG, P., ZHANG, J., WILLIAMS, S., JOHNSON, H., BEHR, J., GENRICH, J., DEAN, J., VAN DOMSELAAR, M., AGNEW, D., WYATT, F., STARK, K., ORAL, B., HUDNUT, K., KING, R., HERRING, T., DINARDO, S., YOUNG, W., JACKSON, D., and GURTNER, W. (1997), *Southern California Permanent GPS Geodetic Array: Continuous measurements of crustal deformation between the 1992 Landers and 1994 Northridge earthquakes*, J Geophys Res *102*, 18,013–18,033.

CHILTON, E., and HASSANAIN, E. (2006), *Phase estimation of minimum phase systems using the Hartley phase Spectrum*, Proc. of 24th IASTED Int. Conf. on Sig. Proc., Pattern Recognition and Applications, pp. 171–176.

DONG, D., FANG, P., BOCK, Y., WEBB, F., PRAWIRODIRDJO, L., KEDAR, S., and JAMASON, P. (2006), *Spatiotemporal filtering using principal component analysis and Karhunen-Loeve expansion approaches for regional GPS network analysis*, J Geophys Res *111*, doi: 10.1029/2005JB003806.

DONG, D., HERRING, T. A., and KING, R. A. (1998), *Estimating regional deformation from a combination of space and terrestrial geodetic data*, J. Geod. *72*, 200–214.

DONG, D., FANG, P., BOCK, Y., CHENG, M. K., and MIYAZAKI, S. (2002), *Anatomy of apparent seasonal variations from GPS-derived site position time series*, J Geophys Res, *107*, doi:10.1029/2001JB000573.

DONNELLAN, A. and LYZENGA, G. A. (1998), *GPS Observations of fault afterslip and upper crustal deformation following the Northridge earthquake*, J Geophys Res *103*, 21,285–21,297.

DONNELLAN, A., PARKER, J. W., and PELTZER, G. (2002), *Combined GPS and InSAR models of postseismic deformation from the northridge Earthquake*, Pure Appl. Geophys. *159*, 2261–2270.

FERNÁNDEZ, J. and RUNDLE, J. B. (2004), *Postseismic viscoelastic-gravitational half-space computations: Problems and solutions*, Geophys. Res. Lt. *31*, doi: 10.1029/2004GL019654.

FERNÁNDEZ, J., YU, T.-T., and RUNDLE, J. B. (1996a), *Horizontal viscoelastic- gravitational displacement due to a rectangular dipping thrust fault in a layered earth model*, J. Geophys. Res. *101*(B6), 13581–13594 (Correction, J. Geophys. Res. *103*, 30,283–30,286, 1998).

FERNÁNDEZ, J., YU, T.-T., and RUNDLE, J. B. (1996b), *Deformation produced by a rectangular dipping fault in a viscoelastic-gravitational layered Earth model. Part I: Thrust fault*, Comput Geosci, *22*, 735–750 (Correction, Comput. Geosci. *25*, 301–307, 1999).

HARTLEY, R. V. L. (1942), *A More Symmetrical Fourier analysis applied to transmission problems*, Proceed. IRE., *30*, 144–150.

HUDNUT, K. W., SHEN, S., MURRAY, M., MCCLUSKY, S., KING, R., HERRING, T., HAGER, B., FENG, Y., FANG, P., DONNELLAN, A., and BOCK, Y. (1996), *Co-seismic displacements of the 1994 Northridge, California, earthquake*, Bull Seismol Soc Am *86*, S19–S33.

KUHL, H. and SACCHI, M. D. (1999), *Least-squares split-step migration using the Hartley transform*, Univ. of Alberta, SEG Expanded Abstracts, 1548–1551.

LEGRAND, L., DIEBOLD, H., TOSSER, A. J., and DUSSERRE, L. (1990), *Computation of functional angiographic images with the Hartley transform*, Computers in Cardiology Proceedings, 423–426.

LIU J. -C. and LIN T. P. (1993), Short-time Hartley transform, IEEE Proc.-F (140)171–174.

MANSINHA, L., STOCKWELL, R. G., and LOWE, R.P. (1997a), *Pattern analysis with two-dimensional spectral localisation: Applications of two-dimensional S transforms*, Physica A, *239*, 286–295.

MANSINHA, L., STOCKWELL, R. G., LOWE, R. P., ERAMANIAN, M., and SCHINCARIOL, R. A. (1997b), *Local S-spectrum analysis of 1-D and 2-D data*, Phys. of the Earth and Planet. Int, *103*, 329–336.

NIKOLAIDIS, R. (2002), *Observation of Geodetic and Seismic Deformation with the Global Positioning System*, Ph.D. Thesis, University of California, San Diego.

OKADA, Y. (1985), *Surface deformation due to shear and tensile faults in a half space*, Bull. Seismol. Soc. Am. *75*, 1135–1154.

PINNEGAR, C. R., and MANSINHA, L. (2004), *Time-frequency localization with the Hartley S-Transform*, Sig. Proc. *84*, 2437–2442.

POLLITZ, F. F. (1997), *Gravitational viscoelastic postseismic relaxation in a layered spherical earth*, J Geophys Res *102*, 17921–17941.

RUNDLE, J. B. (1981), *Vertical displacements from a rectangular fault in a layered elastic-gravitational media*, J Phys Earth *29*, 173–186.

RUNDLE, J. B. (1982), *Viscoelastic-gravitational deformation by a rectangular thrust fault in a layered Earth*, J. Geophys. Res. 87, 7787–7796.

THE SCIGN PROJECT REPORT to NSF (1998), Southern California Earthquake Center.

STOCKWELL R. G., MANSINHA L., and LOWE R. P. (1996), *Localization of the Complex Spectrum: The S transform*, IEEE, Trans. on Sig. Proc. *44*, 998–1001.

STOCKWELL, R. G. (1999), S-Transform Analysis of Gravity Wave Activity, Ph.D. Dissertation, Dept. of Physics and Astronomy, The University of Western Ontario, London, Ont., Canada.

STOCKWELL, R. G. (2007), *A basis for efficient representation of the S-transform*, Digital Signal Processing *17*, 371–393.

THEUSSL, T., TOBLER, R. F., and GROLLER, E. (2000), *The multi-dimensional Hartley transform as a basis for volume rendering*, Winter School of Computer Graphics, The 8th Internat. Conf. in Central Europe on Computer Graphics, Visualization and Interactive Digital Media, Proceedings abstract.

UNRUH, J. R., TWISS, R. J., and HAUKSSON, E. (1997), *Kinematics of postseismic relaxation from aftershock focal mechanisms of the 1994 Northridge, California earthquake*, J. Geophys. Res. *102*, 24,589–24,603.

WALD, D. J., HEATON, T. H., and HUDNUT, K. W. (1996), *The slip history of the 1994 Northridge, California, earthquake determined from strong-motion, teleseismic, GPS, and leveling data*, Bull Seismol Soc Am *86*, S49–S70.

WATSON, K. M., BOCK, Y., and SANDWELL, D. T. (2002), *Satellite interferometric observations of displacements associated with seasonal groundwater*, J. Geophys. Res. *107*, doi:10.1029/2001JB000470.

WILLIAMS, S. D. P., BOCK, Y., FANG, P., JAMASON, P., NIKOLAIDIS, R. M., PRAWIRODIRDJO, L., MILLER, M. and JOHNSON, D. J. (2004), Error analysis of continuous GPS position time series, J. Geophys. Res. *109*, B03412, doi:10.1029/2003JB002741.

ZUMBERGE, J. F., HEFLIN, M. B., JEFFERSON, D. C., WATKINS, M.M., and WEBB, F.H. (1997), *Precise point positioning for the efficient and robust analysis of GPS data from large networks*, J. Geophys. Res. *102*, 5005–5017.

(Received August 10, 2007, revised May 4, 2008, accepted May 6, 2008)

Pure appl. geophys. 165 (2008) 1603–1618
0033–4553/08/081603–16
DOI 10.1007/s00024-004-0391-6

Pure and Applied Geophysics

A Mathematical Study of the Ice Flow Behavior in a Neighborhood of the Grounding Line

Marco A. Fontelos[1] and Ana I. Muñoz[2]

Abstract—The description of the ice flow in marine ice sheets is one of the problems that has attracted more attention in the Scientific community interested in the motion of glaciers. It is widely assumed that the stability of the marine ice sheets, as in the West Antarctic Ice Sheet (WAIS), where ice shelves are formed, is mainly controlled by the dynamics of the grounding line. The grounding line is the line where transition between ice attached to the solid ground and ice floating over the sea takes place. In this paper, we present the analysis of a mathematical model describing the behavior of the ice flow in the neighborhood of the grounding line, when considering the ice to be a fluid with shear-dependent viscosity of power-law type, including, as a particular case, the Newtonian one. We prove the existence of solutions representing the transition from ice sheet to ice shelf and with finite viscous dissipation near the grounding line. The interface between the ice shelf and sea water is proved to be locally flat near the grounding line.

Key words: Free boundary problem, glaciology, Stokes' flow problem, Non-Newtonian fluid, mixed type boundary conditions, convex analysis, existence and uniqueness of weak solutions, numerical resolution.

1. Introduction

Marine ice sheets are characterized by having much of the grounded ice lying on a submarine bed and usually, at the continental margin, the ice flow continues to float on the sea. Then, tongues of ice, which are called ice shelves, are formed. An example of this situation can be found at the West Antarctic Ice Sheet (WAIS). The moving boundary that localizes the transition from grounding ice to floating ice is termed grounding line. It is widely accepted that the dynamics of the grounding line is of considerable importance regarding the stability of the ice sheet, and therefore, of interest for predicting possible sea-level rises. Some distance away from this grounding zone, either in the ice shelf or in the ice sheet, there is some consensus as to which simplifications can be made in the stress equilibrium, either to have flow dominated by shearing in horizontal planes, most of it at the base as in the ice sheet, or to have the flow dominated by lateral shearing and

[1] Instituto de Matemáticas y Física Fundamental, Consejo Superior de Investigaciones Científicas, c/ Serrano, n 123, 28006 Madrid, Spain. E-mail: marco.fontelos@uam.es

[2] Dpto. de Matemática Aplicada, ESCET, Univ. Rey Juan Carlos, c/ Tulipán s/n, 28933, Móstoles, Madrid, Spain. E-mail: anaisabel.munoz@urjc.es

longitudinal stretching, as in the ice shelf. The fundamental difference between the two flow regimes seems to suggest the existence of a transition zone where all the stress components are important and no simplification can be made. The grounding line migration and the coupling of ice sheet flow with ice shelf flow can rightly be considered as one of those challenging modelling problems, which is nevertheless of prime importance because, as we mentioned, it is the predominant mechanism by which the Antarctic ice sheet changes its dimensions. In the context of the study of ice flow near the grounding line, there are several recent contributions mainly due to HINDMARSH (1993), SCHOOF (2007a,b), VIELI and PAYNE (2005), WILCHINSKY and CHUGONOV (2000), and NOWICKI and WINGHAM (2007). In these works various modelling approaches are proposed and the analysis of some stability hypothesis regarding the configuration of the ice sheet-ice shelf junction is presented. One of the main challenges, both from the analysis and the simulation point of view is the possible presence of singularities in the stresses close to moving contact lines. Related to this fact, the analysis of the structure of the fluid flow in the neighborhood of moving contact lines has been developed in relative to the spreading of viscous fluids over solid substrate (cf., FRIEDMAN and VELÁZQUEZ, 1995; FONTELOS and VELÁZQUEZ, 1998). In this survey, we shall analyze a mathematical model describing the ice flow in a neighborhood of the grounding line. From the mathematical point of view, we are going to deal with a nonlinear free boundary problem, being the free boundary the one which corresponds to the part of the ice in contact with the sea. A more detailed treatment of the theory presented here can be found in FONTELOS and MUÑOZ (2007), FONTELOS *et al*. (submitted). The aim of our analysis is to determine the velocity and pressure fields in the neighborhood of the grounding line and also the location and geometry of the free boundary. In sections 2 and 3, we briefly describe the setting of the mathematical problem. In section 4, we shall prove the existence and uniqueness of a solution, with a moving grounding line, to the free boundary problem in the Newtonian case. Moreover, we determine, analytically the ice flow and the asymptotic behavior of the free boundary in the area of the grounding line. In section 5 we solve numerically the problem for a general power-law rheology obtaining the asymptotic properties of the free boundary and of the flow when approaching the grounding line.

2. *The Mathematical Problem*

In the present work we aim to determine the ice flow, together with the geometry and location of the free boundary near the grounding line. In order to do that we make modeling simplifications. First, we consider a two-dimensional domain by assuming independence of all physical quantities in the third variable. This is a strong assumption, since it is known that remoteness from the grounding line flow may be controlled by lateral stresses. Nevertheless, our results on the behavior of the flow near the grounding line are essentially local and are expected to be valid even without the assumptions concerning symmetry. Changes due to temperature variations are neglected, therefore a

steady state and isothermal regime is considered. We assume that the contact line is moving with constant velocity U in the main flow direction (the x-direction, see Fig. 1). The ice is modelled as a fluid with shear-dependent viscosity of power-law type, including, as a particular case, the Newtonian one. In Figure 1, it is depicted the domain $\mathbb{D} := \{(x,z) \in [-M,M] \times [-1 + b(x), 0]\}$, with $b(x) \equiv 0$ in $x \leq 0$, which represents a vicinity of the grounding line. Two flow regions appear where the ice flow is well understood. One is the inland ice sheet, where the ice flow is dominated by shearing on horizontal planes, most of it at the base, and the other one is the ice shelf, where the ice flow is dominated by lateral shearing and longitudinal stretching. Therefore one might suppose the existence of a transition region, near the grounding line, where all the components of the stress should be of importance.

The upper boundary of $\mathbb{D}$, denoted Γ_0, is the one corresponding to the ice in contact with the air. We shall presume it to be flat and located at $z = 0$. The part of the ice in contact with the solid substrate, denoted by Γ_1 is also assumed to be flat and located at $z = -1$. The only free boundary we shall consider is Γ_2, the bottom of the ice floating on the sea, described by $z = -1 + b(x)$. Note that at the grounding line, located at $x = 0$ and $z = -1$, different boundary conditions shall meet. This fact might give rise to singularities in the solution. We shall consider a frame of reference attached to the grounding line, which is equivalent to assume that the solid substrate is moving with constant velocity $-U$ and the velocity field is given by $(-U, 0) + (u,w)$. We shall use indistinctly the notation (u,w) and (v_1,v_2) when referring to the components of the velocity vector. The strain tensor will be denoted by D, where

$$D_{ij} = \frac{1}{2}\left(\frac{\partial v_i}{\partial x_j} + \frac{\partial v_j}{\partial x_i}\right), \quad x_1 = x,\ x_2 = z,\ i, j = 1, 2,\ v_1 = u,\ v_2 = w,$$

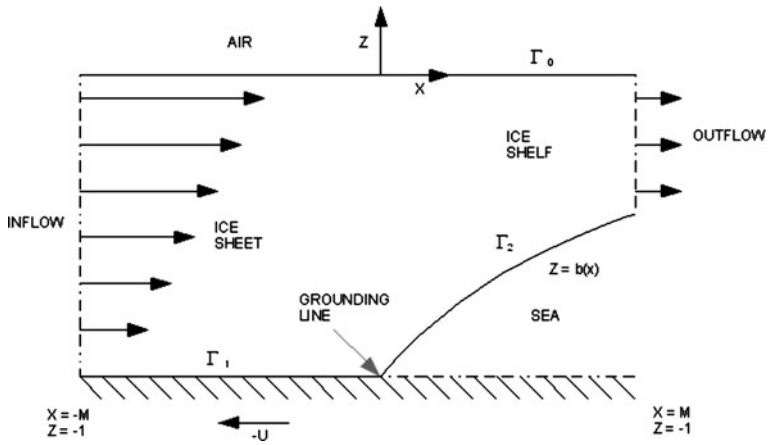

Figure 1
Proximity of the grounding line. Flow domain $\mathbb{D}$.

and the viscosity μ depends on strain in the following way:

$$\mu(|D|) = \mu_0 |D|^{\frac{1}{n}-1}, \text{ with } |D| \text{ given by}$$

$$|D| = \sqrt{2D:D} = \sqrt{\frac{1}{2}\left(2\frac{\partial u}{\partial x}\right)^2 + \frac{1}{2}\left(2\frac{\partial w}{\partial z}\right)^2 + \left(\frac{\partial u}{\partial z} + \frac{\partial w}{\partial x}\right)^2} \tag{2.1}$$

and μ_0 a constant. The exponent n is usually assumed for the ice flow to be $n = 3$ (cf., GLEN, 1958; LLIBOUTRY, 1964; HUTTER, 1981). Note that for $n = 1$, we are considering the ice as a Newtonian fluid. Due to the fact that in the Newtonian case, the problem is simpler because the viscosity is of constant value, we shall devote a subsection to its study alone, since more regularity for the solution can be obtained in this case. The equations to be considered are the equilibrium and mass conservation equations,

$$\nabla \cdot T = 0, \qquad \nabla \cdot \vec{v} = 0 \text{ in } \mathbb{D}, \tag{2.2}$$

with $T_{ij} = -p\delta_{ij} + \mu\, D_{ij}$. The pressure p is in fact a reduced pressure, resulting from the substraction of $\rho_{\text{ice}} g(z+1)$ from the real pressure, in order to absorb the gravity forces acting on ice (see, FONTELOS and MUÑOZ, 2007). In fact, it reduces to the actual pressure in the idealized case $\rho_{\text{ice}} = 0$. Concerning the boundary conditions at the upper part of the sheet which is in contact with air, denoted by Γ_0, and assumed to be flat, i.e., $\Gamma_0 = \{(x, 0), x \in [-M, M]\}$, we impose that both the normal velocity and the shear stress are zero there, i.e.,

$$\vec{v} \cdot \vec{n} = 0, \quad \vec{t}\, T \vec{n} = 0 \quad \text{at } \Gamma_0, \tag{2.3}$$

where $\vec{n}$ and $\vec{t}$ are the normal and tangent vectors to Γ_0, respectively. In the part of the bottom of the ice sheet which is in contact with the solid substrate we impose $\vec{v} = \vec{0}$. In the other part, which is in contact with the sea, we impose a balance between viscous stresses and the hydrostatic pressure. Therefore, at the base, depending on whether the ice is grounded or floating over the sea, we impose:

$$\vec{v} = \vec{0} \quad \text{on } \Gamma_1, \tag{2.4}$$

$$\vec{t}\, T \vec{n} = 0, \quad T\vec{n} = \gamma U b(x) \vec{n} \quad \text{on } \Gamma_2, \tag{2.5}$$

where γ is a dimensionless parameter defined by $\gamma = \rho g [L]^{\frac{1}{n}+1} / U\mu_0$, based on the densities of water and ice, $\rho = \rho_{\text{water}} - \rho_{\text{ice}}$, the velocity U, the typical longitudinal length scale and the factor μ_0 in the law of the viscosity (2.1). As inflow and outflow conditions, we shall impose the values $\vec{v}^{\text{in}}(z)$ and $\vec{v}^{\text{out}}(z)$ of the velocity field, at $x \to -M$ and $x \to +M$, respectively, and assume, by compatibility with the boundary conditions, that $\vec{v}^{\text{in}}(-1) = \vec{0}$, $\vec{v}^{\text{in}}(0) \cdot \vec{n} = 0$, and the shear stress $\vec{t}\, T \vec{n}$ is zero at $(-M, 0)$. We should choose $\vec{v}^{\text{in}}(z)$ to be of Poiseuille flow type according to the physics of the problem, that is

$$\vec{v}^{\text{in}} = \left(\frac{\sigma}{2}(1 - |z|^{n+1}), 0\right). \tag{2.6}$$

However, the study that we shall develop here is valid for more general inflow conditions. The outflow $\vec{v}^{\text{out}}(z)$ is such that $w^{\text{out}}(0) = 0$ and the shear stress at $(M, 0)$ and $(M, -1)$ are zero. We may think, for instance, on a uniform velocity profile, i.e.,

$$\vec{v}^{\text{out}} = (U_\infty, 0). \tag{2.7}$$

Here σ and U_∞ are two arbitrary positive parameters which are nevertheless linked by the conservation of mass constraint which implies

$$-U + \int_{-1}^{0} u^{\text{in}}(z)dz = -U(1 - b(M)) + \int_{b(M)}^{0} u^{\text{out}}(z)dz,$$

hence, the velocity of the grounding line can then be determined from the given physically measurable entities $u^{\text{in}}(z)$, $u^{\text{out}}(z)$ and $b(M)$:

$$U = \frac{1}{b(M)}\left(\int_{-1}^{0} u^{\text{in}}(z)dz - \int_{b(M)}^{0} u^{\text{out}}(z)dz\right). \tag{2.8}$$

Somewhat different outflow conditions appear for example in Schoof (2007) and in Nowicki and Wingham (2007), where ice-shelf stresses are prescribed, and the case in which the ice is allowed to slide over the bed is also considered. The boundary Γ_2 may evolve following the velocity field, but in the stationary situation will be such that $[(-U, 0) + (u, w)]\overrightarrow{n} = 0$, so that

$$0 = Ub_x + w - b_x u. \tag{2.9}$$

The main results and conclusions of this study are stated in the following theorems. We begin with the one referred to the Newtonian case with $n = 1$:

Theorem 2.1. *Consider* $n = 1$, *then if* $\overrightarrow{v}^{\text{in}}$ and $\overrightarrow{v}^{\text{out}}$ *are such that the norms* $\|\overrightarrow{v}^{\text{in}}\|_{C^2[-1,0]}$, $\|\overrightarrow{v}^{\text{out}}\|_{C^2[-1+b(M),0]}$ *are small enough and* $b(M)$ *is also small enough then there exists a unique (weak) solution* $\overrightarrow{v} \in [H^1(\mathbb{D})]^2$ *to the nonlinear free boundary problem given by* (2.2)–(2.7) *with U given by* (2.8). *Moreover, the free boundary* $b(x) \in C^{1+\delta}[\ 0,M]$ *and its asymptotic behavior near the grounding line located at* ($x = 0$, $z = -1$) *is the following*:

$$b(x) = Cx^{\frac{3}{2}} + o(x^{\frac{3}{2}}).$$

Therefore, the velocity does not show any singularity near the grounding line, however, shear stress does, with a singularity of order $O(x^{\frac{-1}{2}})$.

Remark 2.1. *Additional regularity analysis of the weak solution shows that it is in fact* C^3 *in the interior of* $\mathbb{D}$.

Theorem 2.2. *Consider* $n > 1$, *then if* $\overrightarrow{v}^{\text{in}}$ *and* $\overrightarrow{v}^{\text{out}}$ *are such that* $\|\overrightarrow{v}^{\text{in}}\|_{C^2[-1,0]}$ *and* $\|\overrightarrow{v}^{\text{out}}\|_{C^2[-1+b(M),0]}$ *are small enough, and* $b(M)$ *as well, there exists a weak solution* $\overrightarrow{v} \in [W^{1,p}(\mathbb{D})]^2$ *to the nonlinear free boundary problem given by* (2.2)–(2.7) *with* U *given by* (2.8). *The free boundary* $b(x)$ *is in the space* $C^{1+\frac{1}{n+1}}(0, M)$.

Remark 2.2. *In this paper, we shall not address for* $n > 1$, *the existence of weak solutions. We refer the reader to* Fontelos, Muñoz and Schiavi (submitted), *where a detailed analysis of the power law case is developed.*

In order to study the asymptotic behavior of the flow near the grounding line, due to the complexity of the nonlinearities arising for $n > 1$ in the equations, we are forced to solve the problem numerically. The results will be discussed in section 5. Due to the fact that we are dealing with a free boundary, and this fact might complicate the analysis, we first performed a diffeomorphism from the domain $\mathbb{D}$ where the problem is defined to the strip $S = [-M, M] \times [-1, 0]$. In doing that, we are assuming *a priori* that the free boundary Γ_2, located at $z = -1 + b(x)$, is a small perturbation of the curve $z = -1$ and regular enough. Regularity results for $b(x)$ will be obtained in order to justify a posteriori this procedure (cf., Fontelos and Muñoz, 2007). Once we obtain the existence and regularity results for the problem in the strip, we can translate them to the corresponding in the original domain $\mathbb{D}$ via Banach's fixed point theorem (see Fontelos and Muñoz, 2007 for details).

3. The Problem in the Strip

After a suitable change of coordinates and a linearization process of the problem in the domain $\mathbb{D}$ (see Fontelos and Muñoz, 2007 for details), we deduce the following problem in the strip S:

$$\nabla \cdot T = 0, \qquad \nabla \cdot \overrightarrow{v} = 0 \text{ in } S := [-M, M] \times [-1, 0],$$

where the stress tensor T, written in terms of the stream function, defined by $\psi_x = w$ and $\psi_z = -u$ and satisfying $\psi(x, 0) \equiv 0$, reads

$$T = \begin{pmatrix} -p + \mu(|D|)\psi_{xz} & \frac{1}{2}\mu(|D|)(\psi_{zz} - \psi_{xx}) \\ \frac{1}{2}\mu(|D|)(\psi_{zz} - \psi_{xx}) & -p - \mu(|D|)\psi_{xz} \end{pmatrix}.$$

Then, by applying the curl operator to $(2.2)_1$, in order to remove the pressure from the equation, we obtain the equation for the stream function:

$$\mu(|D|)\Delta^2\psi + 2\partial_x(\mu(|D|))[\psi_{xzz} + \psi_{xxx}] + 2\partial_z(\mu(|D|))[\psi_{xxz} + \psi_{zzz}] + 4\partial_{xz}(\mu(|D|))\psi_{xz} + [\partial_{xx}(\mu(|D|)) - \partial_{zz}(\mu(|D|))][\psi_{xx} - \psi_{zz}] = 0. \quad (3.10)$$

Note that in the Newtonian case ($n = 1$), with constant viscosity, the equation reduces to the biharmonic equation for ψ, $\Delta^2 \psi = 0$. Concerning the boundary conditions we impose first zero normal velocity and zero shear stress, i.e.,

$$T_{xz} = 0, w = 0 \text{ at } z = 0. \quad (3.11)$$

The bottom of the ice sheet which is in contact with the solid substrate will satisfy the no slip condition:

$$\overrightarrow{v} = \overrightarrow{0} \text{ at } z = -1,\ x<0. \quad (3.12)$$

At $z = -1$, $x > 0$, we impose zero shear stress and a balance between viscous stress on the ice sheet and hydrostatic pressure,

$$T_{xz} = 0, T_{zz} = -\gamma \int_0^x w(s,-1) \text{ at } z = -1, x > 0, \quad (3.13)$$

where we have replaced b by the integral $\int_0^x w(s,-1)$, which is an expression that results after integration in x of the linearization of (2.9), i.e., $0 = Ub_x + w$. At the lateral boundaries, $x = -M$ and $x = +M$, inflow velocity and outflow velocity field, will be considered given by (2.6) and (2.7), respectively. The boundary conditions written in terms of the stream function are then:

$$\psi_x = 0 \quad \text{and} \quad \psi_{zz} - \psi_{xx} = 0 \ \text{ at } \ z = 0, \quad (3.14)$$

$$\psi_x = \psi_z = 0 \quad \rightarrow \quad \psi = \psi_z = 0 \quad \text{at } z = -1, x<0 \quad (3.15)$$

and

$$\psi_{zz} - \psi_{xx} = 0 \text{ and } [\mu(|D|)(\psi_{zz} - \psi_{xx})]_z + 4[\mu(|D|)\psi_{xz}]_x = -\gamma\psi_x \quad (3.16)$$

at $z = -1$, $x > 0$. The condition $(3.16)_2$ is equivalent (up to a constant) to (3.13). We refer to Fontelos and Muñoz (2007). There is presented, for $n = 1$, a detailed discussion of the argument to follow in order to eliminate the pressure p from the boundary condition (3.13) and obtain the equivalent one, written only in terms of the stream function ψ. The argument is easily translated into the general $n > 1$ case.

4. Analysis of the Newtonian Case

The steps we shall follow in order to tackle the problem, in this section, in the particular case $n = 1$, are the following: Firstly, we shall analyze the one posed in the strip, and secondly, we shall extend the regularity results obtained in the strip S to the domain $\mathbb{D}$.

4.1. The Linearized Problem

In this section, we shall use the formulation of the problem in terms of a stream function, i.e., the one given by (3.10)–(3.16) and the inflow–outflow conditions (2.6)–(2.7). In this framework, we derive the existence and uniqueness of a weak solution result. The solution is weak in the sense that it will be obtained via the Lax-Milgram theorem. Later, we shall comment, that due to the obtention of a result improving the regularity in the surroundings of the grounding line, the solution is, in fact, classical.

Theorem 4.1. *There exists a unique weak solution* $\psi \in H^2(S)$ *to the problem given by* (3.10)*, the boundary conditions* (3.14)–(3.16) *and the inflow-outflow conditions* (2.6)–(2.7).

Proof. We shall sketch the main ideas of the proof. For more details, we refer the reader to Fontelos and Muñoz (2007). First, we express the velocity as an addition of two velocities in the following way: $\overrightarrow{v} = \overrightarrow{v}^0 + \overrightarrow{v}^1$. We assume that $p^0 = 0$ and that $\overrightarrow{v}^0$ is a divergence free $[C^\infty((-M, M) \times (-1, 0))]^2$ velocity field satisfying in terms of a stream function ψ^0, $\overrightarrow{v}^0 = (-\psi^0_z, \psi^0_x)$,

$$\psi^0_x \to v^{\text{in}}_z, \psi^0_z \to -v^{\text{in}}_x \text{ as } x \to -M, \quad \psi^0_x \to v^{\text{out}}_z, \psi^0_z \to -v^{\text{out}}_x \text{ as } x \to +M,$$

$$\psi^0_x, \psi^0_{zz} = 0 \text{ at } z = 0, \psi^0, \psi^0_z = 0 \text{ at } z = -1, x < 0.$$

It is not difficult to find a function $\psi^0 \in C^\infty((-M, M) \times (-1, 0))$ so

$$c_1(x) \equiv \psi^0_{zz} - \psi^0_{xx} \quad \text{and} \quad c_2(x) \equiv \gamma\psi^0_x + \left(\psi^0_{zzz} + 3\psi^0_{zxx}\right)$$

are bounded at $z = -1$, $x > 0$. With regards to the velocity $\overrightarrow{v}^1$ and its associated stress tensor T^1, we have the following system to be satisfied:

$$\nabla \cdot T^1 = \overrightarrow{s_1}, \quad \nabla \cdot \overrightarrow{v}^1 = 0 \text{ in } [-M, M] \times [-1, 0] \tag{4.17}$$

with $\overrightarrow{s_1}$ (depending on ψ^0) bounded. The boundary conditions are then

$$T^1_{xz} = 0, v^1_z = 0 \text{ at } z = 0, \quad \overrightarrow{v}^1 = \overrightarrow{0} \text{ at } z = -1, x < 0,$$

$$T^1_{xz} = -c_1(x), T^1_{zz} + \gamma \int_0^x v^1_z(s, -1) = -\int_0^x c_2(s)ds, \text{ at } z = -1, x > 0,$$

together with the conditions satisfied by the stream function ψ^1 associated to $\overrightarrow{v}^1$. More precisely, ψ^1 and its first derivatives vanish at $x = \pm M$, which is an important fact in order to set a variational formulation of the problem. We consider as a space of test functions X, which is the closure with respect to the norm $\left\|\overrightarrow{\varphi}\right\|_X \equiv \left(\int_S \left|\nabla\overrightarrow{\varphi}\right|^2\right)^{\frac{1}{2}}$ of the set

$$\left\{ \begin{array}{l} \overrightarrow{\varphi} = (\varphi_1, \varphi_2) \in \left[C_0^\infty(\overline{S})\right]^2, \nabla \cdot \overrightarrow{\varphi} = 0, \ \varphi_2(x,0) = 0, x \in [-M, M], \\ \varphi_1(x,-1) = \varphi_2(x,-1) = 0, \ x \in [-M, 0] \text{ and } \overrightarrow{\varphi} = 0 \text{ at } x = \pm M. \end{array} \right\}$$

If we multiply (4.17) by $\overrightarrow{\varphi} \in X$, integrate by parts and take into consideration the boundary conditions, we obtain the following expression:

$$A(\omega, \psi) = L\omega, \quad A(\omega, \psi) \equiv a(\omega, \psi) - b(\omega, \psi),$$

where

$$a(\omega, \psi) = \frac{1}{2} \int_S (\varphi_{i,j} + \varphi_{j,i})(v^1_{i,j} + v^1_{j,i}) \text{ and } b(\omega, \psi) = \gamma \int_{L^+, z=-1} \psi \omega_x,$$

are bilinear forms continuous in Y and

$$L\omega \equiv \int_{L^+, z=-1} c_1(x)\omega_z(x,-1) + \int_{L^+, z=-1} c_2(x)\omega(x,-1) - \int_S (-\omega_z, \omega_x)\overrightarrow{s_1}$$

is a continuous linear functional on Y. The functions ψ and ω are the stream functions associated with $\overrightarrow{v}$ and $\overrightarrow{\varphi}$, respectively, and $L = [-M, M]$, $L^+ = [0, M]$. Taking into account that the trace of functions in $H^2(S)$ lies in $H^1(\partial S)$) and that Poincaŕ's inequality allows us to estimate any φ_i in L^2 by the norms of $\varphi_{i,j}$ in L^2 as well as the norm of ω in L^2. Korn's inequality allows us to estimate the norm of any $\varphi_{i,j}$ in L^2 by $a(\omega, \omega)$, and deduce the coerciveness of $A(\omega, \psi)$. Note that Korn's and Poincaŕ's inequalities are valid in bounded domains with Lipschitz boundaries if $\overrightarrow{\varphi}$ and ω vanish at a part of the boundary. Lax-Milgram's theorem implies then the existence of a unique solution to our linearized problem such that $\psi \in H^2(S)$.

4.2. Regularity in a Neighborhood of the Grounding Line

Next, we shall analyze the regularity of the solution to the linearized problem near the grounding line. In order to do this, we introduce suitable cut-off functions, to isolate different regions. We already know that $\psi \in H^2$, but given the elliptic nature of the system, it can be proved by classical results that the solution ψ has C^4 regularity inside S and outside the critical zone, that is the grounding line. Hence, we shall focus our attention of analyzing the regularity in a realm $\Omega = B_\delta(0, -1) \cap S$ of the grounding line. Note that in Ω, mixed boundary conditions have to be imposed and this fact may give rise to singularities (see FRIEDMAN and VELÁZQUEZ, 1995). Assuming that χ is a suitable cut-off function with support Ω, we get the following problem for $\psi\ \chi$, that will be labelled again in ψ in order to simplify notation,

$$\Delta^2 \psi = J(x, y) \text{ in } \Omega \tag{4.18}$$

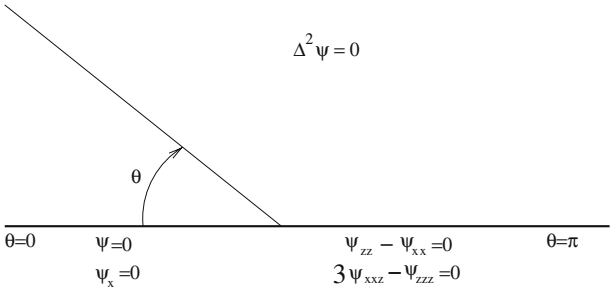

Figure 2
The reduced problem in the neighborhood of the grounding line.

$$\psi = 0, \quad \psi_z = 0 \text{ at } x<0,\ z = -1, \tag{4.19}$$

$$\psi_{zz} - \psi_{xx} = G(x), \quad 3\psi_{xxz} + \psi_{zzz} = F(x) \text{ at } x > 0,\ z = -1, \tag{4.20}$$

with $G(x) = B_1(\psi,\ D\psi)$ and $F(x) = -\gamma\ \chi\ \psi_x + B_2(\psi,\ D\psi,\ D^2\psi)$, $G(x)$, $F(x) \in L^2(I\ R^+)$, $J(x,\ y) \in L^2(I\ R^+ \times [-1, +\infty])$ and compactly supported away from $(0, -1)$.

Next, we write the solution as follows, $\psi = \psi^{(1)} + \psi^{(2)}$. Here, $\psi^{(1)}$ solves (4.18)–(4.20) with homogeneous b.c., so $\psi^{(1)}$ can be written in terms of Green's function for the biharmonic operator with homogeneous boundary conditions (see for instance Maz'ya *et al.*, 2000). Since the source $J(x,y)$ is compactly supported away from $(0, -1)$, we find out that $\psi^{(1)}$ behaves in the vicinity of $(0, -1)$ as a solution to the homogeneous version of (4.18)–(4.20) which is locally in H^2. Correspondingly, $\psi^{(2)}$ solves the homogeneous equation with boundary conditions (4.19)–(4.20).

The study of the behavior of $\psi^{(1)}$ and $\psi^{(2)}$ is carried out separately. Using polar coordinates (r,θ) around the grounding line, i.e., $(0, -1)$, we look for a solution $\psi^{(1)}$ of the form: $\psi^{(1)}(r,\theta) = r^m f(\theta)$. Concerning the problem for $\psi^{(2)}$, we make use of Mellin's transforms (see Fontelos and Muñoz, 2007, for more details) and one finds the behavior is the same as the one for the solution of the homogeneous version of (4.18)–(4.20) defined in the half plane $z > -1$, see Figure 1. This yields an exponent $m = \frac{3}{2}$ and $f(\theta) = \sin(\frac{3\theta}{2}) - 3\sin(\frac{\theta}{2})$. Note that $r^{\frac{3}{2}} f(\theta)$ solves $\Delta\ \psi = 0$ inside the neighborhood, $\psi = \psi_r = 0$ at $\theta = 0$ and $\psi_{rr} - \frac{1}{r^2}\psi_{\theta\theta} - \frac{1}{r}\psi_r = -\frac{1}{r^2}\psi_{\theta\theta\theta} - \frac{3}{r}\psi_{rr\theta} + \frac{3}{r^2}\psi_{r\theta} - \frac{4}{r^3}\psi_\theta = 0$ at $\theta = \pi$ (see Fig. 1). Therefore $\psi_{rr}(r,0) = \frac{C}{r^{\frac{1}{2}}} + O(1)$ and $\psi = \frac{4}{3}Cr^{\frac{3}{2}} + O(r^2)$ as $r \to 0$. Hence, the first order term of the representation of the free boundary is given by $b(x) \sim C' x^{3/2}$.

4.3. The Nonlinear Problem

Once the linearized problem, posed in the strip S, has been studied, we proceed to prove the existence and uniqueness of solutions to the nonlinear one, posed in $\mathbb{D}$ (see Fontelos and Muñoz, 2007, for a more detailed discussion). First, we prove the existence

and uniqueness of flows for a given geometry. We assume that the interface Γ_2 is sufficiently smooth, say $C^{1+\delta}$, and construct a weak solution to the flow problem in a given domain via Lax-Milgram's theorem, arguing as in the linear case. We deduce the existence of a velocity field $\overrightarrow{v} \in (H^1(\mathbb{D}))$ (or equivalently a stream function $\psi \in H^2(\mathbb{D})$). Once we have this result for a known boundary, we continue to study the problem taking into account the free boundary. In order to do that, we consider the following weak formulation of the nonlinear problem. The free boundary problem can be restated as the problem of finding the velocity field $\overrightarrow{v}^1$ such that

$$\begin{aligned}\frac{1}{2}\int_{\mathbb{D}}(v^1_{i,j}+v^1_{j,i})(\varphi_{i,j}+\varphi_{j,i})dxdy = &-\int_{\mathbb{D}}\overrightarrow{\varphi}\,\overrightarrow{J}\,dxdy\\ &+\int_{\Gamma_2}\Big(\Big(\overrightarrow{t}\,T(\overrightarrow{v}^0)\overrightarrow{n}\Big)\overrightarrow{\varphi}\,\overrightarrow{t}\\ &+\Big(\overrightarrow{n}\,T(\overrightarrow{v}^0)\overrightarrow{n}-\gamma\big(\psi^0+\psi^1\big)b(x)\Big)\overrightarrow{\varphi}\,\overrightarrow{n}\Big)ds, \qquad (4.21)\end{aligned}$$

for $\overrightarrow{\varphi}$ a suitable test function, and the curve $z = b(x)$ that describes Γ_2 and satisfies

$$b_x = -\frac{1}{U}\big(b_x(v^0_x+v^1_x)-(v^0_z+v^1_z)\big) \qquad (4.22)$$

so that (4.21) and (4.22) are solved simultaneously. Our strategy will consist of seeking a fixed point "near", in some norm to be defined, to the solution to the linearized problem previously analyzed. We perform a change of variables from $\mathbb{D}$ to the strip S in the integrals (4.21) and change the derivatives of $\overrightarrow{v}^1$ and ϕ accordingly in order to get the formulation of (4.21) in the domain S. We result with a reformulation of (4.21) in the strip, that we can write as the following nonlinear mapping T from $(\overline{b}, \overrightarrow{w})$ to the solution $(b, \overrightarrow{v^1})$:

$$a(\overrightarrow{v^1}, \overrightarrow{\varphi}) = \langle f', \overrightarrow{\varphi}\rangle + \langle G(\overrightarrow{w}, \overline{b}), \overrightarrow{\varphi}\rangle, \quad b_x = \frac{1}{U}(v^0_z+v^1_z) + F\left[\overrightarrow{v^0}+\overrightarrow{w}, \overline{b}_x\right],$$

with a suitable function $G(\overrightarrow{w}, \overline{b})$ that satisfies the following estimate

$$\left\langle G(\overrightarrow{v^1}, b), \overrightarrow{\varphi}\right\rangle \le C\|b\|_{W^{1,\infty}}\left(\|\psi^0\|_{H^3(S)}+\|\overrightarrow{v^1}\|_{H^1(S)}\right)\|\overrightarrow{\varphi}\|_{H^1(S)},$$

where $\|b\|_{W^{1,\infty}} \equiv \sup_x|b| + \sup_x|b_x|$ is assumed to be small enough, and F is such that:

$$b_x = \frac{1}{U}(v^0_z+v^1_z) - \frac{1}{U}b_x(v^0_x+v^1_x) \equiv \frac{1}{U}(v^0_z+v^1_z) + F[\overrightarrow{v^0}+\overrightarrow{v^1}, b_x]. \qquad (4.23)$$

Note that the solution to the original nonlinear problem we wish to find is a fixed point of the mapping T. If $\overrightarrow{w} \in H^1(S)$ and $\overline{b} \in W^{1,\infty}$ then by Lax-Milgram again, the problem (4.23) has a unique solution. However, in order to prove that T is a contraction and to apply the Banach's fixed point theorem, we will need higher regularity on $\overrightarrow{v^1}$. This can be achieved by introducing suitable partitions of unity, local chart diffeomorphisms and classical elliptic estimates. After some delicate estimates one can deduce that the

mapping T is a contraction if $\left\|\psi^0\right\|_{H^3(S)}$ is small enough (see Fontelos and Muñoz, 2007, for more details). Banach's fixed point theorem illustrates that a unique solution exists to the nonlinear free boundary problem.

Remark. The hypothesis concerning the size of the norms of the inflow-outflow velocities $\|\overrightarrow{v}^{\text{in}}\|_{C^2[-1,0]}$, $\|\overrightarrow{v}^{\text{out}}\|_{C^2[-1+b(M),0]}$ and of $b(M)$, mentioned in Theorem 2.1, are required in order to assure that the mapping T is a contraction, allowing for the application of Banach's fixed point theorem. This smallness condition does not prevent our solution from singularities of the shear stress. To finish this section, we conclude with the following estimate regarding the asymptotic behavior of the free boundary near the grounding line:

$$\begin{aligned} b(x) &= \int_0^x \left(\frac{1}{U}(v_z^0 + v_z^1) + F\left[\overrightarrow{v^0} + \overrightarrow{v^1}, b_x\right]\right) dx \\ &\leq Cx^{1+\delta} \sup\left(\frac{1}{x^\delta}\left| \frac{1}{U}(v_z^0 + v_z^1) + F\left[\overrightarrow{v^0} + \overrightarrow{v^1}, b_x\right]\right|\right) \leq Cx^{1+\delta}, \end{aligned}$$

so that the interface is flat near $(0, -1)$. Then, the analysis made for the linear case should be valid and we arrive at the following asymptotic behavior for $b(x)$,

$$b(x) = Cx^{\frac{3}{2}} + o(x^{\frac{3}{2}}), \text{ near } x = 0.$$

Since the free boundary is $C^{1+\delta}$ it can be shown, just as in the linear case, that the weak solutions are in fact strong (i.e., the stream function is C^4) inside $\mathbb{D}$ and up to the boundaries outside $(0, -1)$ (see Fontelos and Muñoz, 2007, for more details).

5. Analysis of the General Case $n > 1$

Due to the complexity of the non linearities appearing in the equations for $n > 1$, we solved the problem near the contact line numerically. As we did analytically for the Newtonian case in section 4.2, we formulate the problem in terms of a stream function and look for separable solutions of the form $\psi = r^m f(\theta)$ being (r,θ), polar coordinates, to the equation (3.10) defined in the half plane $z > -1$ and boundary conditions (3.15) and (3.16). As in the Newtonian case, the asymptotic behavior of the full problem is controlled by the solution to this simpler problem. The aim of our numerical analysis is to obtain a correlation between the exponent n associated with the rheology and the exponent m in ψ, describing the behavior of the flow and therefore the regularity. In this section, we shall briefly comment on the main ideas regarding the numerical resolution and show the obtained results. If we define the operators D_1, D_2, T_1 and T_2, as follows:

$$D_1 \equiv 2\partial_{xz}, D_2 \equiv \partial_{zz} - \partial_{xx}, T_1 \equiv \mu(|D|)D_1(\psi) \text{ and } T_2 \equiv \mu(|D|)D_2(\psi), \tag{5.24}$$

then the definition of $|D|$ and the equation to be satisfied are:

$$|D| = (|D_1(\psi)|^2 + |D_2(\psi)|^2)^{\frac{1}{2}}, \quad D_2T_2 = -D_1T_1. \tag{5.25}$$

Since $\psi = r^m f(\theta)$, we look for separable solutions of the form: $T_1 = \widetilde{r^m} t_1(\theta)$ and $T_2 = r^m t_2(\theta)$, with $\widetilde{m} = m - 2/n$.

The boundary conditions at the interface ice-sea water should be the ones given in (3.16), but due to the fact that we are studying possible singularities near the grounding line, for which higher order derivatives in $(3.16)_2$ are determinant, we shall consider instead of $(3.16)_2$, the condition:

$$[\mu(|D|)(\psi_{zz} - \psi_{xx})]_z + 4[\mu(|D|)\psi_{xz}]_x = 0. \tag{5.26}$$

The boundary conditions at $\theta = \pi$ that we shall consider, written in terms of T_1 and T_2, are:

$$B_1 \equiv T_2 = 0, \quad B_2 \equiv 2\partial_x T_1 + \partial_z T_2 = 0 \text{ at } \theta = \pi. \tag{5.27}$$

At the grounded boundary the following condition should be satisfied: $\psi = 0$, $\psi_\theta = 0$ at $\theta = 0$. The scheme we shall follow is basically based on a shooting method with two parameters, the exponent m and the value of the second derivative with respect to θ of the function $f(\theta)$ at $\theta = 0$, labelled by $s = f''(0)$. We shall shoot from $\theta = 0$ using the data $f(0) = 0$, $f'(0) = 0$, $f''(0) = s$ and $f'''(0) = C$, C a constant, with a fixed value (independent of n) that we choose to be 3. Note that for $n = 1$, $f(\theta) = -3\sin(\theta/2) + \sin(3\theta/2)$, $f''' = 3$.

Thanks to the invariance of the equations under rotations, we are allowed to consider a θ marching scheme and at each level $[pd\theta, (p+1)d\theta]$. We use the identity $\widetilde{r^{m-2}} t_2'' = \partial_{xx} T_2 - D_1 T_1 - \widetilde{m} \widetilde{r^{m-2}} t_2$ at $\theta = pd\theta$, that follows from $(5.25)_2$, in order to obtain the value of the fourth-order derivative of f. Next, we compute by a Euler integration scheme, f and its derivatives at the next step in θ. When we reach the step corresponding to $\theta = \pi$, we evaluate the values of B_1 and B_2, defined by (5.27), for the considered values of the parameters s and m. Note that the values of the parameters s and m are to be tuned in order to minimize the quantity $|B_1| + |B_2|$.

The results for the exponents n and m are represented in Figure 3. Note that for the typical case $n = 3$, the exponent in the Glen's flow law, the obtained value of m is approximately $m \sim 1.25$. Note also that the exponent monotonically decreases with n and that the value for $n = 1$ is $m = 1.5$, which coincides with the one obtained analytically in Fontelos and Muñoz (2007), as expected. From the results we can deduce that $(u, w) \to \overrightarrow{0}$ as $r \to 0$, which implies that the geometry of free boundary, $b(x)$, is planar near the grounding line. As a consequence of this fact, we deduce that the diffeomorphism onto the strip done at the beginning of section 2 is justified as such and that the resolution of the problem in $\mathbb{D}$ can be done following essentially the same lines as in the particular case $n = 1$ (see Fontelos and Muñoz, 2007).

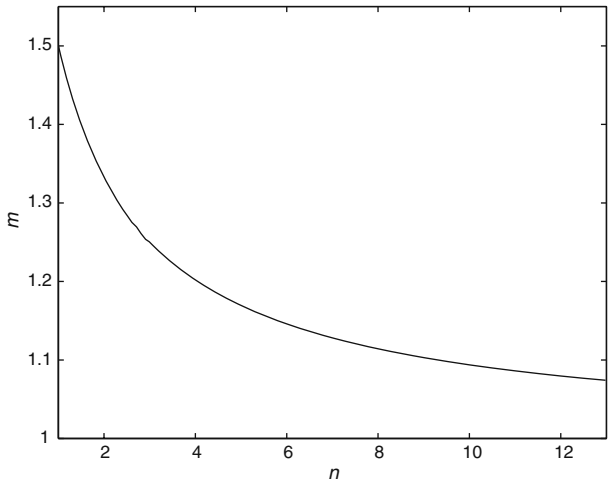

Figure 3
Relation between the exponent m and the exponent of the rheology n.

5.1. Conclusions

In this survey we have presented recent results obtained by the authors concerning the behavior of the fluid flow in the proximity of grounding lines and its impact on the shape of ice shelves. This is a very challenging problem since its analysis encounters three essential difficulties:

1. The nonlinearity of the system of equations modelling the flow. Ice is usually modelled as a non-Newtonian fluid with shear-dependent viscosity which follows a power law of the strain. Classical methods for the analysis of linear systems of partial differential equations, such as separation of variables, use of Fourier transforms, etc., cannot be applied in this context and one has to rely on nonlinear analysis techniques which are, to some extent, still under development. In the context of the present problem, we found that a variational approach based on the definition of suitable functional spaces mimicking physical quantities, such as the total energy dissipation, is a successful one.
2. The existence of mixed boundary conditions in the neighborhood of the grounding line. In the ice-water interface one imposes conditions of equilibrium between fluid stresses and hydrostatic pressure, while in the solid-ice interface we impose no-slip boundary conditions. It is well known that singularities in the solution of partial differential equations may develop in the area of points where different boundary conditions meet. In the present case, by performing a local analysis, we have shown that viscous stresses may, in fact, become singular. We have computed explicitly that which is the form of such singularity and the fluid flow that develops

accordingly. It is worth noting that this result is local in the sense that modifications of boundary conditions in the "far flow field" should not affect the main flow features close to the grounding line. In this sense the imposition of physically more realistic conditions, such as given lateral stresses on the ice shelf, should not alter our results.

3. The existence of a free boundary undetermined *a priori*. We must solve a system of differential equations for the fluid flow in a domain one of whose boundaries (the ice-water interface) is unknown. This characterizes the situation as a "free boundary problem." The main idea to solve it is to transform the unknown domain into a fixed domain -a strip in our case- at the price of adding nonlinear terms to the system. These new nonlinear terms can, nevertheless, be analyzed and controlled so that we can generate the shape of the interface as part of the solution. Our analysis and methodology to solve the difficulties sketched above can potentially be applied without major difficulties to problems incorporating coupling with thermal fields, different boundary conditions away from the grounding line and, possibly partial sliding of the ice sheet over the solid ground. The information on the behavior of the singular flow near the grounding line may also be important for the development of efficient numerical methods. Investigation in these directions are underway.

References

Fontelos, M.A., and Velázquez, J.J.L. (1998), *A free boundary problem for the Stokes system with contact lines*, Commun. in Partial Diff. Eq. *23–7&8*, 1209–1303.

Fontelos, M.A., and Muñoz, A.I. (2007), *A free boundary problem in glaciology: The motion of grounding lines*, Interfaces and Free Boundaries *9*, 67–93.

Fontelos, M.A., Muñoz, A.I., and Schiavi, E., *The ice flow behaviour in the neighborhood of the grounding line. Non Newtonian case*. Submitted.

Fowler, A.C. (1982), *Waves on glaciers*, J. Fluid Mech. *120*, 283–321.

Fowler, A.C. (1987), *Sliding with cavity formation*, J. Glaciology. *33–115*, 255–267.

Friedman, A., and Velázquez, J.J.L. (1995), *The analysis of Coating Flows Near the Contact Line*, J. Differ. Eq. *119–1*, 137–208.

Friedman, A., and Velázquez, J.J.L. (1995), *The analysis of Coating Flows in a Strip*, J. Differ. Eq. *121–1*, 134–282.

Glen (1958), *The flow law of ice*, IAHS, Publ. *47*, 171–183.

Hindmarsh, R.C.A., *Qualitative dynamics of marine ice sheets*. In *Ice in the Climate System*, ed W.R. Peltier (Springer-Verlag, Berlin, 1993), pp. 67–99.

Hutter, K., *Theoretical Glaciology* (Reidel, Dordrecht 1981).

Lliboutry, L.A., *Traité de Glaciologie* (Vol. 1, Masson, Paris, 1964).

Maz'ya, V.G., Kozlov, V.A., and Rossmann, J., *Singularities of solutions to equations of mathematical physics* (Mathematical Surveys and Monographs, AMS 2000).

Nowicki, S.M.J., and Wingham, D.J. (2007), *Conditions for a steady ice sheet-ice shelf junction*. Earth Planet. Sci. Lett. doi:10.1016/j.epsl.2007.10.018.

Schoof, C. (2007a), *Marine ice sheet dynamics. Part1. The case of rapid sliding*, J. Fluid Mech. *573*, 27–55.

Schoof, C. (2007b), *Ice sheet grounding line dynamics: Steady states, stability and hysteresis*, J. Geophy. Res. *112*, F03S28, doi:10.1029/2006JF000664.

VIELI, A., and PAYNE, A.J. (2005), *Assessing the ability of numerical ice sheet models to simulate grounding line migration*, J. Geophys. Res. *110*(F01003), doi: 101029/2004JF000,202.

WILCHINSKY, A.V., and CHUGUNOV, V.A. (2000), *Ice stream-ice-shelf transition: Theoretical analysis of two-dimensional flow*, Annals Glaciology *30*, 153–162.

(Received May 3, 2007, revised March 4, 2008, accepted May 4, 2008)
Published Online First: October 18, 2008

Pure appl. geophys. 165 (2008) 1619–1641
0033–4553/08/081619–23
DOI 10.1007/s00024-008-0392-y

Pure and Applied Geophysics

A Warning System for Stromboli Volcano Based on Statistical Analysis

Giuseppe Nunnari,[1] Giuseppe Puglisi,[2] and Alessandro Spata[1]

Abstract—In this paper we describe a warning system based on statistical analysis for the purpose of monitoring ground deformation at the Sciara del Fuoco (Stromboli Volcano, Sicily). After a statistical analysis of ground deformation time-series measured at Stromboli by the monitoring system known as THEODOROS (THEOdolite and Distancemeter Robot Observatory of Stromboli), the paper describes the solution adopted for implementing the warning system. A robust statistical index has been defined in order to evaluate the movements of the area. A fuzzy approach has been proposed to evaluate an AI (Alarm Intensity) index which indicates the level of hazard of the Sciara del Fuoco sliding.

Key words: Stromboli volcano, warning system, fuzzy logic.

1. Introduction

Like all active volcanoes, the surface of the Stromboli Volcano (Aeolian Island, Sicily) deforms when magma moves beneath it or rises into its conduits. Shallow cracks or deep faults, some tens to hundreds of meters long, may develop in hours or days. The ground can change shape by rising up, subsiding, tilting, or forming fractures that are clearly visible. A variety of methods can be considered to monitor ground deformation in active volcanic areas, such as EDM (Electronic Distance Measuring) or satellite based techniques such as the GPS (Global Positioning Systems) or SAR (Synthetic Aperture Radar). Despite the use of these modern technologies, measuring and evaluating ground deformation data is not an entirely automatic process. However, at present, remote control instrumentation is commercially available to undertake automatic measuring. These measuring systems consist, for instance, of a remote-controlled Total Station that can be programmed to measure slope distances and angles between the sensor and targets appropriately installed in the investigated area at high sampling rate, in the order of 0.01 Hz. Recorded information is then sent to a central control centre (e.g., an observatory) using an appropriate communication link (e.g., radio or/and cable). The use of such kind of equipment is important to attain real-time information on the state of ground deformation and represents a first step in reducing risks in active volcanic areas.

[1] Dipartimento di Ingegneria Elettrica Elettronica e dei Sistemi, Università degli studi di Catania, Viale, A. Doria 6, 95123 Catania, Italy.

[2] Istituto Nazionale di Geofisica e Vulcanologia, Sezione di Catania, Piazza Roma, 2, 95123 Catania, Italy. E-mail: puglisi-g@ct.ingv.it

Despite the availability of real-time information, this is not enough to implement a system able to automatically evaluate the state of ground deformation and eventually issue alarm messages. To achieve this goal, it is necessary to implement appropriate software procedures that can process and interpret ground deformation data, and therefore specific software must be developed.

The main aim of this paper is to present a warning system for deformations occurring within the Sciara del Fuoco (SdF), at Stromboli Volcano, based on statistical data analysis. The first example of a warning system developed to monitor such movements was designed by NUNNARI *et al*. (2006). It was based on the estimation of two quantities referred to as DMV (Daily Maximum Variation) and MPE (Maximum Prediction Error). Given the availability of these parameters the previous warning system was able to evaluate in a fuzzy manner an Alarm Intensity (AI) index representing the strength of the volcanic sources with respect to daily average measurement variation.

Starting from the essential ideas of the previous warning system and exploiting the experience gained over the last three years, we propose in this paper a new design of the warning system. Due to the time-variant dynamic of the SdF we have adopted an approach based on a self-adaptive dynamic threshold updated at every acquisition. By self-adaptive threshold our warning system is able to adapt to variations in the dynamic of the volcano flank investigated. The core of the proposed methodology is based on a statistical index, which was processed through suitable fuzzy rules in order to evaluate the AI index, to give a measure of the hazard connected with movements of the SdF area.

2. *The THEODOROS Measuring System*

Setting up the monitoring system was a real challenge, given the logistic and operative conditions during the 2002–2003 volcanic crisis. In order to monitor the ground deformation affecting the Sciara del Fuoco (SdF), the name of the volcano flank investigated, the chosen instrument was the Leica TCA 2003 Total Station (TS) equipped with GeoMos software (Leica proprietary software; LEICA and GEODETICS, 2002) that allows remote sensor control. The acronym of this system is THEODOROS (THEOdolite and Distance-meter Robot Observatory of Stromboli) (PUGLISI *et al*., 2004) . To ensure a continuous stream of data from the instrument, it requires a constant power supply and a continuous link with the PC controlling the Total Station's activities, installed on the S. Vincenzo Observatory, where the National Department of Civil Protection (DPC) control room is located. A reference system of 5 reflectors (Fig. 1), (400, CURV, BORD, SEMF, SPLB2, here these acronyms indicate the names of the points of the measuring network) was installed around the TS, on sites considered geologically stable. The reference system aims to guarantee the same orientation in space (both horizontally and vertically) through the measurements of appropriate reference baselines. Initially, THEODOROS carried out measurements on only four reflectors installed on the SdF

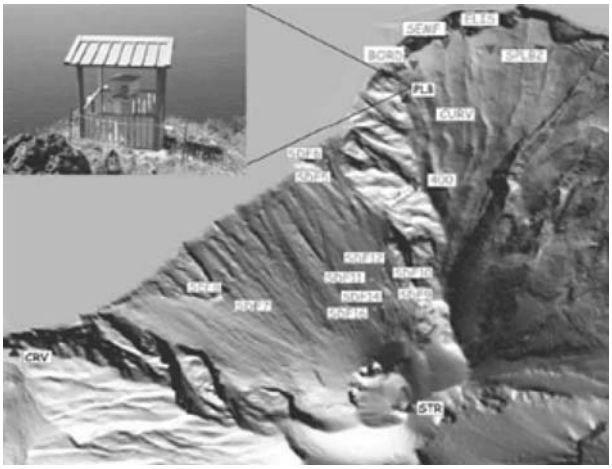

Figure 1
Map of the positions of the reflectors and the Total Station.

(SDF5, SDF6, SDF7 and SDF8) and on three reflectors installed around the site belonging to the reference system (SEMF, 400, SPLB2). After the end of the 2002–2003 eruption, the network was improved by setting up other reflectors in the SdF and redefining the reference network. Before the 2007 eruption, THEODOROS consisted of five reflectors for the reference system (400, BORD, SEMF, SPLB2 plus ELIS), ten reflectors for monitoring movements in the SdF (the four previously installed plus SDF9, SDF10, SDF11, SDF12, SDF14, SDF16) and two more reflectors to check the stability of the measurements both on short and very long distance measurements (CURV and CRV) (Fig. 1). The present system aims to follow the post-eruptive movements of the lava flow field emplaced during the 2007 eruption. The measurement strategy assumes that the horizontal geometry and the relative distance of the reference system are fixed (by fixing the coordinates of the reference system benchmarks), while the TS adjusts its own vertical positions by using only the internal vertical compensators. This geometry is kept fixed through each cycle of measurements during which the TS successively performs the measurements in the group of reference system points and monitoring targets. The sample time indicated as t_c hereafter is set to be $t_c = 30$ minutes so we have 48 cycles per day. Each measurement for each target or reference point provides the instantaneous values of three relevant pieces of information: The slope distance (sd), the horizontal (hz) angle and the vertical angle (ve). Starting from this information, the GeoMos system is able to transform the TS measurement vectors (whose components are sd, hz, ve) into an equivalent vector whose components are expressed in terms of North (N), South (S) and Up (U) with respect to the assumed reference system. In this computation, GeoMos is able to take into account the constraints imposed by the assumption of the reference system.

3. Harmonic Analysis

In this section we describe some analyses with the aim of characterizing features that may be useful to describe normal activity, i.e., quiescent time period of the volcano.

Although the resu1ts of this section are not directly involved in the design of the warning system, they are useful to characterize periodic components which affect the recorded time series. A general overview of this topic can be found in PERCIVAL and WALDEN (1993). Since the measured variables represent ground deformations, it is known that they are affected by several noise sources such as thermo-elastic effects due to temperature, sea and moon tides and so on. The analysis presented in this section is devoted to estimate the strength of such effects in the measured signals.

We have implemented two tests to verify the presence of periodic signal components. These methods are built on the assumption that the noise is white and are based on both the Discrete Fourier Transform (DFT), here calculated by using the Fast Fourier Transform (FFT) algorithm, and the periodogram of the signal to identify the characteristics of the periodic signals.

Let $x_0, x_1, \ldots, x_{N-1}$ be a finite sequence of real or complex numbers of length N. The DFT, X_k, and the periodogram, P_k, are defined respectively by formulas (1) and (2) :

$$X_k = \sum_{n=0}^{N-1} x_n e^{-\frac{2\pi i}{N} nk}, \quad k = 0, \ldots, N-1 \tag{1}$$

$$P_k = \frac{1}{N} |X_k|^2, \quad k = 0, \ldots, N-1, \tag{2}$$

where e is the base of the natural logarithm and i is the imaginary unit ($i^2 = -1$)

The DFT is a mathematical transformation that transforms a discrete-time function, often created by sampling a continuous-time function, into another which is called the frequency domain representation of the original function. The DFT is defined in a frequency domain consisting of a number of discrete components known us Fourier components. As we can see from (1) the number of Fourier components, X_k, are equal to the number N of the input samples. The term periodogram was coined by ARTHUR SCHUSTER (1898). It is an estimate of the spectral density that is usually used to discover evidence of periodicities in any signal.

The first test we have implemented in order to verify the existence of a periodic component is the Fisher Test (FISHER, 1929). It allows assessing if a single periodicity exists in a time series. The test statistic is

$$g = \frac{\max_{1 \le k \le N} P_k}{\sum_{i=1}^{N} P_k}, \tag{3}$$

where N is the number of Fourier components. Critical values for Fisher's test, g_f, can be approximated by

$$g_f = 1 - \left(\frac{\alpha}{N}\right)^{1/(N-1)}. \tag{4}$$

If $g > g_f$ for some α, the null hypothesis (signal is pure white noise) is rejected, and it can be stated with a $(1-\alpha)$ confidence level that a periodic signal is present at the frequency where the periodogram has its maximum. The major disadvantage of Fisher's test is that it only tests the presence of a single periodic component. SIEGEL (1980) extended Fisher's test for cases in which up to three periodic components are present in a time series. Starting from a normalized periodogram

$$\bar{P}_k = \frac{P_k}{\sum_{i=1}^{N} P_i}, \tag{5}$$

the test is based on all values of $\bar{P}_k$ that exceed some level g_s instead of only their maximum as in Fisher's test. g_s is related to g_f by a parameter λ with $0 < \lambda < 1$. The test statistic is

$$T_\lambda = \sum_{k=1}^{N} \left[P_{Nk} - \lambda g_f\right]_+, \tag{6}$$

where $[a]_+ = \max(a,0)$. The choice of λ, between 0 and 1, is to be made from general theoretical considerations regardless a particular data set (SIEGEL, 1980). Fisher's test is obtained when $\lambda = 1$ because $T_1 > 0$ if and only if some P_{Nk} exceeds g_f. A choice of λ close to 1 might therefore be used when at most simple periodicities are expected. A smaller value of λ might be used when compound periodicities are a possibility. Since it is reasonable to think that our observations are affected at least by two or more periodicities we will use both $\lambda = 0.6$ and $\lambda = 0.4$ following the suggestion from the literature (ANDEL, 1994).

For $20 < K < 2000$ critical values of $t_{\lambda,\alpha}$ for the Siegel test can be computed according $t_{\lambda,\alpha} = aK^b$ (PERCIVAL and WALDEN, 1993). Empirical coefficients a and b are given in Table 1 for $\alpha = 0.05$ that is the level of confidence value we have adopted. Similar to Fisher's test, the null hypothesis is rejected if $T_\lambda > t_{\lambda,\alpha}$. In this situation, one or more periodic components are present in the time series at the frequencies where the largest $P_N(f_k)$ values occur. Since the Fisher test provides information regarding an individual component alone, here the Siegel test, which extends the former one, is

Table 1

Coefficients for computing critical values $t_{\lambda;\alpha}$ for Siegel's test

	$\lambda = 0.4$	$\lambda = 0.6$
$\alpha = 0.05$	$a = 0.9842$ $b = -0.51697$	$a = 1.033$ $b = -0.72356$

considered. Now we will investigate how Siegel's test performs on the considered data set, showing its usefulness for data interpretation. This test is strongly related to the periodogram goodness which depends on the frequency resolution f_r used to compute the DFT. The frequency resolution determine's the spacing of the samples in the frequency domain and it is defined as the sample frequency $f_0 = 1/t_c$ divided by the number N of the samples of the input discrete function. In order to reduce the value of f_r we can only increase the number N of sample because our sample time t_c is fixed to 30 minutes. We have found that the minimum number of Fourier components for which in the Siegel test the null hypothesis is rejected is $N = 256$, that correspond to five days of acquisition (240 samples) plus 16 zero-valued samples appended to the end of the discrete sequence (zeropadding technique). The choice of an integer number power of two lets us obtain the maximum efficiency of computation from the FFT algorithm.

As an example, we process the time series referring the point SDF5 (North). The power spectrum of this series is shown in Figure 2. Since $T_{0.6} > t_{0.6;0.05}$ ($T_{0.6} = 0.170$, $t_{0.6,0.05} = 0.018$) and $T_{0.4} > t_{0.4,0.05}$ ($T_{0.4} = 0.1714$, $t_{0.4,0.05} = 0.0545$) the null hypothesis is rejected for both values of λ and therefore we can state on a 0.95 level of confidence ($\alpha = 0.05$) that harmonic components are present at the frequencies where the normalized periodogram $\bar{P}_k$ has its maximum. In particular, the presence of 24 h and 12 h components is evident. The 24 h harmonic component is well known as the daily component that is due to thermo-elastic effects, while the 12 h harmonic component might be interpreted as due to tidal force.

The tool software developed to process THEODOROS measures provides filter design and statistical analysis to better characterize both 24 h and 12 h effects. We use bandpass filters to isolate the single component in order to perform statistical analysis in the time domain.

Figure 3 shows periodic components of SDF5 (North component) target, while Table 2 gives statistical properties of periodic components of several targets. The 24 h and 12 h components shown in Figure 4 are not perfectly sinusoidal due to the finite band of the considered bandpass filters. However, these components allow characterization of some useful information on daily and 12 h ground deformation such as: minimum, maximum and standard deviation.

These tables show the "normal" North, East and Up ground deformation components for each benchmark whose data set allows calculation of them. Since both diurnal and semi-diurnal periodic components act simultaneously on the process of ground deformation, it is therefore possible to extract useful information from the raw data by adequately filtering their combined behaviors. For this purpose, a bandpass filter is used to isolate both periodic components in order to perform an analysis in the time domain. This operation is shown in Figure 4.

The arranged action of the two periodic components involves an increase in the range of variation of the observed data with respect to the action of the single component. Statistical analysis on these data has been useful in order to define and optimize a simple

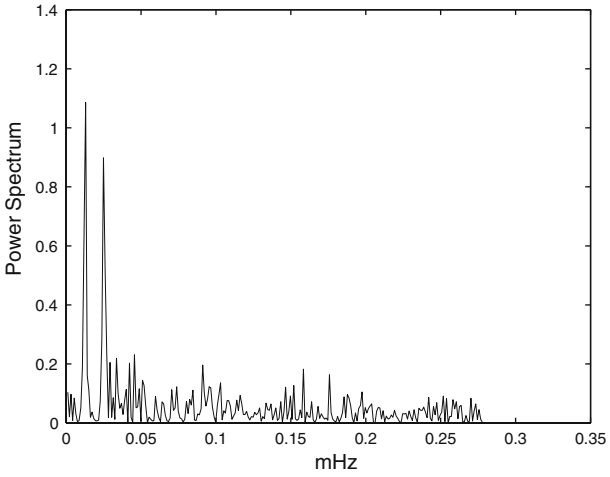

Figure 2
Power Spectrum of SDF5 (North coordinate).

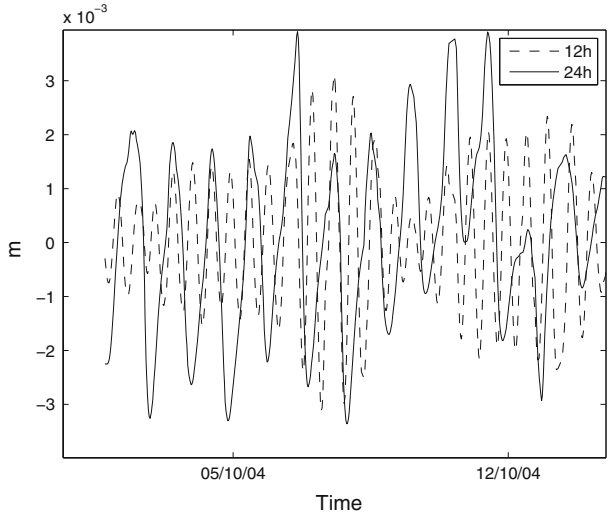

Figure 3
24 h and 12 h periodic components of SDF5 (North coordinate).

analytical model capable of providing an approximation of average behavior of observed components. In order to model the two periodic components, an analytical model consisting in the sum of two sinusoidal functions with periods, respectively, of 24 and 12 hours was defined:

Table 2

Statistical properties of 24 h and 12 h (between brackets) periodic components (mm)

Target	Min.	Max.	StdDev
SDF5 North	*−3.18 (−4.29)*	*2.88 (4.38)*	*1.61 (1.80)*
SDF6 North	*−3.34 (−4.52)*	*3.25 (4.73)*	*1.82 (1.92)*
SDF9 North	*−4.14 (−3.38)*	*4.62 (3.39)*	*1.47 (1.13)*
SDF11 North	*−2.06 (−2.93)*	*2.18 (2.66)*	*0.90 (1.92)*
SDF13 North	*−4.86 (−3.40)*	*5.31 (3.44)*	*1.56 (1.06)*
SDF14 North	*−2.34 (−2.91)*	*2.21 (2.86)*	*1.00 (1.01)*
SDF5 East	*−4.63 (−6.42)*	*5.52 (5.81)*	*2.21 (2.03)*
SDF6 East	*−1.81 (−6.87)*	*6.92 (3.33)*	*1.92 (1.68)*
SDF9 East	*−4.32 (−15.09)*	*14.58 (7.82)*	*3.33 (4.00)*
SDF11 East	*−6.30 (−10.28)*	*12.18 (13.04)*	*2.75 (4.34)*
SDF13 East	*−1.86 (−13.56)*	*11.57 (5.53)*	*2.86 (3.90)*
SDF14 East	*−7.70 (−4.34)*	*16.48 (17.07)*	*3.00 (4.09)*
SDF5 Up	*−5.86 (−3.75)*	*2.26 (1.75)*	*1.79 (1.12)*
SDF6 Up	*−3.33 (−2.57)*	*2.55 (2.00)*	*1.50 (0.98)*
SDF9 Up	*−0.90 (−6.1)*	*1.12 (5.79)*	*1.07 (2.33)*
SDF11 Up	*−1.05 (−2.34)*	*1.37 (7.77)*	*1.21 (2.18)*
SDF13 Up	*−0.94 (−7.95)*	*1.13 (8.05)*	*1.04 (2.54)*
SDF14 Up	*−1.02 (−6.70)*	*1.27 (2.15)*	*1.21 (2.04)*

$$f(nt_c) = A\cos(2\pi fnt_c + \theta_1) + B\cos(2\pi 2fnt_c + \theta_2). \tag{7}$$

Parameters A and B (amplitudes), θ_1 and θ_2 (phases) have been estimated by using a genetic optimization approach since it is recognized as an efficient algorithm to overcome the problem of local minima. The data set has been preliminarily split into two parts of K_I and K_V samples used to identify and validate the model respectively.

The cost function J assumed was the mean-square error defined as follows:

$$J = \frac{1}{K_I}\sum_{n=1}^{K_I}(y_n - f(nt_c))^2, \tag{8}$$

where y_n are the measurements.

In order to evaluate the goodness of the model, the modelling EFficiency index (EF) has been used. It is defined as

$$EF = 1 - \frac{\sum_{n=1}^{K_V}(y_n - f(nt_c))^2}{\sum_{n=1}^{K_V}\left(f(nt_c) - \bar{f}\right)^2}, \tag{9}$$

where $\bar{f}$ is the mean value of the identified model.

For instance, the parameter values found in order to model the average behavior of the North components of the SDF5 benchmark are $A = 0.00231$, $B = -0.00136$,

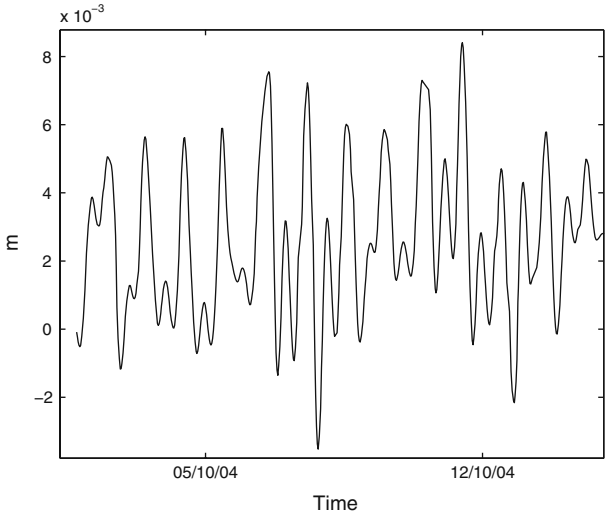

Figure 4
Contribution of 24 h and 12 h periodic components of SDF5 (North coordinate).

$\theta_1 = 1.8776$, $\theta_2 = 4.35601$ and obviously $f = 1/86400$ Hz. The model performed well with a modelling efficiency of 0.82. The result is shown in Figure 5.

4. Data Presentation

Data collected from THEODOROS system allow effective monitoring of ground deformation observed at the SdF. As we can see from Figure 6 the North, East and Up components exhibit trends related to the downslide movements of the SdF.

These temporal series have been preliminarily pre processed in order to remove the offsets affecting the original data set and to handle missing data. Here by offset we intend a sharp variation of the time series which is generally due to either periodical maintenance or instrument malfunctions. The estimation method used to handle missing data was the linear interpolation between the adjacent valid values above and below the missing one.

In Figure 7 the rates of variation of the recorded components are shown. They have been calculated through the linear regression slope of the observed displacements during an interval of 15 days.

Statistical analysis performed on data reported in Figure 7 has shown that the network benchmarks can be roughly classified into three sets, based on the average rates of variations of the North, East and Up components. These sets have been termed Slow, Medium, Fast. The cluster referred to as Slow contains benchmarks SDF5 and SDF6 and the average speed is less than 0.1 mm/day. Similarly, the Medium cluster consists of

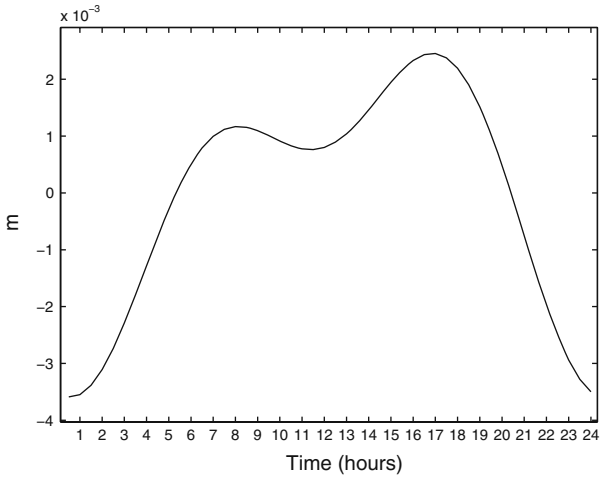

Figure 5
Average behavior of periodic components of SDF5 (North coordinate).

benchmarks SDF7 and SDF10, which exhibit a velocity of about 0.7 mm/day. Finally, the Fast cluster consists of benchmarks SDF9, SDF11, SDF13 and SDF14, which are characterized by a velocity greater than 1 mm/day.

5. *The Warning System*

In order to monitor the movements affecting the SdF, a robust statistical method combined with a fuzzy processing has been developed. The statistical method is based on an opportunely modified version of the ALICE index (Tramutoli, 1998; Di Bello, 2004) for the THEODOROS system. The acronym ALICE stands for Absolutely Local Index of Change of the Environment. This index is then processed through suitable fuzzy rules in order to evaluate the AI index, which gives a measure of the hazard connected with the sliding of the of the Sciara del Fuoco area.

The main feature of this method is the use of a self-adaptive dynamic threshold, instead of a static one. Its value is not assumed *a priori*, but it is computed on the basis of the measurements. This choice is based on the experience gained in processing the considered ground deformation data, highlighting that the deformation phenomena varies both in time and space. By self-adaptive threshold, our method can adapt the value to the variation of ground deformation intensity observed on the SdF. When the movements are intense, the threshold will become higher; and when the movements slow down, the threshold will also drop.

The warning system implementation requires a three-step procedure. The first step consists of the characterization of what is referred to as *normal behavior*. Indeed, as both

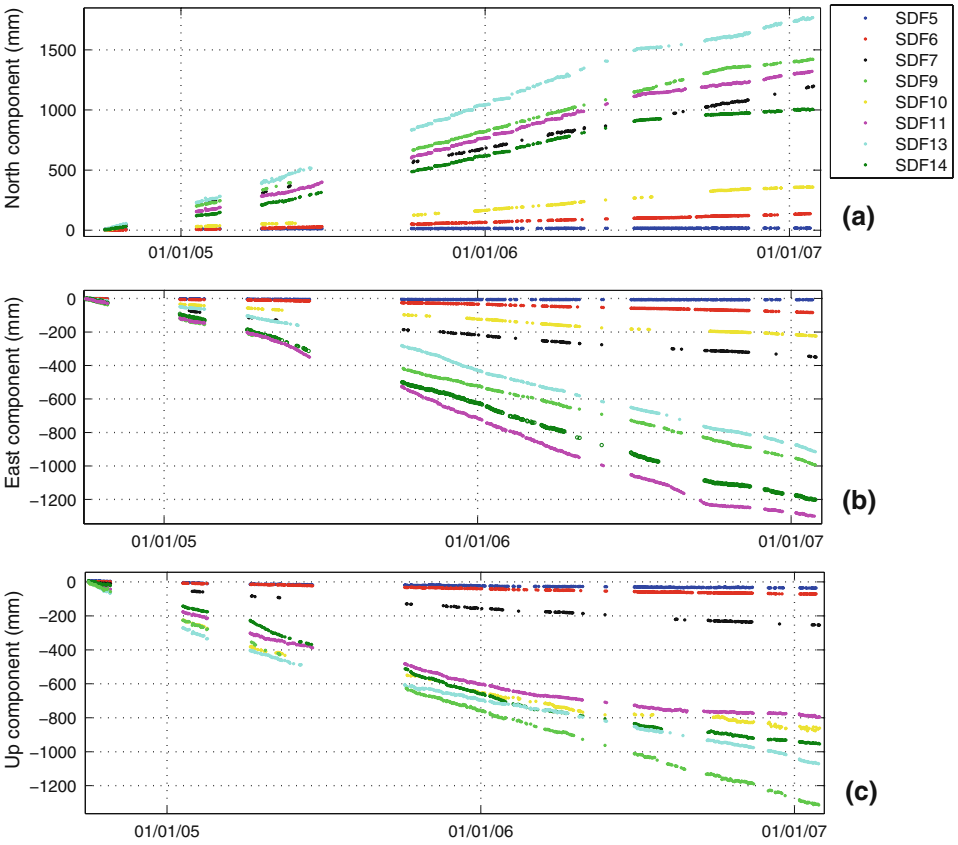

Figure 6
Daily averages of the North (a), East (b) and Up (c) coordinates relevant to the benchmarks within the SdF, from November 2004 to January 2007.

experience and good sense suggest, a signal cannot be interpreted as anomalous *per se*, but only by comparison with a normality which must be preliminarily defined. The second step is to formulate change detection criteria which should be specific for each class of phenomenon under consideration. The third step allows the evaluation of changes.

These steps are based on the following variables. Let $T^i_{SDFx}(t)$ be a generic feature of the benchmark *SDFx* (e.g., the slope distance between TS and the SDF benchmark) at time t of the day i. Let $\Delta T^i_{SDFx}(t)$ be the absolute value of the difference between two subsequent measures at day i:

$$\Delta T^i_{SDFx}(t) = |T^i_{SDFx}(t) - T^i_{SDFx}(t - t_c)|, \tag{10}$$

where t_c is the sample time.

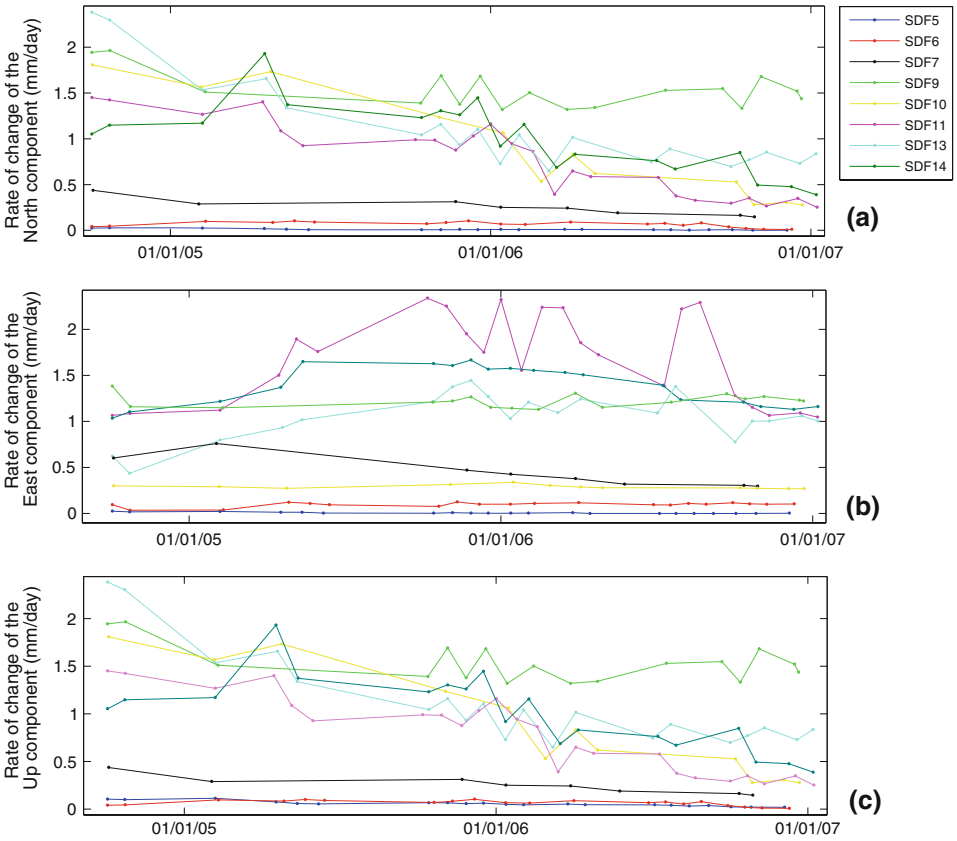

Figure 7
Rate of changes of the North (a), East (b) and Up (c) coordinates (mm/days).

Let S_t^j be the set of the variables $\Delta T^i_{SDFx}(t)$ computed at the same time t of the previous days j with $0 < j \leq i$

$$S_t^j = \left\{\Delta T^j_{SDFx}(t) | 0 < j \leq i\right\}. \tag{11}$$

Let $\bar{S}_t^j$ and $\sigma_{S_t^j}$, respectively, be the mean value and the standard deviation of the set S_t^j

$$\bar{S}_t^j = \frac{1}{N}\sum_{j=1}^{N} \Delta T^j_{SDFx}(t), \tag{12}$$

$$\sigma_{S_t^j} = \sqrt{\frac{1}{N}\sum_{j=1}^{N} (\Delta T^j_{SDFx}(t) - \bar{S}_t^j)^2}, \tag{13}$$

where N is the number of elements of the set S_t^j.

The ALICE index used to detect the anomalous value of the variable $\Delta T^i_{SDFx}(t)$ is defined as

$$A_{\Delta T^i_{SdF_x}(t)} = \frac{\Delta T^i_{SDF_x}(t) - \bar{S}^j_t}{\sigma_{S^j_t}}. \tag{14}$$

This index provides an estimate of the difference between the observed value $\Delta T^i_{SDFx}(t)$ at time t and the mean value $\bar{S}^j_t$ of the previous observations acquired for the same reflector in the past days at the same time t, weighted by the related signal standard deviation σ^j_{St} which includes all possible noise sources not related to the event to be monitored. The robustness of this approach is intrinsic, because the higher the standard deviation σ_S of the signal, the harder it is to achieve high values of ALICE index, reducing, in this way, the problem of false alarms. Due to the fact that the set S^j_t and its statistical properties are updated after each acquisition of the THEODOROS system, the proposed warning approach is based on a self-adaptive dynamic threshold computed on the basis of the measurements and updated after each measurement.

In Figure 8 we show the behavior of ALICE index computed for the slope-distance of SDF5 target plotted together with its statistical properties (mean and variance).

5.1. A Fuzzy Approach to Implement a Warning Systems for the THEODOROS System

The idea underlying the development of the warning system for THEODOROS is based on a fuzzy evaluation of the ALICE indices. Fuzzy logic is based on the premise that the key elements in the activity of human thinking are not numbers but rather indicators of a fuzzy set, i.e. of classes of objects in which the transition between membership and non-membership to the class is gradual, or even distinct. In this way, every element belongs to a set with a determinate degree of membership. The continual presence of imprecise concepts in thinking suggests the idea that human reasoning is founded on imprecise logic that uses fuzzy sets, connectives, and implication, rather than on binary logic (FORTUNA *et al.*, 2001). What is characteristic of fuzzy logic is that it allows imprecise concepts to be dealt with in a well-defined way. It is a theory for representing more or less complex phenomena by defining a certain number of fuzzy sets that are elaborated by means of the appropriate connectives.

Formally, a fuzzy set A can be defined as a collection of objects from the universe of discourse U having some properties in common. The set is characterized by a membership function $\mu_A : U \rightarrow [0,1]$, which associates with every element y of U a real number $\mu_A(y)$ belonging to the interval [0,1]; this represents the degree of membership of y to the fuzzy set A. In general, the greater the value of the function with which the element y belongs to the fuzzy set A, the greater the evidence that the object y belongs to the category described by the set A.

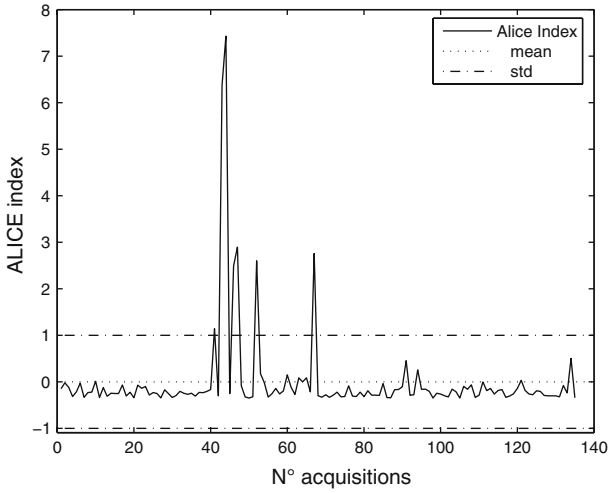

Figure 8
ALICE index of SDF5 target - Slope Distance.

The definition of fuzzy set just given allows us to systematically use linguistic variables, i.e., variables which assume adjectives as values, specified by fuzzy sets.

For example, supposing that the linguistic variable *ALICE* must be defined, and that one wants to represent the linguistic concept of *"low"* for the *ALICE index.* This concept can be expressed, using traditional logic, by a binary membership function defined as follows: If $\mu(ALICE) = 0$, the variable *ALICE* does not belong to the specified set, e.g., to the interval $[-1, 1]$; if instead it does belong, then $\mu(ALICE) = 1$.

In the framework of classical sets utilizing a rectangular function, defined in the universe of discourse, that can be described as reported in Figure 9.

On the other hand, a fuzzy set that represents the same concept can use membership function values $\mu(ALICE)$ that vary continuously in the interval [0, 1], allowing intermediate values to be defined between the conventional evaluations 0 and 1. For example, a fuzzy set suitable for representing this concept can be defined as depicted in Figure 10.

An ordinary set is thus precise in its meaning and presents a definite transition from membership to non-membership.

A fuzzy set, instead, allows representing the imprecision of a given concept by means of the degree of the membership function. Indeed, as we can see from Figure 10, when the ALICE index value is 0 it belongs to the fuzzy set "low" with a degree of membership equal to 1. If the ALICE index is 0.5 then its degree of membership to the fuzzy set "low" is 0.5 and so on.

Similarly, it is possible to represent by means of fuzzy sets the concept of low, mean and high ALICE, referred to the universe of discourse determined by the application, and defining the membership functions of the three fuzzy sets.

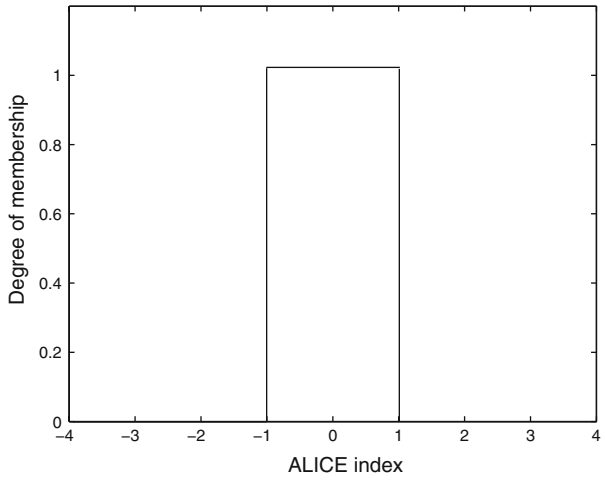

Figure 9
Representation of the "*ALICE low*" set obtained utilizing the concepts of classical sets.

Thus fuzzy logic represents a good approach for the realization of a warning system for THEODOROS. In a such conditions, a key point of the warning system is the fuzzy evaluation of an index, referred to as AI (the Alarm Intensity), which gives a measure of the hazard connected with movements of the SdF area. In order to reduce the complexity of the fuzzy system, we adopt the following strategy. Three sub-AI indices are firstly evaluated for each individual cluster of benchmarks, then the sub-AI indices are

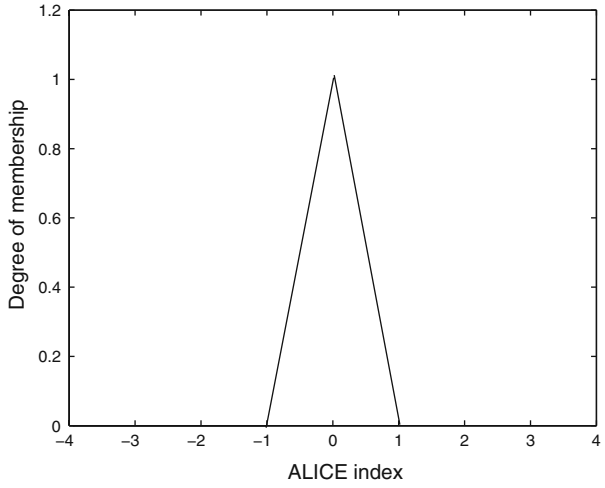

Figure 10
Representation of the "*ALICE low*" set obtained utilizing the concepts of fuzzy logic.

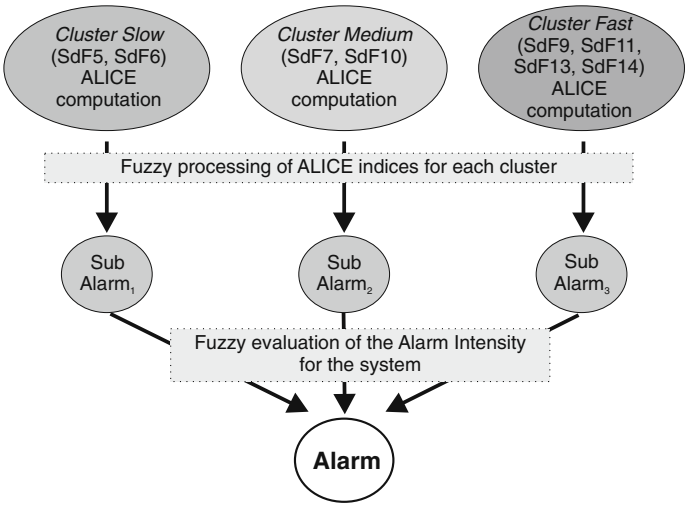

Figure 11
Flow chart of the procedure to evaluate the AI, starting from the single ALICE indices computed for different benchmarks.

integrated in order to obtain a value for AI which takes into account the overall set of benchmarks (Fig. 11).

To verify the reliability of the recording system, a preliminary fuzzy evaluation is performed on the reflectors belonging to the set of the reference system (i.e., 400, CURV, BORD, SEMF, SPLB2) and to the set referred to as check (i.e., CURV and CRV). Either the reference system or the check of the reflectors have anomalous values of AI, then the acquisition cycle is considered unreliable.

The expression of ALICE index (14), contains two normalization terms: The first appears in the mean value and the second is the standard deviation. This double normalization aims to nullify the effects of mean and standard deviation on the data, thus allowing underlying characteristics of different data sets to be compared (MARRADI, 1993). For this reason the statistical pre processing performed by the ALICE index makes comparable variables belonging to different distributions. This feature is very useful for the warning system implementation because due to the nonlinear and time-varying dynamics of the SdF, the benchmarks have different statistical distributions. Therefore, after the double normalization all the benchmarks can be simultaneously processed and evaluated by a unique set of membership functions.

The computation process starts with the definition of the fuzzy sets. The development of the warning system requires two different kinds of fuzzy sets. The first one is necessary to process the ALICE indices of the benchmarks of each cluster in order to evaluate the sub-AI index value of the cluster. The second one simultaneously processes all the sub-AI indices computed in step one in order to evaluate the total AI index value. Due to the ALICE index unitary variance, we assume the universe of discourse of fuzzy set referred

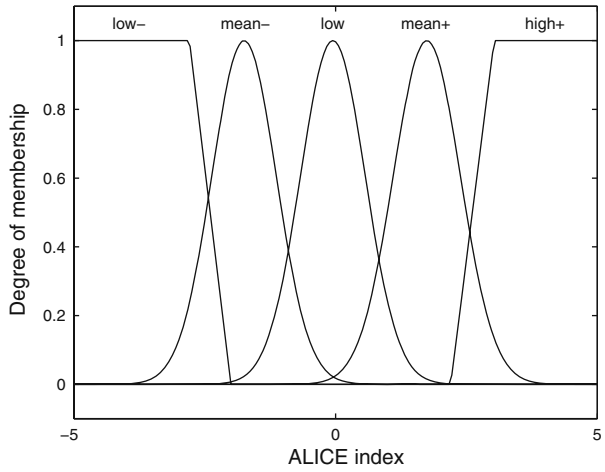

Figure 12
Fuzzy sets for *ALICE* index.

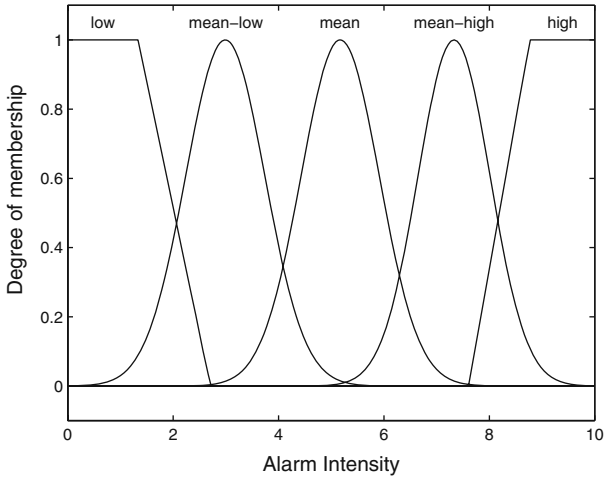

Figure 13
Fuzzy sets for sub-AI and AI.

to as "low" ranging between −1 and 1. Outside the range [−1, 1] we arrange in a symmetrical way the fuzzy sets "mean" and "high" (Fig. 12). As regards the evaluation of the indices sub-AI and AI, we have considered five fuzzy sets, referred to as "low", "mean-low", "mean", "mean-high", "high" (Fig. 13). The range of variation of both sub-AI and AI indices is conventionally assumed to be [0, 10].

Table 3

Fuzzy rules for two benchmarks

ALICE index 1	ALICE index 2	Sub-AI
low	*mean*	*mean-low*
high	*mean*	*mean-high*
high	*low*	*mean*

Table 4

Fuzzy rules for three benchmarks

ALICE index 1	ALICE index 2	ALICE index 3	Sub-AI
low	*mean*	*high*	*mean*
low	*mean*	*mean*	*mean -low*
low	*low*	*high*	*mean*
mean	*mean*	*high*	*mean -high*
mean	*high*	*high*	*high*
low	*high*	*high*	*mean-high*

Table 5

Fuzzy rules for AI evaluation

sub-AI1	sub-AI2	AI
low	*mean-low*	*mean-low*
low	*Mean-high*	*mean*
mean	*Mean-high*	*mean-high*
mean-low	*Mean-high*	*mean*

The composition of the rules for the fuzzy warning system follows a simple linguistic approach. For example, in the case of a cluster consisting of two reflectors, some rules adopted in the definition of the warning system and shown in Table 3 are:

– *if the ALICE index value of the first reflector is "low" and the second one is "mean" then the sub-AI index value of the cluster will be "mean-low";*
– *if the ALICE index value of the first reflector is "high" and the second one is "mean" then the sub-AI index value of the cluster will be "mean-high";*
– *if the ALICE index value of the first reflector is "high" and the second one is "low" then the sub-AI index value of the cluster will be "mean".*

Similar rules in the case of the cluster consisting of three benchmarks are reported in Table 4.

Likewise, the sub-AI are fuzzy evaluated to attain a value for the total AI of the Sciara del Fuoco area. Some adopted rules, reported in Table 5, are the following :

– *if the sub-AI index value of the first cluster is "low" and the second one is "mean-low" then the AI index value of the Sciara del Fuoco will be "mean-low";*
– *if the sub-AI index value of the first cluster is "low" and the second one is "mean-high" then the AI index value of the Sciara del Fuoco will be "mean";*
– *if the sub-AI index value of the first cluster is "mean" and the second one is "mean-high" then the AI index value of the Sciara del Fuoco will be "mean-high".*

5.2. *Fuzzy Processing of ALICE Index*

Due to of the absence of significant ground deformation episodes in the data set analyzed in this paper the test of the proposed methodology was essentially performed on synthetic data. However, the results of a test carried out on data from October 2005 to April 2006, during which the volcano was in *normal* condition, are also reported.

In order to perform a sensitivity analysis of the proposed methodology a synthetic data set consisting of two benchmarks whose dynamics are simulated through two Gaussian random variables has been made. Since the proposed warning system is based on a self-adaptive dynamic threshold, we have chosen to give results of the sensitivity analysis in terms of the percentage increases of the ALICE indices with respect to their mean values. The tests carried out indicate that if both ALICE indices show a percentage increase greater than 30% with respect to their mean value then the AI reaches its maximum value, "high" in fuzzy terms. In the opposite case when the percentage increase of both indices is less than 5% a near zero Alarm Intensity, "low" in fuzzy

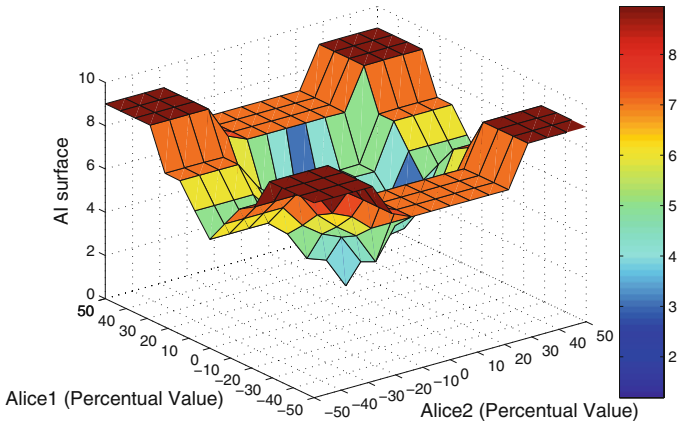

Figure 14
Surface of the Alarm Intensity given in terms of percentage increase with respect to the mean value of the observations; color bar indicates the values of AI.

terms, is given (Fig. 13). The Alarm Intensity becomes "mean-low" when both indices show a percentage increase ranging from 5% to 10%. The situation described above (both indices high, low or mean-low) is extreme. There are of course infinite possible combinations of the two indices and for each the sensitivity of the system can be obtained from analysis results shown in Figure 14.

Testing the data set with actual measurements we have found that the presence of discontinuities, due to offsets and periodical maintenance of the system, results in a number of false alarms issued by the warning system. The example considered here, is relevant to data from October 2005 to April 2006 for two (SDF7, SDF10) and three (SDF9, SDF13, SDF14) benchmarks. In these examples the ALICE indices are computed by acquisition recorded from hours 12:00 to 12:30.

In Figure 15 we show the ALICE indices of SDF7 and SDF10 benchmarks together with their sub-AI values. In proximity of the 40th acquisition, some "mean" values of alarm intensity can be observed. A posterior analysis has shown that they are all false alarms caused by malfunctioning of the acquisition system. After the maintenance of the acquisition system, the AI returned to normal level. Both the sub-AI and AI values are reported also as color bars, in order to highlight their variation in time.

Similarly, the fuzzy evaluation performed on cluster of SDF9, SDF13, SDF14 benchmarks (Fig. 16) has shown "mean" values of sub-AI in the same period. Finally, Figure 17 shows the total AI evaluation.

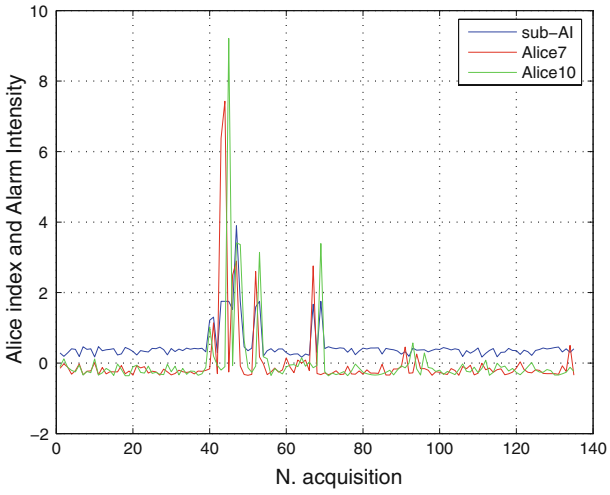

Figure 15
ALICE indices of SDF7 (red), SDF10 (green) and their sub-AI (blue).

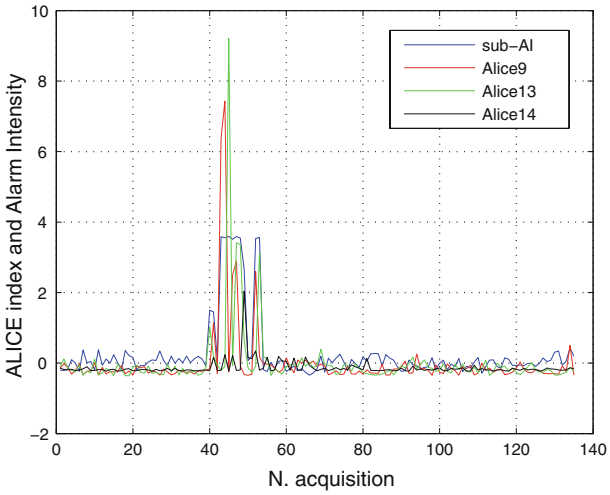

Figure 16
ALICE indices of SDF9 (red), SDF13 (green), SDF14 (grey) and their sub-AI values (blue).

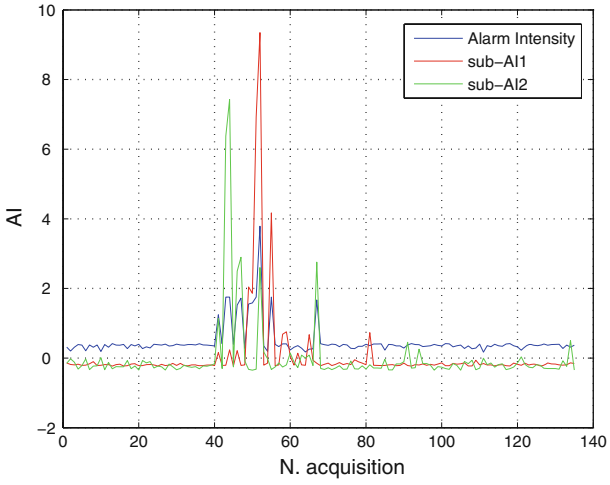

Figure 17
Total AI evaluation.

6. *Conclusions*

In this paper statistical analysis on ground deformation time-series recorded at Stromboli Volcano (Sciara del Fuoco) has been performed. The results obtained have been very useful both for characterizing the *normal* ground deformation pattern in the area of SdF at Stromboli and for implementing a warning system prototype. Spectral analysis of a generic time series, performed by using the Fast Fourier Transform (FFT)

algorithm and Siegel test, highlighted that signals are affected by two marked periodic components: 24 h and 12 h. Statistical analysis on both components has been performed and an analytical model has been defined in order to characterize their contribution to the normal activity of ground deformation at the Stromboli Volcano. A simple ALICE index has been defined to evaluate the movements of the individual benchmark. Finally, a fuzzy approach has been proposed to obtain a synthesis of data referring to the overall set of benchmarks. This allows evaluation of the AI index which gives a measure of the hazard of landslide of the Sciara del Fuoco. The implemented warning system has been tested on a limited data set available to date (about two years of recordings) giving a modest number of false alarms that are interpreted in terms of instrument malfunctioning. More extensive tests are planned with future data acquisition and the new monitoring system implemented after the 2007 erutpion.

Acknowledgments

The Authors are grateful to N. Casagli for encouraging this work, and to A. Bonforte, M. Cantarero and M. Rossi for guaranteeing the correct functioning of the THEODOROS system. The authors are indebted to the National Department of Civil Protection team working at the Advanced Operative Centre at S. Vincenzo Observatory (Stromboli) for their support in installing and managing the complex monitoring system.

We also thank S. Conway for correcting and improving the English of this paper. A. S. fellow was supported by the INGV-DPS Project ''V2-Monitoring and research activity at Stromboli and Panarea'' (RU V2/16, coordinated by N. Casagli, Univ. of Florence).

References

Andel, J., *On critical values of Siegel's test*. In Trans. of the Twelfth Prague Conference (P. Lachout and J. A. Visek, Prague 1994), UTIA AV CR and MFF UK, pp 13–15.

Di Bello, G., Filizzola, C., Lacava, T., Marchese, F., Pergola, N., Pietrapertosa, C., Piscitelli, S., Scaffidi, I., and Tramutoli, V. (2004), *Robust satellite techniques for volcanic and seismic hazards monitoring*, Annals of Geophysics *47*, 1, 49–64.

Fisher, R. A., *Test of Significance in Harmonic Analysis*, Proc. Roy. Soc. (London, 1929), pp. 54–59.

Fortuna, L., Rizzotto, G., Lavorgna, M., Nunnari, G., Xibilia, M.G., and Caponetto, R., *Soft Computing. New Trends and Application* (Springer, 2001).

Leica and Geodetics Inc., Software GeoMos User Manual (2002).

Marradi, A., *L'analisi monovariata* (Franco Angeli Editore, Milano, 1993).

Nunnari, G., Puglisi, G., and Gargaun F. (2006), *Implementation of a warning system for Stromboli Volcano, In Applied Soft Computing Techniques: The Challenge of Complexity*, 9th Online World Congress (Berlin, Springer-Verlag) pp. 209–218.

Percival, D.B. and Walden, A.T. *Spectral Analysis for Physical Applications* (Cambridge University Press, Cambridge, 1993).

Puglisi, G., Bonaccorso, A., Mattia, M., Aloisi, M., Bonforte, A., Campisi, O., Cantarero, M., Falzone G., Puglisi B., and Rossi M. (2004), *New integrated geodetic monitoring system at Stromboli Volcano (Italy)*, Engin. Geology *79*, 13–31.

SCHUSTER, A., (1898), *On the investigation of hidden periodicities with application to a supposed 26 day period of meteorological phenomena*, J. Geophys. Res., *3*, (1), 13–41.

SIEGEL, A. F., (1980), *Testing for periodicity in a time series*, J. Am. Statistical Assoc. *75*, 345–348.

TRAMUTOLI, V. (1998), *Robust AVHRR Techniques (RAT) for environmental monitoring: theory and applications*, In *Earth Surface Remote Sensing II* (G. Cecchi and E. Zilioli eds.), Proc. SPIE, 3496, pp. 101–113.

(Received June 15, 2007, revised August 1, 2008, accepted August 14, 2008)
Published Online First: October 29, 2008

Pure appl. geophys. 165 (2008) 1643–1661
0033–4553/08/081643–19
DOI 10.1007/s00024-004-0393-4

Pure and Applied Geophysics

Potential Symmetry Properties of a Family of Equations Occuring in Ice Sheet Dynamics

J. I. Díaz[1] and R. J. Wiltshire[2]

Abstract—In this paper we derive some similarity solutions of a nonlinear equation associated with a free boundary problem arising in the shallow-water approximation in glaciology. In addition we present a classical potential symmetry analysis of this second-order nonlinear degenerate parabolic equation related to non-Newtonian ice sheet dynamics in the isothermal case. After obtaining a general result connecting the thickness function of the ice sheet and the solution of the nonlinear equation (without any unilateral formulation), a particular example of a similarity solution to a problem formulated with Cauchy boundary conditions is described. This allows us to obtain several qualitative properties on the free moving boundary in the presence of an accumulation-ablation function with realistic physical properties.

Key words: Ice flow dynamics, potential symmetries.

1. A Model for Ice Sheet Dynamics

In recent years there has been considerable interest on modelling ice sheet dynamics especially because of its importance in the understanding of global climate change, global energy balance and circulation models. Although various physical theories for large ice sheet motion have been presented, there still exists many open questions related to its mathematical treatment. In this paper we consider an obstacle formulation of slow, isothermal, one-dimensional ice flow on a rigid bed due to Fowler (1992).

The model describing the ice sheet dynamics is formulated in terms of an obstacle problem associated with a one-dimensional nonlinear degenerate diffusion equation (see Calvo *et al.*, 2002). The original *strong* formulation can be stated in the following terms: Let $T > 0$, $L > 0$ be positive fixed real numbers and let $\Omega = (-L, L)$ be an open bounded interval of $\mathbb{R}$ (a sufficiently large, fixed spatial domain). Given an accumulation/ablation rate function $a = a(x, t)$ and a function $f(x, t)$ (a sliding velocity, eventually zero) defined on $Q = (0, T) \times (-L, L)$ (a large, fixed, parabolic domain) and an initial thickness $h_0 = h_0(x) \geq 0$ (bounded and with $h_0(x) > 0$ on its support $I(0) \subset \Omega$), find two curves S_+,

[1] Departamento de Matemática Aplicada, Facultad de Matemáticas, Universidad Complutense de Madrid, 28004 Madrid, Spain. E-mail: diaz.racefyn@insde.es.

[2] The Division of Mathematics and Statistics, The University of Glamorgan, Pontypridd CF37 1DL, Great Britain. E-mail: rjwiltsh@glam.ac.uk.

$S_- \in C^0([0, T])$, with $S_-(t) \leq S_+(t)$, $I(t) := (S_-(t), S_+(t)) \subset \Omega$ for any $t \in [0, T]$, and a sufficiently smooth function $h(x, t)$ defined on the set $Q_T := \bigcup_{t\in(0,T)} I(t)$ such that

$$(SF) := \begin{cases} h_t = \left[\dfrac{h^{n+2}}{n+2}|h_x|^{n-1}h_x - fh\right]_x + a & \text{in} \quad Q_T, \\ h = \left(\dfrac{h^{n+2}}{n+2}|h_x|^{n-1}h_x - fh\right) = 0, & \text{on} \quad \{S_-(t)\} \cup \{S_+(t)\}, t \in (0, T), \\ h = h_0 & \text{on} \quad I(0), \end{cases}$$

and $h(x, t) > 0$ on Q_T. We recall that n denotes the so-called, Glen exponent, and that several constitutive assumptions are admitted, the most relevant case corresponds to $n = 3$ (see, for example Fowler, 1992).

Notice that, for each fixed $t \in [0, T]$, $I(t) = (S_-(t), S_+(t)) = \{x \in \Omega : h(x, t) > 0\}$ denotes the ice covered region. The curves $S_{\pm}(t)$ are called the interface curves or free boundaries associated with the problem and are defined by:

$$S_-(t) = \text{Inf}\{x \in \Omega : h(x, t) > 0\}, \qquad S_+(t) = \text{Sup}\{x \in \Omega : h(x, t) > 0\}.$$

These curves define the interface separating the regions in which $h(x, t) > 0$ (i.e., ice regions) from those where $h(x, t) = 0$ (i.e., ice-free regions). In the physical context they represent the propagation fronts of the ice sheet.

The qualitative description of solutions of this problem is quite difficult due to the doubly nonlinear terms appearing at the differential operator and, especially, to its formulation involving the unknown fronts $S_{\pm}(t)$ (the free boundaries). Nevertheless, some mathematical and numerical results are already available in the literature. Thus, for instance, the physical problem may be characterized by the following properties as have recently been discussed by Calvo *et al*. (2002):

- Given an initial ice sheet initial $h(x, 0)$, and known $a(x, t)$, $f(x, t)$ the nonlinear partial differential equation determines $h(x, t)$ over its parabolic positivity set.
- The ice free region (melt zone) $h(x, t) = 0$ always exists (from the assumptions on $h(x, 0)$) and defines the two free boundaries $S_-(t)$ and $S_+(t)$ which are extended to the interval $[0, T]$ if, for $t \in [0, T]$, $a(x, t) > 0$ on some subinterval of Ω.
- The more realistic solutions (from a physical point of view) are non-negative solutions $h(x, t) \geq 0$ corresponding to ablation data functions such that $a > 0$ except in a region near the two free boundaries where $a < 0$.

In section 4 we prove that it is possible to obtain estimates on the ice-covered region $I(t)$ and the solution $h(x, t)$ (the thickness of the ice sheet) by means of the comparison with the solution $u(x, t)$ of the nonlinear equation

$$\Psi(x, t, u, u_t, u_x, u_{xx}) \equiv u_t - a - \left[\frac{u^{n+2}}{n+2}|u_x|^{n-1}u_x - fu\right]_x = 0. \tag{1}$$

Therefore, any description of special solutions of the equation (1) (which do not involve obstacle formulation) leads to useful estimates for the more complex formulation for

$h(x, t)$. As a matter of fact, the study of the nonlinear equation (1) is of importance in its own right since the equation arises in many other different contexts (with different values of the exponent n) as, for instance, filtration in porous media with turbulent regimes, suitable non-Newtonian flow problems, and so on (see e.g., the monograph ANTONTSEV *et al.*, 2002 and its references).

We emphasize that very few explicit solutions of the ice sheet free boundary formulation are known in the literature. One of them corresponds to a stationary solution due to PATERSON (1981) and was used as a numerical test in the paper. It corresponds to the special case of a no sliding case (i.e., $f = 0$) with $n = 3$ and the following piecewise constant accumulation-ablation function:

$$a(x) = \begin{cases} a_1 & \text{if } 0 \le |x| < R \\ -a_2 & \text{if } R \le |x| \le L, \end{cases}$$

where $L > 1$, $a_1 > 0$, $a_2 > 0$ and $R \in (0,1)$. Moreover, it is assumed that $a_1 R = a_2(1 - R)$. Thus, for the particular values $a_1 = 0.01$ and $a_2 = 0.03$, we have the steady state solution

$$h(x) = \begin{cases} H\left[1 - \left(1 + \dfrac{a_1}{a_2}\right)^{1/3} \left(\dfrac{|x|}{L}\right)^{4/3}\right]^{3/8} & \text{if } |x| \le R \\ \left(1 + \dfrac{a_2}{a_1}\right)^{1/8} \left(1 - \dfrac{|x|}{L}\right)^{1/2} & \text{if } R \le |x| \le 1 \\ 0 & \text{if } 1 \le |x| \le L, \end{cases} \tag{2}$$

where $H = (40\ a_1\ R)^{1/8}$ represents the thickness at $x = 0$.

In sections 2–4 of this paper we shall carry out the study of some special transient solutions of the equation (1) of a similarity type which are compatible with the above statements. It should be noted that similarity solutions for problems related to ice-sheet dynamics do exist in the literature. However, neither HALIFAR (1981, 1983) or NYE (2000) consider surface accumulation whilth neither HINDMARSH (1990, 1993) or BUELER *et al.* (2005) conduct a comprehensive similarity analysis. In this paper similarity solutions will be obtained by conducting a thorough Lie or classical symmetry analysis of (1). The method is described in the next section. In addition BLUMAN and KUMEI (1989), described how the range of symmetries may be extended whenever a Lie symmetry analysis is conducted on a partial differential equation that may be written in a conserved or a potential form. This is the case with (1) where the corresponding equivalent ice model may be described in terms of the first-order potential system, $\Psi \equiv (\Psi_1, \Psi_2) = \mathbf{0}$ where

$$\begin{aligned} \Psi_1 &= v_x - u + \lambda = 0 \\ \Psi_2 &= v_t - \frac{u^{n+2}|u_x|^{n-1}u_x}{n+2} + fu = 0 \end{aligned} \tag{3}$$

for a potential function $v = v(x, t)$ and with $\lambda = \lambda(x, t)$ chosen such that

$$a \equiv \lambda_t. \tag{4}$$

We recall that, as demonstrated in BLUMAN and KUMEI (1989), and also BLUMAN *et al*. (1988), the Lie point symmetries of the potential system induce non-Lie contact symmetries for the original partial differential equation. The treatment presented in sections 3 and 4 is made independently of the positiveness subset of the solution and so it is carried out directly in terms of equation (1), without any other requisite on the solution (no study on any free boundaries is made in these sections). An application to the strong formulation of the free-boundary problem, for some concrete data, is given in section 4.

2. *Ice Sheet Equation, Conservation and Potential Symmetry Analysis*

In the classical Lie group method, one-parameter infinitesimal point transformations, with group parameter ε are applied to the dependent and independent variables (x, t, u, v). In this case the transformation, including that of the potential variable are

$$\begin{aligned} \bar{x} &= x + \varepsilon\eta_1(x,t,u,v) + O(\varepsilon^2) \qquad & \bar{t} &= t + \varepsilon\eta_2(x,t,u,v) + O(\varepsilon^2) \\ \bar{u} &= u + \varepsilon\phi_1(x,t,u,v) + O(\varepsilon^2) \qquad & \bar{v} &= v + \varepsilon\phi_2(x,t,u,v) + O(\varepsilon^2) \end{aligned} \tag{5}$$

and the Lie method requires form invariance of the solution set:

$$\Sigma \equiv \{u(x,t), v(x,t),\ \boldsymbol{\Psi} = 0\}. \tag{6}$$

This results in a system of overdetermined, linear equations for the infinitesimal η_1, η_2, ϕ_1 and ϕ_2. The corresponding Lie algebra of symmetries is the set of vector fields

$$\mathcal{X} = \eta_1(x,t,u,v)\frac{\partial}{\partial x} + \eta_2(x,t,u,v)\frac{\partial}{\partial t} + \phi_1(x,t,u,v)\frac{\partial}{\partial u} + \phi_2(x,t,u,v)\frac{\partial}{\partial} v. \tag{7}$$

The condition for invariance of (1) is the equation

$$\mathcal{X}_E^{(1)}(\boldsymbol{\Psi})\ |_{\Psi_1=0,\Psi_2=0} = 0, \tag{8}$$

where the first prolongation operator $\mathcal{X}_E^{(1)}$ is written in the form

$$\mathcal{X}_E^{(2)} = \mathcal{X} + \phi_1^{[t]}\frac{\partial}{\partial u_t} + \phi_1^{[x]}\frac{\partial}{\partial u_x} + \phi_2^{[t]}\frac{\partial}{\partial v_t} + \phi_2^{[x]}\frac{\partial}{\partial v_x}, \tag{9}$$

where $\phi_1^{[t]}$, $\phi_1^{[x]}$ and $\phi_2^{[t]}$, $\phi_2^{[x]}$ are defined through the transformations of the partial derivatives of u and v. In particular to the first order in ε:

$$\begin{aligned} \bar{u}_{\bar{x}} &= u_x + \varepsilon\phi_1^{[x]}(x,t,u,v) \qquad & \bar{u}_{\bar{t}} &= u_t + \varepsilon\phi_1^{[t]}(x,t,u,v) \\ \bar{v}_{\bar{x}} &= v_x + \varepsilon\phi_2^{[x]}(x,t,u,v) \qquad & \bar{v}_{\bar{t}} &= v_t + \varepsilon\phi_2^{[t]}(x,t,u,v) \end{aligned} \tag{10}$$

Once the infinitesimals are determined the symmetry variables may be found from the condition for invariance of surfaces $u = u(x, t)$ and $v = v(x, t)$:

$$\begin{aligned}\Omega_1 &= \phi_1 - \eta_1 u_x - \eta_2 u_t = 0\\ \Omega_2 &= \phi_2 - \eta_1 v_x - \eta_2 v_t = 0\end{aligned}. \tag{11}$$

In the following both Macsyma and Maple software have been used to calculate the determining equations. In the case of the ice equation (3) there are nine overdetermined linear determining equations. From these equations it may be shown that

$$\eta_1 = \eta_1(x,t) = (c_0 - z(t))x + s, \tag{12}$$

$$\eta_2 = \eta_2(t), \tag{13}$$

$$\phi_1 = \phi_1(t,u) = z(t)u, \tag{14}$$

$$\phi_2 = \phi_2(x,t,v) = g(x,t) + c_0 v, \tag{15}$$

where c_0 is an arbitrary constant such that

$$(3n+2)z(t) + \eta_{2_t} - (n+1)c_0 = 0, \tag{16}$$

$$(z(t)x - s(t) - c_0 x)\lambda_x - \eta_2(t)\lambda_t + z(t)\lambda - g(t)(x,t)_x = 0, \tag{17}$$

$$x\lambda z(t)_t - \lambda s_t - g(x,t)_t = 0, \tag{18}$$

$$(z(t)x - s(t) - c_0 x)f_x - \eta_2(t)f_t = -f((3n+1)z(t) - nc_0) + xz(t)_t - s(t)_t, \tag{19}$$

when it is assumed that $s(t)$ and $z(t)$ are known (see the next section) then equation (16) may be used to determine $\eta_2(t)$ while (17) to (19) may be used to determine $g(x, t)$, $\lambda(x, t)$ and the sliding velocity $f(x, t)$.

We observe that we have shown that the potential symmetries of the conserved form of the ice dynamics equations (3) are entirely equivalent to those of the single equation (1). This is due according to Bluman *et al*. (1988) additional symmetries can only be induced by the potential system when

$$\eta_{1_v}^2 + \eta_{2_v}^2 + \phi_{1_v}^2 \neq 0. \tag{20}$$

Clearly substitution of equations (12), (13) and (14) demonstrate that this is not the case.

In addition that a differential consequence of equations (17) and (18) incorporating the relation (4) is the differential equation for a, similar in form to (19), namely

$$(z(t)x - s(t) - c_0 x)a_x - \eta_2(t)a_t = -a(n+1)(3z(t) - c_0). \tag{21}$$

Moreover, we note that equation (17) may be obtained directly by differentiating the second surface invariant condition (11) with respect to x and then applying (3), (12)–(15) together with the first of (11).

In summary, the results (16) to (21) together with the first invariant condition at (11) may be simplified by eliminating $z(t)$ using (16) and combined to give three first-order partial differential equations which $u(x, t)$, $a(x, t)$ and $f(x, t)$ must satisfy, namely

$$Q(x,t)u_x + r(t)u_t = \frac{(n+1)c_0 - r_t(t)}{3n+2}u, \tag{22}$$

$$Q(x,t)a_x + r(t)a_t = \frac{(n+1)}{3n+2}(c_0 - 3r_t(t))a, \tag{23}$$

$$Q(x,t)f_x + r(t)f_t = \frac{((2n+1)c_0 - (3n+1)r_t(t))}{3n+2}f + \frac{xr_{tt}(t)}{3n+2} + s_t(t), \tag{24}$$

where $r(t) \equiv \eta_2(t)$ has been used to simplify the notation and also

$$Q(x,t) = s(t) + \frac{((2n+1)c_0 + r_t(t))}{3n+2}x\ . \tag{25}$$

3. Symmetry analysis results for the case $n = 3$

As stated in section 1 the exponent n which occurs in (1) is Glen's exponent and FOWLER (1992) suggests that $n \approx 3$ in physically realistic situations. Thus in the following we will assume that $n = 3$ although the analysis is unchanged for any non-Newtonian values $n > 1$. The results presented assumed that each of the functions u, a and f explicitly depend on x and t.

3.1. The Case $f(x, t) = 0$

Firstly, substitution of $f(x,t) = 0$ into equation (24) gives $r(t) = c_1 t + c_2$ and $s(t) = c_3$.

3.1.1 The subcase $7c_0 + c_1 \neq 0$, $c_1 \neq 0$. The solution of (22) and (23) may be expressed in terms of the similarity variable $\omega = \omega(x, t)$ for which

$$\omega(x,t) = (x + c_3)(c_1 t + c_2)^{-\frac{7c_0+c_1}{11c_1}} \text{ when } 7c_0 + c_1 \neq 0 \tag{26}$$

with

$$u(x,t) = \psi(\omega(x,t))(c_1 t + c_2)^{\frac{4c_0-c_1}{11c_1}} \tag{27}$$

$$a(x,t) = A(\omega(x,t))(c_1 t + c_2)^{\frac{4c_0-12c_1}{11c_1}} \tag{28}$$

Substituting the relationships into equation (1) with $n = 3$ gives rise to the ordinary differential equation

$$\frac{d}{d\omega}\left\{\frac{\psi^5\psi_\omega^3}{5} + \frac{(c_1 + 7c_0)\omega\psi}{11}\right\} - c_0\psi + A = 0. \tag{29}$$

3.1.2 The subcase $7c_0 + c_1 = 0$, $c_1 \neq 0$ For this subcase it may be shown that

$$\omega(x,t) = x + c_3 \ln(c_1 t + c_2) \quad \text{when } 7c_0 + c_1 = 0 \tag{30}$$

with

$$u(x,t) = \psi(\omega(x,t))(c_1 t + c_2)^{-\frac{1}{7}}, \tag{31}$$

$$a(x,t) = A(\omega(x,t))(c_1 t + c_2)^{-\frac{8}{7}}. \tag{32}$$

Substituting the relationships into equation (1) with $n = 3$ gives rise to the ordinary differential equation :

$$\frac{d}{d\omega}\left\{\frac{\psi^5\psi_\omega^3}{5} + 7c_0c_3\psi\right\} - c_0\psi + A = 0. \tag{33}$$

3.1.3 The subcase $c_1 = 0$. Without loss of generality consider the case $c_2 = 1$. The solution of (22) and (23) may be expressed in terms of the similarity variable $\omega = \omega(x, t)$ for which

$$\omega(x,t) = (x + c_3)e^{-\frac{7c_0t}{11}}, \tag{34}$$

with

$$u(x,t) = \psi(\omega(x,t))e^{\frac{4c_0t}{11}}, \tag{35}$$

$$a(x,t) = A(\omega(x,t))e^{\frac{4c_0t}{11}}. \tag{36}$$

Substituting the relationships into equation (1) with $n = 3$ gives rise to the ordinary differential equation

$$\frac{d}{d\omega}\left\{\frac{\psi^5\psi_\omega^3}{5} + \frac{7c_0\omega\psi}{11}\right\} - c_0\psi + A = 0. \tag{37}$$

3.2. The case $s(t) = 0$, $r(t) \neq 0$, $f(x, t) \neq 0$

In this case equations (22) to (24) may be integrated immediately to give solutions in terms of the similarity variable $\omega = \omega(x, t)$ for which

$$\omega(x,t) = xr(t)^{-\frac{1}{11}}\exp\left(-\frac{7c_0}{11}\int\frac{dt}{r(t)}\right), \tag{38}$$

with

$$u(x,t) = \psi(\omega(x,t))r(t)^{-\frac{1}{11}}\exp\left(\frac{4c_0}{11}\int\frac{dt}{r(t)}\right), \tag{39}$$

$$a(x,t) = A(\omega(x,t))r(t)^{-\frac{12}{11}}\exp\left(\frac{4c_0}{11}\int\frac{dt}{r(t)}\right), \tag{40}$$

$$f(x,t) = \left[\frac{\omega(x,t)r_t(t)}{11} + F(\omega(x,t))\right] r(t)^{-\frac{10}{11}} \exp\left(\frac{7c_0}{11}\int \frac{dt}{r(t)}\right). \tag{41}$$

Substituting the relationships into equation (1) with $n = 3$ gives rise to the ordinary differential equation

$$\frac{3\psi^5\psi_\omega^2\psi_{\omega\omega}}{5} + \psi^4\psi_\omega^4 + \frac{7c_0\omega\psi_\omega}{11} - \frac{4c_0\psi}{11} - \psi F_\omega - \psi_\omega F + A = 0. \tag{42}$$

That is

$$\frac{d}{d\omega}\left\{\frac{\psi^5\psi_\omega^3}{5} + \frac{7c_0\omega\psi}{11} - \psi F\right\} - c_0\psi + A = 0. \tag{43}$$

3.3. The Case s(t) ≠ 0, r(t) ≠ 0, f (x, t) ≠ 0

In this case the similarity variable has the form

$$\omega(x,t) = xr(t)^{-\frac{1}{11}} \exp\left(-\frac{7c_0}{11}\int \frac{dt}{r(t)}\right) - b(t), \tag{44}$$

where

$$b(t) = \int \left\{\frac{s(t)}{r(t)^{\frac{12}{11}}} \exp\left(-\frac{7c_0}{11}\int \frac{dt}{r(t)}\right)\right\} dt, \tag{45}$$

and the solutions (39) and (40) for $u(x, t)$ and $a(x, t)$ still apply. However the solution for $f(x, t)$ now becomes:

$$f(x,t) = \left[\frac{\omega(x,t)r_t(t)}{11} + F(\omega(x,t)) + h(t)\right] r(t)^{-\frac{10}{11}} \exp\left(\frac{7c_0}{11}\int \frac{dt}{r(t)}\right), \tag{46}$$

where

$$h(t) = \frac{\left(r(t)_t + 7c_0\right)}{11} b + r(t)b_t. \tag{47}$$

The resulting ordinary differential equation is once again (43).

3.4. The Case r(t) = 0, f (x, t) ≠ 0

In the following only the non-trivial case $c_0 \neq 0$ is considered. Equations (22) to (24) may be integrated immediately to give the following solutions

$$u(x,t) = m(11s + 7c_0x)^{\frac{4}{7}}, \tag{48}$$

$$a(x,t) = n(11s + 7c_0x)^{\frac{4}{7}}, \tag{49}$$

$$f(x,t) = p(11s + 7c_0x) - \frac{xs_t}{7c_0}, \tag{50}$$

where the relationship between the functions $m = m(t)$, $n = n(t)$ and $p = p(t)$ may be found upon substitution of equations (48) to (50) into (1). The following equation holds

$$m_t = -11c_0mp - n + \frac{704c_0^4m^8}{5}. \tag{51}$$

4. A Comparison Result and Some Particular Examples

We start by showing a useful result connecting the solution of the obstacle problem and the solutions of the nonlinear equation (1).

Theorem 1. *Let $a \in L^\infty(Q)$, $f \in L^\infty(Q)$ and a compactly supported initial data $h_0 \in L^\infty(\Omega)$. Let $h(x, t)$ be the unique solution of the obstacle problem (SF). Also let $u(x, t)$ be any continuous solution of the equation* (1) *corresponding to an ablation function $\widetilde{a} \in L^\infty(Q)$ and for which there exists two Lipschitz curves $x_{\pm}(t)$ such that*

$$u(x_\pm(t), t) = 0 \text{ and } u(x,t) > 0 \text{ for a.e. } x \in (x_-(t), x_+(t)) \text{ and any } t \in [0,T].$$

Assume that

$$\widetilde{a}(x,t) \le a(x,t) \quad \text{for a.e. } (x,t) \in Q,$$
$$u(x,0) \le h_0(x) \quad \text{for a.e. } x \in (x_-(0), x_+(0)).$$

Then, if $S_{\pm}(t)$ denotes the free boundaries generated by function $h(x, t)$ we have that

$$S_-(t) \le x_-(t) \le x_+(t) \le S_+(t) \text{ and any } t \in [0,T],$$

and

$$h(x,t) \ge u(x,t) \quad \text{for a.e. } x \in (x_-(t), x_+(t)) \text{ and any } t \in [0,T].$$

Moreover, if

$$\widetilde{a}(x,t) = a(x,t) \text{ a.e. } (x,t) \in Q,\ u(x,0) = h_0(x) \text{ a.e. } x \in (x_-(0), x_+(0)), \tag{52}$$

and

$$\frac{u^{n+2}}{n+2}|u_x|^{n-1}u_x - fu = 0 \quad \text{on} \quad \{(x_-(t),t)\} \cup \{(x_+(t),t)\}, \text{ for } t \in (0,T), \tag{53}$$

then $S_-(t) = x_-(t)$, $x_+(t) = S_+(t)$ and $h(x, t) = u(x, t)$ for a.e. $x \in (x_-(t), x_+(t))$ any for any $t \in [0, T]$.

Proof. We shall assume, additionally that h_t, $u_t \in L^1(Q)$ and that $f \equiv 0$. The general case, without this information, follows some technical arguments which can be found, for instance, in CARRILLO and WITTBOL (1999). We take as a test function the following approximation of the $sign_0^+(u^m - h^m)$ function (with $m = 2(n+1)/n$) given by $\Psi_\delta(\eta) := \min(1, \max(0, \frac{\eta}{\delta}))$, for $\delta > 0$ small. Then we define $v = \Psi_\delta(u^m - h^m)$. Notice that $v \in L^\infty(\cup_{t\in[0,T]}(x_-(t), x_+(t)) \times \{t\})$ and that $v(.,t) \in W_0^{1,p}((x_-(t), x_+(t)))$ for $p = n+1$ with

$$v_x = \begin{cases} \frac{1}{\delta}(u^m - h^m)_x & \text{if } 0 < u - h < \delta \\ 0 & \text{otherwise.} \end{cases}$$

Then, defining the set

$$A_\delta := \{(x,t), \text{ such that } t \in [0,T],\ x \in (x_-(t), x_+(t)) \text{ and } 0 < u(t,x) - h(t,x) < \delta\},$$

and multiplying the difference of both partial differential equations and integrating by parts (that is, by taking v as a test function) we find

$$\int_0^T \int_{(x_-(t), x_+(t))} (u_t - h_t)\Psi_\delta(u^m - h^m) dx\, dt + I(\delta) \le 0$$

where

$$I(\delta) = \frac{1}{\delta}\int_0^T \int_{A_\delta} \{\phi((u^m)_x) - \phi((h^m)_x\}((u^m)_x - (h^m)_x)\, dx\, dt,$$

with $\phi(r) = \mu |r|^{n-1} r$, $\mu = n^n/[2^n(n+1)^n(n+2)]$ and where we used the fact that $u(x_\pm(t), t) = 0 \le h(x_\pm(t), t)$ for any $t \in [0, T]$. Then, from the monotonicity of $\phi(r)$ we can pass to the limit when $\delta \searrow 0$ and conclude that

$$\int_{(x_-(t), x_+(t))} \max\{u(t,x) - h(t,x), 0\}\, dx\, dt \le 0,$$

which implies that $u \le h$ on the set $(x_-(t), x_+(t))$.

In the special case of u satisfying (52) and (53) we find that the function $u^\#(x, t)$ defined as

$$u^\#(x,t) = \begin{cases} u(x,t) & \text{if } x \in (x_-(t), x_+(t)), t \in [0,T], \\ 0 & \text{otherwise,} \end{cases}$$

satisfies all the conditions required to be a weak solution of the obstacle problem and by the uniqueness of such solutions we also find that $h(x, t) = u^\#(x, t)$.

Remark 2. We note that no information on the global boundary conditions satisfied by u on $\partial\Omega \times [0, T]$ is required in the above result.

Remark 3. Notice also that the conditions satisfied by $h(x, t)$ on the free boundary $S_{\pm}(t)$ indicate that the Cauchy problem on the curves $\cup_{t\in[0,\,T]}(S_{\pm}(t), t)$ does not satisfy the unique continuation property since h is identically zero to the left or the right sides of those curves. Some sharper information on the growth with t and the study of the differential equation satisfied by the free boundaries can be found by means of some arguments involving Lagrangian coordinates. This is the main object of the work of DIAZ and SHMAREV (2008) concerning a different simplified obstacle problem.

We consider now the particular example of a non-sliding ice sheet at the base so that $f(x, t) = 0$ and assume that $c_2 = 1$ and $c_3 = 0$.

4.1. Example 1: A Co-sinusoidal Ice Sheet Profile

In this example suppose that the initial profile of the ice sheet satisfies

$$u(x,0) = \psi(\omega(x,0)) = \cos\left(\frac{\pi\omega(x,0)}{2}\right) \quad |\omega| \le 1. \tag{54}$$

This has been chosen as a simple mathematical example of an initial profile with compact support. Clearly in a more detailed enquiry it would be interesting to discuss broader classes of families of initial conditions with this property. In this case equation (29) becomes

$$\begin{aligned} A(\omega) = &-\frac{\pi^4}{16}\cos^4\left(\frac{\pi\omega}{2}\right)\sin^4\left(\frac{\pi\omega}{2}\right) + \frac{3\pi^4}{80}\cos^6\left(\frac{\pi\omega}{2}\right)\sin^2\left(\frac{\pi\omega}{2}\right) \\ &+ A_0\cos\left(\frac{\pi\omega}{2}\right) + A_b\omega\sin\left(\frac{\pi\omega}{2}\right), \end{aligned} \tag{55}$$

where

$$A_1 = A(1) = A(-1) = \frac{\pi}{22}(c_1 + 7c_0) \tag{56}$$

is the boundary value of the initial accumulation function profile and

$$A_0 = A(0) = -\frac{1}{11}(c_1 - 4c_0) \tag{57}$$

is the value of the initial profile at $\omega = 0$. Thus using equations (26), (27) and (28), the similarity solution with $c_3 = 0$ and $c_2 = 1$ is defined by

$$\omega(x,t) = x\left[1 - \left(7A_0 - \frac{8A_1}{\pi}\right)t\right]^{\frac{2A_1}{7\pi A_0 - 8A_1}}, \tag{58}$$

$$u(x,t) = \psi(\omega(x,t))\left[1 - \left(7A_0 - \frac{8A_1}{\pi}\right)t\right]^{-\frac{\pi A_0}{7\pi A_0 - 8A_1}}, \tag{59}$$

$$\widetilde{a}(x,t) = A(\omega)\left[1 - \left(7A_0 - \frac{8A_1}{\pi}\right)t\right]^{-\frac{8(A_1-\pi A_0)}{7\pi A_0 - 8A_1}}, \tag{60}$$

where the accumulation-ablation function is now denoted by $\widetilde{a}(x,t)$.

In this case the propagation fronts of the ice-sheet region are found from

$$\psi(x,t) = 0 \tag{61}$$

so

$$x_{\pm}(t) = \pm\left[1 - \left(7A_0 - \frac{8A_1}{\pi}\right)t\right]^{-\frac{2A_1}{7\pi A_0 - 8A_1}} \tag{62}$$

and the finite velocity is

$$\frac{d}{dt}x_{\pm}(t) = \pm\frac{2A_1}{\pi}\left[1 + \left(7A_0 - \frac{8A_1}{\pi}\right)t\right]^{-\frac{7\pi A_0 - 6A_1}{7\pi A_0 - 8A_1}}. \tag{63}$$

In the case when $A_0 = 2$ and $A_1 = -1$ these equations become

$$\omega(x,t) = x[1 - 16.55t]^{-0.03847}, \tag{64}$$

$$u(x,t) = \psi(\omega(x,t))[1 - 16.55t]^{-0.1209}, \tag{65}$$

$$\widetilde{a}(x,t) = A(\omega)[1 - 16.55t]^{-1.1209}, \tag{66}$$

$$x_{\pm}(t) = \pm[1 - 16.55t]^{0.03847}, \tag{67}$$

$$\frac{d}{dt}x_{\pm}(t) \simeq \mp 0.64[1 - 16.55t]^{-0.9615}. \tag{68}$$

Figures 1–3 illustrate the time evolution of the ice sheet $u(x, t)$ and also the accumulation-ablation function $\widetilde{a}(x,t)$ for this case.

4.2. Example 2: A Quartic Powerlaw Ice-sheet Profile

Consider now an initial ice-sheet profile given by

$$u(x,0) = \psi(\omega(x,0)) = 1 - \omega(x,0)^4, \quad |\omega| \leq 1. \tag{69}$$

On this occasion (29) becomes

$$\begin{aligned} A(\omega) = {} & -832\omega^{12} + 2176\omega^{16} - 2688\omega^{20} + 1600\omega^{24} - \frac{1856}{5}\omega^{28} + \frac{576}{5}\omega^{8} \\ & + A_0\left(1 - \omega^4\right) + A_1\omega^4, \end{aligned} \tag{70}$$

where

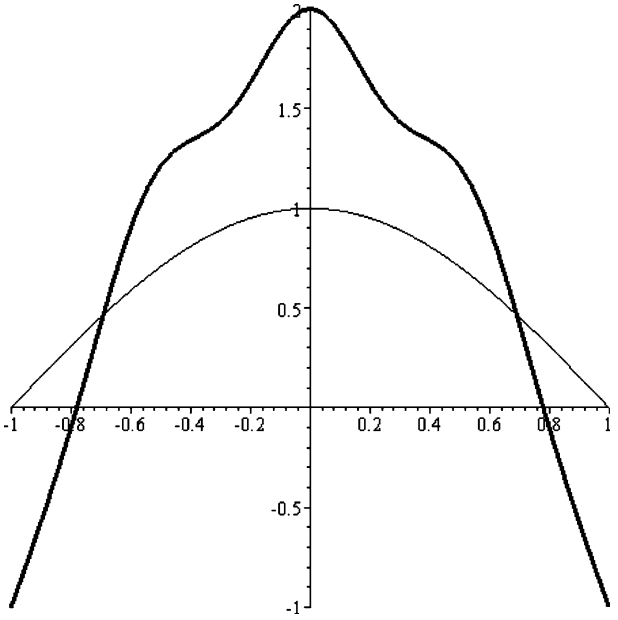

Figure 1
Initial profile for the height, u and the accumulation, ã (*solid line*) on $x = [-1,1]$.

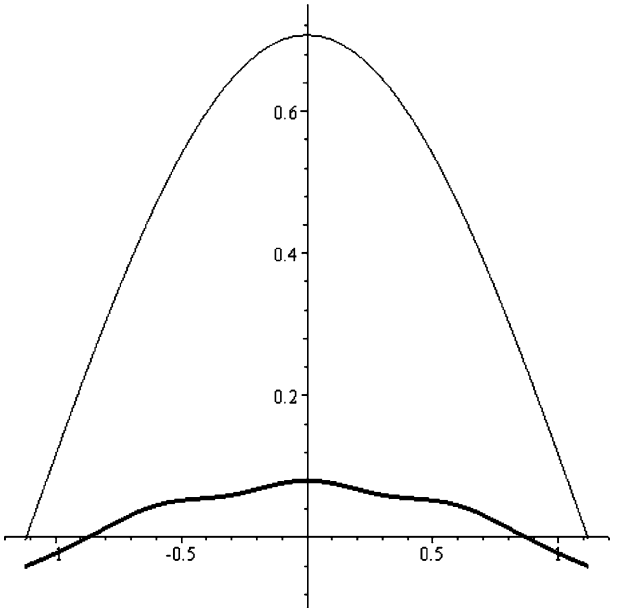

Figure 2
Profile at time $t = 0.02$ for the height u, and the accumulation, ã (*solid line*) versus x.

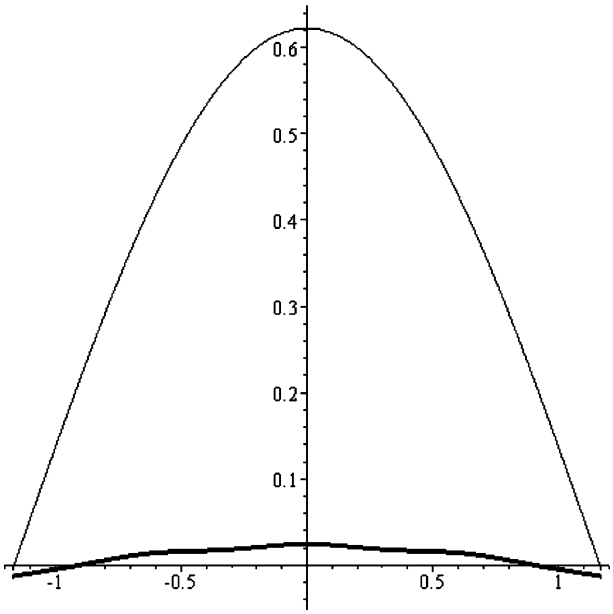

Figure 3
Profile at time $t = 0.04$ for the height u, and the accumulation, ã (*solid line*) versus x.

$$A_1 = A(1) = A(-1) = \frac{4}{11}(c_1 + 7c_0), \quad A_0 = A(0) = -\frac{1}{11}(c_1 - 4c_0). \tag{71}$$

Thus using equations (26), (27) and (28), the similarity solution with $c_3 = 0$ and $c_2 = 1$ is defined by

$$\omega(x,t) = x[1 - (7A_0 - A_1)t]^{\frac{A_1}{4(7A_0 - A_1)}}, \tag{72}$$

$$u(x,t) = \psi(\omega(x,t))[1 - (7A_0 - A_1)t]^{-\frac{A_0}{7A_0 - A_1}}, \tag{73}$$

$$\widetilde{a}(x,t) = A(\omega)[1 - (7A_0 - A_1)t]^{\frac{A_1 - 8A_0}{7A_0 - A_1}}, \tag{74}$$

where the accumulation-ablation function is again denoted by $\widetilde{a}(x,t)$. The propagation fronts of the ice-sheet region are found from $\psi(x, t) = 0$ and so

$$x_\pm(t) = \pm[1 - (7A_0 - A_1)t]^{-\frac{A_1}{4(7A_0 - A_1)}} \tag{75}$$

and the finite velocity is

$$\frac{d}{dt}x_\pm(t) = \pm\frac{A_1}{4}[1 - (7A_0 - A_1)t]^{-\frac{A_1}{4(7A_0 - A_1)} - 1}. \tag{76}$$

In the case when $A_0 = 4$ and $A_1 = -1$ these equations become

$$\omega(x,t) = x[1-29t]^{-\frac{1}{116}}, \tag{77}$$

$$u(x,t) = \psi(\omega(x,t))[1-29t]^{-\frac{4}{29}}, \tag{78}$$

$$\widetilde{a}(x,t) = A(\omega)[1-29t]^{-\frac{33}{29}}, \tag{79}$$

$$x_{\pm}(t) = \pm[1-29t]^{\frac{1}{116}}, \tag{80}$$

$$\frac{d}{dt}x_{\pm}(t) = \mp\frac{1}{4}[1-32t]^{-\frac{115}{116}}. \tag{81}$$

Figures 4–6 illustrate the time evolution of the ice sheet $u(x, t)$ and also the accumulation-ablation function $\widetilde{a}(x,t)$ for this case.

As a consequence of Theorem 1 and using example 2 we have

Corollary 1. *Let* $\Omega = (-L, L)$ *with* $L > 1$ *and* $f(x, t) \equiv 0$. *Let* $a \in L^{\infty}(Q)$ *with* $\widetilde{a}(x,t) \leq a(x,t)$ for a.e. $(x, t) \in Q$, *where* $\widetilde{a}(x,t)$ *is given by* (60) *and assume that*

$$h_0(x) \geq \begin{cases} 1-x^4 & \text{if } x \in (-1,1), \\ 0 & \text{if } x \in (-L-1) \cup (L,1). \end{cases}$$

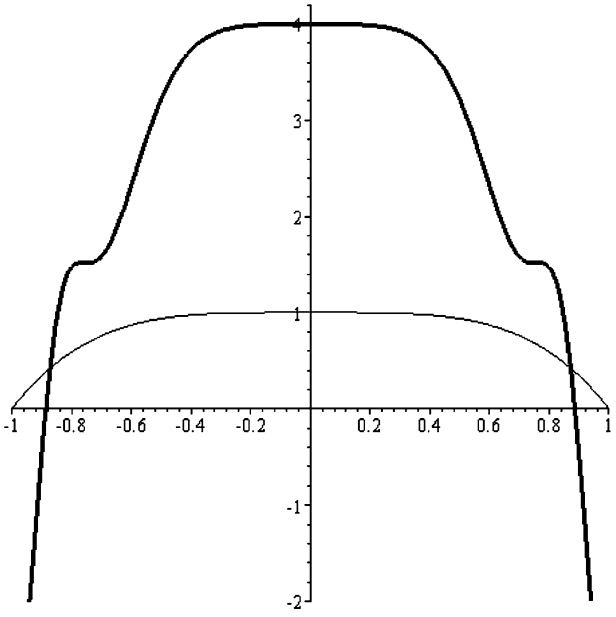

Figure 4
Initial profile for the height, u and the accumulation, ã (*solid line*) on $x = [-1,1]$

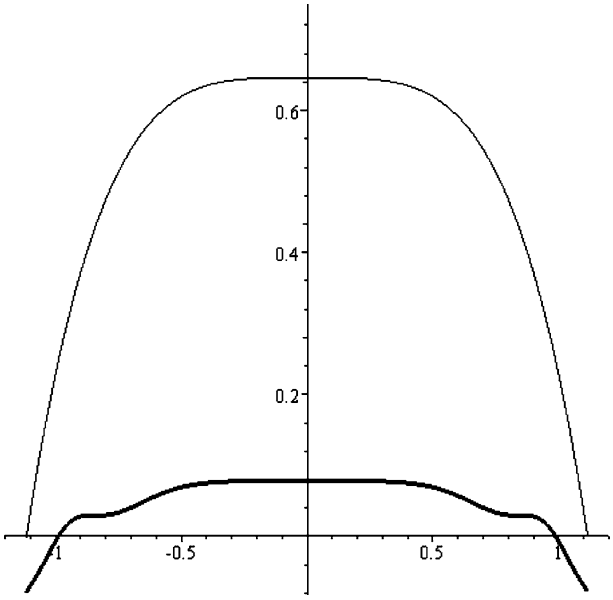

Figure 5
Profile at time $t = 0.01$ for the height u, and the accumulation, ã (*solid line*) versus x.

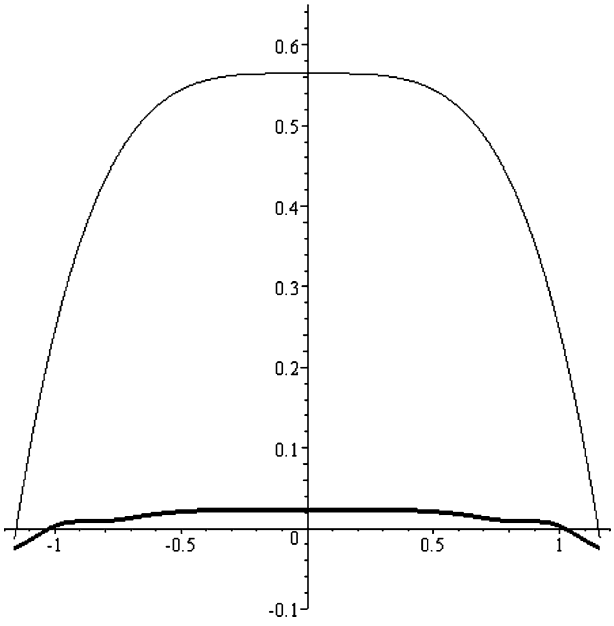

Figure 6
Profile at time $t = 0.02$ for the height u, and the accumulation, ã (*solid line*) versus x.

Let $h(x, t)$ be the (unique) solution of the obstacle formulation (with $f(x, t) \equiv 0$) associated with the data a and h_0. Then

$$S_-(t) \leq -[1-29t]^{\frac{1}{116}} < [1-29t]^{\frac{1}{116}} \leq S_+(t) \ ,$$

and

$$h(x,t) \geq \frac{\psi\left(x[1-29t]^{-\frac{1}{116}}\right)}{[1-29t]^{\frac{4}{29}}},$$
$$\text{for a.e. } x \in (-[1-29t]^{\frac{1}{116}},\ [1-29t]^{\frac{1}{116}}),$$

where $\psi(\omega)$ satisfies (69).

This example clearly demonstrates the useful properties of the closed form solutions of (1) for an accumulation-ablation function which changes sign and is negative near the propagation fronts.

Remark. The research will be continued elsewhere and in the next phase we are seeking similarity solutions corresponding to the strong formulation of the problem, when it is written (in other equivalent terms, as indicated in Diaz and Schiavi, 1995, 1999) by using the multivalued maximal monotone graph $\beta(u)$ of $\mathbb{R}^2$ given by $\beta(r) = \phi$ (the empty set) if $r < 0$, $\beta(0) = (-\infty, 0]$ and $\beta(r) = \{0\}$ if $r > 0$. Then, the formulation is

$$\begin{cases} \Psi(x,t,u,u_t,u_x,u_{xx}) \equiv u_t - a - \left[\dfrac{u^{n+2}}{n+2}|u_x|^{n-1}u_x - fu\right]_x + \varphi = 0 \\ \text{with } \varphi(x,t) \in \beta(u(x,t)) \text{ a.e. } (x,t) \in \Omega \times (0,T). \end{cases}$$

In this case the focus is on both a classical and a non-classical symmetry reduction of the equation. If, for instance, we assume that $f = 0$ then it is possible to find sharper assumptions on function $a(x, t)$ guaranteeing the formation of the free boundary. This is the main goal of the paper currently being prepared by the authors which deals with the multivalued formulation of general obstacle problems (also arising in many other contexts: see, e.g. Duvaut and Lions, 1972).

5. Summary and Conclusions

In this paper we have concentrated on the problem of determining closed-form similarity solutions of equation (1) (using potential symmetries) and its connections with the thickness function $h(x, t)$ of ice sheets as the solution of the associate obstacle problem. The main aim has been to demonstrate that classes of such solutions exist and

that they contain physically realistic properties. We observe that equation (1) contains certain modelling deficiencies (with respect the obstacle problem formulation) because inadmissible solutions for which $u(x, t) < 0$ (in some subset) are possible. Certainly the similarity solution approach presented here demonstrates the possibility of such unrealistic solutions for equation (1) and so we obtain only certain estimates for the physical by relevant function $h(x, t)$. We use certain comparison results in order to extend several conclusions to the case of the free-boundary formulation. Our paper illustrates the potential of exact solution techniques based on classical Lie group methods when they are coupled with an *ad hoc* additional analysis of free-boundary formulations.

Acknowledgments

The research of the first author was partially supported by the projects MTM2005-03463 of the DGISGPI (Spain) and CCG07-UCM/ESP-2787 of the DGUIC of the CAM and the UCM.

References

Antontsev, S.N., Diaz, J.I., and Shmarev, S.I., *Energy Methods for Free Boundary Problems* (Birkhäuser, Boston, 2002).

Bueler, E, Lingle, C.S., Kallen-Brown, J.A., Covey, D.N., and Bowman L.N. (2005), *Exact solutions and verification of numerical models for isothermal ice sheets*, J. Glaciol. *51*, 291–306.

Bluman, G.W. and Kumei, S., *Symmetries and Differential Equations* (Springer-Verlag, New York, 1989).

Bluman, G.W., Reid, G.J., and Kumei, S. (1988), *New classes of symmetries for partial differential equations*, J. Math. Phys. *29*, 307–318.

Calvo, N., Diaz, J. I. Durany, J., Schiavi, E., and Vazquez, C. (2002), *On a doubly non-linear obstacle problem modelling ice sheet dynamics*, SIAM J. Appl. Math. *29*, 683–707.

Carrillo, J., and Wittbol, P. (1999), *Uniqueness of renormalized solutions of degenerate elliptic-parabolic problems*, J. Diff. Eq. *156*, 93–121.

Diaz, J.I. and Schiavi, S., *Tratamiento matematico de una ecuacion parabolica cuasilineal degenerada en Glaciologia*, (Electronic Proceedings of the XIV CEDYA-IV Congreso de Matemática Aplicada, Vic, Barcelona, 1995, http://www.mal.upc.es/cedya/cedya.html)

Diaz, J.I. and Schiavi, S. (1999), *On a degenerate parabolic/hyperbolic system in glaciology giving rise to free boundary*, Nonlinear Anal, *38*, 649–673.

Diaz, J.I. and Shmarev, S.I., *On the free boundary associate to some nonlinear parabolic equations with discontinuous perturbations*. In press: Archive Rational Mechanics and Analysis, 2008.

Duvaut, G. and Lions, J.L., *Les Inéquations en Mécanique el en Physique* (París, Dunod, 1972).

Fowler, A.C. (1992), *Modelling ice sheet dynamics*, Geophys. Astrophys. Fluid Dyn. *63*, 29–65.

Halifar, P., (1981), *On the dynamics of ice sheets*, J. Geophys. Res. *86* C11, 11065–11072.

Halifar, P., (1983), *On the dynamics of ice sheets 2*, J. Geophys. Res. *88* C10, 6043–6051.

Hindmarsh, R.C.A. (1990), *Time-scales and degrees of freedom operating in the evolution of continental ice sheets*, Trans R. Soc. Edinburgh, Earth Sci. *81*, 371–384.

Hindmarsh, R.C.A., *Qualitative Dynamics of Marine Sheets*, In *Ice in the climate system, Berlin* (ed. Peltier, W.R.) (Springer-Verlag, NATO ASI Series I: Global Environmental Change *12*, 1993) pp. 67–93.

NYE, J.F., (2000), *A flow model for the polar caps of Mars*, J. Glaciol. *46*, 438–444.
PATERSON, W.S.B., *The Physics of Glaciers* (Pergamon, Oxford, 1981).

(Received June 19, 2007, revised August 18, 2008, accepted August 18, 2008)
Published Online First: October 20, 2008

Pure appl. geophys. 165 (2008) 1663–1682
0033–4553/08/081663–20
DOI 10.1007/s00024-004-0394-3

Pure and Applied Geophysics

Mathematical Analysis of a Model of River Channel Formation

J. I. Díaz,[1] A. C. Fowler,[2] A. I. Muñoz,[3] and E. Schiavi[3]

Abstract—The study of overland flow of water over an erodible sediment leads to a coupled model describing the evolution of the topographic elevation and the depth of the overland water film. The spatially uniform solution of this model is unstable, and this instability corresponds to the formation of rills, which in reality then grow and coalesce to form large-scale river channels. In this paper we consider the deduction and mathematical analysis of a deterministic model describing river channel formation and the evolution of its depth. The model involves a degenerate nonlinear parabolic equation (satisfied on the interior of the support of the solution) with a super-linear source term and a prescribed constant mass. We propose here a global formulation of the problem (formulated in the whole space, beyond the support of the solution) which allows us to show the existence of a solution and leads to a suitable numerical scheme for its approximation. A particular novelty of the model is that the evolving channel self-determines its own width, without the need to pose any extra conditions at the channel margin.

Key words: River models, landscape evolution, nonlinear parabolic equations, free boundaries, singular free boundary flux.

1. Introduction

In a recent paper, Fowler *et al*. (2007) addressed the question of how rivers form in the landscape. They derived a nonlinear partial differential equation of diffusive type to describe the depth of an evolving channel, and it is the mathematical analysis of this equation which forms the substantive part of the present paper. In this introduction we begin by indicating the physical context within which this equation arises, and we sketch the way in which it is derived.

It is a matter of common experience that rainfall on land surfaces does not drain uniformly. Even on short time scales, small-scale channels called *rills* form, and over longer time scales, these rills evolve and merge, forming progressively larger channels. At the same time, the flow in the developing channels erodes the hillslope, cutting its way down, and the overland flow into the channels causes sub-channels or tributaries to form,

[1] Departamento de Matemática Aplicada, Universidad Complutense de Madrid, 28040 Madrid, Spain. E-mail: ji_diaz@mat.ucm.es.

[2] MACSI, Department of Mathematics and Statistics, University of Limerick, Limerick, Ireland. E-mail: fowler@math.ox.ac.uk.

[3] Departamento de Matemática Aplicada, E.S.C.E.T. Universidad Rey Juan Carlos, E 28933 Móstoles, Madrid, Spain. E-mail: anaisabel.munoz@urjc.es, emanuele.schiavi@urjc.es.

so that in a mature landscape, such as that shown in Figure 1, a fractal-like pattern of river channels dissects the landscape.

The mathematical understanding of the drainage process on the large scale of a catchment is challenging. Just as for air transport in the lungs, or for liquid transport in crystallizing mushy zones, the medium may be best represented as a porous network, but (like the second example) it is one whose transport properties are formed by the transport process itself. We thus need to understand the mechanisms whereby channels form in the first place, and which govern their size and transport capacity.

The ingredients of a suitable model are variables describing water flow and sediment transport, and the mechanism of channel formation arises through an instability, in which locally increased flow causes increased erosion, which in turn increases the flow depth and thus also the flow. This positive feedback induces instability, as was shown by SMITH and BRETHERTON (1972), in their pioneering study.

Smith and Bretherton's study was later elaborated by LOEWENHERZ (1991), and LOE-WENHERZ-LAWRENCE (1994), who was particularly concerned with the issue of wavelength selection, something which also formed the principal concern of IZUMI and PARKER (1995, 2000). Nonlinear studies of channel development and topographic evolution focussed on catchment scale problems, such as that of WILLGOOSE *et al.* (1991), however such efforts were unable to compute the solution of the governing models directly, essentially because of the stiffness of the system. WILLGOOSE *et al.* (1991) reverted to an artificial channel indicator variable, and KRAMER and MARDER (1992) used cellular lattice models, a development which has formed the thrust of simulation models since, e.g., those of HOWARD (1994) and TUCKER and SLINGERLAND (1994). There have been efforts to solve the Smith-Bretherton model directly (e.g., SMITH *et al.*, 1997; BIRNIR *et al.*, 2001), although these are problematical, unsurprisingly since the original Smith–Bretherton model is actually ill-posed.

The starting point for Smith and Bretherton's study was a coupled set of partial differential equations describing $s(x, y, t)$, the hill slope elevation, and $h(x, y, t)$, the water depth. The model takes the form

Figure 1
Hillslope topography. Photograph courtesy (Gary Parker).

$$\begin{aligned} \nabla\cdot(h\mathbf{u}) &= r, \\ s_t + \nabla\cdot\mathbf{q} &= U, \end{aligned} \tag{1.1}$$

and represents conservation of mass of water and sediment. The mean water velocity $\mathbf{u}$ is determined through a momentum balance equation, while the sediment flux $\mathbf{q}$ is usually taken as an empirically prescribed function of flow-induced bed stress and bed slope, the resulting combination (the effective bed stress) being denoted $\boldsymbol{\tau}$. The source term r represents rainfall, while U represents tectonic uplift. The time derivative in the water mass equation is ignored, on the basis that the time scale for evolution of the hill slope is considerably longer than that for water flow.

In order to complete this model, we assume it has been written in dimensionless form, so that the variables are $O(1)$. One can show that suitable models for the flow speed $\mathbf{u}$ and effective bed stress $\boldsymbol{\tau}$ are

$$\begin{aligned} \mathbf{u} &= h^{1/2}|\nabla\eta|^{1/2}\mathbf{n}, \\ \boldsymbol{\tau} &= \mathbf{u}|\mathbf{u}| - \beta\nabla s, \end{aligned} \tag{1.2}$$

where typically $\beta = O(1)$, and the down-water slope normal $\mathbf{n}$ is defined by

$$\mathbf{n} = -\frac{\nabla\eta}{|\nabla\eta|}. \tag{1.3}$$

η represents the water surface elevation, and in dimensionless terms is related to hillslope elevation s and water film thickness h by

$$\eta = s + \delta h. \tag{1.4}$$

The parameter δ is very small, a typical estimate being 10^{-5}. Finally, the sediment flux is taken to have the form

$$\mathbf{q} = V(\tau)\mathbf{N}, \tag{1.5}$$

where $\tau = |\boldsymbol{\tau}|$ and the down-sediment flow normal $\mathbf{N}$ is

$$\mathbf{N} = \frac{\boldsymbol{\tau}}{\tau}. \tag{1.6}$$

V is an increasing function of τ, with $V \approx \tau^{3/2}$ being a popular choice (this essentially stemming from the model of Meyer-Peter and Müller, 1948).

This model admits steady solutions corresponding to overland flow, in which the variables $\eta = \eta_0(X)$ and $h = h_0(X)$ are functions only of the downslope coordinate X, and the flow of both water and sediment is in the X direction, thus $\mathbf{n} = \mathbf{N} = \mathbf{i}$, the unit vector along the X axis. The Smith–Bretherton analysis was based on taking the limit $\delta \to 0$, and in this case it is easy to see that always $\mathbf{n} = \mathbf{N}$, even for non-unidirectional flows. Smith and Bretherton then found instability to arise in an ill-posed way, through a negative effective diffusivity in the cross-stream y direction. This leads to unbounded growth at small transverse wavelengths, but Loewenherz-Lawrence (1994) was able to show that

the instability was regularized at high wave number by including the small term δ in (1.4), which has the crucial effect of making $\mathbf{n} \neq \mathbf{N}$.

It is this observation which allows analytic progress in the model. Uniform overland flow is unable to y–dependent perturbations of small wavelength, and we can examine the nonlinear evolution of these by directly seeking asymptotic expansions in terms of δ. To do so, we firstly suppose that the channels which form are aligned in the X direction, and (sensibly) that the perturbation to the water surface is small, comparable to the overland flow depth:

$$\eta = \eta_0 + \delta Z. \tag{1.7}$$

We may then linearize the geometry of the system, to find that

$$\begin{aligned} \mathbf{n} &= \mathbf{i} - \frac{\delta Z_y}{S}\mathbf{j} + \cdots, \\ \mathbf{N} &= \mathbf{i} - \frac{\delta}{S}\left\{ Z_y - \frac{\beta}{h+\beta} h_y \right\}\mathbf{j} + \cdots, \end{aligned} \tag{1.8}$$

where $\mathbf{j}$ is the unit vector in the y direction and $S(X) = |\eta'_0(X)|$ is the unperturbed downhill slope.

The nonlinear channel evolution then arises from a rescaling of the hillslope evolution equation, in which we put

$$y = \delta^{1/2} Y, \quad h = \frac{H}{\delta^{1/3}}, \quad t = \delta^{7/6} T; \tag{1.9}$$

after some algebra, we find the leading order sediment transport equation takes the form

$$\frac{\partial H}{\partial T} = S' S^{1/2} H^{3/2} + S^{1/2} \frac{\partial}{\partial Y}\left[\beta H^{1/2} \frac{\partial H}{\partial Y} \right], \tag{1.10}$$

where $S' = dS/dX$.

It is important to note that this equation arises through conservation of sediment. Only Y derivatives are present, because the lateral length scale is so much smaller than the downslope one. The perturbation Z to the water surface is in fact then determined by quadrature of the water conservation equation, but integration of this equation in the across stream direction yields the integral constraint

$$\int_{-\infty}^{\infty} H^{3/2} dY = \frac{2LrX}{S^{1/2}}, \tag{1.11}$$

where L is the spacing (on the original hillslope length scale for y) between channels; the limits in (1.11) are, however, infinite because the integral is with respect to the much smaller channel width length scale. Suitable initial and boundary conditions for the channel depth are that

$$H \to 0 \quad \text{as} \quad Y \to \pm\infty, \quad H = H_0(Y) \quad \text{at} \quad T = 0. \tag{1.12}$$

An alternative to the initial condition is to assume that $H \to 0$ as $T \to -\infty$, corresponding to the evolution of an initial infinitesimal perturbation. (1.12) mimics this if we suppose that H_0 is everywhere small in value.

The equation (1.10), together with the integral constraint (1.11) and initial/boundary conditions (1.12), form the basis of our study. We will assume that $S' > 0$, so that the nonlinear term in (1.10) is a source. Since the downslope coordinate only appears in the coefficients, it can be scaled out of the problem. Indeed, if we define

$$H = \left(\frac{6}{\beta}\right)^{1/3} (LrX)^{2/3} u, \quad T = \left(\frac{\beta}{6}\right)^{1/6} \frac{t}{S^{1/2} S' (LrX)^{1/3}}, \quad Y = \left(\frac{2\beta}{3S'}\right)^{1/2} x \tag{1.13}$$

(note that this definition of t is distinct from that used previously), the problem to be studied can be written in the form

$$\begin{gathered} u_t = u^{3/2} + (u^{3/2})_{xx}, \\ \int_{-\infty}^{\infty} u^{3/2}\, dx = 1, \quad u \to 0 \quad \text{as} \quad x \to \pm\infty, \\ u = u_0(x) \quad \text{at} \quad t = 0. \end{gathered} \tag{1.14}$$

2. Mathematical Analysis

We consider problem (1.14) assuming an initial thickness perturbation $u_0(x)$ satisfying some natural physically based hypothesis, i.e., a bounded and nonnegative function with a compact and connected support $[-\zeta_0, \zeta_0]$ such that $\int_0^{+\infty} u_0^m(x)\, dx = M/2$, for $m > 1$ (including the case of $m = 3/2$ of (1.14)). For the sake of simplicity of the exposition we also assume symmetric initial data.

In the rest of the paper, we shall be especially interested in the question of *global solvability* (in time) of the following problem: Find a continuous curve $\zeta : [0, +\infty) \to \mathbb{R}^+$ and a function $u : \mathcal{P} \to [0, +\infty)$ (regular enough) such that

$$(SL) \begin{cases} u_t = (u^m)_{xx} + u^m, & \text{in } \mathcal{D}'(\mathcal{P}), \\ u(x,0) = u_0(x) & \text{a.e. } x \in \Omega_0, \\ u(x,t) > 0, & \text{a.e. } (x,t) \in \mathcal{P}, \\ u(x,t) \equiv 0, & \text{a.e. } (x,t) \notin \mathcal{P}, \\ u(\zeta(t),t) = 0, \quad (u^m)_x(0,t) = 0 & \text{a.e. } t \in (0, +\infty), \\ \zeta(0) = \zeta_0 \text{ and } \zeta(t) > 0 & \text{for any } t \geq 0, \\ \displaystyle\int_0^{\zeta(t)} u^m(x,t)\, dx = \frac{M}{2} & \text{a.e. } t \in (0, +\infty). \end{cases}$$

where $\Omega_0 = (0, \zeta_0)$, $\Omega_t = (0, \zeta(t)) \times \{t\}$, $\mathcal{P} = \cup_{t>0}\Omega_t$. Notice that $\mathcal{D}'(\mathcal{P})$ denotes the space of *distributions* on $\mathcal{P}$ and $\mathcal{P}$ is the *positivity subset* of the solution. Later on we shall make more precise the (minimal) regularity of the solution. The function $\zeta(t)$ is called *the interface* separating the (connected) region where $u(x, t) > 0$ from the region where $u(x, t) = 0$. It is unknown and it is usually called the *free* or *moving boundary* of the problem. Due to the free boundary, we shall refer to the strong formulation (*SL*) as the *strong-local* formulation. We emphasize that the mass conservation constraint

$$\int_0^{\zeta(t)} u^m(x,t)\,dx = \frac{M}{2} \qquad \text{a.e. } t \in (0,+\infty)$$

prevents possible blow-up phenomena which could arise (without this condition) due to the presence of the source term u^m in the equation.

An important difficulty, in order to get a global formulation (i.e., extended to the entire domain $(x, t) \in (0, +\infty) \times (0, +\infty)$, and not only on $(x,t) \in \mathcal{P}$), is the necessity to provide a suitable description of the flux $-(u^m)_x(\zeta(t), t)$ at the free boundary. This leads to a new constrained global formulation suitable for mathematical analysis and numerical resolution. In the next subsections we propose the global formulation of the model for the stationary regime. The transient regime is dealt with in subsection 2.2. Finally, in subsection 2.3, a finite element method is described and numerical results are presented.

2.1. The Stationary Case

We first consider the *strong* formulation of the stationary problem associated to (*SL*). Let M be a positive, fixed, real number and define $v = u^m$. Then we look for a solution of

$$-v_{xx} - v = 0, \qquad v'(0) = 0, \quad \lim_{x\to+\infty} v(x) = 0, \qquad \int_0^{+\infty} |v(x)|dx = \frac{M}{2}.$$

We first observe that the formulation does not correspond to a standard constrained problem of the Calculus of Variations. Indeed, if we were dealing with a standard constrained problem, the solution would coincide with the solution of the problem:

$$\text{Min}_{v\in X} J(v), \qquad \text{such that} \qquad v'(0) = 0, \quad \lim_{x\to+\infty} v(x) = 0, \qquad \int_0^{+\infty} G(v)\,dx = \frac{M}{2}$$

where

$$J(v) = \frac{1}{2}\int_0^{\zeta(t)} |v_x|^2 dx - \frac{1}{2}\int_0^{\zeta(t)} |v|^2 dx, \quad \text{and} \quad G(v) = |v|.$$

Then, by using the theory of Lagrange multipliers we would have that v would solve the unconstrained minimization problem:

$$\mathrm{Min}_{v\in X} J(v) + \lambda \int_0^{+\infty} G'(v)\,dx, \qquad \text{such that} \qquad v'(0) = 0, \quad \lim_{x\to+\infty} v(x) = 0,$$

for some constant λ, where $G'(v) = sign(v) = \pm 1$ depending on the (positive or negative) sign of v. Thus, v would be the solution of the associate Euler-Lagrange optimality equation

$$-v_{xx} - v = \lambda G'(v),$$

and so, on the set where $v > 0$ we would have $-v_{xx} - v = \lambda$, which is not the equation stated in the original formulation, i.e., $-v_{xx} - v = 0$. Then, we derive the conclusion that the equation is not verified in the whole halfline $(0, +\infty)$ and that the integral constraint must be carefully considered.

We recall that here we look for a continuous nonnegative function $v \geq 0$ and that the differential equation must be verified at the interior of the set $\{v > 0\} := \{x \in (0, +\infty) : v(x) > 0\}$. Since the solutions of the ODE, $v_{xx} + v = 0$, are explicitly given by $v(x) = A\cos x + B\sin x$, we see that none of them can satisfy $v_x(\zeta_\infty) = 0$ if $\{v > 0\} = (0,\zeta_\infty)$. So, necessarily, the limit $\lim_{x\nearrow\zeta_\infty} v_x(x)$ is strictly negative (since the function is passing from positive values to zero). Moreover, if we extend v by zero to the rest of $(0, +\infty)$ (as in Fowler *et al.*, 2007) we obtain that $v_x(x)$ has a discontinuity at $x = \zeta_\infty$. In particular, v_{xx} is not an integrable function on $(0, +\infty)$ but a measure with a nonzero singular part.

This introduces our formulation of the constraint by means of the "measure"

$$\mu = -v_{xx} \in \mathcal{M}(0, +\infty),$$

where $\mathcal{M}(0, +\infty)$ is the space of Radon measures (see, for instance, Evans and Gariepy, 1992). In fact, from the identity $v_{xx} = -v$ on $\{v > 0\}$ we see that the (signed) Jordan decomposition of μ (in the form $\mu = \mu_+ - \mu_-$, with $\mu_+ \perp \mu_-$) is given by

$$\mu_+ = v \text{ (which is in } L^1(0,\infty)) \quad \text{and} \quad \mu_- = -c\delta_{\zeta_\infty} \text{ for some } c > 0,$$

where δ_{ζ_∞} is the Dirac delta distribution located at interface $\zeta_\infty \in \mathbb{R}^+$, i.e., where $v(\zeta_\infty) = 0$ (sometimes we shall use the alternative notation $\delta_{\zeta_\infty} = \delta_{\partial\{v=0\}}$). Thus, μ_- is a singular measure with respect to the Lebesgue measure.

Moreover, we see that in other problems in which $v_x(\zeta_\infty) = 0$, i.e., when the flux is continuous at the free boundary, we obtain

$$\int_0^{+\infty} d\mu = -\int_0^{+\infty} v_{xx}\,dx = 0, \tag{2.15}$$

since $v_x(0) = 0$ and $v_x(x) = 0$ if $x > \zeta_\infty$. In our case the relation (2.15) is equivalent to the constraint $\int_0^{+\infty} v\,dx = M/2$ even if $v_x(\zeta_\infty) < 0$. Indeed, as mentioned above we know that

$$-v_{xx} - v = c\delta_{\partial\{v=0\}}, \tag{2.16}$$

which, in this stationary case, allows us to compute c explicitly

$$0 = \int_0^{+\infty} d\mu = \int_0^{+\infty} v\,dx - \int_0^{+\infty} d\mu_- = \frac{M}{2} - c\langle \delta_{\zeta_\infty}, 1\rangle = \frac{M}{2} - c,$$

i.e., $c = M/2$ and thus, necessarily, $\mu_- = -M/2\delta_{\zeta_\infty}$. Moreover, integrating in (2.16) we have:

$$0 = \int_0^{+\infty} d\mu = -\int_0^{\zeta_\infty} v_{xx}\,dx + \int_{\zeta_\infty}^{+\infty} d\mu_- = -v_x(\zeta_\infty) - \frac{M}{2}$$

and we deduce that, in the stationary case, the flux is determined by the integral constraint $(-v_x(\zeta_\infty) = M/2)$ and reciprocally. Notice that, despite of (2.15), we have

$$\|\mu\|_{\mathcal{M}(0,+\infty)} = \|\mu_+\|_{\mathcal{M}(0,+\infty)} + \|\mu_-\|_{\mathcal{M}(0,+\infty)} = \int_0^{+\infty} v\,dx + \frac{M}{2} = M.$$

The (symmetric) global formulation can be stated in the following terms: Find a stationary state $v(x)$ and a point $\zeta_\infty \in \mathbb{R}^+$ satisfying

$$(SP)\begin{cases} v_{xx} + v = (M/2)\delta_{\zeta_\infty}, & \text{in } \mathcal{D}'(0,+\infty), \\ v(x) > 0, & x \in [0, \zeta_\infty), \\ v(x) \equiv 0, & x \geq \zeta_\infty, \\ v_x(0) = 0. \end{cases}$$

We have

Proposition 1. *Given $M > 0$ there exists a unique solution $(v(x), \zeta_\infty)$ of (SP) given by*

$$\zeta_\infty = \frac{\pi}{2} \quad \textit{and} \quad v(x) = \frac{M}{2}\cos x\Big[1 - H\Big(x - \frac{\pi}{2}\Big)\Big], \tag{2.17}$$

where $H(x - \pi/2)$ denotes the Heaviside function located at $\pi/2$ i.e.,

$$v(x) = \begin{cases} (M/2)\cos x & \text{if } x \in [0, \pi/2], \\ 0 & \text{if } x \in (\pi/2, +\infty). \end{cases}$$

Proof. We shall use a shooting argument. Obviously any solution of (*SP*) must satisfy $v(0) > 0$. Let α, $\xi > 0$ be positive parameters. By using the Laplace transform we can solve the initial value problem

$$\begin{cases} v'' + v = (M/2)\delta_\xi, & \text{in } \mathcal{D}'(0,+\infty), \\ v(0) = \alpha, \\ v'(0) = 0, \end{cases}$$

so proving the uniqueness and the extension to $(0, +\infty)$ of the local solution of the stationary strong-local formulation. Indeed, if we denote by

$$Y(s) = L[v](s) = \int_0^\infty e^{-sx} v(x)\, dx,$$

the Laplace transform of v, we get that $L[v''] + L[v] = \frac{M}{2} L[\delta_\xi]$, and so

$$s^2 Y(s) - sv(0) - v'(0) + Y(s) = \frac{M}{2} e^{-\xi s}.$$

Using the initial conditions this becomes

$$s^2 Y(s) - s\alpha + Y(s) = \frac{M}{2} e^{-\xi s},$$

whence

$$Y(s) = \alpha\left(\frac{s}{s^2+1}\right) + \frac{M}{2}\left(\frac{e^{-\xi s}}{s^2+1}\right).$$

The inverse transform is direct:

$$v(x) = \alpha \cos x + \frac{M}{2} H(x-\xi)\sin(x-\xi),$$

where $H(x-\xi)$ denotes the Heaviside function located at ξ. The free boundary condition $v(\xi) = 0$ leads to the characteristic equation $v(\xi) = \alpha\cos\ \xi = 0$, of solutions $\xi_n = (n + 1/2)\ \pi$, $n = 0, 1, \ldots$ and of corresponding eigenfunctions

$$v_{\alpha,n}(x) = \alpha\cos x + \frac{M}{2} H\left(x - \left(n+\frac{1}{2}\right)\pi\right)\sin\left(x - \left(n+\frac{1}{2}\right)\pi\right)$$

$$= \cos x\left[\alpha - (-1)^n \frac{M}{2} H\left(x - \left(n+\frac{1}{2}\right)\pi\right)\right]$$

and the solutions $v_{\alpha,n}(x)$ have a compact support $[0, \xi]$, with $v_\alpha(x) \equiv 0$ for $x \notin [0, \xi]$ only if $\alpha = \alpha(n) = (-1)^n(M/2)$. Notice that n odd shall imply changing sign solutions. The requirement $v(x) > 0$ on $[0, \xi_n]$, with $v \equiv 0$ for $x \notin [0, \xi_n]$ fixes the unique solution of the original stationary free boundary problem which corresponds to the value $n = 0$ and so we get (2.17).

Remark 1. The function (2.17) was obtained in Fowler *et al*. (2007), for the local/strong formulation (i.e., without any global formulation). As we shall see in the next subsection, the global formulation is especially useful for the parabolic case. In Figure 2 the steady-state solution (2.17) for the global formulation (SP) is represented. We showed that it can be characterized as the first eigenfunction of the free boundary problem, where $\zeta_\infty = \pi\ /2$ ($v(x)$ has a compact and connected support). Its total mass, in $\mathbb{R}^+$, is $M/2$. Notice the discontinuity of the flux at the free boundary ζ_∞ where a Dirac's delta is generated by the diffusion operator.

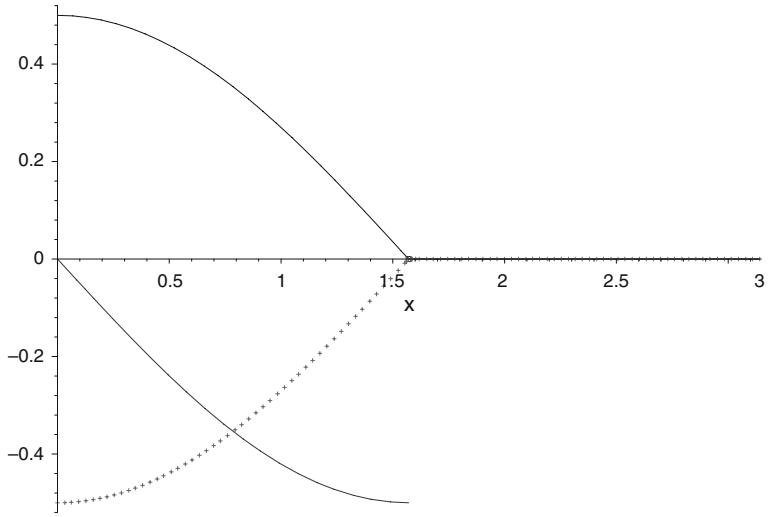

Figure 2
The (positive) stationary solution (2.17), its (negative and decreasing) derivative and the negative, increasing diffusive term $(v^m_{M/2,0})''(x)$ (dotted-line) for the global formulation (SP).

Remark 2. Problems of this type arise in fluid mechanics (problems of the Bernoulli type), in combustion and in plasma physics (see, e.g., Díaz *et al.*, 2007, and references therein).

2.2. Parabolic Case

Given $T > 0$ (arbitrary) and a continuous, symmetric, nonnegative initial data $u_0(x)$, with compact support $[0, \zeta^0]$ such that $\int_0^{+\infty} u_0^m(x)\, dx = M/2$, we look for a continuous curve $\zeta : [0, T] \to \mathbb{R}^+$ and a function $u : \mathbb{R}^+ \times [0, T] \to [0, +\infty)$ such that u satisfies the strong-local formulation (SL). To prove their existence we shall use an auxiliary global formulation on the whole domain $\mathbb{R}^+ \times [0, T]$. As in the stationary case, the global formulation of the partial differential equation includes a Dirac delta distribution located, for each $t \in (0, T]$, at the free boundary $x = \zeta(t)$ since the free boundary flux is discontinuous there (due to the mass constraint). To be precise we introduce the notation $\delta_{\partial\{u(t,\cdot)=0\}}$ to design the Dirac delta distribution located at the interface $x = \zeta(t)$ for each $t \in (0, T)$ (i.e., $\delta_{\partial\{u(t,\cdot)=0\}} = \delta_{(\zeta(t),t)}$). Nevertheless, the naturally associated problem

$$(P_0)\begin{cases} u_t = (u^m)_{xx} + u^m - \frac{M}{2}\,\delta_{\partial\{u(t,\cdot)=0\}}, & \mathcal{D}'(\mathbb{R}^+ \times (0,T)), \\ u(x,0) = u_0(x) & \text{a.e. } x \in (0, \zeta^0) \\ u(x,t) > 0, & \text{a.e. } (x,t) \in \mathcal{P}_T, \\ u(x,t) \equiv 0, & \text{a.e. } (x,t) \notin \mathcal{P}_T, \\ u(\zeta(t),t) = 0, \quad u_x(0,t) = 0 & \text{a.e. } t \in (0,T), \\ \zeta(0) = \zeta^0 \text{ and } \zeta(t) > 0 & \text{for any } t \in [0,T], \end{cases} \tag{2.18}$$

where $\mathcal{P}_T$ (the *positivity subset of u*) is defined by $\mathcal{P}_T = \{(x,t) \in \mathbb{R}^+ \times [0,T] : 0 \le x < \zeta(t)\}$, has blow-up solutions. In fact, it is important to observe that the mere presence of the Dirac delta, in the parabolic case, does not prevent the occurrence of the blow-up phenomenon (well-known for the case of zero, continuous free boundary flux, see SAMARSKI *et al.*, 1995, Chapter IV, Section 1.1). Indeed, the following result proves that it is possible to construct an infinite number of initial data such that the corresponding solutions $\{u_{T_e}\}$, with T_e be a positive parameter, of problem (P_0) (i.e., with a discontinuous free boundary flux condition) are not globally defined in time (the solution u_{T_e} being defined on a finite time interval $[0, T_e)$). Moreover, u_{T_e} verifies that

$$\int_0^{+\infty} u^m(x,t)\,dx = \frac{M{T_e}^{1/(m-1)}}{2(T_e - t)^{1/(m-1)}} \quad \text{for } t \in [0, T_e).$$

Remark 3. There is a long list of references dealing with nonlinear parabolic equations involving similar Dirac delta distributions (see, e.g. CAFFARELLI *et al.*, 1995, 1997, and their references) but the case of the simultaneous presence of the Dirac delta with a perturbation term of the form u^m and with prescribed mass seems not to have been considered before. We also mention that some other problems formulated in terms of a quasi-linear parabolic equation with a constraint of total mass type were treated in NAZARET (2001).

Inspired by SAMARSKI *et al.* (1995) (see Chapter IV, Section 1.1), we search for some separable solutions, u, of the form

$$u(x,t) = (T_e - t)^{-1/(m-1)}\theta(x).$$

Then, by using the phase plane associated with the ordinary differential equation for $\theta(x)$ it is proved in DÍAZ *et al.* (in preparation), that the following result holds:

Proposition. *i) For any $c > 0$, the problem*

$$\begin{cases} w'' + w - \frac{1}{m-1}w^{1/m} = c\delta_{\zeta^0}, & \mathcal{D}'(0,+\infty), \\ w(x) = 0 & x > \zeta^0, \\ w'(0) = 0, \end{cases}$$

admits a unique nonnegative solution w such that

$$\int_0^{+\infty} w(x)\,dx = c.$$

ii) If we take $\theta = w^{1/m}$ and $c = (M/2){T_e}^{m/(m-1)}$ then the pair $u_{T_e}(x,t) = (T_e - t)^{-1/(m-1)}\theta(x)$ and $\zeta(t) \equiv \zeta^0$ satisfies (P_0) for $u_0(x) := T_e^{-1/(m-1)}w^{1/m}(x)$.

The above result explains that the reformulation of the mass constraint in terms of the solution of a global partial differential equation in the whole domain $\mathbb{R}^+ \times (0,T)$ requires

some additional condition (besides the presence of the mentioned Dirac delta at the equation). To do that, we start by noting that if we define (for a.e. $t \in (0, T)$ fixed) the spatial distribution

$$\mu(t,\cdot) := u_t(t,\cdot) - (u^m)_{xx}(t,\cdot),$$

then we must expect to know that, in fact, such a distribution is a bounded measure $\mathcal{M}(0,+\infty)$ (with compact support) since

$$\mu(t,\cdot) = u^m(t,\cdot) - \frac{M}{2}\delta_{\partial\{u(t,\cdot)=0\}}.$$

Moreover its signed (Jordan) decomposition, $\mu(t,\cdot) = \mu_+(t,\cdot) - \mu_-(t,\cdot)$, must be given by $\mu_+(t,\cdot) = u^m(t,\cdot)$ and $\mu_-(t,\cdot) = (M/2)\delta_{\partial\{u(t,\cdot)=0\}}$. Now, as in the stationary case, we recognize that the mass constraint $\int_0^{+\infty} u^m(x,t)\,dx = M/2$ is equivalent to the "zero total measure" condition

$$\int_0^{+\infty} d\mu(t,\cdot) = 0, \qquad \text{for a.e. } t \in (0,T). \tag{2.19}$$

So, we arrive at the global formulation: Find a nonnegative function $u : \mathbb{R}^+ \times [0,T) \to [0,+\infty)$ such that

$$(P)\begin{cases} u_t = (u^m)_{xx} + u^m - \frac{M}{2}\delta_{\partial\{u(t,\cdot)=0\}}, & \mathcal{D}'(\mathbb{R}^+ \times (0,T)), \\ u(x,0) = u_0(x) & \text{a.e. } x \in (0,+\infty), \\ u_x(0,t) = 0,\ u(x,t) \to 0 \text{ as } x \to +\infty & \text{a.e. } t \in (0,T), \\ \mu(t,\cdot) := u_t(t,\cdot) - (u^m)_{xx}(t,\cdot) \text{ satisfies (2.19)} & \text{a.e. } t \in (0,T). \end{cases} \tag{2.20}$$

Notice that now the compact support condition is not explicitly required. In fact, following the numerical experiences of FOWLER et al. (2007), we conjecture that problem (P) can be solved for suitable, strictly positive initial data $u_0(x)$ such that $u_0(x) \to 0$ as $x \to +\infty$. Notice also that if a solution u of (P) gives rise to a free boundary $\zeta(t) := \partial\{u(t,\cdot) = 0\}$ then, the *zero total measure condition* (2.19) implies that the free boundary flux must be given by

$$-(u^m)_x(\zeta(t),t) = \frac{M}{2} - \int_0^{\zeta(t)} u_t(x,t)\,dx \qquad \text{a.e. } t \in (0,+\infty).$$

Here (and, in fact, also in (2.19)) there is a slight abuse of notation since, *a priori*, $u_t(x,t)$ (respectively $\mu(t,\cdot)$) does not need to be a $L^1(\mathbb{R}^+)$ function, but merely a bounded measure. Nevertheless we keep the classical notation for simplicity reasons. In any case, we see that in the transient regime the boundary flux at the free boundary is unknown (being also discontinuous), as opposed to the stationary case in which the flux (also discontinuous) can be explicitly known. Moreover, the above considerations allow us to conclude that any solution of the *strong-local* formulation (SL) solves problem (P) and that any (regular enough) solution of (P) with compact support satisfies the *strong-local*

formulation (SL). In order to show the existence of a global solution u of problem (P) we use a two-step iterative approximation. The main idea is to construct $\{u_{2n+1} : n = 0, 1, 2\ldots\}$ as solutions of the problem with a semi-implicit linear source term

$$(P_{2n+1}) := \begin{cases} (u_{2n+1})_t = ((u_{2n+1})^m)_{xx} + (u_{2n})^{m-1}(u_{2n+1}) - \frac{M}{2}\delta_{\partial\{(u_{2n+1})(t,\cdot)=0\}}, & \mathcal{D}'(\mathbb{R}^+ \times (0,T)), \\ (u_{2n+1})(x,0) = u_0(x) & \text{a.e. } x \in (0,+\infty), \\ (u_{2n+1})_x(0,t) = 0, (u_{2n+1})(x,t) \to 0 \text{ as } x \to +\infty & \text{a.e. } t \in (0,T), \end{cases}$$

(where for $n = 0$ we use as u_{2n} the initial condition u_0) and then to construct the sequence $\{u_{2n} : n = 1, 2\ldots\}$ by requiring that

$$(P_{2n}) := \begin{cases} u_{2n}(x,t) = C_{2n}(t)u_{2n-1}(x,t) & \text{for a.e. } (x,t) \in \mathbb{R}^+ \times (0,T), \\ \int_0^{+\infty} ((u_{2n}(x,t))^{m-1}(u_{2n-1}(x,t))\,dx = \frac{M}{2} & \text{for a.e. } t \in (0,T), \end{cases}$$

for some $C_{2n}(t) > 0$.

The detailed proof of the convergence of the algorithm (contained in Díaz *et al.* (in preparation)) is quite technical and will not be presented here. For instance, many of the *a priori* estimates on u_{2n+1} were obtained previously for the solutions $u_{2n+1,\varepsilon}$ of the equation obtained by replacing the singular equation of (P_{2n+1}) by the more regular equation

$$(u_{2n+1,\varepsilon})_t = ((u_{2n+1,\varepsilon})^m)_{xx} + (u_{2n})^{m-1}(u_{2n+1,\varepsilon}) - \beta_\varepsilon(u_{2n+1,\varepsilon}),$$

where $\beta_\varepsilon(r)$ is a regular nonnegative and bounded function, approximating $M/2$ times the Dirac delta. Moreover, it is not difficult to show that

$$u_{2n+1}(x,t) \geq U(x,t) \text{ for any } n \text{ and a.e. } (x,t) \in \mathbb{R}^+ \times (0,T), \tag{2.21}$$

where $U(x,t)$ is the (bounded) solution of

$$\begin{cases} U_t = (U^m)_{xx} - \frac{M}{2}\delta_{\partial\{U(t,\cdot)=0\}}, & \mathcal{D}'(\mathbb{R}^+ \times (0,T)), \\ U(x,0) = u_0(x) & \text{a.e. } x \in (0,+\infty), \\ U_x(0,t) = 0, U(x,t) \to 0 = \text{ as } x \to +\infty & \text{a.e. } t \in (0,T), \end{cases}$$

obtained by approximating the equation

$$U_{\varepsilon t} = ((U_\varepsilon)^m)_{xx} - \beta_\varepsilon(U_\varepsilon),$$

and passing to the limit as $\varepsilon \to 0$. Indeed, it is enough to apply the comparison principle (recall that $(u_{2n})^{m-1}(u_{2n+1}) \geq 0$) to the approximate solutions to show that $u_{2n+1,\varepsilon} \geq U_\varepsilon$ on $\mathbb{R}^+ \times (0,T)$ and then, passing to the limit, we obtain (2.21). Function U is bounded since if we introduce the function V, solution of the unperturbed problem

$$\begin{cases} V_t = (V^m)_{xx} & \mathcal{D}'(\mathbb{R}^+ \times (0,T)), \\ V(x,0) = u_0(x) & \text{a.e. } x \in (0,+\infty), \\ V_x(0,t) = 0, V(x,t) \to 0 \text{ as } x \to +\infty & \text{a.e. } t \in (0,T), \end{cases}$$

then we know that

$$0 \le U(x,t) \le V(x,t) \quad \text{for any } t \in [0,T] \text{ and a.e. } x \in \mathbb{R}^+.$$

Indeed, it is enough to multiply the difference of the equations verified by U and V, by an approximation of the test function $\text{sign}_+(V-U)$ and use that $\frac{M}{2}\delta_{\partial\{U(t,\cdot)=0\}}$ $\text{sign}_+(V-U) \le 0$. On the other hand, by applying the results of Benilan (1978), we derive

$$0 \le U(x,t) \le V(x,t) \le C\frac{\|u_0\|^{2/(m+1)}_{L^1(\mathbb{R}^+)}}{t^{1/(m+1)}} \text{ for any } t \in [0,T] \text{ and a.e. } x \in \mathbb{R}^+.$$

Note that we can write that $\{u_{2n+1}\}$ is a set of mild solutions satisfying

$$\begin{cases} (u_{2n+1})_t - ((u_{2n+1})^m)_{xx} = f_{2n+1}(t,x) & \mathcal{D}'(\mathbb{R}^+ \times (0,T)), \\ (u_{2n+1})(x,0) = u_0(x) & \text{a.e. } x \in (0,+\infty), \\ (u_{2n+1})_x(0,t) = 0,\ (u_{2n+1})(x,t) \to 0 \text{ as } x \to +\infty & \text{a.e. } t \in (0,T), \end{cases}$$

with f_{2n+1} uniformly integrable in $\mathcal{M}(0,+\infty)$ in the sense that

$$\|f_{2n+1}\|_{L^1((0,T):\mathcal{M}(0,+\infty))} \le K \quad \text{for any } n, \text{ for some } K > 0.$$

Then by a variation of the main result of Díaz and Vrabie (1989) (see also p. 70 of Vrabie 1987: both results concerning the special case in which f_{2n+1} is uniformly integrable in $L^1(0,+\infty)$), we obtain that $\{u_{2n+1}\}$ is a relatively compact set of $C([0,T]:L^1(\mathbb{R}^+))$. Then there exists a subsequence strongly convergent $\{u_{2n+1}\} \to u$ in $C([0,T]:L^1(\mathbb{R}^+))$. This, and the special construction of $\{u_{2n}(x,t)\}$, implies the *a priori* estimate

$$0 < C_{2n}(t) \le \left[\frac{M}{2\int_0^{+\infty}(U(x,t))^m dx}\right]^{1/(m-1)} \quad \text{for a.e. } t \in (0,T).$$

Moreover, at least under a physically natural assumption on the initial datum $u_0(x)$, we can ensure that $C_{2n}(t)$ is uniformly bounded from above by a positive function for each $t \in [0,T]$ (notice that we do not have such conclusion in the trivial case of $u_0(x) \equiv 0$). Indeed, let us assume that

$$u_0(x) > 0 \quad \text{for any } x \in [0,\zeta(0)). \tag{2.22}$$

Then, as function $U(t,.)$ satisfies $U_t(t,.) = (U^m(t,.))_{xx}$ on $(0,\zeta(t))$, and $m > 1$, we can apply a well-known local result (see Kalashnikov, 1987) showing that if $U(0,x_1) > 0$ then $U(t,x_1) > 0$ for any $t > 0$. In particular, we get that $U(t,x) > 0$, for any $x \in [0,\zeta(0))$ and for any $t > 0$. Thus, $\int_0^{+\infty}(U(x,t))^m\,dx > 0$ for any $t > 0$ and $0 < C_{2n}(t)$. This shows that $\{C_{2n}(t)\}$ is uniformly bounded (and uniformly far from zero) in $L^\infty(0,T)$ and so, there exists $C^*(t)$ such that $C_{2n}(.) \rightharpoonup C^*(.)$ weakly-* in $L^\infty(0,T)$. But, as $\{u_{2n+1}\} \to u$ strongly in $C([0,T]:L^1(\mathbb{R}^+))$ we obtain:

$$\lim_{n\to\infty} u_{2n}(x,t) = \lim_{n\to\infty} (C_{2n}(t)u_{2n-1}(x,t)) = \lim_{n\to\infty} C_{2n}(t) \lim_{n\to\infty} u_{2n-1}(x,t) = C^*(t)u(x,t).$$

Moreover, we can read the algorithm as

$$(u_{2n+1})_t = ((u_{2n+1})^m)_{xx} + C_{2n}(t)^{m-1}(u_{2n-1})^{m-1}(u_{2n+1}) - \frac{M}{2}\delta_{\partial\{(u_{2n+1})(t,\cdot)=0\}},$$

and so we get (by the Lebesgue's dominated convergence theorem) that $(u_{2n-1})^{m-1}(u_{2n+1}) \to u^m$ in $L^1(\mathbb{R}^+ \times (0,T))$.

In conclusion, we have shown

Theorem. *Assume that $u_0(x)$ satisfies (2.22), then, there exists a function $C^*(t) > 0$, $C^* \in L^\infty(0,T)$ and a function $u \in C([0,T] : L^1(\mathbb{R}^+))$ such that*

$$\begin{cases} u_t = (u^m)_{xx} + C^*(t)^{m-1}u^m - \frac{M}{2}\delta_{\partial\{u(t,\cdot)=0\}}, & \mathcal{D}'(\mathbb{R}^+ \times (0,T)), \\ u(x,0) = u_0(x) & a.e.\ x \in (0,+\infty), \\ u_x(0,t) = 0,\ u(x,t) \to 0 \text{ as } x \to +\infty & a.e.\ t \in (0,T), \end{cases}$$

and

$$C^*(t)^{m-1} \int_0^{+\infty} u(x,t)^m\, dx = \frac{M}{2}.$$

Remark. We do not know if $C^*(t) = 1$, but by a rescaling $\widetilde{t} = k(t)$, $y = Y(t,x)$ and $V = V(u,y,\widetilde{t})$ it is possible to reformulate the above equation in the terms

$$V_{\widetilde{t}} = (V^m)_{yy} + V^m - \frac{M}{2}\delta_{\partial\{V(\widetilde{t},\cdot)=0\}}.$$

3. Numerical Results

This section briefly describes the different techniques we used in the numerical resolution of the problem (*P*). For each initial condition h_0, we compute its mass, say $M/2$, and the associated stationary solution $v(x)$ given in (2.17) to which the solution should converge when $t \to +\infty$, (see Fowler *et al.*, 2007). As observed before, (P) is a free boundary problem with a non-local integral term and a Dirac's delta distribution in the absorption term. These characteristic features, along with the (*weak*) nature of the problem, suggest the development of the numerical resolution of the problem in the framework of finite elements. We first consider a time marching scheme in the coordinate t, of step dt. At each level in the time discretization, we shall employ a semi-implicit scheme in order to

deal with the nonlinearities. An iterative (splitting) numerical scheme is implemented in order to impose the mass conservation constraint. In order to discretize with respect to the coordinate x, at each time level $l\cdot\, dt$, we will employ piecewise linear finite elements $L_{l,k}:=\{\phi \in C^0([0,+\infty)):\phi|E \in \mathbf{P}_1,\ \forall\ E \in \mathbf{T}_{l,k}\}$ in a uniform grid, $\mathbf{T}_{l,k}$, of step k. Also, $\mathbf{B}_{l,k}:=\{\phi_i\}$ is a base of finite linear elements in $L_{l,k}$.

Then, the discretized problem is formulated as follows:

Find $(u_{l+1})_k \in L_{l,k}$, $(u_{l+1})_k = \sum_j (u_{l+1})_k^j \phi_j$, *such that*

$$\int_{\mathbf{T}_{l,k}} (u_{l+1})_k \phi_i\, dx = \int_{\mathbf{T}_{l,k}} (u_l)_k \phi_i\, dx - \frac{3dt}{2} \int_{\mathbf{T}_{l,k}} (u_l)_k^{\frac{1}{2}} ((u_{l+1})_k)_x \phi_{ix}\, dx + dt \int_{\mathbf{T}_{l,k}} (u_{l+1})_k^{\frac{3}{2}} \phi_i\, dx - dt \int_{\mathbf{T}_{l,k}} \frac{M}{2} \delta(u_l) \phi_i\, dx, \forall \phi_i \in \mathbf{B_{l,k}}. \tag{3.23}$$

Note that δ is evaluated at the boundary obtained in the previous time step. In order to deal with the nonlinearities present in (3.23), as above stated and taking into consideration the mass conservation constraint, we shall consider the following iterative scheme: for $p = 2n+1$ from 1 to N, $n = 0,\ 1,\ 2\ldots$, and N an odd number to be fixed, we consider the problem

$$\int_{\mathbf{T}_{l,k}} (u_{l+1,2n+1})_k \phi_i\, dx = \int_{\mathbf{T}_{l,k}} (u_l)_k \phi_i\, dx - \frac{3dt}{2} \int_{\mathbf{T}_{l,k}} (u_{l+1,2n})_k^{\frac{1}{2}} ((u_{l+1,2n+1})_k)_x \phi_{ix}\, dx + dt \int_{\mathbf{T}_{l,k}} (u_{l+1,2n})_k^{\frac{1}{2}} (u_{l+1,2n+1})_k \phi_i\, dx - dt \int_{\mathbf{T}_{l,k}} \frac{M}{2} \delta(u_l) \phi_i\, dx, \forall \phi_i \in \mathbf{B_{l,k}}, \tag{3.24}$$

where $(u_{l+1,2n})_k$ has been rescaled before being introduced in (3.23) so that $\int (u_{l+1,2n}) k^{3/2} = M/2$ according to (P_{2n}), i.e., $(u_{l+1,2n})_k = C_{l+1,2n}(u_{l+1,2n\text{-}1})_k$. The resulting system of equations for the nodal values at the $(2n+1)$th-step is solved with the Gauss-Seidel method. In order to initiate the iterative scheme, one can take as $(u_{l+1,p=1})_k$ the values obtained in the previous time step, that is to say, $(u_{l+1,p=1})_k = u_l$. The scheme finishes assuming the values for the $(l+1)$-time level given by $u_{l+1} = (u_{l+1,p=N})_k$.

In Figure 3 we present the numerical results obtained considering as an initial condition the function $u_0(x) = 1 - x^2$, where we have plotted the graphics obtained for different steps in time. The results reveal the convergence, as expected, to the support of the stationary solution in a monotonic way. We also can see how the maximum of the solution does not blow up (by the contrary, it is decreasing in time in this special case).

In Figures 4 and 5, we present 3-D graphics of the results corresponding to $u(x,\ t)$ and $-u(x,t)$, respectively. We also present two tables in which we show results concerning the values of the constant of the scaling at the final step N and the location of the boundary for different levels in time.

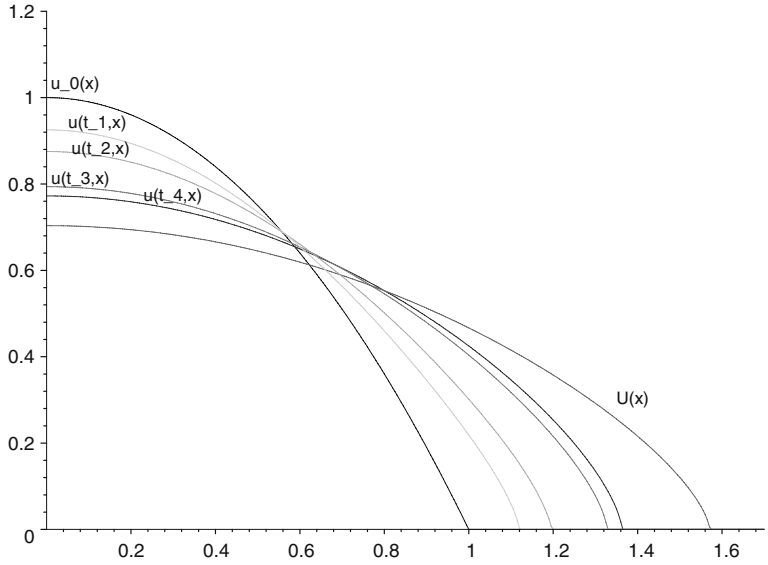

Figure 3
Numerical results obtained for $u(x, t)$ for different time levels. The initial condition is labelled by u_0 and the stationary solution by u.

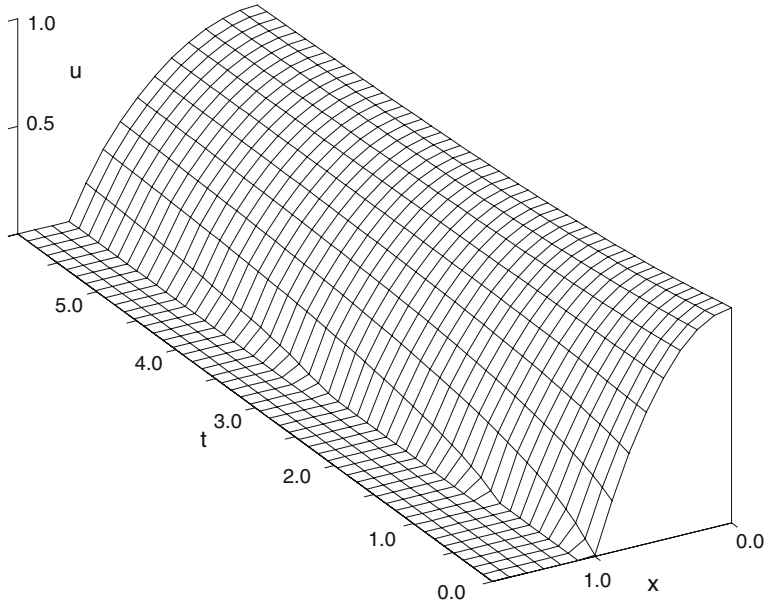

Figure 4
3-D representation of the numerical results obtained for $u(x, t)$.

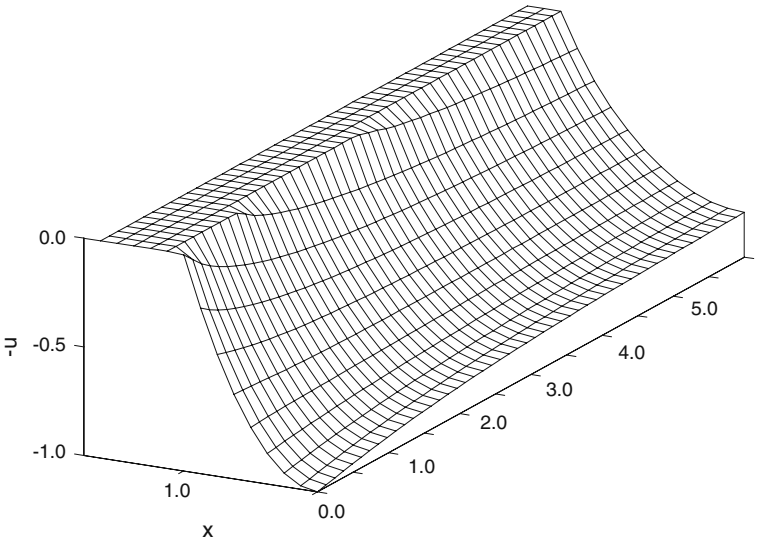

Figure 5
3-D representation of the numerical results obtained for $-u(x, t)$.

3.1. Summary and Conclusions

A coupled model describing the evolution of the topographic elevation and the depth of the overland water film is studied here when considering the overland flow of water over an erodible sediment. The instability of the spatially uniform solution corresponds to the formation of rills, which in reality then grow and coalesce to form large-scale river channels.

We started by considering the deduction and mathematical analysis of a deterministic model describing river channel formation and the evolution of its depth. We complete the previous modeling of the problems by SMITH and BRETHERTON (1972) and FOWLER *et al.* (2007), obtaining a model which involves a degenerate nonlinear parabolic equation (satisfied on the interior of the support of the solution) with a superlinear source term and a prescribed constant mass. We propose here a global formulation of the problem (formulated in the whole space, beyond the support of the solution) which allows us to show the existence of a solution and leads to a suitable numerical scheme for its approximation. As we show, the solution does not blow up despite the presence of the superlinear forcing term at the equation thanks to the mass constraint.

A particular feature of the model for channel evolution which we have studied is that the degeneracy of the equation causes the channel width to be self-selecting. This is of some interest in the geomorphological literature, since the issue of channel width determination is one that has caused some difficulties (e.g., PARKER, 1978).

Table 1

Time (t)	Results for C_N
1.0	1.00000071770833
2.0	1.00000061614692
3.0	1.00000056130953
4.0	1.00000051022114
5.0	1.00000050094979
6.0	1.00000046809999

Table 2

Time (t)	Location of the boundary (x)
1.0	1.31999997049570
2.0	1.36999996937811
3.0	1.37499996926036
4.0	1.38849999690422
5.0	1.38999996893108
6.0	1.39499996881932

Acknowledgments

The research of the four authors was partially supported by the projects MTM2005-03463 of the DGISGPI (Spain). A. C. F. acknowledges the support of the Mathematics Applications Consortium for Science and Industry (http://www.macsi.ul.ie) funded by the Science Foundation Ireland mathematics initiative grant 06/MI/005. The research of J.I.D., A.I.M and E.S. was also supported by the project CCG07-UCM/ESP-2787 of the DGUIC of the CAM and the UCM.

References

Benilan, P. (1978), *Operateurs accretifs et semigroups dans les espaces L^p*, Functional Analysis and Numerical Analysis, France-Japan Seminar (H. Fujita, ed.), Japan Society for the Promotion of Science, Tokio, pp. 15–53.

Birnir, B., Smith, T. R., and Merchant, G. E. (2001), *The scaling of fluvial landscapes*. Comput. Geosci. *27*, 1189–1216.

Caffarelli, L. A., Lederman, C., and Wolanski, N. (1997), *Pointwise and viscosity solutions for the limit of a two-phase parabolic singular perturbation problem*, Indiana Univ. Math. J. *46*(3), 719–740.

Caffarelli, L. A. and Vázquez, J. L. (1995), *A free-boundary problem for the heat equation arising in flame propagation*, Trans. Amer. Math. Soc. *347*(2), 411–441.

Díaz, J. I., Fowler, A. C., Muñoz, A. I., and Schiavi, E., Article in preparation.

Díaz, J. I., Padial, J. F., and Rakotoson, J. M. (2007), *On some Bernouilli free boundary type problems for general elliptic operators*, Proc. Roy. Soc. Edimburgh *137A*, 895–911.

Díaz, J. I. and Vrabie, I. (1989), *Proprietés de compacité de l'opérateur de Green généralisé pour l'équation des milieux poreux*, Comptes Rendus Acad. Sciences, París *309*, Série I, 221–223.

Evans, L. C. and Gariepy, R. F., *Measure Theory and Fine Properties of Functions* (Studies in Advanced Mathematics, CRC Press, Boca Raton, 1992).

Fowler, A. C., Kopteva, N., and Oakley, C. (2007), *The formation of river channels*, SIAM J. Appl. Math. *67*, 1016–1040.

Howard, A. D. (1994), *A detachment-limited model of drainage basin evolution*, Water Resour. Res. *30*, 2261–2285.

Izumi, N. and Parker, G. (1995), *Inception and channellization and drainage basin formation: Upstream-driven theory*, J. Fluid Mech. *283*, 341–363.

Izumi, N. and Parker, G. (2000), *Linear stability analysis of channel inception: Downstream-driven theory*, J. Fluid Mech. *419*, 239–262.

Kalashnikov, A. S. (1987), *Some problems of the qualitative theory of second-order nonlinear degenerate parabolic equations*, Uspekhi Mat. Nauk *42*, 135–176.

Kramer, S. and Marder, M. (1992), *Evolution of river networks*, Phys. Rev. Lett. *68*, 205–208.

Loewenherz, D. S. (1991), *Stability and the initiation of channelized surface drainage: A reassessment of the short wavelength limit*, J. Geophys. Res. *96*, 8453–8464.

Loewenherz-Lawrence, D. S. (1994), *Hydrodynamic description for advective sediment transport processes and rill initiation*, Water Resour. Res. *30*, 3203–3212.

Nazaret, B. (2001), *Heat flow for extremal functions in some subcritical Sobolev inequalities*, Appl. Anal. *80*, 95–105.

Meyer-Peter, E. and Müller, R. (1948), *Formulas for bed-load transport*, Proc. Int. Assoc. Hydraul. Res., 3rd Annual Conference, Stockholm, 39–64.

Parker, G. (1978), *Self-formed straight rivers with equilibrium banks and mobile bed, Part 1. The sand-silt river*, J. Fluid Mech. *89*, 109–125.

Samarski, A. A., Galaktionov, V. A., Kurdyumov, S. P., and Mikhailov, A. P., *Blow-up in quasilinear parabolic equations* (Walter de Gruyter, Berlin, 1995).

Smith, T. R., Birnir, B., and Merchant, G. E. (1997), *Towards an elementary theory of drainage basin evolution: II. A computational evaluation*, Comput. Geosci. *23*, 823–849.

Smith, T. R. and Bretherton, F. P. (1972), *Stability and the conservation of mass in drainage basin evolution*, Water Resour. Res. *8, 11*, 1506–1529.

Tucker, G. E. and Slingerland, R. L. (1994), *Erosional dynamics, flexural isostasy, and long-lived escarpments: A numerical modeling study*, J. Geophys. Res. *99*, 12.229–12.243.

Vrabie, I. I., *Compactness Methods for Nonlinear Evolutions* (Pitman Longman, London, 1987).

Willgoose, G., Bras, R. L., and Rodríguez-Iturbe, I. (1991), *A coupled channel network growth and hillslope evolution model: I. Theory*, Water Resour. Res. *27*, 1671–1684.

(Received September 19, 2007, revised July 17, 2008, accepted August 14, 2008)
Published Online First: October 29, 2008

Pure appl. geophys. 165 (2008) 1683–1706
0033–4553/08/081683–24
DOI 10.1007/s00024-008-0395-8

Pure and Applied Geophysics

Asymmetric Delamination and Convective Removal Numerical Modeling: Comparison with Evolutionary Models for the Alboran Sea Region

JUAN-LUIS VALERA,[1] ANA-MARÍA NEGREDO,[1] and ANTONIO VILLASEÑOR[2]

Abstract—Convective removal and mantle delamination are geodynamical mechanisms proposed to explain the presence of extension in the Alboran Sea within a regional context of compression. Using a new thermo-mechanical algorithm, we present here a quantitative evaluation and comparison of conceptual models based on these geodynamical mechanisms. In contrast to the *in situ* convective removal process, the laterally propagating delamination mechanism is shown here to be consistent with first-order features of the Alboran Sea such as the thinning/thickening distribution, intermediate-depth seismicity and upper mantle structure imaged by seismic tomography. The lower crust is predicted to reach depths of 100–150 km in some areas, due to mechanically-driven viscous drag of the downwelling mantle.

Key words: Delamination, convective removal, numerical modeling, Alboran Sea.

1. Introduction

The evolution of the Alboran Sea has attracted keen interest during recent years due to its complexity. Despite the regional framework of compression between the African and Eurasian plates during the early and middle Miocene, this zone underwent extension and thinning of a previously thickened crust. The extension was active simultaneously with thrusting and shortening of the external zones of the Betic and Rif Chains (e.g., GARCÍA-DUEÑAS *et al*., 1992; COMAS *et al*., 1992). The present-day structure in the region is characterized by the presence of thinned continental crust, varying from 35-km thick beneath the internal zones of the Betic and Rif Chains to 15–20 km beneath the central Alboran Sea, and by thinned lithospheric mantle, varying from less than 50 km in the easternmost Alboran Basin to more than 140 km in the Gibraltar Arc-West Alboran Basin region. This characterization was obtained by TORNÉ *et al*. (2000) on the basis of a three-dimensional gravity and elevation modeling combined with heat flow, using the assumption of local isostasy. These results agree with those obtained by FULLEA *et al*.

[1] Dept. of Geophysics, Facultad CC. Físicas, Universidad Complutense de Madrid. Av. Complutense, 28040 Madrid, Spain. E-mail: jlvalera@fis.ucm.es; anegredo@fis.ucm.es

[2] Instituto de Ciencias de la Tierra 'Jaume Almera', CSIC, Lluís Solé i Sabarís, s/n. 08028 Barcelona, Spain. E-mail: antonio@ija.csic.es

(2007), who used elevation and geoid anomaly data to determine the crustal and lithospheric thickness, also under the assumption of local isostasy. Moreover, the three-dimensional model from FULLEA (2008), which integrates elevation and geoid anomaly data together with thermal field, predicts higher lithospheric thickness under the Gibraltar Arc, exceeding 180 km under the Strait of Gibraltar.

Different authors have proposed several conceptual models to explain the Neogene evolution of the Alboran Sea. Here we briefly summarize the most representative. A first class of models proposes a mechanism of convective removal (Fig. 1a; HOUSEMAN and MOLNAR, 2001 and references therein for a detailed explanation of this mechanism). Following PLATT and VISSERS (1989), the convergence between Africa and Eurasia created an orogen that was gravitationally unstable because its lithospheric root was colder and denser than the surrounding mantle. As a result, the lithospheric root sunk in the surrounding mantle and was replaced by less dense asthenospheric material. The detached material sunk into the asthenosphere leaving a thickened crust underlain by a thinned lithospheric mantle.

A second set of models is based on the delamination mechanism (GARCÍA-DUEÑAS *et al.*, 1992; DOCHERTY and BANDA, 1995; SEBER *et al.*, 1996; MÉZCUA and RUEDA, 1997; PLATT *et al.*, 1998). The physical process of delamination was introduced by BIRD (1979). This author proposed that, given an asthenospheric conduit through the lithospheric mantle connecting the asthenosphere with the lower crust, the asthenospheric material would expand laterally along the base of the crust, peeling away the lithospheric mantle which would sink into the surrounding asthenosphere due to the density contrast. To explain the results of their detailed seismic tomography study, CALVERT *et al.* (2000) proposed a conceptual model for the evolution of the Alboran Sea, based on a modification of the model from PLATT and VISSERS (1989). This evolutive model proposed a mechanism of asymmetric delamination of a lithospheric mantle previously thickened by the convergence between Africa and Eurasia (Fig. 1b). According to this model the observed intermediate-depth seismicity takes place at the upper part of a lithospheric slab sinking into the asthenosphere.

Different studies of P- and S-wave seismic tomography reveal that this intermediate-depth seismicity is located in an area of low seismic velocity, which has been interpreted as indicating active subduction of continental crust below the Betic Chain and Alboran Sea (SERRANO *et al.*, 1998; MORALES *et al.*, 1999). At greater depths (between 200 and 700 km), a number of tomographic studies (e.g., BLANCO and SPAKMAN, 1993; CALVERT *et al.*, 2000; SPAKMAN and WORTEL, 2004) have shown a high seismic velocity anomaly below the Betic Chain and Alboran Sea, oriented approximately SW-NE and dipping towards the SE. These studies also show the presence of a low-velocity anomaly beneath the southeastern coast of the Iberian Peninsula, which has been associated with a detachment process of the slab, due to a delamination (Fig. 1b; CALVERT *et al.*, 2000) or subduction process (SPAKMAN and WORTEL, 2004).

Figure 2 shows a vertical cross-section of the P-wave global tomographic model of VILLASEÑOR *et al.* (2003) across the Gibraltar Arc and the Alboran Sea. The tomographic model has been obtained using the same method described in BIJWAARD *et al.* (1998), but

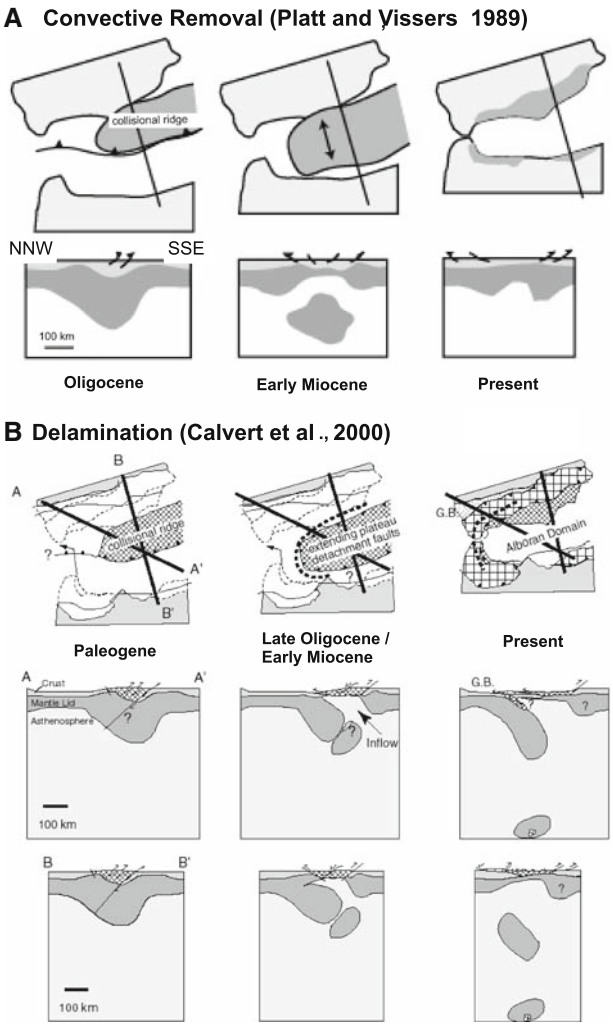

Figure 1
Conceptual models proposed for the evolution of the Alboran Sea analyzed in this paper (from CALVERT *et al.*, 2000). (a) Model that explains the evolution using the mechanism of convective removal. (b) Model based on the delamination mechanism.

using a much larger dataset of arrival times of earthquakes listed in the bulletins of the International Seismological Centre (ISC) reprocessed using the EHB methodology (ENGDAHL *et al.*, 1998). The vertical section runs NW-SE and is approximately perpendicular to the strike of the high P-wave velocity anomaly observed in the upper mantle beneath the Betic Chain and the Alboran Sea. This section roughly coincides with the AA' section used by CALVERT *et al.* (2000) to illustrate their continental delamination model (Fig. 1b). This tomographic image is consistent with previous studies (SERRANO

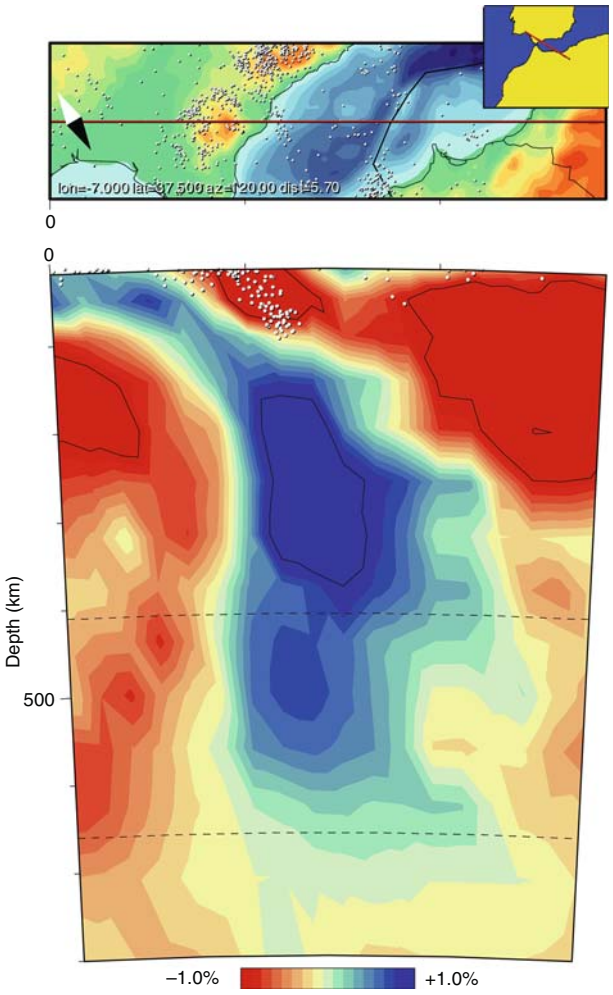

Figure 2
Vertical sections of the global P-wave tomographic model of VILLASEÑOR *et al.* (2003) across the Gibraltar Arc and the Alboran Sea. The tomographic model has been obtained using the same method described in BIJWAARD *et al.* (1998), but using a much larger data set of arrival times of earthquakes listed in the bulletins of the International Seismological Centre (ISC) reprocessed using the EHB methodology (ENGDAHL *et al.*, 1998). The contour interval is 1%. White dots are the projection over the tomographic image of earthquakes occurring in a 100-km wide band, centered on the section.

et al., 1998; MORALES *et al.*, 1999) showing that intermediate-depth seismicity occurs in an area of low P-wave velocity.

A third set of models explains the evolution of this region as the result of the roll-back of an east-dipping subduction, either active (e.g., GUTSCHER *et al.*, 2002) or extinguished (e.g., LONERGAN and WHITE, 1997), of continental (MORALES *et al.*, 1999) or oceanic lithosphere (e.g., GUTSCHER *et al.*, 2002; DUGGEN *et al.*, 2003, 2004, 2005) reaching the

present position of the Gibraltar Arc (e.g., LONERGAN and WHITE, 1997) or the Horseshoe Seamounts in the eastern Atlantic (e.g., ROYDEN, 1993) or the central Gulf of Cadiz (GUTSCHER *et al*., 2002).

In this study we have developed and applied a MATLAB numerical code named TEMESCH capable of simulating the thermo-mechanical evolution of the lithosphere during *in situ* convective removal and asymmetric, laterally-propagating delamination processes to evaluate, in a quantitative and comparative way, convective removal and delamination conceptual models and to investigate which geodynamical process is in better agreement with first-order features of the Alboran Sea. For the delamination case, our aim is to numerically reproduce the conceptual model proposed by CALVERT *et al*., (2000), considering that this is the most consistent conceptual model of delamination among those proposed to explain the evolution of this zone.

It is important to note that the aim of this modeling is not to reproduce in a very detailed fashion the evolution of such a complex region, with a remarkable three-dimensional geometry at lithospheric scale, but to quantitatively evaluate geodynamical processes which involve the entire upper mantle. For these processes, according to the seismic velocity structure and the proposed conceptual models, the two-dimensional flow hypothesis adopted in this study is acceptable as a first-order approximation.

By adopting a viscous approach instead of an elastic one, we are not able to model significant aspects of subduction such as the coupling between the upper and subducting plates. Therefore, we focus on the comparison between the proposed mechanisms of convective removal and delamination. We will compare our results with tomographic images of the region, seismicity distribution, and crustal and lithospheric mantle thinning/thickening distribution.

2. Governing Equations

Physically, delamination and convective removal are the consequence of the balance of buoyancy forces. Therefore they can be described by the conservation equations of mass (1), momentum (2) and energy (3).

$$\frac{1}{\rho}\frac{D\rho}{Dt} = \frac{\partial u_k}{\partial x_k}, \tag{1}$$

$$\frac{\partial \sigma_{ij}}{\partial x_j} + \rho g \delta_{iz} = \frac{D(\rho u)_i}{Dt} \tag{2}$$

$$\rho T \frac{Ds}{Dt} = \Phi + \frac{\partial q_i}{\partial x_i} + \rho H. \tag{3}$$

Here ρ is the density; t is the time; u_k the k-th component of the velocity vector; σ, the stress tensor; g is the acceleration of gravity; T, the temperature; s, the entropy; Φ is the

viscous dissipation or shear heating; q is the heat flow; H, the internal heat production; and x_k denotes the spatial coordinates: x for horizontal, z for vertical, which is positive downwards, in the same direction as gravity.

We have developed a dynamically and thermally self-consistent code that solves the equations of conservation of mass, momentum and energy in a coupled fashion. Our mathematical formulation is based on that of SCHMELING (1989) but here we have developed it in a dimensional fashion.

The stress tensor σ can be expressed in terms of the sum of isotropic and deviatoric stresses. The isotropic stresses have been assumed to be equal to the lithostatic pressure P and the deviatoric stresses are related to the strain rate tensor $\dot{\varepsilon}$ by

$$\sigma_{ij} = -P\delta_{ij} + 2\mu\dot{\varepsilon}_{ij}, \tag{4}$$

where μ is the viscosity of the fluid. The strain rate $\dot{\varepsilon}_{ij}$ is calculated as

$$\dot{\varepsilon}_{ij} = \frac{1}{2}\left(\frac{\partial u_i}{\partial x_j} + \frac{\partial u_j}{\partial x_i}\right). \tag{5}$$

We have applied the following hypothesis. First, we have assumed two-dimensional flow. Second, we have neglected the inertial forces (this hypothesis can only be applied to very viscous flows, that is, to fluids with very high Prandtl number). Third, we have applied the Extended Boussinesq Approximation (EBA). According to the Standard Boussinesq Approximation (BOUSSINESQ, 1903), density variations may be neglected except when they are coupled to the gravitational acceleration in the buoyancy force. Following SCHMELING (1989) the EBA differs from the Standard Boussinesq Approximation in that the thermal effect of compression is also accounted for (e.g., TRITTON, 1988; SCHMELING, 1989; ITA Y KING, 1994). Neglecting the inertial forces in a viscous flow under the EBA implies that the fluid is incompressible, which simplifies the equation of the conservation of mass.

Therefore, equation (2) is transformed to

$$\frac{\partial}{\partial x_j}\left[-P\delta_{ij} + \mu\left(\frac{\partial u_i}{\partial x_j} + \frac{\partial u_j}{\partial x_i}\right)\right] + \rho g\delta_{iz} = 0. \tag{6}$$

The viscous dissipation, according to our hypothesis, can be expressed as

$$\Phi = \tau_{ij}\frac{\partial u_i}{\partial x_j} = 8\mu\dot{\varepsilon}_{ij}\dot{\varepsilon}_{ij} \tag{7}$$

being τ_{ij} the deviatoric stresses.

Our code takes into account the phase transformation from olivine to high-pressure polymorphs with spinel structure, whose final stage is the ringwoodite or γ-olivine. For the sake of simplicity, we will always use the term spinel to refer to these polymorphs.

To take into account the heating effect of this transformation, the entropy term was expanded as

$$\frac{Ds}{Dt} = \frac{C_P}{T}\frac{DT}{Dt} - \frac{\alpha}{\rho}\frac{DP}{Dt} + \frac{L_T}{T}\frac{D\beta}{Dt}, \tag{8}$$

where C_p is the heat capacity; α, the thermal expansion coefficient; L_T is the latent heat released in the transformation, β is the fraction of transformed material in the phase transition (therefore, spinel) which is only dependent on temperature and depth. Consequently, we have included temperature, phase-transformation and pressure terms. Expanding the material derivatives of equation (8) and assuming constant hydrostatic pressure, equation (3) can be rewritten as

$$\rho C_P\left(\frac{DT}{Dt} + \frac{\alpha T u_z g}{C_P}\right) + \rho L_T\left(\frac{\partial\beta}{\partial T}\frac{DT}{Dt} + \frac{\partial\beta}{\partial z}u_z\right) = 8\mu\dot{\varepsilon}_{ij}\dot{\varepsilon}_{ij} + \frac{\partial}{\partial x_i}\left(k\frac{\partial T}{\partial x_i}\right) + \rho H, \tag{9}$$

where k is the thermal conductivity.

Under the mentioned assumptions, the equation for the conservation of the mass and momentum is combined and simplified to obtain the Navier-Stokes system of equations (10):

$$\begin{aligned}\frac{\partial P}{\partial x} &= \frac{\partial}{\partial x}\left[\mu\left(\frac{\partial u_x}{\partial x} + \frac{\partial u_x}{\partial x}\right)\right] + \frac{\partial}{\partial z}\left[\mu\left(\frac{\partial u_x}{\partial z} + \frac{\partial u_z}{\partial x}\right)\right]\\ \frac{\partial P}{\partial z} + \rho g &= \frac{\partial}{\partial x}\left[\mu\left(\frac{\partial u_z}{\partial x} + \frac{\partial u_x}{\partial z}\right)\right] + \frac{\partial}{\partial z}\left[\mu\left(\frac{\partial u_z}{\partial z} + \frac{\partial u_z}{\partial z}\right)\right].\end{aligned} \tag{10}$$

Following the classical procedure of applying cross-derivatives and, then, subtracting both equations, we are able to remove the pressure term. We rewrote the equation using the stream function Ψ, and obtained a nonlinear, fourth-order motion equation. Rearranging and simplifying terms, the resulting system of equations is reduced to the following:

$$\frac{\partial}{\partial x}(\rho g) = 4\frac{\partial^2}{\partial x\partial y}\left[\mu\frac{\partial^2}{\partial x\partial y}\Psi\right] + \left(\frac{\partial^2}{\partial y^2} - \frac{\partial^2}{\partial x^2}\right)\left[\mu\left(\frac{\partial^2}{\partial y^2} - \frac{\partial^2}{\partial x^2}\right)\Psi\right] \tag{11}$$

$$\begin{aligned}&\left(1 + \frac{L_T}{C_P}\frac{\partial\beta}{\partial T}\right)\left(\frac{\partial T}{\partial t} + u_x\frac{\partial T}{\partial x} + u_z\frac{\partial T}{\partial z}\right)\\ &= \frac{H}{C_P} - \frac{1}{\rho C_P}\frac{\partial}{\partial x_i}\left(k\frac{\partial T}{\partial x_i}\right) + \left(\frac{\alpha g}{C_P}T - \frac{L_T}{C_P}\frac{\partial\beta}{\partial z}\right)u_z + \frac{8\mu}{\rho C_P}e_{xz}e_{xz},\end{aligned} \tag{12}$$

where the velocity u is related to the stream function Ψ by

$$u_x = \frac{\partial\Psi}{\partial y} = \Psi_y; \quad u_y = -\frac{\partial\Psi}{\partial x} = -\Psi_x. \tag{13}$$

The heat sources considered here are the terms in the right-hand side of (12) which correspond to: the radiogenic heat production, the heat conduction, the adiabatic heating, the latent heat released in the phase transition (plus the term with L_T on the left-hand side of the equation) and the shear heating or viscous dissipation. The values of the parameters used are listed in Table 1.

Table 1

Fixed parameters used in the calculations

Symbol	Meaning	Value
g	Acceleration of gravity	9.8 m s^{-2}
Q_b	Basal heat flow	0.014 W m^{-2}
b	b-parameter of Rüpke Law	15
H_p	Crustal radiogenic heat production	8×10^{-7} W m^{-3}
$\Delta\rho_{ol\text{-}sp}$	Density change due to ol-sp phase transition	181 kg m^{-3}
	Horizontal extent	1376 km
L_T	Latent heat released in olivine-spinel transformation	-9×10^4 J/Kg
L	Lithospheric thickness	120 km.
	Lower bound for the viscosity	10^{17} Pa s
$h_{\_LC}$	Lower Crust thickness	22 km
w_{max_L}	Maximum amplitude of the Lithospheric Mantle perturbation	121.8 km
$w_{max\_\ LC}$	Maximum amplitude of the Lower Crust perturbation	33 km
$w_{max\_\ UC}$	Maximum amplitude of the Upper Crust perturbation	15 km
x_{pert}	Position of the perturbation	688 km
c_P	Specific heat	1.3×10^3 J K^{-1} kg^{-1}
T_0	Temperature at the base of the lithosphere	1350°C
k	Thermal conductivity	3.2 W m^{-1} K^{-1}
α	Thermal expansion coefficient	3.7×10^{-5} K^{-1}
	Time step	0.25 Ma
	Upper bound for the viscosity	2.5×10^{22} Pa s
$h_{\_UC}$	Upper Crust thickness	15 km
	Vertical extent	680 km
λ	Wavelength of the perturbation	487.2 km

Density and viscosity are strongly temperature-dependent and are responsible for the coupling between the motion (11) and thermal (12) equations. Our modeled domain includes four different layers: upper crust, lower crust, lithospheric mantle and asthenosphere (with asthenosphere we refer to the entire sublithospheric upper mantle). In all cases presented here, constant values of viscosity and density were assumed for the upper and lower crust (see Table 2). These values take into account the mobility

Table 2

Variable parameters used in each model

		Upper Crust	Lower Crust	Lithospheric Mantle	Asthenosphere
T-independent model	Density (kg m^{-3})	2800	3050	3225	3200
	Viscosity (Pa s)	10^{23}	10^{20}	10^{22}	10^{20}
T-dependent model	Reference density (at T = 0 °C) (kg m^{-3})	2800	3050	3400	3400
	Reference viscosity μ_0 (Pa s)	10^{23}	10^{20}	2.5×10^{19}	2.5×10^{19}

of the lower crust and the stiffness of the upper crust (e.g., SCHOTT and SCHMELING, 1998; MAROTTA *et al*., 1998). The boundary between the lithospheric mantle and the asthenosphere is only a thermal boundary and therefore we have assumed no chemical difference between them. When we considered a temperature- and chemically-dependent density, the equation of state was

$$\rho = \rho_0(1 - \alpha T) + \Delta\rho_{ol-rw}\beta, \tag{14}$$

where ρ_0 is the reference density and $\Delta\rho_{ol\text{-}sp}$ is the difference between spinel and olivine density, neglected if this transformation is not considered. In the mantle, following RÜPKE *et al*. (2004), we have used a Newtonian temperature-dependent (exponential) viscosity law and augmented it with a pressure dependence that crudely simulates an increase in viscosity beneath 450 km:

$$\mu(T, z) = \mu_0\mu(z)\exp\left[b\left(\frac{T_0}{T} - 1\right)\right], \tag{15}$$

$$\mu(z) = 1 + \left(\frac{250 - 1}{2}\right)\{1 + \tanh[0.01(z - 450)]\}, \tag{16}$$

where μ_0 is a reference viscosity for each layer, b is a parameter characterizing the temperature dependence of viscosity, and T_0 is the reference temperature at the base of the lithospheric mantle. The maximum and minimum values allowed for the viscosity in the mantle were fixed to 2.5×10^{22} Pa s and 10^{17} Pa s, respectively. The values of fixed and variable parameters are given in Tables 1 and 2, respectively.

When the phase transition is considered, to calculate the fraction of spinel β and its derivatives at any temperature and depth, and the depth at which phase transformation occurs, we followed the approach described by SCHMELING *et al*. (1999) and TEZLAFF and SCHMELING (2000). More details are given by NEGREDO *et al*. (2004).

Despite the fact that the conservation equations of mass, momentum and energy must be solved in a coupled way, for a better comprehension of the physical processes involved, we have first evaluated separately the buoyancy due to thermal effects and the buoyancy due to chemical differences. Therefore, we first present some runs using temperature-independent values for density and viscosity for each material. By doing so, it was unnecessary to solve the thermal equation (12) to obtain the velocity field, so we were using a somehow purely 'dynamical version' of the program TEMESCH. After that, we present here other runs with temperature-dependent density and viscosity for the lithospheric mantle and asthenosphere, solving the fully coupled system of equations (11) and (12). In the models presented here, for the sake of simplicity, we neglected shear heating and the latent heat release during the olivine to spinel transformation, consequently these terms were neglected in equation (12). However, we do include one example in which the olivine-spinel phase transformation in the transition zone is considered, taking into account the density increase and the latent heat release.

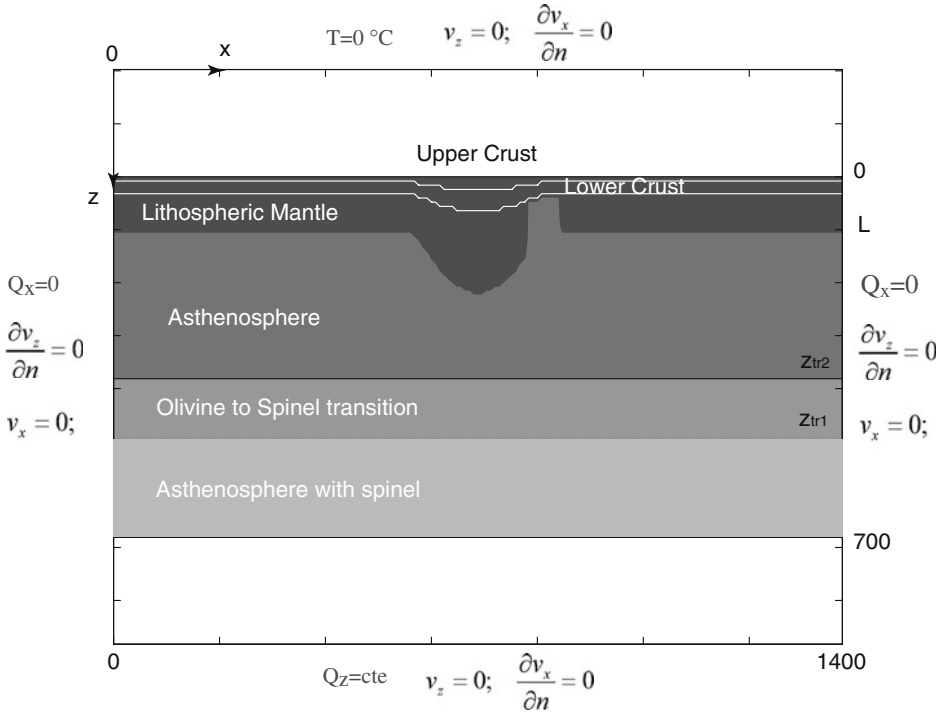

Figure 3
Model domain illustrating the initial geometry and boundary conditions. Free slip (zero shear stress) boundary conditions are considered at all boundaries. The thermal boundary conditions are fixed temperature at surface and heat flow constant at the base, and zero horizontal heat flow at the side boundaries.

3. Numerical Approach

To solve the equation of motion we have applied a second-order, central finite-difference scheme. We considered free slip (zero shear stress) boundary conditions at all boundaries (Fig. 3). The solution of the equation on each node was then computed in terms of the 12 nearest nodes. The system matrix was square, symmetric and diagonally dominant, with only 12 non-null diagonals. This system could be solved by a very robust method based on a LU triangular factorization by Gaussian elimination with partial pivoting, which is already implemented in the standard MATLAB code.

To solve the thermal equation we have applied a second order, central ADI scheme. ADI stands for Alternative Difference Implicit Method and solves implicitly the dependent variable in one direction at time $p + 1/2$ and, afterwards, in the other direction at time $p + 1$. Each step is solved by applying the Thomas Algorithm (see NEGREDO *et al.*, 2004 for further details). The boundary thermal conditions consisted of a fixed temperature at the surface and constant heat flow at the base. We imposed zero horizontal heat flow at the side boundaries (Fig. 3).

We have used two different grids: An Eulerian grid with fixed nodes and a Lagrangian grid with moving markers carrying the material properties. The Eulerian grid was a Cartesian box of aspect ratio 2 (1376 $\times$ 680 km) with 173 $\times$ 86 nodes in the x and z directions and a step size of 8 km. The Lagrangian grid had three times more markers than nodes in each direction. The horizontal extent of the box was chosen to be large enough to prevent boundary effects.

The initial state considered for the convective removal model mimics the presence of an area of orogenic lithosphere with both crustal and lithospheric roots. This orogenic root can be explained as the unsupported part of a subducting slab, (e.g., SCHOTT and SCHMELING, 1998) or as lithospheric mantle thickened due to convergence (e.g., HOUSEMAN and MOLNAR, 2001). However, in both cases, we consider that convergence has already ceased. We start with an initial distribution of material according to which an initial temperature state is computed. Following SCHOTT and SCHMELING (1998), we assume an orogenic cosine-shaped root in the physical model. The wave amplitude w of the perturbation is computed with this expression:

$$w = h + w_{\max} \cos\left(\frac{2\pi\left(x - x_{\text{pert}}\right)}{\lambda}\right), \tag{17}$$

where h is the non-perturbed width of the layer; $w_{\max}$ is the maximum amplitude variation; x is the horizontal coordinate; x_{pert} is the horizontal position of the perturbation (usually at the center of the box); and λ is the wavelength of the perturbation (see Table 1). The lower crust, the upper crust and the initial (unperturbed) lithospheric mantle thicknesses are modified according to this equation to mimic a lithospheric root. The perturbed thickness of each layer doubles its initial thickness. In this way we have an initial maximum crustal thickness of 64 km in the orogenic zone, consistent with the 60 km crustal thickness obtained from the thermal calculation of PLATT *et al*. (1998). The isotherms of each layer are displaced downwards following the thickness of the layer. We considered an adiabatic temperature profile for the asthenosphere. This initial state differs from that considered by MORENCY and DOIN (2004), who introduced a crustal structure superimposed and forced on the computed thermal initial state. The values assumed in each run for density and viscosity can be found in Table 2. They are in general agreement with values given in the lithospheric modeling by TORNÉ *et al*. (2000) and by FULLEA (2008).

For the lower crust we have chosen relatively high values for the density, consistent with values commonly used for the lithospheric modeling of orogenic zones (e.g., JIMÉNEZ-MUNT *et al.*, 2008) or for numerical models of evolution of orogens (e.g., SCHOTT and SCHMELING, 1998). To avoid the numerical complexities associated with dealing with numerous bodies, we have adopted the same density values in the non-perturbed zone. The mean crustal density in the nonperturbed zone (2950 kg/m^3) is significantly higher than any values deduced for the region. However, we have performed tests that show that these high values insignificantly affect the results, as long as the evolution of the model is mainly controlled by the characteristics of the thickened zone.

The convergence of the results has been checked varying the spatial and time resolution. In addition, sensitivity tests have been performed to choose the spatial resolution which provides a good compromise between accuracy of the solution and computing time. Like other similar codes (e.g., SCHMELING and MARQUART, 1991), TEMESCH becomes unstable with very strong viscosity contrasts. In our case, the instability is related to the used interpolation algorithms. We have performed more than thirty runs combining different interpolation methods. The best results were obtained using MATLAB Method V4 for interpolation from nodes to markers and linear interpolation from markers to nodes. The V4 Method, based on the algorithm of SANDWELL (1987), is optimized for interpolation from a regular grid to an irregular cloud of points, whereas it is too slow for the inverse process.

4. Results of Models with Constant Density and Viscosity

4.1. Convective Removal Model

The first conceptual model we have investigated with this 'dynamical version' of the code is the convective removal model. The initial state was described previously. The constant values for the density and viscosity for each layer are listed in Table 2. The evolution is shown in Figure 4. The cold, dense lithospheric root sinks progressively into the asthenosphere, reaching the base of the upper mantle. After 30 Ma of evolution, according to our numerical model this mechanism produces insignificant lithospheric or crustal thinning. There is no detachment, in contrast with the proposed conceptual model, although the lithospheric mantle is dragged until 350 km depth. In the discussion we will explain these results in more detail.

4.2. Delamination Model

The results for the delamination model with the 'dynamical version' of the code are more interesting. Our goal is to test physically the conceptual model of delamination from CALVERT *et al.* (2000). To do this, we begin with the same initial state as in the convective removal model however, following BIRD (1979), we impose a vertical 'conduit' connecting the lower crust with the asthenosphere. This 'conduit' is shown to be crucial to trigger the delamination process by allowing the ascent of asthenospheric material to replace the denser lithospheric material.

The constant values for the density and viscosity for each layer are listed in Table 2. The calculated evolution (Fig. 5) is completely different from that obtained for the convective removal model (Fig. 4). After 30 Ma of evolution, the asthenosphere is in contact with the lower crust, which likely produces topographic uplift and extension. The crust is thinned in some areas, and this thinning is accommodated by the less viscous lower crust. There is a strong suction of lower crust material dragged by the down-going

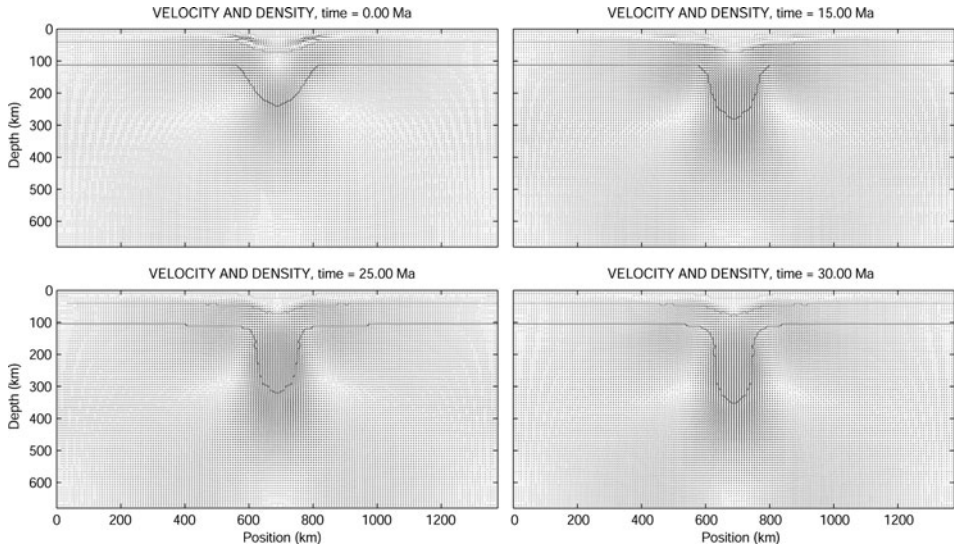

Figure 4
Evolution of the convective removal mechanism with constant parameters. The initial state shows a perturbation simulating an orogen in which crust and lithospheric mantle have doubled their initial thickness. Arrows show the velocity field and lines are for equal density. Continuous line indicates, from top to bottom, the base of the upper crust, the base of the lower crust and the base of the lithospheric mantle. After 30 Ma of evolution, no significant lithospheric or crustal thinning is not obtained.

lithosphere to large depths. We have not included any transformation (e.g. eclogitization) which would have increased the density and varied the viscosity of the crustal material. However, this simplistic model with temperature-independent density and viscosity is shown here to properly reproduce the first order characteristics of the conceptual model proposed by CALVERT *et al.* (2000). Further explanations of model predictions for the delamination process are given for the more realistic models assuming temperature-dependent density and viscosity.

5. Results of Models with Temperature-dependent Density and Viscosity

5.1. Convective Removal Model

We have applied the fully coupled thermo-mechanical version of the program TEMESCH to the convective removal model in order to evaluate the influence of the temperature dependence of density and viscosity. The viscosity and density vertical profiles at the initial state, for a nonperturbed column and for a column located at the center of the perturbation, are shown in Figure 6. We consider the same initial state as in the previous dynamical case and the evolution is qualitatively very similar.

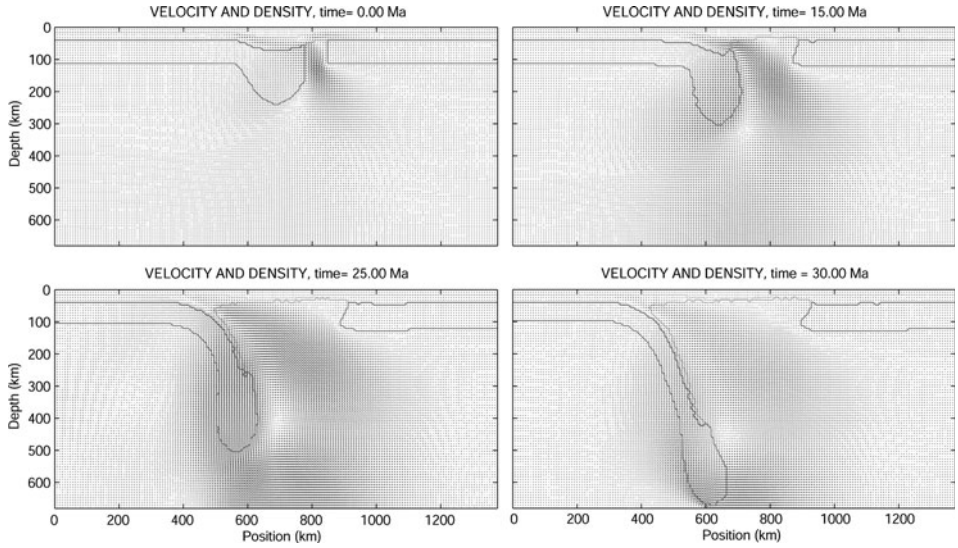

Figure 5
Evolution of the delamination mechanism with constant parameters. The same initial state as the previous model is used, except that we have imposed a conduit connecting the lower crust with the asthenosphere. The layer limits are the same as in Figure 3. After 30 Ma, lower crust thinning is reproduced and there is lower crust material dragged down by the lithospheric slab to great depths.

Figure 7 shows the results obtained for this model. Similarly to the results of the model with constant parameters, the lithospheric root sinks progressively into the asthenosphere, with in significant lithospheric mantle or crustal thinning and without any detachment. After 30 Ma of evolution the lithospheric mantle is dragged down to the base of the upper mantle.

5.2. Delamination Model

The last model presented in this paper is the delamination model with temperature-dependent density and viscosity. We impose the same temperature, viscosity and density initial distributions as in the convective removal temperature-dependent model, except for the asthenospheric 'conduit' introduced at the right side of the lithospheric root.

We use the same initial structure as in the previous temperature-independent case and the modeled evolution is qualitatively similar (Fig. 8). In a first stage of the process (0–15 Ma), the asthenospheric mantle rises through the 'conduit' and forces the lateral migration of the lower crust towards the left, while the lithospheric root sinks slowly into the asthenosphere. In a second stage (15–25 Ma) the lithospheric root is deep and heavy enough to sink into the asthenosphere faster than in the first stage. This lithospheric material drags down the lower crust and accelerates the lateral migration of the uppermost part of the lower crust towards the left.

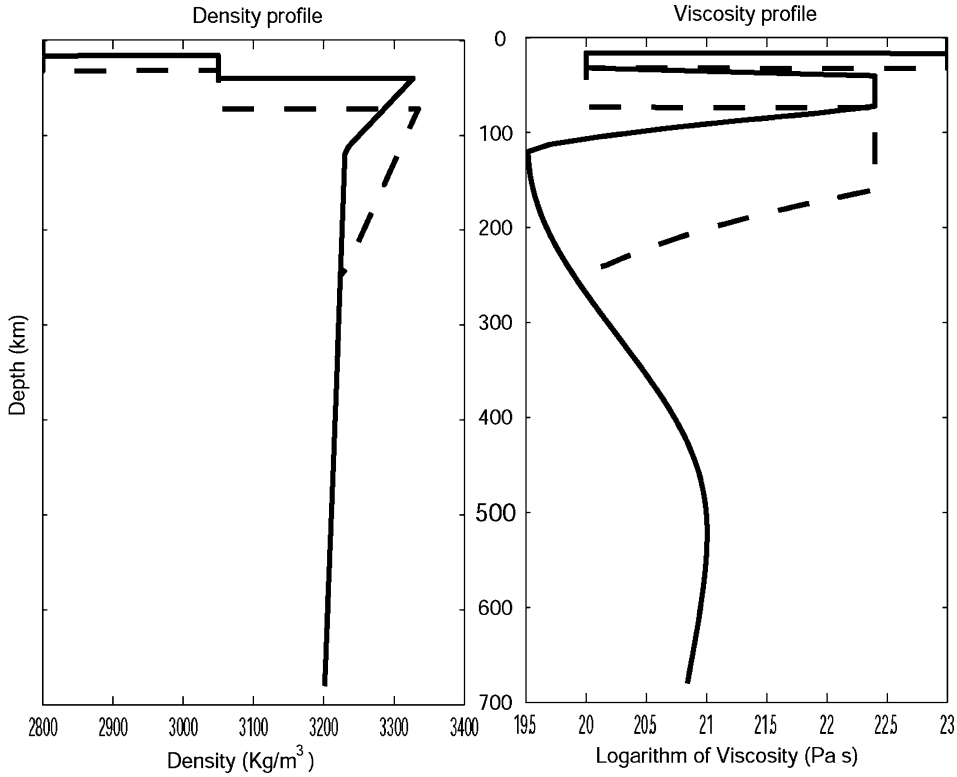

Figure 6
Viscosity and density vertical profiles of the initial state for temperature-dependent models for an unperturbed column (solid line) and for a column located at the centre of the perturbation (dashed line).

After 30 Ma of evolution, the temperature-dependent model properly reproduces the conceptual model of delamination proposed by CALVERT *et al*. (2000). The lower crust material is dragged by the down-going lithosphere to about 150 km depth. Because the slab tends to equilibrate thermally with the surrounding mantle, the viscous drag exerted on the lower crust is reduced with respect to the model with constant density and viscosity (Fig. 5). For this reason the lower crust now reaches much shallower depths.

The sensitivity tests that we have performed reveal that lateral migration of the position of the delaminating slab is required to obtain significant crustal and mantle lithospheric thinning. This migration only occurs for relatively low values of viscosity in the lower crust, lithospheric mantle and asthenosphere, as those used in the models presented. For high values of viscosity, the predicted evolution is similar to the convective removal model, in which *in situ* sinking of the lithospheric root occurs without producing lithospheric thinning.

The area of maximum lithospheric thinning migrates towards the location of downwelling mantle, whereas lithospheric mantle material is progressively recovered by

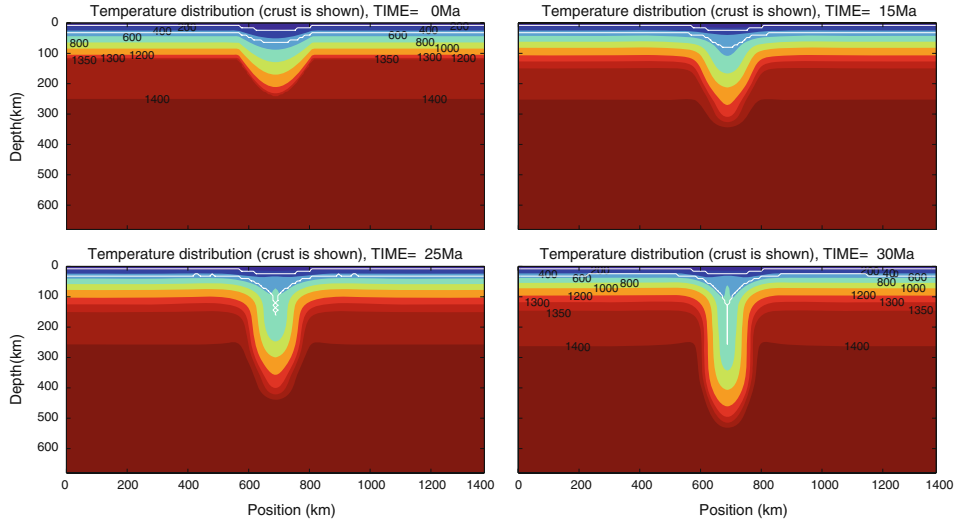

Figure 7

Evolution of the convective removal model with temperature-dependent parameters. White lines show the bases of the upper and lower crust. Lithospheric thinning or crustal thinning is not observed. The lithospheric mantle descends until the base of the upper mantle without detachment from the upper material.

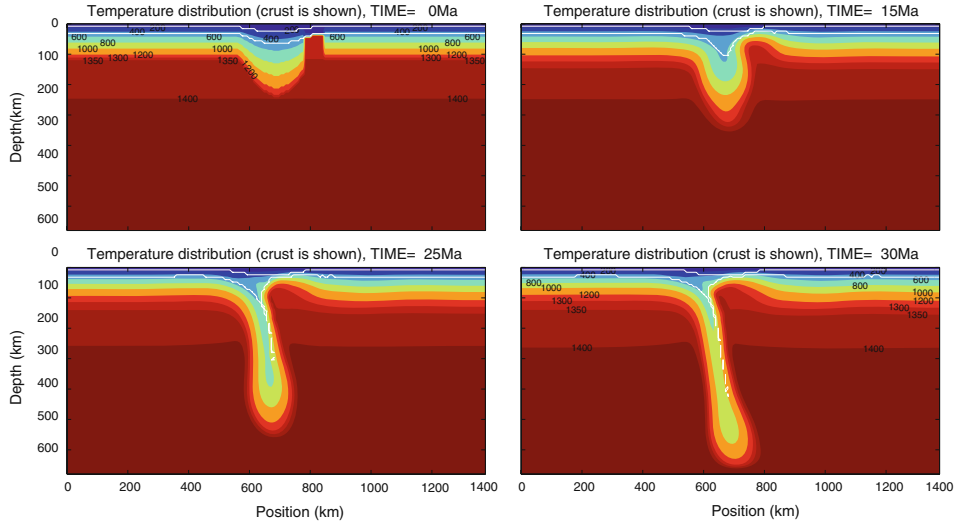

Figure 8

Evolution of the delamination model with temperature-dependent parameters. There is lower crust material dragged down by the lithospheric slab until about 150 km depth. Lithospheric mantle is progressively recovered by thermal relaxation under the lower crust.

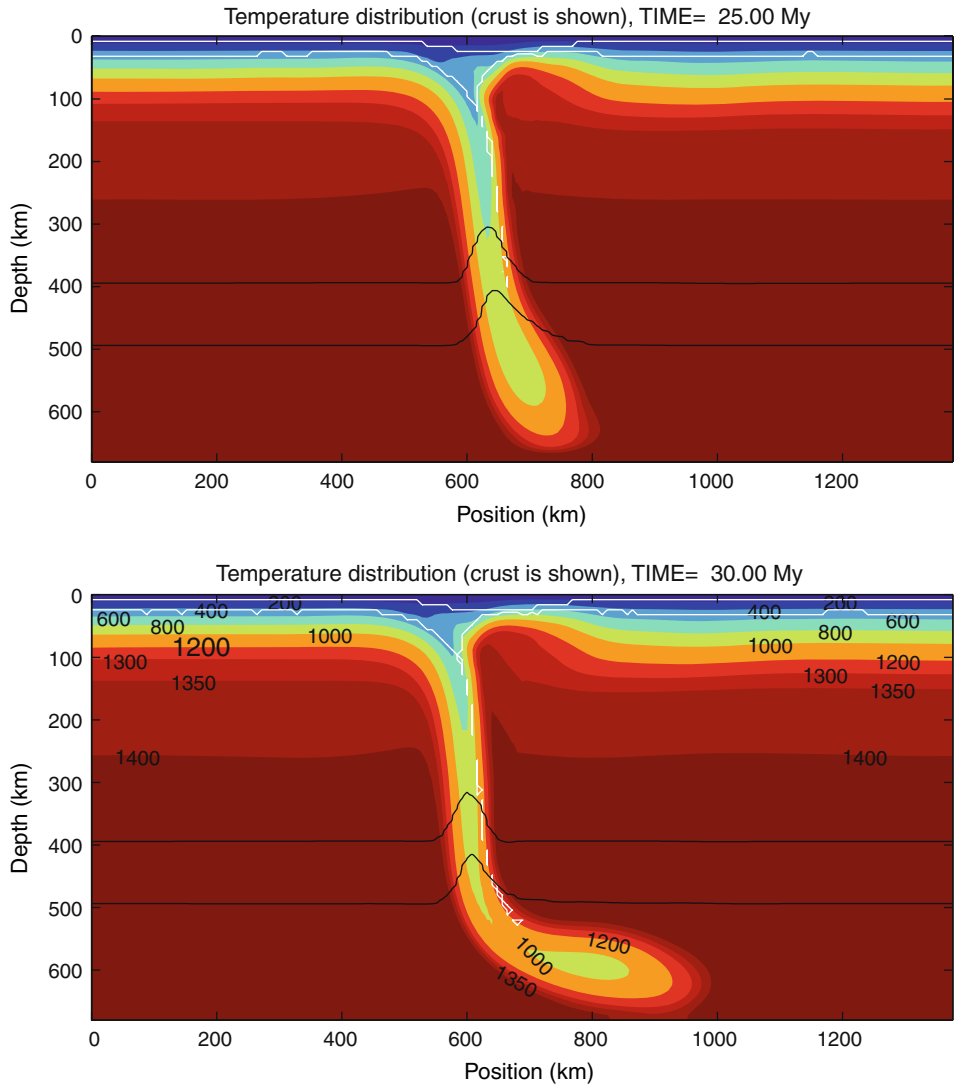

Figure 9

Evolution of the delamination model with the same parameters as in Figure 8, excepting that we include the density increase and the latent heat release associated with the olivine-spinel phase transformation. The increased negative buoyancy of the slab accelerates downwelling. Therefore, the slab reaches the base of the upper mantle at about 25 Ma, earlier than in previous runs. After that, the deepest portion of the slab deflects to move horizontally. Contours for 1% and 99% of spinel are also shown.

thermal relaxation in the area of initiation delamination (x $\approx$ 800 km). Therefore, the area affected by lithospheric mantle thinning in this model (Fig. 8) is narrower than the region in which the asthenosphere is in contact with the lower crust in the model with

temperature-independent parameters (Fig. 4). This difference between both models is expected to strongly influence the uplift/subsidence evolution inferred using both approaches.

Figure 9 illustrates a delamination model with exactly the same parameters as in Figure 8, except in that we include the density increase and the latent heat released associated with the olivine-spinel phase transformation in the transition zone. The increased negative buoyancy of the slab accelerates downwelling, and the slab reaches the base of the upper mantle at about 25 Ma. When this occurs, the deepest portion of the slab deflects and begins to move horizontally.

6. Discussion

In this study we have performed a quantitative study of the processes of convective removal and continental delamination, commonly proposed as responsible for the Neogene evolution of the Alboran Sea. Because we have used the same methodology for both processes, we are able to discuss, in comparative terms, the geodynamic implications from our modeling. It is important to note that we are not trying to model in detail the evolution of such a complex zone, but to quantitatively evaluate geodynamical processes which involve the entire upper mantle. From the modeling results presented here (and bearing in mind the hypothesis and approximations used) we obtain that the only process able to produce significant crustal and mantle lithosphere thinning is delamination with lateral migration of the lithospheric slab.

Associated with this thinning our modeling also predicts significant crustal thickening caused by lower crust material dragged down by the lithospheric slab. This deep lower crust material is likely affected by high rates of internal strain and could therefore be related to the occurrence of intermediate-depth earthquakes (with maximum depths of about 130 km) in the western part of the Alboran Sea. These earthquakes exhibit near-vertical tensional axes (Buforn *et al.*, 1991), which is compatible with the negative buoyancy of the delaminated slab. On the other hand, a number of studies using seismic reflection and refraction and potential field data show that the thicknes of the lower crust in this region is not larger than 35–40 km (Torné *et al.*, 2000; Fullea *et al.*, 2007; and references therein). It is worth noting that our model predicts a narrow zone for the dragging of the lower crust which is compatible with the narrow band of the intermediate-depth seismicity. Moreorer, the dragged lower crust presumably undergoes high pressure metamorphism which increases its density with respect to the typical values for the lower crust (see discussion in Leech, 2001). For this reason the capability of the seismic and potential field studies for detecting a crustal structure like the one predicted by our modeling is unclear.

As we have shown, the presence of the vertical asthenospheric ‘conduit’ through the lithospheric mantle is crucial to reproduce the delamination process. It triggers the delamination by allowing the hotter and less dense asthenospheric material to replace

the colder and denser lithospheric material. Different mechanisms have been proposed to enable the ascent of asthenospheric material to the base of the crust. TURCOTTE (1983) proposed that the asthenosphere can rise through a volcanic line associated with a subduction zone. SCHOTT and SCHMELING (1998) introduced a wide low viscosity zone of about 200 km width to enhance the input of asthenospheric material into the Moho. These authors proposed that this 'low viscosity zone' was the relict of a previous subduction in which the dehydration reactions in the slab minerals released water, creating a hydrated low viscosity zone above the slab. In contrast with these authors, we assume that the conduit consists of asthenospheric material (Fig. 5). In this sense, ARCAY *et al*. (2007) performed 2-D numerical thermo-mechanical modeling of subduction, including the mantle wedge flow and the weakening effect in the mantle rocks due to the presence of water. Their results demonstrates that this weakening can produce a strong thermal thinning in the upper plate above the hydrated zone. This kind of process would be consistent, once continental collision has occurred, with the initial geometry of our model of the asymmetric delamination.

There is a clear similarity between the upper mantle structure mapped in the tomographic image from VILLASEÑOR *et al.* (2003) (Fig. 2) and that one predicted by he delamination model after 30 Ma of evolution (Fig. 8), with a mantle lithosphere slab reaching the base of the upper mantle. The low velocity anomaly above the slab is consistent with predicted continental lower crust material dragged down by the downwelling mantle to depths of about 100–150 km. In this scenario, intermediate-depth seismicity is likely related to high strain rates in this continental crust.

Interestingly, a very similar west-east tomographic cross section in the same area has been interpreted by GUTSCHER *et al*. (2002) as mapping a slab of Mesozoic oceanic lithosphere. Following these authors, the low velocity anomaly above the slab would be consistent with induced corner flow in the asthenospheric wedge. As pointed out by CALVERT *et al*. (2000), the tomography results alone do not allow discrimination between subduction and delamination processes, as both likely produce very similar velocity signatures. However there is a feature that, to our understanding, clearly undermines the oceanic subduction interpretation and it is the fact that intermediate-depth earthquakes do not describe a typical Wadati-Benioff zone along the upper part of the oceanic slab, but are located in the low-velocity area interpreted by GUTSCHER *et al*. (2002) as asthenospheric wedge.

The continuity of the high P-wave velocity anomaly along the upper mantle shown in this tomographic cross section (Fig. 2) also indicates that detachment of the lithospheric root, as postulated in the convective removal conceptual model (Fig. 1A; PLATT and VISSERS, 1989), has not occurred, at least in the area of the Gibraltar Arc.

Our physical-numerical modeling successfully reproduces the main features of the conceptual model of delamination proposed by CALVERT *el al*. (2000) (Fig. 1B), although we are unable to obtain the detachment of the slab, under the eastern part of the Betic Chain proposed by these authors. Moreover, we are not able to reproduce

with the assumed hypothesis (e.g., linear rheology) the evolution of a convective removal process as proposed by PLATT and VISSERS (1989) (Fig. 1A). According to our modeling the lithospheric root sinks to the base of the model domain without being detached from the overlying lithosphere and without producing significant lithospheric thinning. This result coincides with those from numerous previous studies of the evolution of lithospheric roots, which show that the high lithospheric viscosity does not allow for significant thinning of the lithospheric mantle, using neither linear (MAROTTA *et al.*, 1998, 1999) nor nonlinear (CONRAD and MOLNAR, 1997; SCHOTT and SCHMELING, 1998) rheologies. Even in the models by MAROTTA *et al.* (1999), where a mechanical detachment of the lithospheric root is forced by introducing in the upper part of the root a low viscosity (due to high temperature) viscosity channel, a significant lithospheric mantle thinning is not obtained. According to SCHOTT and SCHMELING (1998), only when using a *weak quasi brittle* rheology in the lithosphere is it possible to obtain significant thinning in the lithospheric mantle and detachment of the lithospheric root. These authors explain this weak rheology as due to the possible presence of free water, which would decrease the pore pressure, allowing for a reduction in the brittle strength.

GEMMER and HOUSEMAN (2007) present a purely dynamic model for the evolution of the Alpine-Carpathian-Pannonian system. This region shares interesting characteristics with the Alboran and Betic-Rif Chains region, such as the basin formation simultaneously with the contractional deformation of the surrounding orogens. According to this model, the presence of a low density crustal root (created by the Europe-Adria convergence) caused asthenospheric upwelling under the basin and lithospheric mantle downwelling under the surrounding orogens. The final geometry is very similar to that created by a delaminated slab or a retreating subducting zone. Again, the models by GEMMER and HOUSEMAN (2007) require extremely low values for the viscosity of the lithospheric mantle (about 2×10^{20} Pa s), in order to obtain significant crustal and lithospheric mantle thinning below the basin.

The main limitation of our modeling is that the assumed 2-D flow and other approximations do not allow for a detailed modeling of the evolution of the Alboran Sea region, which shows a complex 3-D lithospheric structure. However, we have focused on processes that affect the entire upper mantle, without considering their interaction with processes that mainly affect the lithosphere, like the NNO-SSE convergence between Africa and Eurasia. Our approach has been to evaluate quantitatively different conceptual models previously proposed to explain the geodynamical evolution of the Alboran Sea, and to discuss which model better agrees with first-order features of the region. As regards proposed subduction models, our viscous flow modeling is not appropriate to evaluate proposed models of subduction and slab roll-back, which would require incorporating, in a mechanically consistent fashion, the coupling between the subducting and overriding plates to allow subduction migration and upper plate extension.

7. Conclusions

We have developed a new numerical algorithm that allow us to evaluate quantitatively and comparatively two conceptual models commonly proposed to explain the Neogene evolution of the Alboran Sea. We have compared our numerical results with observations in the region like tomographic images, intermediate-depth seismicity, crustal and distribution of lithospheric mantle thickening/thinning to analyze which geodynamical mechanism better agrees with first-order features of the region.

The model designed to reproduce convective removal predicts downwelling of the lithospheric root until the base of the upper mantle without being detached from the overlying material, and without producing significant crustal or mantle lithosphere thinning. In contrast, our physical-numerical modeling indicates that the model of continental mantle lithosphere delamination with lateral migration of the delaminated slab (as proposed in the conceptual model by CALVERT *et al*., 2000, Fig. 1B) successfully reproduces first-order features of the evolution of the Alboran Sea, such as the crustal and mantle lithosphere thinning in the area of the basin occurring simultaneously with crustal thickening above the downwelling mantle lithosphere slab. This crustal thinning/thickening is mainly accommodated by the less viscous lower crust.

The lower crust, despite its low density, is predicted to sink to depths of 100–150 km due to mechanically-driven viscous drag of the downwelling lithospheric mantle slab. Delamination model predictions are also consistent with the upper mantle structure imaged by seismic tomography (Fig. 2). In contrast with studies that suggest active subduction of oceanic lithosphere (e.g., GUTSCHER *et al*., 2002), which are also compatible with tomographic images, the continental delamination model is consistent with intermediate-depth seismicity occurring in an area of low seismic velocity. In agreement with previous studies (e.g., SERRANO *et al*., 1998), we infer from our modeling that this seismicity is related to the presence of highly strained continental crust.

Acknowledgments

This work was funded by the Spanish Plan Nacional del MEC projects CTM2006-13666-C02-02/MAR and CTM2005-08071-C03-03/MAR; and funding for UCM Research Groups. This is a contribution of the Consolider-Ingenio 2010 team CSD2006-00041 (TOPO-IBERIA). J. L. Valera acknowledges the support of a UCM grant. Figure 2 has been made with the graphic program P developed by Wim Spakman. Calculations were partially carried out in the Fiswulf cluster of the Faculty of Physics. Many thanks to the Editor for his patience and assistance. We thank M. FERNÁNDEZ for discussions and two anonymous referees for their thorough reviews which greatly facilitated enhancement of the manuscript.

References

Arcay, E., Tric, E., and Doin, M.-P. (2007), *Slab surface temperature in subduction zones: Influence of the interplate decoupling depth and upper plate thinning processes*., Earth Planet. Sci. Lett., *255*, 324–338.

Bijwaard, H., Spakman, W., and Engdahl, E.R. (1998), *Closing the gap between regional and global travel-time tomography*, J. Geophys. Res. *103*, 30055–30078.

Bird, P. (1979), *Continental delamination and the Colorado Plateau*, J. Geophys. Res. *84*, 7561–7571.

Blanco, M.J. and Spakman, W. (1993), *The P-wave velocity structure of the mantle below the Iberian Peninsula: evidence for subducted lithosphere below southern Spain*, Tectonophysics *221*, 13–34.

Boussinesq, J., *Théory analytique de la chaleur mise en harmonie avec la thermodynamique et avec la théory de la lumière*, Volume II (Gauthier-Villars, Paris. 1903).

Buforn, E., Udias, A., and Madariaga, R. (1991), *Intermediate and deep earthquakes in Spain*, Pure Appl. Geophys. *136*, 375–393.

Calvert, A., Sandvol, E., Seber, D., Barazangi, M., Roecker, S., Mourabit, T., Vidal, F., Alguacil, G., and Jabour, N. (2000), *Geodynamic evolution of the lithosphere and upper mantle beneath the Alboran region of the western Mediterranean: Constraints from travel time tomography*, J. Geophys. Res. *105*, 10871–10898.

Conrad, C.P. and Molnar, P. (1997), *The growth of Rayleigh–Taylor-type instabilities in the lithosphere for various rheological and density structures*, Geophys. J. Internat. *129*, 95–112.

Comas, M. C., García-Dueñas, V., and Jurado, M. J. (1992), *Neogene tectonic evolution of the Alboran Basin from MCS data*, Geo. Mar. Lett. *12*, 157–164.

Docherty, C. and Banda, E. (1995), *Evidence for eastward migration of the Alboran Sea based on regional subsidence analysis: A case for basin formation by delamination of the subcrustal lithosphere?* Tectonics *14*, 804–818.

Duggen, S., Hoernle, K., van den Bogaard, P., Rüpke, L. and Phipps-Morgan, J. (2003), *Deep roots of the Messinian salinity crisis*, Nature *422*, 602–606.

Duggen, S., Hoernle, K., van den Bogaard, P., and Harris, C. (2004), *Magmatic evolution of the Alboran Region: The role of subduction in forming the western Mediterranean and causing the Messinian Salinity Crisis*, Earth Planet. Sci. Lett. *218*, 91–108.

Duggen, S., Hoernle, K., van den Bogaard, P., and Garbe-Schönberg, D. (2005), *Post-collisional transition from subduction to intraplate-type magmatism in the westernmost Mediterranean: Evidence for continental-edge delamination of subcontinental lithosphere*, J. Petrol. *46*, (6), 1155–1201, doi: 10.1093/petrology/egi013.

Engdahl, E.R., van der Hilst, R., and Buland, R.P. (1998), *Global teleseismic earthquake relocation with improved travel times and procedures for depth determination*, Bull. Seismol. Soc. Am. *88*, 3295–3314.

Fullea, J. (2008), *Development of numerical methods to determine the litospheric structure combining geopotential, litosthatic and heat transport equations. Application to the Gibraltar arc system*, P.h.D, Univ. Barcelona, 240 pp.

Fullea, J., Fernàndez, M., Zeyen, H., and Vergés, J. (2007), *A rapid method to map the crustal and lithospheric thickness using elevation, geoid anomaly and thermal analysis. Application to the Gibraltar Arc System, Atlas Mountains and adjacent zones*, Tectonophysics *430*, 97–117.

García-Dueñas, V., Balanyá, J. C., and Martínez-Martínez, J. M. (1992), *Miocene extensional detachments in the outcropping basement of the northern Alboran basin (Betics) and their tectonic implications*, Geo. Mar. Lett. *12*, 88–95.

Gemmer, L. and Houseman, G.A. (2007), *Convergence and extension driven by lithospheric gravitacional instability: Evolution of the Alpine–Carpathian–Pannonian system*, Geophys. J. Internat., *168*, 1276–1290.

Gutscher, M.-A., Malod, J., Rehault, J.-P., Contrucci, I., Klingelhoefer, F., Mendes-Victor, L., and Spakman, W. (2002), *Evidence for active subduction beneath Gibraltar*, Geology *30*, (12), 1071–1074.

Houseman, G. and Molnar, P. (2001), *Mechanisms of lithospheric rejuvenation associated with continental orogeny*. In (Miller, J.A., Holdsworth, R.E., Buick, I.S., and Hand, M., eds) *Continental Reactivation and Reworking*, Geological Society, London Special Publications *184*, 13–38.

Ita, J. and King, S.D. (1994), *Sensitivity of convection with an endothermic phase change to the form of governing equations, initial conditions, boundary conditions and equation of state*. J. Geophy. Res. *99*, 15919–15938.

JIMÉNEZ-MUNT, I., FERNÀNDEZ, M., VERGÉS, J., and PLATT, J.P. (2008), *Lithosphere structure underneath the Tibetan plateau inferred from elevation, gravity and geoid anomalies*, Earth Planet. Sci. Lett. *267*, 276–289.

LEECH, M.L. (2001), *Arrested orogenic development: Eclogitization, delamination, and tectonic collapse*, Earth Planet. Sci. Lett. *185*, 149–159.

LONERGAN, L. and WHITE, N. (1997), *Origin of the Betic-Rif mountain belt*, Tectonics *16*, 504–522.

MAROTTA, A.M., FERNÁNDEZ, M., and SABADINI, R. (1998), *Mantle unrooting in collisional settings*, Tectonophys. *296*, 31– 46.

MAROTTA, A.M., FERNÀNDEZ, M., and SABADINI, R. (1999), *The onset of extension during lithospheric shortening: A two-dimensional thermomechanical model for lithospheric unrooting*, Geophys. J. Interna. *139*, 98–114.

MÉZCUA, J. and RUEDA, J. (1997), *Seismological evidence for a delamination process in the lithosphere under the Alboran Sea*, Geophys. J. Int. *129*, F1–F8.

MORALES, J., SERRANO, I., JABALOY, A., GALINDO-ZALDIVAR, J., ZHAO, D., TORCAL, F., VIDAL, F. and GONZALEZ-LODEIRO, F. (1999), *Active continental subduction beneath the Betic Cordillera and Alboran Sea*, Geology *27*, 735–738.

MORENCY, C. and DOIN, M.-P. (2004), *Numerical simulations of the mantle lithosphere delamination*, J. Geophys. Res. *109*, B03410, doi: 10.1029/2003JB002414.

NEGREDO, A.M., VALERA, J.L., and CARMINATI, E. (2004), *TEMSPOL: A MATLAB thermal model for deep subduction zones including major phase transformations*, Computers and Geosciences *30*, 249–258.

PLATT, J.P., SOTO, J-I., WHITEHOUSE, M.J., HURFORD, A.J., and KELLEY, S.P. (1998), *Thermal evolution, rate of exhumation, and tectonic significance of metamorphic rocks from the floor of the Alboran extensional basin, western Mediterranean*, Tectonics *17*, 671–689.

PLATT, J. P. and VISSERS, R. L. M. (1989), *Extensional collapse of the thickened continental lithosphere: A working hypothesis for the Alboran Sea and Gibraltar Arc*, Geology *17*, 540– 543.

ROYDEN, L. H. (1993), *Evolution of retreating subduction boundaries formed during continental collision*, Tectonics *12*, 629–638.

RÜPKE, L. H., PHIPPS- MORGAN, J., HORT, M., and CONNOLLY, J. A. D. (2004), *Serpentine and the subduction zone water cycle*, Earth Planet. Sci. Lett. *223*, 17–34.

SANDWELL, D. T. (1987.), *Biharmonic spline interpolation of GEOS-3 and SEASAT altimeter data*, Geophys. Res. Lett. *2*, 139–142.

SCHMELING, H. (1989), *Compressible convection with constant and variable viscosity: The effect on slab formation, geoid and topography*, J. Geophys. Res. *94*(B9), 12463–12481.

SCHMELING, H., MONZ, R., and RUBIE, D.C. (1999), *The influence of olivine metastability on the dynamics of subduction*, Earth Planet. Sci. Lett. *165*, 55–66.

SCHMELING, H. and MARQUART, G. (1991), *The influence of second-scale convection on the thickness on continental lithosphere and crust*, Tectonophysics *189*, 281–306.

SCHOTT, B. and SCHMELING, H. (1998), *Delamination and detachment of a lithospheric root*, Tectonophysics *296*, 225–247.

SEBER, D., BARAZANGI, M., IBENBRAHIM, A., and DEMNATI, A. (1996), *Geophysical evidence for lithospheric delamination beneath the Alboran Sea and Rif-Betic mountains*, Nature *379*, 785–790.

SERRANO I., MORALES, J., ZHAO, D., TORCAL, F., and VIDAL, F. (1998), *P-wave tomographic images in the Central Betics-Alborán Sea (South Spain) using local earthquakes: Contribution for a continental collision*, Geophys. Res. Lett. *25*(21), 4031–4034.

SPAKMAN, W. and WORTEL, R., *A tomographic view on western Mediterranean geodynamics.* In *The TRANSMED Atlas. The Mediterranean Region from Crust to Mantle* (Cavazza, W., F. Roure, W. Spakman, G. Stampfli, and Ziegler, P., eds.), (Springer, 2004) pp. 31–52.

TEZLAFF, M., and SCHMELING, H. (2000), *The influence of olivine metastability on deep subduction of oceanic lithosphere*, Phys. Earth and Planet. Inter. *120*, 29–38.

TORNÉ, M., and BANDA, E. (1992), *Crustal thinning from the Betic Cordillera to the Alboran Sea*, Geo. Marine Lett. *12*, 76–81.

TORNÉ, M., FERNÁNDEZ, M., COMAS M. C., and SOTO, J. I. (2000), *Lithospheric structure beneath the Alboran Basin: Results from 3-D Gravity modeling and tectonic relevance*, J. Geophys. Res. *105* (B2), 3209–3228.

TRITTON, D.J., *Physical Fluid Dynamics* (Oxford Clarendon Press, Oxford Science Publications, 1988) pp 519.
VILLASEÑOR, A., SPAKMAN, W., and ENGDAHL, E.R. (2003, *Influence of regional travel times in global tomographic models*, Geophy. Res., Abstracts, *5*, EAE03-A-08614.

(Received September 19, 2007, revised July 17, 2008, accepted August 14, 2008)